UNIVERSITY OF SOUTHAMPTON

FACULTY OF SOCIAL, HUMAN AND MATHEMATICAL SCIENCES

Mathematical Sciences

Gravitational waves from deformed neutron stars: mountains and tides

by

Fabian Gittins

Thesis for the degree of Doctor of Philosophy

September 2021

UNIVERSITY OF SOUTHAMPTON

ABSTRACT

FACULTY OF SOCIAL, HUMAN AND MATHEMATICAL SCIENCES

Mathematical Sciences

Thesis for the degree of Doctor of Philosophy

GRAVITATIONAL WAVES FROM DEFORMED NEUTRON STARS: MOUNTAINS AND TIDES

by Fabian Gittins

With the remarkable advent of gravitational-wave astronomy, we have shed light on previously shrouded events: compact binary coalescences. Neutron stars are promising (and confirmed) sources of gravitational radiation and it proves timely to consider the ways in which these stars can be deformed. Gravitational waves provide a unique window through which to examine neutron-star interiors and learn more about the equation of state of ultra-dense nuclear matter. In this work, we study two relevant scenarios for gravitational-wave emission: neutron stars that host (non-axially symmetric) mountains and neutron stars deformed by the tidal field of a binary partner. Although they have yet to be seen with gravitational waves, rotating neutron stars have long been considered potential sources. By considering the observed spin distribution of accreting neutron stars with a phenomenological model for the spin evolution, we find evidence for gravitational radiation in these systems. We study how mountains are modelled in both Newtonian and relativistic gravity and introduce a new scheme to resolve issues with previous approaches to this problem. The crucial component of this scheme is the deforming force that gives the star its non-spherical shape. We find that the force (which is a proxy for the star's formation history), as well as the equation of state, plays an pivotal role in supporting the mountains. Considering a scenario that has been observed with gravitational waves, we calculate the structure of tidally deformed neutron stars, focusing on the impact of the crust. We find that the effect on the tidal deformability is negligible, but the crust will remain largely intact up until merger.

This, I dedicate to my Uncle,

Robert Ekblom (1956–2015),

who suggested I become a quantum physicist...

Contents

List of Figures

List of Tables

Declaration of Authorship

I, Fabian Gittins, declare that the thesis entitled *Gravitational waves from deformed neutron stars: mountains and tides* and the work presented in the thesis are both my own, and have been generated by me as the result of my own original research. I confirm that:

- this work was done wholly or mainly while in candidature for a research degree at this University;
- where any part of this thesis has previously been submitted for a degree or any other qualification at this University or any other institution, this has been clearly stated;
- where I have consulted the published work of others, this is always clearly attributed;
- where I have quoted form the work of others, the source is always given. With the exception of such quotations, this thesis is entirely my own work;
- I have acknowledged all main sources of help;
- where the thesis is based on work done by myself jointly with others, I have made clear exactly what was done by others and what I have contributed myself;
- parts of this work have been published as:
  - Gittins and Andersson (2019),
  - Gittins *et al.* (2020),
  - Gittins *et al.* (2021),
  - Gittins and Andersson (2021).

Signed: .....

Date: .....

Acknowledgements

All I have accomplished has been made possible through the Lord, "for it is God who works in you to will and to act in order to fulfil his good purpose" (Philippians 2:13). For everything involved in the pursuit of a PhD, I want to thank and praise my Lord Jesus Christ, through whom "all things were created: things in heaven and on earth, visible and invisible, whether thrones or powers or rulers or authorities; all things have been created through him and for him. He is before all things, and in him all things hold together" (Colossians 1:16-17). He is not only the creator and sustainer of the Universe, including upholding the rich and intricate physical laws of nature that govern the magnificent stars, Jesus is also my personal saviour, who "was pierced for our transgressions, he was crushed for our iniquities; the punishment that brought us peace was on him, and by his wounds we are healed" (Isaiah 53:5). This was the ultimate manifestation of his love for us.

It has been a privilege to study at the University of Southampton and I wish to acknowledge some of the main blessings I have enjoyed during my time here.

Firstly, I thank my supervisor, Nils Andersson, who has been a superb mentor to me. Never has there been a moment when he was not willing to fit in time to give advice on my research and I have always looked forward to our discussions. I am sincerely grateful for his unwavering assistance and his excellent teaching and support.

I would also like to extend my gratitude to the rest of the Gravity Group at the University of Southampton, in particular the members focused on neutron-star physics. It has been a pleasure to be among such a talented ensemble of physicists, who have played an important role in my education.

In addition to the academic support I have benefited from, I would like to acknowledge the encouragement and prayer of my dear friends at Christ Church Southampton. I am grateful for the family that I have found there and the manifold ways in which I have been supported. In particular, I wish to thank three of my closest friends that I have made during my time here: Tom Bell, Thomas Emerson and Matt Magee. I have truly been blessed to have met such wise and thoughtful brothers in Christ, who continually challenge me and bring out my best qualities. "Walk with the wise and become wise, for a companion of fools suffers harm" (Proverbs 13:20).

Many teachers, peers, friends and relatives that I had before moving to Southampton have continued to offer advice and support. They are too numerous to acknowledge personally, but they should know that I am incredibly grateful.

Finally, the greatest debt of gratitude that I have to offer, under Christ, is to my family. My parents, Mark and Caroline Gittins, loved me since before I was born and have wonderfully modelled self-sacrificial love to me and my siblings. My brother, Adam Gittins, has been

my best friend for our entire lives and can always make me smile. My sister, Caitlin Gittins, has taught me much about kindness, compassion and unwavering loyalty. Without their love and support, I would certainly not be the man I am today.

Notation

Constants and units.

For relativistic calculations, we work in geometric units,

$$G = 6.674\,28 \times 10^{-8}\,\mathrm{cm}^3\,\mathrm{g}^{-1}\,\mathrm{s}^{-2} = 1$$

and

$$c = 2.997\,924\,58 \times 10^{10}\,\mathrm{cm}\,\mathrm{s}^{-1} = 1,$$

where G is Newton's gravitational constant and c is the speed of light in a vacuum. In these units, the mass of the Sun is $M_\odot = 1.988\,92 \times 10^{33}\,\mathrm{g} = 1.477\,00\,\mathrm{km}$.

Indices, Einstein summation convention, metric signature.

Spatial indices are denoted with late Latin characters $i, j, k, \ldots$ and spacetime indices are denoted with early Latin characters $a, b, c, \ldots$. We will reserve the indices ℓ and m exclusively for spherical-harmonic modes.

The Einstein summation convention will be used, where repeated indices indicate a summation, *e.g.*,

$$v^i v_i = \sum_i v^i v_i, \quad u^a u_a = \sum_a u^a u_a,$$

where v^i and u^a are an arbitrary three-vector and four-vector, respectively. We do not assume summations over repeated ℓ, m.

The signature of the spacetime metric g_{ab} is $(-,+,+,+)$. Hence, time-like four-vectors have negative lengths.

Covariant and partial derivatives.

The covariant and partial derivatives are denoted by ∇_a and ∂_a, respectively. We use the traditional conventions for the covariant derivative so that it reduces to the partial derivative for scalars,

$$\nabla_a f = \partial_a f,$$

where f is an arbitrary scalar quantity, and it commutes with the metric,

$$\nabla_a g_{bc} = 0.$$

We work in a coordinate basis,

$$\partial_a f \equiv \frac{\partial f}{\partial x^a},$$

thus, indices will run over the coordinates, *e.g.*, in spherical polar coordinates, we have $x^t = t, x^r = r, x^\theta = \theta, x^\phi = \phi$, which can be written compactly as $x^a = (t, r, \theta, \phi)$. It should be noted that the distinction between raised and lowered indices will be meaningful (as opposed to when working with an orthonormal basis).

Covariant derivatives obey the following law for an arbitrary tensor $T_{ab\ldots}{}^{cd\ldots}$:

$$\begin{aligned}\nabla_a T_{bc\ldots}{}^{de\ldots} = \partial_a T_{bc\ldots}{}^{de\ldots} &- \Gamma^f{}_{ba} T_{fc\ldots}{}^{de\ldots} - \Gamma^f{}_{ca} T_{bf\ldots}{}^{de\ldots} - \ldots \\ &+ \Gamma^d{}_{fa} T_{bc\ldots}{}^{fe\ldots} + \Gamma^e{}_{fa} T_{bc\ldots}{}^{df\ldots} + \ldots,\end{aligned}$$

where the connection coefficients (known as *Christoffel symbols* for coordinate bases) are given by

$$\Gamma^a{}_{bc} = \frac{1}{2} g^{ad} (\partial_b g_{cd} + \partial_c g_{bd} - \partial_d g_{bc}).$$

Riemann, Ricci and Einstein tensors.

The Riemann tensor is defined as

$$R^a{}_{bcd} = \partial_c \Gamma^a{}_{bd} - \partial_d \Gamma^a{}_{bc} + \Gamma^a{}_{ec} \Gamma^e{}_{bd} - \Gamma^a{}_{ed} \Gamma^e{}_{bc}.$$

The Ricci tensor is $R_{ab} = R^c{}_{acb}$ and the Ricci scalar is $R = R_a{}^a$.

The Einstein tensor is given by

$$G_{ab} = R_{ab} - \frac{1}{2} g_{ab} R.$$

Eulerian and Lagrangian perturbations, Lie derivatives.

Generally, we will reserve the symbols δ and Δ to denote the Eulerian and Lagrangian

perturbations, respectively, of a quantity. The perturbations are related by

$$\Delta f = \delta f + \mathcal{L}_\xi f,$$

where $\mathcal{L}_\xi$ is the Lie derivative along the Lagrangian displacement vector ξ^a.

The Lie derivative along a scalar is simply

$$\mathcal{L}_\xi f = \xi^a \nabla_a f.$$

For an arbitrary tensor, the Lie derivative gives

$$\begin{aligned}\mathcal{L}_\xi T_{ab\ldots}{}^{cd\ldots} = \xi^e \nabla_e T_{ab\ldots}{}^{cd\ldots} + T_{eb\ldots}{}^{cd\ldots}\nabla_a \xi^e + T_{ae\ldots}{}^{cd\ldots}\nabla_b \xi^e + \ldots \\ - T_{ab\ldots}{}^{ed\ldots}\nabla_e \xi^c - T_{ab\ldots}{}^{ce\ldots}\nabla_e \xi^d - \ldots .\end{aligned}$$

Because of the symmetry of the connection coefficients, $\Gamma^a{}_{bc} = \Gamma^a{}_{cb}$, one can equivalently express the Lie derivatives in terms of partial derivatives. This is intuitive as the Lie derivative $\mathcal{L}_\xi$ is with respect to a frame that is dragged by ξ^a and should not depend on the precise geometry.

CHAPTER 1

Introduction

Over a century ago, Einstein (1916a) completed his formulation of what was to become one of the most rich and elegant theories in the history of physics: the *general theory of relativity*. It was a revolutionary theory of gravity that replaced the steadfast (but ultimately fundamentally flawed) description provided by Newton two hundred years earlier. Remarkably, Einstein showed that gravity should not be interpreted as a force, but instead as a curved geometry.

General relativity was highly controversial to begin with. In order to assess its validity, Einstein proposed three tests: the precession of the perihelion of Mercury, the bending of light in gravitational fields and the gravitational redshift. The theory of gravity passed these three classical tests with flying colours and, indeed, all subsequent tests (for a review, see Will, 2014)!

What was to become the most contentious prediction of general relativity was the existence of *gravitational waves*. Einstein himself was the first to show that relativity permitted small wave-like solutions that travelled at the speed of light on flat, Minkowskian spacetime (Einstein, 1916b, 1918). However, questions were raised whether these waves were physical in nature or if they were geometric artefacts that could be transformed away. This issue would not be theoretically resolved until the Chapel Hill conference in 1957 (Bergmann, 1957). At the conference, Pirani argued that if one considered a pair of freely falling particles subjected to a gravitational wave, the particles would experience genuine motions

with respect to one another (Pirani, 1956, 1957). Thus, such waves must be physical. This insight inspired Bondi's famous "sticky bead" argument (Bondi, 1957) and eventually culminated in the development and construction of kilometre-long interferometers designed to measure these minute ripples in spacetime. Indeed, the very fact that gravitational waves interact so weakly with matter meant that a combination of cataclysmic events and ultra-sensitive instruments were required in order to have any hope of detecting them. It was a truly gargantuan task.

Eventually, history was made on 14th September 2015. After decades of experimental and theoretical toil, the two laser interferometers that constitute LIGO heard a faint whisper that lasted a fraction of a second (Abbott *et al.*, 2016b). This whisper excellently matched the predictions from numerical simulations of the merger of two black holes with masses $36\,M_\odot$ and $29\,M_\odot$. This event was dubbed *GW150914* and with it began an entirely new era of astronomy.

Subsequently, gravitational-wave detectors (including the Virgo instrument that joined the network during the second observing run in 2017) have detected a plethora of binary-black-hole mergers (Abbott *et al.*, 2019b; Abbott *et al.*, 2021b). Within this impressive catalogue, there exists a particularly special event that occurred on 17th August 2017, *GW170817* (Abbott *et al.*, 2017f).

The signal from GW170817 was quite unlike any of the previous black-hole mergers (see Fig. 1.1). The event was observed by the ground-based detectors for over a minute and, given how faint the signal was in the Virgo instrument, it was reasonably well localised. Soon after this source was observed with gravitational waves, a trigger message was circulated around electromagnetic observers across the world. What followed was an unprecedented symphony of detections all across the electromagnetic spectrum; from low-frequency radio waves, all the way up to high-frequency gamma rays. This has been heralded as the first *multi-messenger event* and is deservedly the most celebrated observation in neutron-star astronomy. One of the many exciting results from this multi-messenger event was the confirmation that neutron-star mergers are (quite literally) treasure troves: they are the centres of production for gold, platinum and uranium (Kasen *et al.*, 2017; Pian *et al.*, 2017)! In addition, the electromagnetic counterpart to the gravitational-wave signal provided a *standard siren* that enabled an independent distance measurement to the source in order to estimate the Hubble parameter (Schutz, 1986; Abbott *et al.*, 2017a). Thus, nicely demonstrating how such detections will facilitate precision cosmology. The electromagnetic signals also presented further opportunities to test general relativity by investigating the speed of gravity, Lorentz invariance and the equivalence principle (Abbott *et al.*, 2017e), as well as providing constraints on various modified theories of gravity (Baker *et al.*, 2017; Creminelli and Vernizzi, 2017; Ezquiaga and Zumalacárregui, 2017).

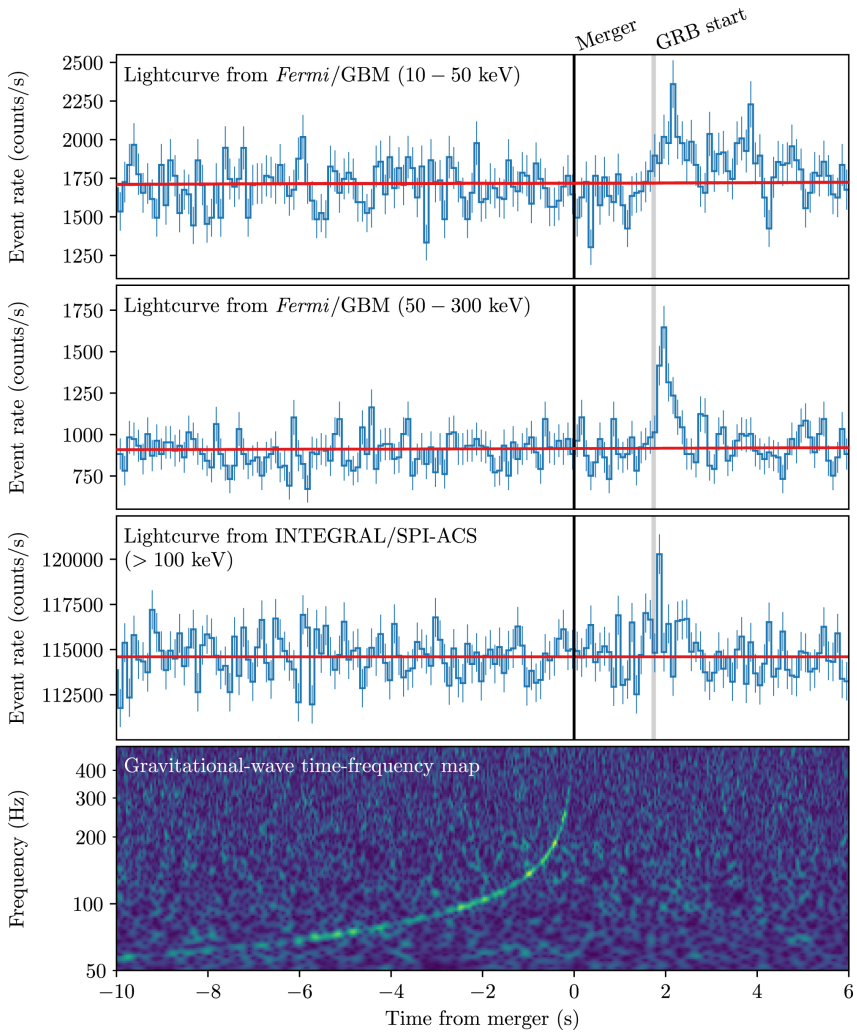

Figure 1.1: The joint multi-messenger detection of GW170817 and the short gamma-ray burst GRB 170817A. The top three panels show the gamma-ray observations with different instruments and energy ranges. The bottom panel shows the time-frequency map of the gravitational-wave detection obtained from a coherent combination of the signals in the two LIGO detectors. [Reproduced from Abbott *et al.* (2017e).]

At present, the third LIGO/Virgo observing run has completed. During it, a second binary-neutron-star system was observed (Abbott *et al.*, 2020a). The mass of this system was significantly larger than that of any other known neutron-star binary. Additionally, for the first time ever, the gravitational-wave instruments detected not one but two neutron star-black hole coalescences, just ten days apart from one another (Abbott *et al.*, 2021c). The question is what more can we learn about these curious objects.

1.1 Neutron stars

Neutron stars are fated to begin their lives in a particularly dramatic fashion: in the explosive and cataclysmic furnaces known as supernovae. They are one of two possible

endpoints of stellar evolution for massive stars (with initial masses $\gtrsim 8\,M_\odot$) – the other being the remarkably simple black holes.[1] Massive stars begin their lives on the main sequence and evolve off it as subsequent millions of years of nuclear fusion burns the elements in the core all the way up to iron. Once the fuel in the core has been exhausted, the star starts to collapse, as there is no longer any outward-acting radiative pressure and the core is left with just the degeneracy pressure to counteract the inward gravitational force. This results in a Type II supernova explosion and leaves a compact remnant behind in the form of a neutron star. Assuming the remnant is stable (with a mass $\lesssim 3\,M_\odot$), it will not collapse further to form a black hole.

Neutron stars are extremely compact bodies, with typical masses around $1.4\,M_\odot$ and radii of the order of 10 km, that support the star against gravity by neutron-degeneracy pressure. Since they are so compact, relativistic effects become important and they are able to spin-up to high frequencies (~ 700 Hz). Neutron stars harbour strong magnetic fields that can reach magnitudes of $\sim 10^{15}$ G. For these reasons, neutron stars make excellent, extreme, astrophysical laboratories that can probe conditions we could not possibly hope to synthesise in terrestrial experiments. They enable us to study physics on a vast range of scales; from the very small nuclear interactions that dictate their ultra-dense structure, all the way up to the gravitational effects that come into play in neutron-star binaries and give rise to gravitational radiation.

Baade and Zwicky (1934a,b) were the first to propose the existence of neutron stars, motivated by seeking an explanation for the origin of supernovae. This came just two years after the neutron had been discovered by Chadwick (1932). Not long after, Tolman (1939) and Oppenheimer and Volkoff (1939) derived the general-relativistic hydrostatic equations of equilibrium that could describe non-rotating neutron-star models. However, it was not until 1967 that they were originally discovered in the form of a radio pulsar with a period of 1.33 s (Hewish *et al.*, 1968). The source of the radio emission initially posed quite the puzzle and was humorously designated LGM-1, standing for "Little Green Men". More discoveries of these *pulsars* (pulsating stars) followed in the succeeding years, unveiling the mystery and associating these sources with fast rotation rates and strong magnetic fields. These sources were identified as neutron stars.

Another famous discovery came in 1974. Hulse and Taylor (1975) observed the first pulsar in a neutron-star binary. It was quickly realised that the Hulse-Taylor binary could serve as an indirect test for gravitational waves (Wagoner, 1975). The test was a simple one: if the binary was emitting gravitational waves, which would take away energy and angular

[1] The apparent mathematical simplicity of black holes has culminated in the so-called no-hair theorem. The no-hair theorem states (but does not rigorously prove) that isolated black holes in equilibrium can be fully characterised by three externally observable parameters: their mass M, angular momentum J and electric charge Q. Because there are so few astrophysically motivated evolutionary paths that may produce a black hole with a non-zero charge, it is common to assume that realistic black holes will have $Q = 0$.

momentum from the system, its orbit would shrink. This prediction of general relativity was confirmed with excellent accuracy, resulting in Hulse and Taylor being awarded the Nobel Prize in 1993, and provided observational support for the existence of gravitational radiation. Recent measurements have continued to show remarkable agreement with general relativity (Weisberg *et al.*, 2010), as shown in Fig. 1.2.

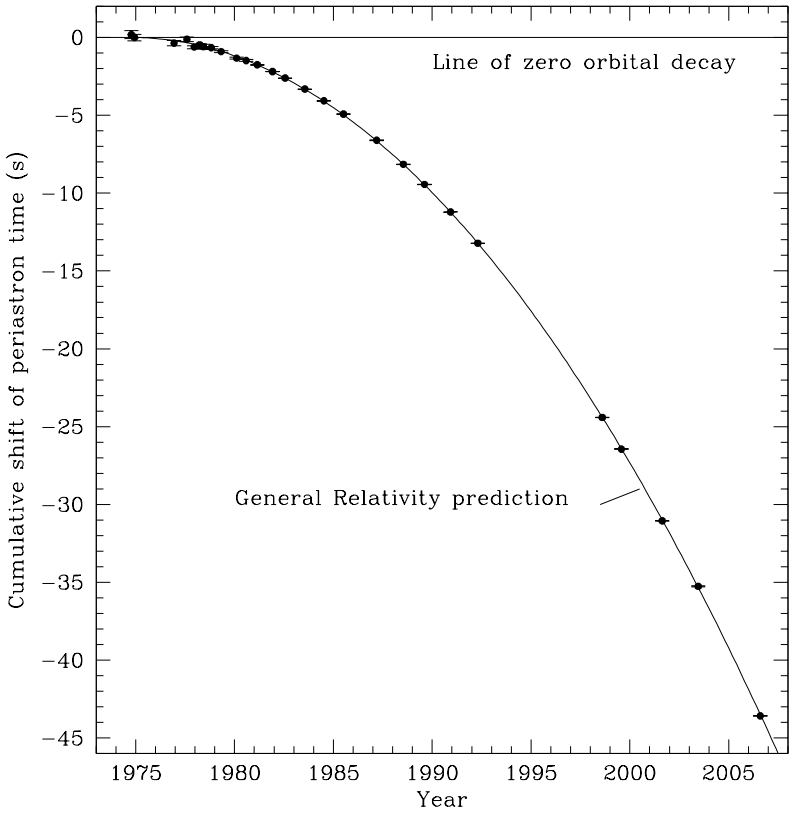

Figure 1.2: The orbital decay of the Hulse-Taylor binary pulsar PSR B1913+16 compared with the prediction of general relativity. The data points record the observed change in the periastron and the solid line indicates the theoretical prediction from general relativity for the binary radiating gravitational waves. [Reproduced from Weisberg *et al.* (2010).]

Neutron stars are known to exist in accreting binaries. In 1971, the Uhuru satellite detected a pulsating, compact X-ray source that was confirmed to be a neutron star in a binary with a massive O-type star (Schreier *et al.*, 1972). This provided proof of neutron stars existing in close binary systems accreting gas from companion stars which gives rise to their characteristic X-ray pulsations. Such systems in which the stellar companion has a mass $\lesssim M_\odot$ are referred to as low-mass X-ray binaries. Shortly after the discovery of the first millisecond pulsar (Backer *et al.*, 1982), low-mass X-ray binaries became candidate systems for producing these rapidly spinning neutron stars. In the same year, Alpar *et al.* (1982) and Radhakrishnan and Srinivasan (1982) suggested that accretion could transfer angular momentum to the neutron star, thus providing a mechanism for the star to spin

up. This has since been called the *recycling scenario*, owing its name to the ability of the mechanism to spin-up and "revive" pulsars that have stopped their radio emission and entered the *pulsar graveyard*. The first accreting millisecond X-ray pulsar to be observed was SAX J1808.4–3658, which was detected by the Rossi X-ray Timing Explorer in 1998 (Wijnands and van der Klis, 1998). This provided an exciting confirmation of the recycling scenario.

The biggest unknown in neutron-star astrophysics is the elusive *equation of state*. The equation of state encodes the detailed microscopic interactions that take place at ultra-high densities. Such a description is crucial in order build astrophysically correct neutron-star models. A plethora of candidates have been proposed and used to generate stellar models. Traditionally, one has constrained the equation of state by observing two macroscopic neutron-star parameters: the mass and radius. Promisingly, with the advent of gravitational-wave astronomy, we can now examine neutron-star interiors using gravitational radiation.

The interior of a neutron star has a series of distinct regions from the surface to the centre, as shown in Fig. 1.3. As one progresses to the core of the star, the density increases monotonically and (in some sense) so does our uncertainty of the physics. The outermost layer of a mature, isolated neutron star is a thin *ocean*; at most a few metres thick. Beneath the ocean, it becomes energetically favourable for nuclei to capture electrons and undergo inverse beta decay. This region is the solid *outer crust* and is composed of nuclei. At a critical density, around $4 \times 10^{11}\,\mathrm{g\,cm^{-3}}$, one reaches *neutron drip* – so called because this is the point neutrons begin to drip out of the nuclei to form a superfluid that permeates the solid lattice. This marks the top of the *inner crust* and is where our understanding becomes increasingly challenged.

The inner crust is expected to contain remarkable nuclear structures that occur as the matter becomes frustrated and undergoes a series of phase transitions. These are known as the *nuclear-pasta phases*. At higher densities still, one enters the *core* at $\sim 1.7 \times 10^{14}\,\mathrm{g\,cm^{-3}}$. This region is primarily a neutron superfluid. However, in the very depths of the core – a few times the nuclear-saturation density, $\rho_{\mathrm{sat}} \approx 2.8 \times 10^{14}\,\mathrm{g\,cm^{-3}}$ – various exotic states of matter may be present, such as deconfined quarks.

1.2 Gravitational-wave scenarios

In order to generate gravitational radiation, massive bodies must be accelerated in curved spacetime. For this reason, neutron stars have long been considered promising candidate sources of gravitational waves (Papaloizou and Pringle, 1978; Wagoner, 1984). This is owed to their extreme compactness (rivalled only by black holes) and their role in some of the most cataclysmic events in the Universe.

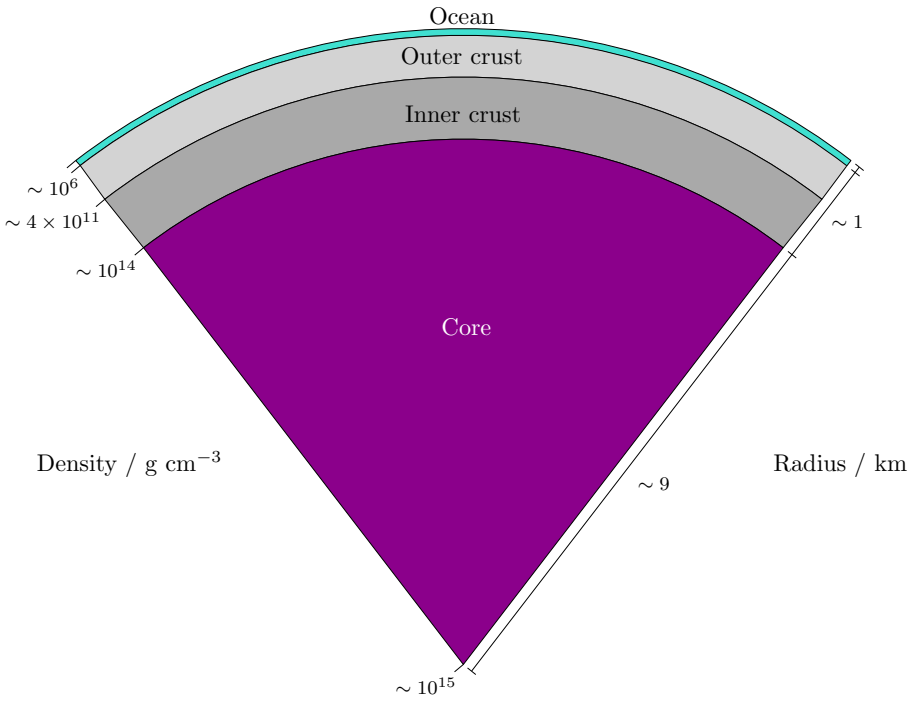

Figure 1.3: Illustration of the interior layers in a neutron star indicating (from low to high density; from the surface to the centre) the ocean, outer crust, inner crust and core.

There are a variety of probable mechanisms through which neutron stars can radiate gravitational waves. These include binary inspiral and merger (Abadie *et al.*, 2010), various modes of oscillation (and their corresponding instabilities; Andersson, 1998; Andersson *et al.*, 1999) and rotating neutron stars that are deformed away from perfect sphericity (Bildsten, 1998). Indeed, the exciting, recent gravitational-wave detections of binary neutron stars has ignited a revitalised effort in searching for gravitational waves from other neutron-star scenarios.

1.2.1 Deformed, rotating neutron stars

Rotating neutron stars with non-axisymmetric deformations are natural gravitational-wave emitters. Indeed, provided the deformation is misaligned with the rotation axis, such stars will continuously radiate at twice their spin frequency.[2] The associated (quadrupole) deformations are commonly known as *mountains*. Rapidly rotating neutron stars have enjoyed the attention of a large number of searches using gravitational-wave data. These searches have been split into two strategies: looking for evidence of gravitational radiation in specific pulsars (Abbott *et al.*, 2004, 2005b, 2007b, 2008b; Abbott *et al.*, 2010; Abadie *et al.*, 2011a,b; Aasi *et al.*, 2014, 2015a,b; Abbott *et al.*, 2017c,d,g,h, 2018a, 2019c,e,f; Abbott *et al.*, 2020b, 2021a; Zhang *et al.*, 2021) and wide-parameter surveys for unobserved sources (Abbott *et al.*, 2005a, 2007a, 2008a, 2009; Abadie *et al.*, 2012; Aasi *et al.*, 2013; Abbott

[2]In general, spinning neutron stars will precess. When precession is involved, the gravitational waves will be radiated at a frequency equal to the sum of the spin frequency and the frequency of precession, as well as twice this value.

et al., 2016a, 2017b, 2018b, 2019a; Dergachev and Papa, 2020, 2021; Steltner *et al.*, 2021).

Assuming torque balance, the brightest X-ray sources should be the loudest in gravitational-wave emission. Hence, Scorpius X-1 has long been considered a potential candidate for gravitational-wave emission and has been the focus of a number of targeted gravitational-wave searches (Abbott *et al.*, 2007a; Aasi *et al.*, 2015a; Abbott *et al.*, 2017g,h, 2019e). These searches, while only yielding upper limits so far, have helped develop and improve data-analysis techniques that can be used in the future, as the sensitivities of gravitational-wave detectors are improved. Detecting gravitational waves from rotating neutron stars will be a challenge, since only a few of the most rapidly accreting neutron stars are expected to be detectable with the current generation of gravitational-wave detectors (Watts *et al.*, 2008). The main limiting factors in detecting gravitational waves from these systems are the precision with which the spin and the orbital parameters are measured. If these are not well known, then it becomes computationally very expensive to run gravitational-wave searches, since the searches need to run over a large parameter space.

1.2.2 Binary neutron stars

Binaries are also intuitive sources for gravitational radiation. By virtue of orbiting a common centre of mass, the two components of a binary generate a time-dependent mass asymmetry with respect to the orbital axis. Both binary black holes and binary neutron stars have been successfully detected using gravitational waves. Indeed, it has almost become routine for the LIGO/Virgo detectors to observe binary-black-hole mergers.

As gravitational waves are radiated from a binary, they carry energy and angular momentum away. This means the orbit of the binary shrinks and thus, provided enough time within the lifetime of the Universe, the fate of all binaries is to coalesce and merge. Because these binaries are expected to be less massive than the vast majority of black-hole binaries, the signal associated with the inspiral lasts for a longer time in the detectability frequency band of ground-based detectors. This signal includes information about the extended nature of neutron stars, known as *finite-size effects*, where the dominant contribution is due to the tidal deformation that each star's gravitational field induces on the other. Promisingly, this information can be used to provide model-independent constraints on the equation of state. This is quite an appealing prospect since it would seem that there is no current model-independent technique to measure the neutron-star radius. Various radius estimates have been made using X-ray spectroscopy from quiescent neutron stars (Steiner *et al.*, 2018), thermonuclear X-ray bursts (Steiner *et al.*, 2010; Özel *et al.*, 2016; Nättilä *et al.*, 2017) and accretion-powered millisecond pulsars (Salmi *et al.*, 2018). However, all these methods suffer from being susceptible to systematic errors (Miller, 2013; Miller and Lamb, 2016). With the detection of GW170817, studies have been able to use the lack of an observed tidal imprint to obtain constraints on the equation of state using gravitational waves (Abbott *et al.*, 2017f; Bauswein *et al.*, 2017;

Abbott *et al.*, 2018c; Annala *et al.*, 2018; De *et al.*, 2018; Most *et al.*, 2018; Raithel *et al.*, 2018; Abbott *et al.*, 2019d).

1.3 Outlook

This thesis is concerned with the structure and dynamics of deformed neutron stars and focuses on two scenarios in which they can emit gravitational radiation: rotating neutron stars with mountains and tidally deformed binaries.

In Chap. 2, we delve into the fundamental physics that will be needed for the rest of the thesis. We discuss how the structure of neutron stars is formally described in Newtonian and relativistic gravity and how non-spherical stellar models are built. We also describe some basic gravitational-wave theory. In Chap. 3, we study the spin evolution of accreting neutron stars – systems which have long been considered potential sources of gravitational waves. In particular, we explore whether gravitational waves are likely to play an important role in their dynamics by considering different torques acting on the stars and evolving the systems through their lifetimes. Should such systems host non-axisymmetric mountains, they will naturally radiate gravitational waves. Thus, we go on to analyse how mountains are modelled in Newtonian gravity in Chap. 4. We describe how non-spherical stellar models with and without elastic crusts can be constructed. By considering previous studies of this problem, we show that the deforming force that sustains the mountains is a crucial component and consider some simple examples. We take this problem one step closer to realism by generalising the calculation to general relativity in Chap. 5. We derive the relativistic equations of structure for non-spherical stars subjected to a deforming force and consider how the equation of state affects the size of the mountains. In Chap. 6, we use our derived relativistic formalism to study the relevance of the elastic crust in tidally deformed neutron stars. We calculate the tidal deformabilities for realistic stellar models and also consider when the crust may fracture during the inspiral. We conclude and provide an outlook on future directions in Chap. 7.

Supplemental material is provided in the appendices. In Appendix A, we discuss solving the equations of stellar structure for non-rotating, spherical fluid stars. In Appendix B, we summarise the properties of the spherical harmonics. Appendix C is dedicated to the numerical techniques used for solving the perturbation equations. We obtain the interface conditions for the perturbation functions in relativity in Appendix D.

CHAPTER 2

The structure of neutron stars

This chapter serves as an introduction to some fundamental aspects of neutron-star structure. Throughout this chapter, we will work in both arenas of gravitation: Newtonian physics and general relativity. We begin with some thermodynamics in Sec. 2.1, in order to motivate and introduce the infamous neutron-star equation of state. We shall see how the equation of state plays an important role in the interior structure of neutron stars as we derive the equations of structure for non-rotating, fluid stars in Sec. 2.2. To construct more complex and realistic stellar models later in the thesis, we provide a brief introduction to perturbation theory in Sec. 2.3. Armed with an understanding of perturbation theory, in Sec. 2.4, we go on to derive and analyse the gravitational multipole moments that describe the shape of a star and are crucial in generating gravitational radiation. At the end of the chapter, Sec. 2.5, we provide a brief introduction to how gravitational waves arise in relativity and how they are produced.

2.1 The equation of state

It is well established that stellar material is excellently approximated as a perfect fluid; neutron stars are no exception to this. (Although this treatment needs to be refined when one considers additional physics such as superfluidity and magnetic fields. Indeed, we will include an elastic crust from Chap. 4 onwards.) Fluids consist of many fluid elements and

each fluid element is a collection of particles.[1] In order to understand the many-particle interactions, it is natural to consider the thermodynamics of the system. In this way, one need not concern themselves with the behaviour of individual particles, but instead track the parameters of the fluid elements.

The natural starting point is the first law of thermodynamics, which states that the change in energy dE of a many-particle-species system is given by

$$dE = TdS - pdV + \sum_{\mathrm{x}} \mu_{\mathrm{x}} dN_{\mathrm{x}}, \tag{2.1}$$

where T is the temperature, dS is the change in entropy, p is the pressure, dV is the change in volume and μ_{x} and dN_{x} are the chemical potential[2] and change in particle number, respectively, of a species x. The first term, TdS, may be identified as the heat into the system; the second, $-pdV$, corresponds to the work done on the system; and the final term, $\mu_{\mathrm{x}} dN_{\mathrm{x}}$, is associated with the change in particle number of species x. Thus, there is an equation of state for the system $E(S, V, \{N_{\mathrm{x}}\})$ from which one can obtain the following:

$$T = \left(\frac{\partial E}{\partial S}\right)_{V,\{N_{\mathrm{x}}\}}, \quad p = -\left(\frac{\partial E}{\partial V}\right)_{S,\{N_{\mathrm{x}}\}}, \quad \mu_{\mathrm{x}} = \left(\frac{\partial E}{\partial N_{\mathrm{x}}}\right)_{S,V,\{N_{\mathrm{y}}\}}, \tag{2.2}$$

where $\{N_{\mathrm{y}}\}$ is the set of particle numbers excluding N_{x}. Here, the subscripted notation next to a bracket makes explicit the variables that are being treated as constants in the partial derivative. One describes the variables E, S, V and N_{x} as *extensive* variables, since any variation in S, V and N_{x} changes the energy of the system. Conversely, variables T, p and μ_{x} are called *intensive* variables. We may call $E(S, V, \{N_{\mathrm{x}}\})$ the equation of state since it is a thermodynamic relation from which one can obtain the other state variables through (2.1).

From (2.1), one can derive the Euler relation (Andersson and Comer, 2021)

$$E = TS - pV + \sum_{\mathrm{x}} \mu_{\mathrm{x}} N_{\mathrm{x}}. \tag{2.3}$$

The Euler relation (2.3) is essentially the integrated form of the first law (2.1). It is convenient to write (2.3) in terms of densities,

$$\varepsilon = nTs - p + n \sum_{\mathrm{x}} \mu_{\mathrm{x}} Y_{\mathrm{x}}, \tag{2.4}$$

where $\varepsilon = E/V$ is the total energy density, $s = S/N$ is the entropy per particle, $Y_{\mathrm{x}} =$

[1] Each fluid element comprises a large number of particles that all undergo individual motions on a scale associated with the mean-free path. The central assumption behind fluids is that the size of a fluid element is much greater than the mean-free path of the particles. At this scale, the fluid is a continuum.

[2] This should not be confused with the magnetic moment μ in Chap. 3.

N_{x}/N is the abundance of species x, $n = N/V$ is the total number density and N is the total number of particles. We assume that the total number of particles in the system is conserved,

$$N = \sum_{\mathrm{x}} N_{\mathrm{x}} = \text{const}, \tag{2.5}$$

so we can write the first law (2.1) as

$$d\varepsilon = nTds + \frac{\varepsilon + p}{n} dn + n \sum_{\mathrm{x}} \mu_{\mathrm{x}} dY_{\mathrm{x}}, \tag{2.6}$$

with

$$nT = \left(\frac{\partial \varepsilon}{\partial s}\right)_{n,\{Y_{\mathrm{x}}\}}, \quad \frac{\varepsilon + p}{n} = \left(\frac{\partial \varepsilon}{\partial n}\right)_{s,\{Y_{\mathrm{x}}\}}, \quad n\mu_{\mathrm{x}} = \left(\frac{\partial \varepsilon}{\partial Y_{\mathrm{x}}}\right)_{s,n,\{Y_{\mathrm{y}}\}}. \tag{2.7}$$

Therefore, we have $\varepsilon = \varepsilon(s, n, \{Y_{\mathrm{x}}\})$.[3] We may identify the enthalpy from (2.6) as $h = (\varepsilon + p)/n$. Putting this into (2.4), we have

$$p = -\varepsilon + \left(\frac{\partial \varepsilon}{\partial s}\right)_{n,\{Y_{\mathrm{x}}\}} s + \sum_{\mathrm{x}} \left(\frac{\partial \varepsilon}{\partial Y_{\mathrm{x}}}\right)_{s,n,\{Y_{\mathrm{y}}\}} Y_{\mathrm{x}}. \tag{2.8}$$

The fact we can obtain all the intensive parameters of the system from $\varepsilon(s, n, \{Y_{\mathrm{x}}\})$, via Eqs. (2.7) and (2.8), justifies naming it the equation of state for our system.

If one assumes that the system is in chemical equilibrium with respect to microscopic reactions that involve the different particle species, over reaction timescales we have

$$\sum_{\mathrm{x}} \mu_{\mathrm{x}} dY_{\mathrm{x}} = 0 \tag{2.9}$$

and (2.6) reduces to

$$d\varepsilon = nTds + \frac{\varepsilon + p}{n} dn. \tag{2.10}$$

This assumption applies well to equilibrium neutron stars, where diffusive processes may be neglected. Furthermore, since the lepton contribution to the total energy is small relative to the baryons, the total number of particles can be assumed to simply be the total number of baryons. This means that the energy density depends solely on the entropy per baryon s and baryon-number density n, $\varepsilon = \varepsilon(s, n)$.

Mature neutron stars are cold, so one can assume that $T = 0$. Thus, the equation of state is reduced by one parameter, $\varepsilon = \varepsilon(n)$. Such an equation of state is termed *barotropic*. However, since the thermodynamic quantities are all related via the first law, we are free

[3] It should be noted that the particle abundances are not independent, $\sum_{\mathrm{x}} Y_{\mathrm{x}} = 1$. This illustrates a feature of extensive systems: the number of variables required to describe the system has been reduced by one in working with densities and removing V.

to work with a different quantity. For cold stars,

$$p(n) = -\varepsilon(n) + \mu(n)n, \tag{2.11}$$

where $\mu(n) = d\varepsilon/dn = (\varepsilon + p)/n$. It is, therefore, common in neutron-star astrophysics to refer to $p = p(n)$ [or, equivalently, $p = p(\varepsilon)$] as the cold-matter equation of state.

It should be emphasised that a single fluid pressure-density relation does not entirely tell the full story. Neutron stars exhibit different phases of matter. For example, the crust of a neutron star is solid and its modelling will require an understanding of the shear stresses. In particular, it is common to treat the crust as an elastic solid, which requires a shear modulus (as we shall consider from Chap. 4 onwards). We will now see how the equation of state is a crucial ingredient in producing spherical, fluid bodies.

2.2 Equations of stellar structure

In order to construct models of the stellar interior, one uses the equations of stellar structure. In this section, we derive the Newtonian and relativistic equations of stellar structure for non-rotating, spherically symmetric, fluid stars.

2.2.1 Newtonian stars

Spherical stars are modelled as perfect fluids. A perfect fluid has, by definition, no viscosity or heat flow. It is also isotropic, so the magnitude of the pressure is the same in all directions. We will neglect temperature (or, at the very least, assume our stars are cold), so we assume that the equation of state is barotropic. A barotropic perfect-fluid configuration, with mass density ρ, isotropic pressure p and velocity v^i, is a solution (ρ, p, v^i) to the following standard fluid equations (for a modern reference on fluid mechanics, and other aspects of classical physics, the reader is referred to Thorne and Blandford, 2017):

$$\partial_t \rho + \nabla_i(\rho v^i) = 0, \tag{2.12}$$

$$\rho(\partial_t + v^j \nabla_j) v_i = -\nabla_i p - \rho \nabla_i \Phi, \tag{2.13}$$

$$p = p(\rho) \tag{2.14}$$

and the gravitational potential Φ is provided by *Poisson's equation*,

$$\nabla^2 \Phi = 4\pi G \rho. \tag{2.15}$$

Equation (2.12) is the differential law of mass conservation, also known as the *continuity equation*. In the absence of a source term on the right-hand side, the continuity equation relates the rate of change of mass in a fixed volume to the flux of mass into that volume.

The mass density is simply related to baryon-number density by $\rho = m_{\rm b} n$, where $m_{\rm b}$ is the baryon mass. Therefore, the continuity equation can also be interpreted as the Newtonian law of baryon conservation, $\partial_t n + \nabla_i (n v^i) = 0$.

The equation of motion for a perfect fluid is the *Euler equation* (2.13). This is the differential law of momentum conservation. The Euler equation provides the following physical interpretation. The acceleration felt by the fluid, given by the convective derivative of the velocity $(\partial_t + v^j \nabla_j) v^i$ has two contributions: the gravitational field and the pressure gradient.

Poisson's equation (2.15) is the Newtonian field equation for gravity. It accounts for the coupling between the gravitational field and the matter that sources it.

Finally, we use the equation of state (2.14) to close this system of equations. These expressions have been written in a fully covariant way, which means that one has the freedom to work in whichever inertial reference frame they wish.

Non-rotating equilibrium stars are self-gravitating fluid spheres. Since they are in equilibrium and static, the time derivatives and velocity vanish.[4] This means the continuity equation (2.12) is trivially satisfied and we obtain the equation of hydrostatic equilibrium from (2.13),

$$\nabla_i p = -\rho \nabla_i \Phi. \tag{2.16}$$

This shows how a non-rotating star is supported against gravity by the fluid pressure gradient.

Since the star is static, it must be spherically symmetric and all quantities will depend solely on the radius from the centre. The continuity equation (2.12) indicates the presence of a conserved quantity with density ρ. This quantity is the total mass

$$M \equiv \int_0^R 4\pi r^2 \rho(r) dr, \tag{2.17}$$

where R is the stellar radius. (Equivalently, the total number of baryons is conserved.) Therefore, the mass enclosed in radius r, $m(r)$, is given by

$$\frac{dm}{dr} = 4\pi r^2 \rho. \tag{2.18a}$$

Equation (2.15) integrates to

$$\frac{d\Phi}{dr} = \frac{Gm}{r^2}. \tag{2.18b}$$

[4] It is natural to adopt a reference frame that is at rest relative to the fluid.

Equation (2.16) becomes

$$\frac{dp}{dr} = -\rho\frac{d\Phi}{dr} = -\frac{Gm\rho}{r^2}. \tag{2.18c}$$

Equations (2.18) constitute the *Newtonian equations of stellar structure*. They describe a non-rotating, fluid star with (ρ, p, Φ), supplemented by an equation of state (2.14).

With an equation of state specified, one solves the stellar-structure equations by imposing the following boundary conditions:

At the centre, the enclosed mass must vanish, $m(0) = 0$, and the central density (or, equivalently, the central pressure) may be freely specified, $\rho(0) = \rho_c$ $[p(0) = p_c]$.

At the surface, the pressure must go to zero, $p(R) = 0$, and the internal potential needs to match to the exterior, $\Phi(R) = -GM/R$.[5]

Since the central density may be chosen arbitrarily, the structure equations admit a one-parameter family of solutions that depend on the equation of state to close the system. For a given equation of state, varying the central density provides a variety of equilibrium configurations with different masses and radii, $[M(\rho_c), R(\rho_c)]$. This results in the *mass-radius diagram* for that equation of state, $M = M(R)$, which is a common diagnostic to differentiate between equations of state (see Fig. 2.1). We will discuss the mass-radius diagram in more detail below for the relativistic structure equations.

It is convenient to note that (2.18b) decouples from the other equations. Therefore, one can obtain the quantities $\rho(r)$, $p(r)$, $m(r)$ and R without needing to compute the interior gravitational potential $\Phi(r)$.

Accurate descriptions of neutron-star interiors will rely on calculations in full general relativity. However, Newtonian models can still be very useful. Usually, such calculations are easier to conduct and the physics is simpler to understand. A convenient simplification in generating spherical Newtonian stars is to assume the equation of state is polytropic, that is

$$p(\rho) = K\rho^{1+1/n}, \tag{2.19}$$

where K and n are real, positive constants.[6] In fact, because the relativistic corrections to neutron-star models are more significant than variations in the description of nuclear matter, polytropic equations of state are quite suitable for Newtonian calculations of neutron stars. Polytropes are described in Appendix A.1.

[5] Although, the total mass is calculated as an integral of the density over its total volume (2.17), we choose to define the total mass from the exterior potential. Conceptually, this is a subtle distinction that enables us to also use m and M to denote the analogous quantities in the relativistic case, as we shall elucidate below. This definition is commonly distinguished as the total *gravitational mass* because it is read off from the gravitational potential.

[6] One should be careful to not confuse the index n with the baryon-number density.

2.2.2 Relativistic stars

At this point, we will depart from the above Newtonian equations of structure and look for a relativistic description. As we will see, the procedure we need to follow in order to derive the relativistic equations is quite similar in spirit. We will need to use the relativistic equivalents of Poisson's equation (2.15) and the equation of hydrostatic equilibrium (2.16) in order to construct static relativistic stars. For a comprehensive description of general relativity, the reader is referred to Misner *et al.* (1973), Schutz (1985) and Hartle (2003).

In general relativity, space and time are unified to build a four-dimensional continuum, known as *spacetime*, and gravity manifests itself as a geometric property of this continuum, referred to as *curvature*. Thus, space need not be flat as in Newtonian gravity and space and time are intricately entwined. Indeed, different observers at different points in spacetime will no longer agree upon where and when events happen. Any source of matter content in a spacetime deforms the fabric and gives rise to curvature.

How the matter shapes the geometry is encoded in the relativistic field equations, known as the *Einstein equations*. These are given by

$$G_a{}^b = 8\pi T_a{}^b, \tag{2.20}$$

where $G_a{}^b$ is the Einstein tensor and $T_a{}^b$ is the stress-energy tensor corresponding to the matter content. Equation (2.20) is the relativistic analogue of the Newtonian field equation (2.15). One should not be fooled by the apparent simplicity of (2.20). In its true form, it is a highly non-linear, coupled system of ten second-order partial differential equations. To solve this system, one must simultaneously calculate the metric, g_{ab}, and the stress-energy tensor, T_{ab} (that explicitly depends on the metric). Without significant symmetries to take advantage of, it can be very difficult task. The Bianchi identities imply

$$\nabla_b T_a{}^b = 0, \tag{2.21}$$

which is the relativistic conservation law for energy and momentum. It should be emphasised that Eqs. (2.20) and (2.21) are not independent. Indeed, the information in (2.21) is also contained in (2.20). However, due to the challenge in evaluating (2.20), it is occasionally convenient to also use (2.21) in order to simplify the calculation.

Before we concern ourselves with the gravity of the situation, we will begin with some relativistic fluid dynamics. For a perfect fluid – that is, again, free of viscosity and heat – the stress-energy tensor is

$$T_a{}^b = (\varepsilon + p)u_a u^b + p\,\delta_a{}^b = \varepsilon\, u_a u^b + p \perp_a{}^b, \tag{2.22}$$

where ε and p correspond to the energy density[7] and isotropic pressure, respectively, as measured by an observer co-moving with the fluid with four-velocity u^a. Here, we have introduced the projection operator orthogonal to the observer, $\perp_a{}^b \equiv u_a u^b + \delta_a{}^b$. By considering projections of (2.21) along u^a and $\perp_b{}^a$, one can show that a relativistic, barotropic perfect fluid is a solution (ε, p, u^a) to the following system (Andersson and Comer, 2021):

$$\nabla_a(nu^a) = 0, \tag{2.23}$$

$$(\varepsilon + p)u^b \nabla_b u_a = -\perp_a{}^b \nabla_b p, \tag{2.24}$$

$$p = p(\varepsilon), \tag{2.25}$$

where the geometry of the spacetime is given by the Einstein equations (2.20).

Equation (2.23) is the conservation law of baryons and is the relativistic generalisation of the continuity equation (2.12). In both Newtonian and relativistic gravity, the total number of baryons must remain constant. For this reason, it is common to distinguish $\rho = m_{\mathrm{b}} n$ as the *baryon-mass density* or *rest-mass density* to bridge the two descriptions of gravity.

Equation (2.24) is the relativistic Euler equation [*cf.* (2.13)]. We note that $u^b \nabla_b u^a$ corresponds to the fluid four-acceleration and takes into account the spacetime geometry. From (2.24) we may identify the inertial mass per unit volume in relativity as $(\varepsilon + p)$; this replaces ρ from the Newtonian case.

In order to proceed, we must consider the geometry and choose a frame of reference. For the interior of a static, spherical star it is appropriate to use the line element

$$ds^2 = g_{ab} dx^a dx^b = -e^{\nu} dt^2 + e^{\lambda} dr^2 + r^2(d\theta^2 + \sin^2\theta \, d\phi^2), \tag{2.26}$$

where dx^a denotes the infinitesimal coordinate differences and ν and λ are functions of r to be determined.[8] It should be noted that the coordinates in relativity are analogous but do not perfectly coincide with the coordinates in Newtonian gravity. One can consider the two-surface when $t, r = \text{const}$ in (2.26),

$$ds^2 = r^2(d\theta^2 + \sin^2\theta \, d\phi^2). \tag{2.27}$$

Thus, the coordinate r corresponds to the two-sphere, centred around $r = 0$, with circumference $2\pi r$ and surface area $4\pi r^2$. We can, therefore, identify θ and ϕ as the usual angles from spherical polar coordinates. However, r is not the radial distance from the centre.

[7] This is an important difference to Newtonian gravity, where the corresponding quantity is the (rest-)mass density, ρ. The energy density is made up of the rest mass-energy and internal energy densities. This is a manifestation of the famous mass-energy equivalence.

[8] One should be careful to not confuse the metric potential with the spin frequency ν in Chap. 3.

Instead, we have the proper distance,

$$l = \int_0^r e^{\lambda(r')/2} dr'. \tag{2.28}$$

Similarly, the proper time is given by $\tau = \int_0^t e^{\nu(r)/2} dt' = e^{\nu(r)/2} t$, where we observe the famous red-shift factor.

Because the star is static, it is convenient to choose an observer at rest with the fluid.[9] The only non-vanishing component of the fluid four-velocity is the t component. So, by normalisation, $u^a u_a = -1$, we have

$$u^t = e^{-\nu/2}, \qquad u^i = 0. \tag{2.29}$$

Similar to what we saw in the Newtonian case, baryon conservation (2.23) is, thus, trivially satisfied. We find the relativistic equation of hydrostatic equilibrium from (2.24),

$$\nabla_i p = -\frac{1}{2}(\varepsilon + p)\nabla_i \nu. \tag{2.30}$$

This conveniently provides us with a physical interpretation for ν by comparing this expression with its Newtonian analogue (2.16): ν is proportional to the Newtonian potential Φ.

Working through the Einstein equations (2.20), we have

$$G_t{}^t = 8\pi T_t{}^t \quad \longrightarrow \quad \frac{1}{r^2}\frac{d}{dr}[r(1 - e^{-\lambda})] = 8\pi\varepsilon \tag{2.31a}$$

and

$$G_r{}^r = 8\pi T_r{}^r \quad \longrightarrow \quad -\frac{1}{r^2}(1 - e^{-\lambda}) + \frac{1}{r}e^{-\lambda}\frac{d\nu}{dr} = 8\pi p. \tag{2.31b}$$

To obtain the final form of the structure equations we define (motivated by the exterior Schwarzschild solution; Schwarzschild, 1916)

$$e^{\lambda} \equiv \frac{1}{1 - 2m/r}, \tag{2.32}$$

which turns (2.31a) into

$$\frac{dm}{dr} = 4\pi r^2 \varepsilon. \tag{2.33a}$$

Equation (2.31b) becomes

$$\frac{d\nu}{dr} = \frac{2(m + 4\pi r^3 p)}{r(r - 2m)}. \tag{2.33b}$$

[9] As with the Newtonian case, there is considerable freedom in the frame one chooses to work in. As before, the simplest choice is the fluid's rest frame.

From (2.30), we have

$$\frac{dp}{dr} = -\frac{1}{2}(\varepsilon + p)\frac{d\nu}{dr} = -\frac{(\varepsilon + p)(m + 4\pi r^3 p)}{r(r - 2m)}. \tag{2.33c}$$

Equations (2.33) make up the *relativistic equations of stellar structure* – also known as the *Tolman-Oppenheimer-Volkoff equations* (Oppenheimer and Volkoff, 1939; Tolman, 1939). As in the Newtonian case, one must provide an equation of state (2.25). The boundary conditions are essentially the same as described above. The only change is that the metric potential must match the exterior Schwarzschild solution, $e^{\nu(R)} = 1 - 2M/R$, where M corresponds to the total mass-energy of the star.[10] The numerical evaluation of Eqs. (2.33) is described in Appendix A.2.

There are a couple of details worth noting at this point, when comparing the relativistic equations to the Newtonian ones. We have pointed out that the radial coordinate r, in relativity, no longer corresponds to the physical distance from the centre of the star. Hence, R does not give the proper radius of the star. Instead, the proper radius is

$$L = \int_0^R e^{\lambda(r)/2} dr, \tag{2.34}$$

which is different to R by $\mathcal{O}(1)$. Thus, r should be interpreted strictly as a coordinate and not a physical distance an observer would measure.

The total mass-energy is given by [*cf.* (2.33a)]

$$M = \int_0^R 4\pi r^2 \varepsilon(r) dr. \tag{2.35}$$

Contrary to the Newtonian mass, it is interesting to note that M need not be conserved for a relativistic isolated star. This is because it does not solely include the rest mass-energy of the star. The simple form of Eq. (2.35), which is reminiscent of the Newtonian result (2.17), slightly obfuscates the identification of M as the total mass-energy. However, one can convince themselves that (2.35) does indeed include all the relevant contributions to the total mass-energy by considering the proper volume element for the spacetime (2.26), $dV = e^{\lambda/2} r^2 \sin\theta \, dr \, d\theta \, d\phi$, and noting that the energy density contains the rest mass-energy density ρ and internal energy density u, so $\varepsilon = \rho + u$. Thus, (2.35) can be written as

$$\begin{aligned} M &= \int_V \rho dV + \int_V u dV - \int_V (1 - e^{-\lambda/2}) \varepsilon dV \\ &= \int_0^R 4\pi e^{\lambda/2} r^2 \rho dr + \int_0^R 4\pi e^{\lambda/2} r^2 u dr - \int_0^R 4\pi (e^{\lambda/2} - 1) r^2 \varepsilon dr. \end{aligned} \tag{2.36}$$

[10] Because of our choice to define the total mass using the exterior potential, we are justified in identifying the quantities m and M with the mass(-energy) in radius r and the total mass(-energy), respectively.

The first and second terms in (2.36) are simply the total rest mass-energy and the total internal energy, respectively. The third term in (2.36) is the total gravitational potential energy. This exercise further justifies our recognition of m in (2.32) as the mass-energy within r.

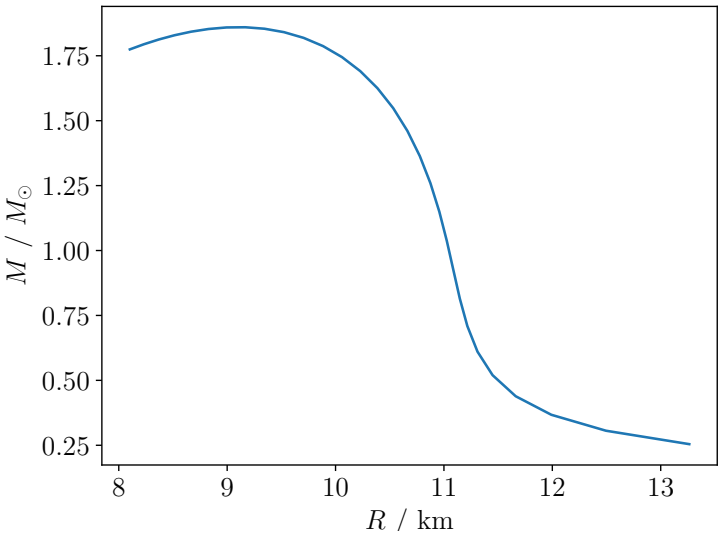

Figure 2.1: The mass-radius diagram for the BSk19 equation of state (Potekhin *et al.*, 2013). The $M = M(R)$ curve is obtained by integrating the relativistic equations of stellar structure (2.33) for different values of the central density ε_c. The range of values for the central density in this diagram are $4.0 \times 10^{14} - 6.6 \times 10^{15}\,\mathrm{g\,cm^{-3}}$.

We show an example mass-radius diagram obtained from the relativistic structure equations in Fig. 2.1. The main features of a neutron-star mass-radius diagram are shared among (realistic) equations of state. The larger values of the central density correspond to smaller radii and a larger compactness. Each equation of state admits a maximum mass that it can support. This is a relativistic result and comes from the denominator in (2.33c) that prevents m from becoming as large as $r/2$. The maximum mass is particularly of interest in excluding certain candidate matter models. It is important to note that not all equilibrium configurations correspond to *stable* solutions. In general, configurations that lie on the left of the maximum mass in the mass-radius diagram are unstable – small density perturbations will grow exponentially in time, leading the star to collapse or expand. On the other hand, configurations to the right of the maximum mass are stable – the perturbations away from equilibrium are restored by pressure or gravity forces.

It is worth mentioning a common way equation-of-state candidates are categorised: equations of state are described as *soft* or *stiff*. The stiffness depends on how fast the isotropic pressure p increases as a function of the energy density ε – the faster, the stiffer. Stiff equations of state are so named because the fluid is difficult to compress and, therefore, can support larger masses. On the other hand, soft equations of state are easier to compress

and result in more compact stars.

Although there are presently many questions to be answered concerning what the true equation of state must be, there are a number of natural physical constraints that realistic equation-of-state candidates must satisfy. A couple of key restrictions are: (i) the speed of sound in the fluid $c_{\rm s}$, where $c_{\rm s}^2 \equiv dp/d\varepsilon$, must respect causality, $c_{\rm s}^2 < 1$, and (ii) the fluid must be thermodynamically stable, that is $c_{\rm s}^2 > 0$. However, these restrictions are not particularly constraining and a variety of popular models violate causality at high densities.

2.3 Linear perturbations

In physics, it is common to approach problems in a perturbative manner. In linear perturbation theory, one considers small departures away from an equilibrium solution and linearises – neglecting terms that are of quadratic order and higher in the small quantities. Therefore, the problem is split into two components: the *equilibrium* (or *background*) solution and the *perturbative* part. This technique is particularly powerful when one already knows the background solution, *e.g.*, the structure of a non-rotating, spherical star. We will make use of perturbation theory in order to construct non-spherical stars. In this section, it will be sufficient to focus the discussion on Newtonian perturbations.

In hydrodynamics, there are two methods of describing a fluid. The first involves monitoring the behaviour of the fluid at a *given point in space*, corresponding to a frame that is at rest. This is known as the *Eulerian* description. The other method characterises the behaviour of a *given fluid element*, which is represented by a frame that is co-moving with the fluid flow. This is the *Lagrangian* description. We have, in some sense, already encountered these two descriptions. For example, in the Euler equation (2.13), we see two types of time derivative: the ordinary partial derivative ∂_t, that keeps the location fixed, and the convective derivative $(\partial_t + v^i \nabla_i)$, that measures changes from the perspective of a fluid element travelling with velocity v^i. In relativity, the Lagrangian frame has the same meaning. However, an Eulerian frame is a little more complicated (Andersson and Comer, 2021).

An Eulerian perturbation, denoted by the δ symbol, of a quantity f (which, in general, can be a scalar, vector or tensor) at a point x_0^i is defined by

$$f(t, x_0^i) = f_0(x_0^i) + \delta f(t, x_0^i), \tag{2.37}$$

where f_0 is the equilibrium value (which is independent of time). A Lagrangian perturbation, denoted by the Δ symbol, can be expressed by

$$f(t, x^i) = f_0(x_0^i) + \Delta f(t, x_0^i), \tag{2.38}$$

where x_0^i is the position the fluid element was at in the equilibrium configuration and x^i is the position it has moved to due to the perturbation. Note that, we have defined the Lagrangian perturbation to be a function of the equilibrium position.[11] This provides the motivation for the introduction of the Lagrangian displacement vector ξ^i, which connects fluid elements in the perturbed configuration to their positions in the background (Friedman and Schutz, 1978a),

$$x^i = x_0^i + \xi^i(t, x_0^i). \tag{2.39}$$

To be precise, a fluid element at position x_0^i in the background has moved by ξ^i to position x^i in the perturbed configuration. Therefore, one can obtain a relation between the Eulerian and Lagrangian perturbations,

$$\begin{aligned} \Delta f(t, x_0^i) &= f[t, x_0^i + \xi^i(t, x_0^i)] - f_0(x_0^i) \\ &= f(t, x_0^i) + \xi^j(t, x_0^i)\partial_j f_0(x_0^i) - f_0(x_0^i) + \mathcal{O}(|\xi^i|^2). \end{aligned} \tag{2.40}$$

Note that we have taken the perturbative parameters ξ^i, δf and Δf to be small and have assumed f to be a scalar. The perturbative terms of second order and above are contained in $\mathcal{O}(|\xi^i|^2)$. Thus, to linear order,

$$\Delta f = \delta f + \mathcal{L}_\xi f_0, \tag{2.41}$$

where we have identified the Lie derivative $\mathcal{L}_\xi$ along the vector ξ^i. Although f has been taken to be a scalar, Eq. (2.41) also applies for vectors and tensors.

To obtain the Lagrangian perturbation of the velocity, we must consider the velocity in the perturbed configuration, which can be written as

$$v^i(t, x^i) = \frac{dx^i}{dt} = \frac{d}{dt}[x_0^i + \xi^i(t, x_0^i)] = v_0^i(x_0^i) + v_0^j(x_0^i)\partial_j \xi^i(t, x_0^i) + \partial_t \xi^i(t, x_0^i). \tag{2.42}$$

We can also expand the velocity as

$$v^i(t, x^i) = v^i[t, x_0^i + \xi^i(t, x_0^i)] = v^i(t, x_0^i) + \xi^j(t, x_0^i)\partial_j v_0^i(x_0^i) + \mathcal{O}(|\xi^i|^2). \tag{2.43}$$

Hence, we have

$$\delta v^i(t, x_0^i) + \mathcal{L}_\xi v_0^i(x_0^i) = \partial_t \xi^i(t, x_0^i) + \mathcal{O}(|\xi^i|^2). \tag{2.44}$$

By (2.41), to leading perturbative order, we find

$$\Delta v^i = \partial_t \xi^i. \tag{2.45}$$

[11] This is an important detail since, in practice, the perturbation equations will tend to be coupled to the background structure. Therefore, when one solves the perturbation equations, they do this over the background domain, x_0^i. Thus, the perturbed quantities ξ^i, δf and Δf only have support at x_0^i.

The perturbations also induce a change on the metric. By virtue of the nature of the covariant derivative, $\nabla_i g_{jk} = 0$, and the fact the metric in Newtonian gravity is flat, $\delta g_{ij} = 0$, we have

$$\Delta g_{ij} = \nabla_i \xi_j + \nabla_j \xi_i. \tag{2.46}$$

Another useful expression for fluid perturbations comes from the conservation-of-mass principle. Consider an infinitesimal mass dm_0 in the background configuration. This is given by

$$dm_0 = \rho_0(x_0^i) dV_0, \tag{2.47}$$

where dV_0 is an infinitesimal volume in the background configuration. Each fluid element undergoes the transformation (2.39) due to the perturbations. The Jacobian of this transformation is $[1 + \nabla_i \xi^i + \mathcal{O}(|\xi^i|^2)]$. Therefore, the infinitesimal volume in the perturbed configuration, to linear order, is

$$dV = [1 + \nabla_j \xi^j(t, x_0^i)] dV_0. \tag{2.48}$$

Here, we see that the divergence of ξ^i corresponds to the change in volume of a fluid element in the perturbation. The variation in the density follows from the conservation of mass contained in the volume,

$$dm_0 = \rho_0(x_0^i) dV_0 = \rho(t, x^i) dV. \tag{2.49}$$

The two densities are, thus, related by

$$\rho(t, x^i) = [1 - \nabla_j \xi^j(t, x_0^i)] \rho_0(x_0^i) + \mathcal{O}(|\xi^i|^2) \tag{2.50}$$

The Lagrangian perturbation of the density, to first order, is

$$\Delta\rho = -\rho_0 \nabla_i \xi^i. \tag{2.51}$$

Note that this expression is completely general and must be satisfied in order to conserve the mass in the perturbations. This is equivalently a statement about the Newtonian conservation of baryon number, $\Delta n = -n_0 \nabla_i \xi^i$.

For relativistic perturbations, we have [*cf.* Eqs. (2.45), (2.46) and (2.51); Andersson and Comer (2021)]

$$\Delta u^a = \frac{1}{2} u_0^a u_0^b u_0^c \Delta g_{bc}, \tag{2.52}$$

$$\Delta g_{ab} = h_{ab} + \nabla_a \xi_b + \nabla_b \xi_a \tag{2.53}$$

and

$$\Delta n = -\frac{1}{2} n_0 \perp^{ab} \Delta g_{ab}, \tag{2.54}$$

where $h_{ab} = \delta g_{ab}$.

Linear perturbations are useful for a variety of neutron-star problems, including asteroseismology and gravitational waves. We will omit the subscript denoting background quantities forthwith.

2.4 Multipole moments

When characterising the shape of a star, one often considers the star's *multipole moments*. Multipole moments quantify the degree of non-sphericity of a star and help to determine whether the star in question is a promising gravitational-wave emitter. These are most straightforwardly obtained from the far-field expansion of the gravitational potential.

2.4.1 Newtonian multipole moments

Consider a star described by the mass-density distribution $\rho(x^i)$, where x^i is a point inside the star. This mass distribution sources a gravitational potential field $\Phi(x^i)$ through Poisson's equation (2.15). The solution to (2.15) is

$$\Phi(X^i) = -\int_V \frac{G\rho(x^i)}{|X^j - x^j|} dV, \tag{2.55}$$

where X^i is the position of an observer measuring the field, outside the mass distribution. The volume integration is over the volume of the star. In the far-field limit, we have $r \ll \mathcal{R}$, where $r^2 = x^i x_i$ and $\mathcal{R}^2 = X^i X_i$. Equation (2.55) may be expanded in terms of $\mathcal{R}$ away from the source using Legendre polynomials $\mathcal{P}_\ell(x)$,

$$\Phi(X^i) = -\sum_{\ell=0}^{\infty} \frac{G}{\mathcal{R}^{\ell+1}} \int_V \rho(x^i) r^\ell \mathcal{P}_\ell(\cos\alpha) dV, \tag{2.56}$$

where α is the angle between X^i and x^i,

$$\cos\alpha = \hat{X}^i \hat{x}_i, \tag{2.57}$$

and $\hat{X}^i = X^i/\mathcal{R}$ and $\hat{x}^i = x^i/r$ are the corresponding unit vectors. Consequently, we may decompose the potential (2.56) into a series of multipole moments,

$$\Phi(X^i) = -\sum_{\ell=0}^{\infty} \frac{G Q_\ell(\hat{X}^i)}{\mathcal{R}^{\ell+1}}, \tag{2.58}$$

where

$$Q_\ell(\hat{X}^i) = \int_V \rho(x^i) r^\ell \mathcal{P}_\ell(\cos\alpha) dV \tag{2.59}$$

is the 2^ℓ-pole moment of the mass distribution $\rho(x^i)$. Or, more precisely, it is the component of the 2^ℓ-pole moment in the $\hat{X}^i$ direction. In assuming the far-field limit, each multipole with increasing ℓ will be successively suppressed by $1/\mathcal{R}^{\ell+1}$ and provide small contributions. Let us examine the first few multipoles.

$\ell = 0$: The monopole moment is simply the net charge of the distribution,

$$Q_0 = \int_V \rho(x^i) dV = M, \tag{2.60}$$

which is independent of the direction $\hat{X}^i$. Hence, the monopole term in the potential is isotropic,

$$\Phi_0(\mathcal{R}) = -\frac{GM}{\mathcal{R}}. \tag{2.61}$$

$\ell = 1$: The dipole moment is the vector

$$p^i = \int_V \rho(x^i) x^i dV \tag{2.62}$$

and its component in the $\hat{X}^i$ direction is

$$Q_1(\hat{X}^i) = \int_V \rho(x^i) r\cos\alpha dV = p_i \hat{X}^i. \tag{2.63}$$

The dipole potential has the form

$$\Phi_1(X^i) = -\frac{G p_i \hat{X}^i}{\mathcal{R}^2}. \tag{2.64}$$

Note that if the star is at rest, one is always free to work in a mass-centred coordinate system where the dipole vanishes.

$\ell = 2$: We introduce the quadrupole-moment tensor

$$Q_{ij} = \int_V \rho(x^i) \left(x_i x_j - \frac{1}{3} r^2 g_{ij} \right) dV, \tag{2.65}$$

which is a symmetric and trace-free tensor. Therefore, the quadrupole moment is

$$Q_2(\hat{X}^i) = \int_V \rho(x^i) r^2 \left(\frac{3}{2}\cos^2\alpha - \frac{1}{2} \right) dV = \frac{3}{2} Q_{ij} \hat{X}^i \hat{X}^j. \tag{2.66}$$

Thus, the quadrupole potential is

$$\Phi_2(X^i) = -\frac{3}{2}\frac{GQ_{ij}\hat{X}^i\hat{X}^j}{\mathcal{R}^3}. \tag{2.67}$$

$\ell \geq 3$: Similar to the quadrupole-moment tensor, the octupole and higher-order moments are all symmetric and of the form

$$Q^\ell_{ij\ldots q} = \int_V \rho(x^i)(\text{homogeneous polynomial of degree } \ell)_{ij\ldots q} dV, \tag{2.68}$$

where the polynomial follows from the expansion of

$$r^\ell \mathcal{P}_\ell(\cos\alpha) = \frac{(2\ell-1)!!}{\ell!}(\text{homogeneous polynomial of degree } \ell)_{ij\ldots q}\hat{X}^i\hat{X}^j\ldots\hat{X}^q. \tag{2.69}$$

Note that $i, j, \ldots, q$ constitute a total of ℓ indices. The potential due to the 2^ℓ-pole moment is

$$\Phi_\ell(X^i) = -\frac{(2\ell-1)!!}{\ell!}\frac{GQ^\ell_{ij\ldots q}\hat{X}^i\hat{X}^j\ldots\hat{X}^q}{\mathcal{R}^{\ell+1}}. \tag{2.70}$$

In general, the 2^ℓ-pole tensor $Q^\ell_{ij\ldots q}$ has 3^ℓ components. However, there are symmetries that reduce the number of independent components. For example, the quadrupole tensor Q_{ij} has 9 entries, but is symmetric and traceless,

$$Q_{ij} = Q_{ji}, \quad Q_i{}^i = 0. \tag{2.71}$$

These make up $3 + 1 = 4$ symmetry conditions and so Q_{ij} has $9 - 4 = 5$ independent components. For a given 2^ℓ-pole tensor, there are $(2\ell + 1)$ independent components. Likewise, for a given ℓ there are $(2\ell + 1)$ spherical harmonics $Y_{\ell m}(\theta, \phi)$.[12] In fact, instead of describing the angular dependence of the multipoles' components in the direction $\hat{X}^i$ in terms of symmetric tensors, we may expand them in spherical harmonics. We discuss some of the properties of the relevant spherical harmonics in Appendix B.

For any integer $\ell = 0, 1, 2, \ldots$ and any two unit vectors $\hat{a}^i$ and $\hat{b}^i$, the Legendre polynomial of their scalar product may be expressed as

$$\mathcal{P}_\ell(\hat{a}^i\hat{b}_i) = \frac{4\pi}{2\ell+1}\sum_{m=-\ell}^{\ell} Y_{\ell m}(\hat{a}^i)Y^*_{\ell m}(\hat{b}^i), \tag{2.72}$$

where the star denotes a complex conjugate. We can apply this result to the definition of

[12] One should not confuse the harmonic number m with the mass inside a star.

the multipoles (2.59),

$$Q_\ell(\hat{X}^i) = \frac{4\pi}{2\ell+1}\sum_{m=-\ell}^{\ell} Y_{\ell m}(\hat{X}^i)\int_V \rho(x^i) r^\ell Y^*_{\ell m}(\hat{x}^i) dV. \tag{2.73}$$

Hence, we choose to define the spherical-harmonic decomposition of the multipoles by[13]

$$Q_{\ell m} \equiv \int_V \rho(x^i) r^\ell Y^*_{\ell m}(\theta,\phi) dV, \tag{2.74}$$

where (θ,ϕ) describe the direction of $\hat{x}^i$. The full gravitational potential is then given by

$$\Phi(X^i) = -\sum_{\ell=0}^{\infty}\sum_{m=-\ell}^{\ell} \frac{4\pi G}{2\ell+1}\frac{Q_{\ell m} Y_{\ell m}(\vartheta,\varphi)}{\mathcal{R}^{\ell+1}}, \tag{2.75}$$

where (ϑ,φ) are the angles characterising $\hat{X}^i$. We may identify two approaches to obtaining the multipole moments. (1) Provided the density distribution $\rho(x^i)$, one can integrate through the volume of the star, evaluating (2.74). (2) If one knows the exterior potential at a point X^i, then the multipoles can be read off from (2.75) (since the potential must be continuous, it is often convenient to do this examination at the surface).

It is straightforward to generate spherical background stars using the equations of stellar structure (2.18). These models are fully described by the $\ell = 0$ monopole. If one assumes that the star is deformed away from sphericity in a perturbative way, then the multipoles that arise due to the corresponding Eulerian density perturbation $\delta\rho(x^i)$ are[14]

$$Q_{\ell m} = \int_V \delta\rho(x^i) r^\ell Y^*_{\ell m}(\theta,\phi) dV. \tag{2.76}$$

Motivated by (2.75), it is useful to decompose the rest of the perturbations using spherical harmonics, *e.g.*,

$$\delta\rho(x^i) = \sum_{\ell=0}^{\infty}\sum_{m=-\ell}^{\ell} \delta\rho_{\ell m}(r) Y_{\ell m}(\theta,\phi). \tag{2.77}$$

However, it is important to note that, should one wish to focus on a specific harmonic mode (ℓ, m), care must be taken since $Y_{\ell m}$ are, in general, complex. One resolves this issue by taking the real part, as physical quantities must be real, *e.g.*, $\delta\rho(x^i) = \delta\rho_{\ell m}(r)\mathrm{Re}[Y_{\ell m}(\theta,\phi)]$. With this decomposition, (2.76) becomes

$$Q_{\ell m} = \int_0^R \delta\rho_{\ell m}(r) r^{\ell+2} dr. \tag{2.78}$$

[13] Note that this definition of the multipole moments is different to that of Thorne (1980) [*cf.* his Eq. (5.27a)], which is commonly used in the tidal-deformation literature (see, *e.g.*, Hinderer, 2008).

[14] To formally show this, one must consider the full multipole [given by (2.74)] of the perturbed configuration under the transformation (2.39), make use of the Lagrangian relation (2.38) and linearise.

The perturbation to the gravitational potential in the exterior can be written as

$$\delta\Phi(X^i) = \sum_{\ell=0}^{\infty}\sum_{m=-\ell}^{\ell} \delta\Phi_{\ell m}(\mathcal{R})Y_{\ell m}(\vartheta,\varphi), \quad \delta\Phi_{\ell m}(\mathcal{R}) = -\frac{4\pi G}{2\ell+1}\frac{Q_{\ell m}}{\mathcal{R}^{\ell+1}}. \tag{2.79}$$

Note that, for many problems of astrophysical interest, the total mass of the star will remain conserved. In these cases, the $\ell = 0$ monopole of the perturbation will vanish. [Indeed, this is guaranteed when the constraint (2.51) is applied.] Additionally, one might prefer to work in a mass-centred coordinate system, in which there is no $\ell = 1$ dipole contribution.

It is important to note that, in the absence of a perturbing force, the star will remain spherical. For example, by perturbing the mass density, say, the star will simply move to a neighbouring equilibrium configuration along the mass-radius curve (Fig. 2.1). One must introduce non-sphericity into the situation via some deforming force. Simply put: an unforced, fluid equilibrium is spherical. Suppose we introduce another potential χ that is related to a deforming force the star is subject to. This potential will adjust the total potential by

$$\Phi(\mathcal{R})+\delta\Phi(X^i)+\chi(X^i) = -\frac{GM}{\mathcal{R}}+\sum_{\ell=0}^{\infty}\sum_{m=-\ell}^{\ell}\left[-\frac{4\pi G}{2\ell+1}\frac{Q_{\ell m}}{\mathcal{R}^{\ell+1}}+\chi_{\ell m}(\mathcal{R})\right]Y_{\ell m}(\vartheta,\varphi). \tag{2.80}$$

We will make use of this result when we calculate mountains in Newtonian gravity in Chap. 4.

2.4.2 Relativistic multipole moments

In general relativity, the spacetime metric g_{ab} replaces the Newtonian potential Φ. In the far-field exterior, one may write

$$-\frac{1+g_{tt}}{2} = \Phi + \chi. \tag{2.81}$$

Although in Newtonian gravity one is usually able to analyse the gravitational and deforming potentials separately, such a neat decoupling does not exist in relativity. In relativity, one has the metric that accounts for all the potentials acting on the body. For this reason, in some cases it is not possible to disentangle the separate potentials from the metric and ambiguities arise.[15] However, there are no ambiguities when one considers multipoles of pure ℓ. [Indeed, we will ultimately focus on pure multipoles of order (ℓ, m).] In this case,

[15] To be specific, ambiguities occur when different potentials mix in powers of $\mathcal{R}$. Much of the work concerning separating multiple gravitational effects in relativity has come from studies on tidal deformations (see, *e.g.*, Gralla, 2018).

we have [*cf.* a variation of (2.81)]

$$-\frac{1+g_{tt}+h_{tt}}{2} = -\frac{M}{\mathcal{R}} + \sum_{m=-\ell}^{\ell}\left[-\frac{4\pi}{2\ell+1}B_\ell(\mathcal{R})\frac{Q_{\ell m}}{\mathcal{R}^{\ell+1}} + \chi_{\ell m}(\mathcal{R})\right]Y_{\ell m}(\vartheta,\varphi), \tag{2.82}$$

where $h_{ab} = \delta g_{ab}$ is the linearised metric and $B_\ell(\mathcal{R})$ is a function that goes to unity in the Newtonian limit (this is given as B_1 in Table I of Binnington and Poisson, 2009). Equation (2.82) is obtained by looking for a solution to the Einstein equations in the vacuum around the star (as we shall discuss in Chap. 5).

2.5 Gravitational waves

Having discussed how one formally describes the interior structure and shape of a neutron star, we have reached an appropriate point to consider how gravitational waves emerge in general relativity. For more detail, the following textbooks are recommended: Maggiore (2008) and Andersson (2019).

2.5.1 The wave equation

The most straightforward way to see how gravitational waves arise is through the linearised theory of gravity. One considers a region of spacetime where the metric is close to flat,

$$g_{ab} = \eta_{ab} + h_{ab}, \qquad |h_{ab}| \ll 1, \tag{2.83}$$

where η_{ab} is the Minkowski metric. In Cartesian coordinates, the Minkowski metric is given by

$$\eta_{ab}dx^a dx^b = -dt^2 + dx^2 + dy^2 + dz^2. \tag{2.84}$$

In linearised gravity, one substitutes (2.83) into the Einstein equations (2.20) and then retains terms up to linear order in h_{ab}. One can show, through the definition $\delta_a{}^b = g_{ac}g^{cb}$, that the inverse metric is

$$g^{ab} = \eta^{ab} - h^{ab} + \mathcal{O}(|h_{ab}|^2), \tag{2.85}$$

where $h^{ab} = \eta^{ac}\eta^{bd}h_{cd}$. Therefore, indices of terms of $\mathcal{O}(|h_{ab}|)$ can be raised and lowered with the flat metric η_{ab}.

It should be noted that in writing the metric as in (2.83), we have made a specific choice of frame such that $|h_{ab}| \ll 1$ holds on a sufficiently large region of space. In choosing this frame, a residual gauge freedom remains. A gauge freedom corresponds to the invariance of a quantity under a coordinate transformation. Consider a transformation of coordinates such that

$$x^a \to x'^a = x^a + \zeta^a(x^a), \tag{2.86}$$

where ζ^a is the generator of the transformation and the derivatives $|\partial_a\zeta_b|$ are of the same

order of smallness as $|h_{ab}|$. By the transformation law for tensors under coordinate changes,

$$g_{ab}(x^a) \to g'_{ab}(x'^a) = \frac{\partial x^c}{\partial x'^a}\frac{\partial x^d}{\partial x'^b} g_{cd}(x^a), \tag{2.87}$$

we find

$$h_{ab}(x^a) \to h'_{ab}(x'^a) = h_{ab}(x^a) - [\partial_a \zeta_b(x^a) + \partial_b \zeta_a(x^a)], \tag{2.88}$$

to leading order. If $|\partial_a \zeta_b|$ are small, then the condition $|h_{ab}| \ll 1$ is preserved under a transformation.

Since the curvature terms vanish for flat space, one can show that the Riemann tensor for the metric (2.83), to linear order in h_{ab}, is

$$R_{abcd} = \frac{1}{2}(\partial_b \partial_c h_{ad} + \partial_a \partial_d h_{bc} - \partial_a \partial_c h_{bd} - \partial_b \partial_d h_{ac}). \tag{2.89}$$

Pleasingly, one can show by inserting the transformation (2.88) into (2.89) that the Riemann tensor is invariant under the residual gauge transformation, as it should be.

It turns out that the linearised equations of motion can be expressed in a more compact form if one introduces the trace-reversed metric perturbation

$$\bar{h}_{ab} \equiv h_{ab} - \frac{1}{2}\eta_{ab} h, \tag{2.90}$$

where $h = \eta^{ab} h_{ab}$. One can invert this to show that $h_{ab} = \bar{h}_{ab} - \eta_{ab}\bar{h}/2$, where $\bar{h} = \eta^{ab}\bar{h}_{ab} = -h$. Thus, the Einstein equations (2.20) may be expressed as

$$G_{ab} = -\frac{1}{2}(\Box \bar{h}_{ab} + \eta_{ab}\partial^c \partial^d \bar{h}_{cd} - \partial^c \partial_b \bar{h}_{ac} - \partial^c \partial_a \bar{h}_{bc}) = 8\pi T_{ab}, \tag{2.91}$$

where $\Box \equiv \partial^a \partial_a$ is the flat-space d'Alembertian. It is worthwhile noting that the stress-energy tensor in linearised gravity enters the problem at $\mathcal{O}(|\bar{h}_{ab}|)$ as the background must be flat. Clearly, this will simplify considerably if we make the following gauge choice:

$$\partial^b \bar{h}_{ab} = 0. \tag{2.92}$$

This is known as the *Lorenz gauge*. The freedom to impose the gauge condition (2.92) comes from (2.88), which, in terms of the trace-reversed metric perturbation, is

$$\bar{h}_{ab} \to \bar{h}'_{ab} = \bar{h}_{ab} - (\partial_a \zeta_b + \partial_b \zeta_a - \eta_{ab}\partial_c \zeta^c). \tag{2.93}$$

Thus,

$$\partial^b \bar{h}_{ab} \to (\partial^b \bar{h}_{ab})' = \partial^b \bar{h}_{ab} - \Box \zeta_a. \tag{2.94}$$

Therefore, we can always ensure (2.92) is satisfied if we transform the coordinates such

that $\Box\zeta_a = \partial^b \bar{h}_{ab}$. In this gauge, Eq. (2.91) provides the wave equation

$$\Box\bar{h}_{ab} = -16\pi T_{ab}. \tag{2.95}$$

By Eqs. (2.92) and (2.95), the condition $\partial^b T_{ab} = 0$ is automatically satisfied.

To summarise, we have seen how general relativity permits small perturbations on an otherwise flat background that satisfy the wave equation (2.95). These solutions correspond to gravitational waves that travel at the speed of light.

We should note the approximations implicit in linearised theory. The bodies that generate the gravitational waves are assumed to move in flat spacetime. This essentially means the dynamics are described using Newtonian gravity.

2.5.2 Interaction with test masses

To understand how gravitational waves propagate and interact with test masses, we consider (2.95) outside the source,

$$\Box\bar{h}_{ab} = 0. \tag{2.96}$$

We note that the Lorenz gauge is not sufficient to fix the full gauge freedom. Further analysis shows that one can introduce an additional coordinate transformation $x^a \to x^a + \zeta^a$, where

$$\Box\zeta_a = 0, \tag{2.97}$$

that leaves (2.94) unspoiled. Thus, one can impose four further conditions. It is convenient to choose $\bar{h} = 0$ so $\bar{h}_{ab} = h_{ab}$ and $h_{ti} = 0$. Therefore, the Lorenz condition (2.92) reads

$$\partial^t h_{tt} = 0, \qquad \partial^j h_{ij} = 0. \tag{2.98}$$

One should note that h_{tt} corresponds to the static part of the gravitational interaction, which is related to the Newtonian potential of the source of the waves. The gravitational wave is the time-dependent part of the perturbation and so we are free to set $h_{tt} = 0$. The time-varying aspect of the wave is contained in h_{ij}. In summary, the gauge is fixed with

$$h_{ta} = 0, \qquad h_i{}^i = 0, \qquad \partial^j h_{ij} = 0. \tag{2.99}$$

This defines the *transverse-traceless gauge* which we will denote using h_{ij}^{TT}.[16] It should be noted that the transverse-traceless gauge does not provide the same level of simplification inside the source where $T_{ab} \neq 0$.

[16] One can show by analysing the geodesics of test masses in the transverse-traceless gauge that it corresponds to a frame where masses which were at rest before the gravitational wave arrives remain at rest after it has passed.

In the transverse-traceless gauge, the solution to (2.96) is

$$h_{ij}^{\mathrm{TT}} = e_{ij} \exp(ik_a x^a), \tag{2.100}$$

where $k^a = (\omega, k^i)$ is the wave four-vector, ω is the angular frequency of the waves and e_{ij} is the polarisation tensor. Assuming the waves propagate along the z-axis and ensuring that h_{ij}^{TT} is symmetric and traceless, we have

$$h_{ij}^{\mathrm{TT}} dx^i dx^j = h_+ \cos[\omega(t-z)]dx^2 + 2h_\times \cos[\omega(t-z)]dxdy - h_+ \cos[\omega(t-z)]dy^2, \tag{2.101}$$

where h_+ and $h_\times$ are the two independent wave polarisations corresponding to the two degrees of freedom.

Given a plane wave h_{ab} travelling in the direction of the unit vector $\hat{n}^i$, already in the Lorenz gauge, one can transform the solution to the transverse-traceless gauge using the projection operator

$$\Lambda_{ij}{}^{kl} = P_i{}^k P_i{}^l - \frac{1}{2} P_{ij} P^{kl}, \qquad P_{ij} = \delta_{ij} - \hat{n}_i \hat{n}_j, \tag{2.102}$$

where δ_{ij} are the spatial parts of η_{ab}. Thus, one projects the solution into the transverse-traceless gauge by $h_{ij}^{\mathrm{TT}} = \Lambda_{ij}{}^{kl} h_{kl}$.

With the gauge freedom fully exploited, we can consider how test masses move due to a gravitational wave. Both masses are treated as point particles freely falling in flat space. They are separated by four-vector $\zeta^a(\tau)$ such that one test mass is at $x^a(\tau)$ and the other is at $x^a(\tau) + \zeta^a(\tau)$, where τ is the proper time as measured by a clock carried along the trajectory x^a. The masses follow geodesics, given by the *geodesic equation*

$$u^b \nabla_b u^a = \frac{du^a}{d\tau} + \Gamma^a{}_{bc} u^b u^c = 0, \tag{2.103}$$

where $u^a = dx^a/d\tau$. In flat space with Cartesian coordinates, $\Gamma^a{}_{bc} = 0$ and we obtain the classical result that particles follow straight lines in the absence of a force. Assuming that $|\zeta^a|$ is smaller than the variation of the gravitational field, one can show by analysing the geodesics followed by both test masses that, to first order in ζ^a,

$$\frac{D^2 \zeta^a}{D\tau^2} = -R^a{}_{bcd} u^b \zeta^c u^d, \tag{2.104}$$

where $D/D\tau \equiv u^a \nabla_a$ is the directional derivative along the four-velocity u^a. This is the *equation of geodesic deviation*, a well-known result in general relativity. It demonstrates that two nearby time-like geodesics experience a tidal gravitational force, given by the Riemann tensor. When spacetime is flat, $R^a{}_{bcd} = 0$ and the separation is fixed or changes at a constant rate. However, in curved spacetime, the four-vector ζ^a will accelerate.

Geodesics that are initially parallel will eventually converge or diverge.

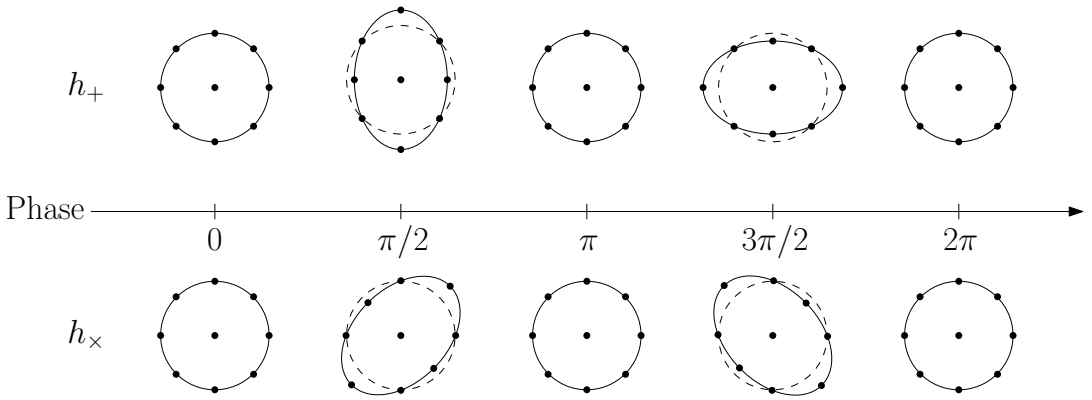

Figure 2.2: The effect of a gravitational wave on a ring of freely falling test masses in the transverse-traceless frame due to the + and × polarisations. Note that the separation illustrated corresponds to the proper distances between the masses in the transverse-traceless frame.

The Riemann tensor is effected by the gravitational wave according to (2.89) and (2.104) returns

$$\partial_t^2 \zeta^i = \frac{1}{2}\delta^{ij}\partial_t^2 h_{jk}^{\mathrm{TT}} \zeta^k, \tag{2.105}$$

where we have limited ourselves to linear order in h_{ij} so $t = \tau$. The solution to (2.105) is simply

$$\zeta^i(t) = \left[\delta^i{}_k + \frac{1}{2}\delta^{ij} h_{jk}^{\mathrm{TT}}(t)\right] \zeta^k(0). \tag{2.106}$$

Equation (2.106) shows how freely falling test masses move according to a gravitational wave h_{ij}^{TT} in the transverse-traceless frame. We show the motion of a ring of test masses due to the two polarisations in Fig. 2.2. As the wave passes through the ring, the proper distance between the masses is stretched and squeezed. This periodic behaviour is the basic principle that is exploited by gravitational-wave detectors.

2.5.3 Generation of gravitational waves

We now turn our attention to how the gravitational waves are sourced. Although the wave solution (2.100) was known in the 1920s, much confusion surrounded the idea of whether the waves were physical in nature (Kennefick, 2007). Many leading physicists weighed into the debate, including Eddington (1922) who observed problems with the gauge artefacts where they propagated at velocities that depended on the choice of coordinates. Einstein himself believed at some point that (2.100) was an artefact of the linear approximation and no wave solution would exist in the full non-linear theory. Einstein and Rosen (1937) initially concluded that gravitational waves were unphysical upon finding a singularity in a non-linear cylindrical wave solution in 1936, only to retract this with the realisation that it was merely a coordinate singularity. A recurring theme was the issue of coordinate and gauge dependencies, in particular the properties of the Lorenz and transverse-traceless

gauges. Also problematically, the stress-energy tensor of a gravitational field was found to not be invariant under the transformation (2.88), casting further doubt on the physical nature of gravitational waves.

It turns out that the stress-energy tensor of gravitational waves t_{ab} not being gauge invariant is a manifestation of the equivalence principle of general relativity: one is free to choose a local inertial frame at any point in spacetime where the gravitational wave vanishes. This indicates that we cannot localise the effect of the wave. While t_{ab} is not well-defined locally, it certainly carries energy. In order to understand the physical effect of the wave, one must average over several wavelengths. Indeed, one can show that the averaged stress-energy tensor $\langle t_{ab} \rangle$ is gauge invariant. One finds that the averaging procedure cancels the gauge terms in (2.88) and obtains (Isaacson, 1968)

$$\langle t_{ab} \rangle = \frac{1}{32\pi} \langle \partial_a h_{ij}^{\mathrm{TT}} \partial_b h^{\mathrm{TT}ij} \rangle. \tag{2.107}$$

The solution of (2.95) can be obtained using a retarded Green's function,

$$\bar{h}_{ab}(t, X^i) = 4 \int_V \frac{1}{|X^i - x^i|} T_{ab}(t - |X^i - x^i|, x^i) dV, \tag{2.108}$$

where the integration is over the volume of the star. For simplicity, we assume that the waves are generated by a weak source and are observed far from the source, $r \ll \mathcal{R}$. In this limit, we have

$$\bar{h}_{ab}(t, X^i) = \frac{4}{\mathcal{R}} \int_V T_{ab}(t - r, x^i) dV + \mathcal{O}\left(\frac{1}{\mathcal{R}^2}\right). \tag{2.109}$$

What we have done here, in exploiting a Newtonian limit, forms the basis of the post-Newtonian expansion. As we have discussed, general relativity is a highly non-linear theory, which makes it challenging to evaluate. This contributes to the appeal of linear perturbation theory in relativistic problems. The post-Newtonian expansion bridges the gap between the linear approximation and the full non-linear theory by expanding the relativistic expressions in terms of small parameters (see, *e.g.*, Blanchet, 2006; Poisson and Will, 2014).

By using the conservation law $\partial^b T_{ab} = 0$ and noting how the divergence terms vanish on the surface, one can derive the relation

$$2 \int_V T_{ij} dV = \int_V \partial_t^2 T_{tt} x_i x_j dV. \tag{2.110}$$

Hence, we can write

$$\bar{h}_{ij}(t, X^i) = \frac{2}{\mathcal{R}}\partial_t^2 \left[\int_V T_{tt}(t-r, x^i)x_i x_j dV\right] \equiv \frac{2}{\mathcal{R}}\partial_t^2 M_{ij}(t-r), \tag{2.111}$$

where we have introduced the (non-traceless) mass-quadrupole moment M_{ij}. The justification for this identification lies in the fact that, in the Newtonian limit, $T_{tt} = \rho$. Transforming to the transverse-traceless frame, we arrive at the result

$$h_{ij}^{\rm TT}(t, X^i) = \frac{2}{\mathcal{R}}\Lambda_{ij}{}^{kl}\partial_t^2 M_{kl}(t-r) = \frac{2}{\mathcal{R}}\partial_t^2 Q_{ij}(t-r), \tag{2.112}$$

where Q_{ij} is the trace-reduced analogue of M_{ij}, given by (2.65) in this limit. Equation (2.112) is the *quadrupole formula* and it provides the basis for many useful gravitational-wave estimates. We see that (i) gravitational waves are generated by accelerating sources of matter (entirely analogous to how waves are produced in electromagnetism), (ii) the radiation falls off, to leading order, as $1/\mathcal{R}$ and (iii) gravitational waves are quadrupolar. This result is true in the full non-linear theory; monopole and dipole radiation are absent in general relativity. The lack of monopole radiation turns out to be a consequence of Birkhoff's theorem (Jebsen, 1921; Birkhoff and Langer, 1923), that any spherically symmetric spacetime must be static and asymptotically flat. Dipole radiation does not exist because there are no opposite charges in gravity.

One can show that the gravitational-wave luminosity is (Einstein, 1918)

$$L_{\rm GW} = \frac{1}{5}\langle \partial_t^3 Q_{ij}(t-r)\partial_t^3 Q^{ij}(t-r)\rangle \tag{2.113}$$

This characterises how gravitational waves carry energy away from the source. It was the Hulse-Taylor binary that enabled a first observational test for this result by studying the binary's orbital decay (see Fig. 1.2; Hulse and Taylor, 1975).

CHAPTER 3

Gravitational waves from accreting neutron stars

In this chapter, we shall consider the question of whether gravitational waves are expected to play a meaningful role in the dynamics of accreting neutron stars. This was the subject of Gittins and Andersson (2019), which we follow in this chapter. In particular, we investigate whether an additional component is needed in order to explain the spin evolution of accreting neutron stars. We consider gravitational-wave emission as the source of such a component and explore what may be the dominant gravitational-wave production mechanism.

To begin with, in Sec. 3.1, we provide a brief overview of accreting neutron stars and the puzzle observing their spins has presented. In Sec. 3.2, we introduce the basic theory regarding accretion in low-mass X-ray binaries and discuss how transient accretion can affect the spin evolution of accreting neutron stars. In Sec. 3.3, we provide a brief review of gravitational radiation in these systems and the different mechanisms that can give rise to such emission. We describe our model for the spin evolution of accreting neutron stars in Sec. 3.4. In Sec. 3.5, we summarise the results of our neutron-star population simulations, that include the different gravitational-wave-production mechanisms. Finally, we summarise and suggest future work in Sec. 3.6.

3.1 Accreting neutron stars

A promising subset of rotating neutron stars in the context of gravitational-wave searches are the accreting neutron stars (Papaloizou and Pringle, 1978; Wagoner, 1984). The reason for this is quite intuitive. In order for a star to emit gravitational radiation, it must be deformed. Suppose a star is accreting from a companion. As the accreted matter gets close to the star, it begins to follow the magnetic-field lines. Provided the magnetic poles of the star are misaligned with respect to its axis of rotation, then the star quite naturally develops a mass asymmetry as matter piles up around the poles. This picture is overly simplified, since there are many aspects to this that we do not fully understand. Nevertheless, there is a strong case to study these systems more.

The classical picture for the evolution of rapidly spinning neutron stars begins with a neutron star accreting gas via a circumstellar accretion disc from their companion in a low-mass X-ray binary (Alpar *et al.*, 1982; Radhakrishnan and Srinivasan, 1982). This process causes the neutron star to spin up and, eventually, the neutron star accretes all the gas from its companion such that all that is left of the binary is a radio millisecond pulsar. This scenario should, in theory, have no difficulty in spinning neutron stars up to their centrifugal break-up frequency (Cook *et al.*, 1994), which is generally above $\sim 1\,\mathrm{kHz}$ for most equations of state (Lattimer and Prakash, 2007). However, the fastest-spinning pulsar that has been observed to date is PSR J1748-2446ad, which spins at 716 Hz (Hessels *et al.*, 2006); well below the limit set by the break-up frequency. In fact, the distribution of spins for both low-mass X-ray binaries and radio millisecond pulsars has been shown to have a statistically significant cut-off at 730 Hz (Chakrabarty *et al.*, 2003; Patruno, 2010).

Accreting millisecond X-ray pulsars are a sub-class of low-mass X-ray binaries that have been spun up to millisecond periods through accretion [see Patruno and Watts (2021) for a review on these systems]. They are characterised by accretion rates $\gtrsim 10^{-11}\,M_\odot\,\mathrm{yr}^{-1}$ and comparatively weak magnetic fields ($\sim 10^8\,\mathrm{G}$). Another important sub-class of low-mass X-ray binaries are the nuclear-powered X-ray pulsars. These pulsars show short-lived burst oscillations during thermonuclear burning on their surfaces and are distinct from accreting millisecond X-ray pulsars due to being powered by nuclear burning rather than accretion. Nineteen accreting millisecond X-ray pulsars and eleven nuclear-powered X-ray pulsars have been observed to date.

Haskell *et al.* (2018) showed that the observed rotation rate limit of neutron stars does not correspond to centrifugal break-up and argued that additional spin-down torques are required to explain this effect. It is unclear what physical process prevents these neutron stars from spinning up to sub-millisecond periods. One candidate is the interaction between the magnetic field and the accretion disc (Ghosh and Lamb, 1978; White and Zhang, 1997; Andersson *et al.*, 2005). Patruno *et al.* (2012) demonstrated that a magnetic-

field strength at the magnetosphere of $\sim 10^8$ G could be enough to explain the deficiency in accreting neutron stars above ~ 700 Hz. More recently, it has been shown that transient accretion can have a significant impact on the spin evolution of an accreting neutron star (Bhattacharyya and Chakrabarty, 2017; D'Angelo, 2017). In fact, Bhattacharyya and Chakrabarty (2017) noted that in the case of transient accretion, a magnetosphere of $\sim 10^8$ G would no longer be sufficient to explain the spin limit. It was suggested by Bildsten (1998) and Andersson *et al.* (1999) that one would observe a spin-frequency limit to accreting neutron stars if they were emitting gravitational waves, thus, providing a torque to balance the accretion torques (Papaloizou and Pringle, 1978; Wagoner, 1984).

3.2 Accretion in low-mass X-ray binaries

In a low-mass X-ray binary, the companion star has overfilled its Roche lobe and is donating matter to the neutron star through the inner Lagrange point. Given this donated gas has some large specific angular momentum, it cannot be transferred directly to the surface of the neutron star and instead forms a circumstellar accretion disc around it. The gas from the accretion disc is channelled onto the magnetic poles of the neutron star along the magnetic-field lines. This channelling occurs at what is known as the *magnetospheric radius*, $r_{\rm m}$, which is the characteristic radius where the magnetic field dominates interactions. At this boundary the magnetic field can, in turn, be distorted by the accreting gas. This coupling, between the field lines and the disc, results in a torque acting on the star that can spin it up or down depending on the relative difference between $r_{\rm m}$ and the *co-rotation radius*,

$$r_{\rm c} \equiv \left(\frac{GM}{\Omega^2}\right)^{1/3}, \tag{3.1}$$

which is the location of a Keplerian disc that rotates with the same frequency of the neutron star, where $\Omega = 2\pi\nu = 2\pi/P$ is its angular frequency, ν is the spin frequency[1] and P is the spin period. If $r_{\rm m} < r_{\rm c}$, the neutron star spins slower than the accretion disc and so the gas that is channelled onto the neutron star has greater specific angular momentum than it, thus, acting to spin it up. Conversely, if $r_{\rm m} > r_{\rm c}$, the neutron star spins faster than the disc, which spins it down.

The magnetospheric radius is a somewhat poorly understood quantity. It is generally defined as the point where the kinetic energy of in-falling gas becomes comparable to the magnetic energy of the magnetosphere. For the straightforward case where the gas is radially accreted onto the neutron star, one can calculate the Alfvén radius, $r_{\rm A}$, from:

$$\frac{1}{2}\rho(r_{\rm A})v(r_{\rm A})^2 = \frac{B(r_{\rm A})^2}{8\pi}, \tag{3.2}$$

where $\rho(r_{\rm A})$, $v(r_{\rm A})$ and $B(r_{\rm A})$ are the gas density, gas speed and magnetic-field strength,

[1] We re-emphasise that this is distinct from the metric potential ν.

respectively, at $r_{\rm A}$. This calculation gives the standard expression for the magnetospheric radius (Pringle and Rees, 1972):

$$r_{\rm A} = \left(\frac{\mu^4}{2GM\dot{M}^2}\right)^{1/7}, \tag{3.3}$$

where $\mu = BR^3$ is the magnetic moment of the neutron star[2] and $\dot{M}$ is the mass-accretion rate from the disc to the neutron-star surface. This picture becomes more complicated when considering accretion from a circumstellar disc. A phenomenological factor ξ of order unity is introduced to correct for the non-spherical geometry of the problem and also account for the extended transition region between where mass is accreted onto the star and where mass is ejected in an outflow. This gives the magnetospheric radius as

$$r_{\rm m} = \xi r_{\rm A} = \xi \left(\frac{\mu^4}{2GM\dot{M}^2}\right)^{1/7}. \tag{3.4}$$

Typically, ξ is assumed to fall in the range $0.5 - 1.4$ (Wang, 1996). This correction demonstrates that $r_{\rm m}$ is sensitive to the coupling between the field lines and the accretion disc that plays a key role in understanding the magnetospheric radius.

3.2.1 Accretion-torque models

The spin evolution of a neutron star is dictated by the torques acting upon the star. By measuring the time derivative of the spin period, $\dot{P}$, (or, equivalently, the time derivative of the angular frequency, $\dot{\Omega}$) one can gain insight into the physics of accretion processes, as well as other aspects such as magnetic-field strengths and gravitational-wave emission. The variation in spin is related to the torque exerted onto the neutron star by the standard expression

$$N = I_{zz}\dot{\Omega} = -\frac{2\pi I_{zz}\dot{P}}{P^2}, \tag{3.5}$$

where I_{zz} is the principal stellar moment of inertia about the rotation axis.

For a neutron star accreting from an accretion disc truncated at the magnetospheric transition, with $r_{\rm m} < r_{\rm c}$, the standard spin-up torque is

$$N_{\rm acc} = \dot{M} r_{\rm m}^2 \Omega_{\rm K}(r_{\rm m}) = \dot{M}\sqrt{GMr_{\rm m}}, \tag{3.6}$$

where $\Omega_{\rm K}(r_{\rm m})$ is the Keplerian angular frequency at $r_{\rm m}$. For $r_{\rm m} > r_{\rm c}$, the coupling between the magnetosphere and the accretion disc becomes important as the magnetic-field lines are threaded through the disc, so extra torques due to magnetic stresses come into play. Ghosh and Lamb (1979) developed an accretion model based on detailed calculations of

[2]It should be re-emphasised that this is separate from the chemical potential μ.

this coupling. The torque from this model predicts

$$\dot{P} \approx -5.0 \times 10^{-5} \left(\frac{M}{1.4\,M_\odot}\right)^{3/7} \left(\frac{I_{zz}}{10^{45}\,\mathrm{g\,cm^2}}\right)^{-1} \left(\frac{\mu}{10^{30}\,\mathrm{G\,cm^3}}\right)^{2/7} \times \left[\left(\frac{P}{1\,\mathrm{s}}\right)\left(\frac{\dot{M}}{10^{-9}\,M_\odot\,\mathrm{yr^{-1}}}\right)^{3/7}\right]^2 n(\omega_\mathrm{s})\ \mathrm{s\,yr^{-1}}, \tag{3.7}$$

where $n(\omega_\mathrm{s})$ is the dimensionless torque that accounts for the magnetic field-accretion disc coupling and is a function of the fastness parameter ω_s. The fastness parameter is defined as the ratio of the neutron-star spin frequency to the Keplerian orbital frequency at the magnetospheric boundary,

$$\omega_\mathrm{s} \equiv \frac{\Omega}{\Omega_\mathrm{K}(r_\mathrm{m})} \approx 3.1\,\xi^{3/2} \left(\frac{M}{1.4\,M_\odot}\right)^{-5/7} \left(\frac{\mu}{10^{30}\,\mathrm{G\,cm^3}}\right)^{6/7} \times \left[\left(\frac{P}{1\,\mathrm{s}}\right)\left(\frac{\dot{M}}{10^{-9}\,M_\odot\,\mathrm{yr^{-1}}}\right)^{3/7}\right]^{-1}. \tag{3.8}$$

The sign of $n(\omega_\mathrm{s})$ depends on whether the neutron star accretes the gas and spins up (the 'slow rotator' regime, $\omega_\mathrm{s} < 1$) or ejects the gas and spins down (the 'fast rotator' regime, $\omega_\mathrm{s} > 1$; Wang, 1995). It is interesting to note that a neutron star can still be spun down at long spin periods ($P \gg 1\,\mathrm{s}$) as the magnetic field can be strong enough to mean it would still be classified as a fast rotator.

Ho *et al.* (2014) introduced a simple approximation to the Ghosh and Lamb (1979) model by considering angular momentum changes on the neutron star. Matter accreting at the magnetosphere, r_m, has specific angular momentum

$$l_\mathrm{acc} = \pm r_\mathrm{m}^2 \Omega_\mathrm{K}(r_\mathrm{m}), \tag{3.9}$$

where the sign of l_acc depends on whether there is prograde rotation between the accretion disc and the neutron star ($l_\mathrm{acc} > 0$) or retrograde rotation ($l_\mathrm{acc} < 0$). Prograde rotation will be assumed here. What must also be accounted for is matter that is ejected from the neutron star, that will carry specific angular momentum

$$l_\mathrm{m} = r_\mathrm{m}^2 \Omega. \tag{3.10}$$

Both of these effects produce a torque on the neutron star. The net torque is obtained by summing these contributions:

$$N = \dot{M}(l_\mathrm{acc} - l_\mathrm{m}) = \dot{M} r_\mathrm{m}^2 \Omega_\mathrm{K}(r_\mathrm{m})(1 - \omega_\mathrm{s}). \tag{3.11}$$

In this relation, one can see the standard spin-up torque due to disc accretion (3.6) that is

corrected by the fastness parameter to account for interactions spinning down the neutron star. (This model phenomenologically accounts for effects such as accretion disc-magnetic field coupling and outflows.) This expression can be related to the change in spin period using (3.5) to obtain

$$\dot{P} \approx -8.1\times10^{-5}\,\xi^{1/2}\left(\frac{M}{1.4\,M_\odot}\right)^{3/7}\left(\frac{I_{zz}}{10^{45}\,\mathrm{g\,cm^2}}\right)^{-1}\left(\frac{\mu}{10^{30}\,\mathrm{G\,cm^3}}\right)^{2/7} \times\left[\left(\frac{P}{1\,\mathrm{s}}\right)\left(\frac{\dot{M}}{10^{-9}\,M_\odot\,\mathrm{yr^{-1}}}\right)^{3/7}\right]^2(1-\omega_\mathrm{s})\,\mathrm{s\,yr^{-1}}. \tag{3.12}$$

It is clear from (3.12) that the fastness parameter dictates whether the neutron star spins up or down.

A commonly considered aspect of a neutron star's spin evolution is the spin equilibrium. This occurs when the spin rate is gradually adjusted until the net torque on the star is approximately zero and the accretion flow is truncated at the magnetospheric radius, $r_\mathrm{m} \simeq r_\mathrm{c}$. When a neutron star reaches spin equilibrium, it is straightforward to estimate its magnetic field, assuming that the accretion rate and spin are known. One can estimate the spin-equilibrium period, P_eq, from (3.12) by setting $\dot{P}=0$, when $\omega_\mathrm{s}=1$:

$$P_\mathrm{eq} \approx 8.2\,\xi^{3/2}\left(\frac{M}{1.4\,M_\odot}\right)^{-5/7}\left(\frac{\mu}{10^{26}\,\mathrm{G\,cm^3}}\right)^{6/7}\left(\frac{\dot{M}}{10^{-11}\,M_\odot\,\mathrm{yr^{-1}}}\right)^{-3/7}\mathrm{ms}, \tag{3.13}$$

where we have scaled the period to characteristic accreting millisecond X-ray pulsar values. Here, we see that, provided fast accretion rates and small magnetic-field strengths (therefore, negligible magnetic-dipole spin-down), it should not be difficult for (at least some) accreting neutron stars to reach sub-millisecond periods.

The magnetic-field lines rotate with the neutron star. This produces magnetic-dipole radiation which causes the neutron star to spin down. The torque due to this is well approximated by (see, *e.g.*, D'Angelo, 2017)

$$N_\mathrm{EM} = -\frac{2\mu^2\Omega^3}{3c^3}. \tag{3.14}$$

The change in spin due to magnetic-dipole radiation is

$$\dot{P}_\mathrm{EM} \approx 3.1\times10^{-8}\left(\frac{\mu}{10^{30}\,\mathrm{G\,cm^3}}\right)^2\left(\frac{I_{zz}}{10^{45}\,\mathrm{g\,cm^2}}\right)^{-1}\left(\frac{P}{1\,\mathrm{s}}\right)^{-1}\mathrm{s\,yr^{-1}}. \tag{3.15}$$

The vast majority of pulsars are isolated and their spin evolution can be generally described by magnetic-dipole radiation. However, in the case of rapidly accreting neutron stars this effect can be essentially negligible. There are more accurate numerical models one can use

to describe these torques (*e.g.*, see Spitkovsky, 2006).

3.2.2 Transient accretion

Up until now, the accretion rate has been implicitly assumed to be steady. However, many low-mass X-ray binaries exhibit long periods of quiescence, that can be of the order of months to years, and short transient outbursts, that can last from days to weeks. These outbursts are believed to be caused by instabilities in the accretion disc and occur when the mass-accretion rate rises above a certain threshold (see, *e.g.*, Lasota, 1997). As the companion star donates a steady flow of gas to the accretion disc, the disc gets larger and eventually reaches a critical mass to trigger an instability. This causes the accretion rate from the disc to the surface of the neutron star to increase by several orders of magnitude, giving rise to a transient outburst. Once the accretion disc has donated a sufficient amount of gas, the system returns to a quiescent state until a new outburst occurs when the disc has accumulated enough mass from the companion and the cycle repeats (Done *et al.*, 2007).

D'Angelo (2017) and Bhattacharyya and Chakrabarty (2017) have shown that transient accretion with a varying accretion rate has a significant impact on the spin evolution of a neutron star. Both found that for a given long-term average accretion rate, these transients can spin up neutron stars to rates several times higher than that of persistent accretors, however, it takes approximately an order of magnitude longer to reach these spin-equilibrium periods. This demonstrates that for transient systems, like most low-mass X-ray binaries, it is not accurate to assume a time-averaged accretion rate but instead one must consider the outburst/quiescence phases. D'Angelo (2017) noted that the two key changes when considering transient accretion are: (i) the torque over an outburst is significantly smaller than for the persistent case at a given accretion rate and (ii) the equilibrium accretion rate is shifted to a lower value. This has the combined effect to increase the time it takes for a transient source to reach spin equilibrium and decrease its spin-equilibrium period.

D'Angelo (2017) and Bhattacharyya and Chakrabarty (2017) found that the spin-equilibrium period and time to reach spin equilibrium are sensitive to the features of the accretion profile. They found that by increasing the duration of an outburst by a factor of 10 the spin-equilibrium period can decrease by up to a factor of 2.

For her analysis, D'Angelo (2017) used a fast-rise, exponential-decay function to model the accretion profile [whereas Bhattacharyya and Chakrabarty (2017) used a simple sawtooth function]:

$$f(t) = \exp\left(\sqrt{\frac{2}{F_{\rm t}}}\right) \exp\left(-\frac{1}{10t} - \frac{10t}{F_{\rm t}}\right) + f_{\rm min}, \tag{3.16}$$

where t denotes the time from the beginning of the outburst, $F_{\rm t}$ is an approximate measure

of the duration of the outburst and $f_{\rm min}$ is the minimum. It should be noted that this function models a single outburst/quiescence cycle, so in order to model multiple cycles one repeats this after a given recurrence time, $T_{\rm recurrence}$. Time has arbitrary units in this model. The ratio of the maximum to the minimum is

$$\frac{f_{\rm max}}{f_{\rm min}} = \frac{1}{f_{\rm min}} \exp\left(\frac{\sqrt{2}-2}{\sqrt{F_{\rm t}}}\right) + 1. \tag{3.17}$$

This accretion profile requires two normalisations. The first normalisation chooses $f_{\rm max}/f_{\rm min}$ to obtain $f_{\rm min}$ for a fixed $F_{\rm t}$ using (3.17). The second normalisation is to demand that $\langle f(t)\rangle = 1$. This normalisation depends on $T_{\rm recurrence}$ and results in $f_{\rm min}$ no longer corresponding precisely to the minimum value. These normalisations allow one to choose the magnitude of the accretion outburst, with respect to the quiescent accretion rate, and also mean that one can simply choose an average accretion rate over one cycle by multiplying (3.16) by the chosen average. Thus, the time-dependent accretion rate is given by

$$\dot{M}(t) = \langle \dot{M} \rangle f(t), \tag{3.18}$$

where $f(t)$ has been appropriately normalised. The canonical profile used by D'Angelo (2017) had $F_{\rm t} = 10$, $f_{\rm max}/f_{\rm min} = 693.97$ and $T_{\rm recurrence} = 100$ and is shown in Fig. 3.1.

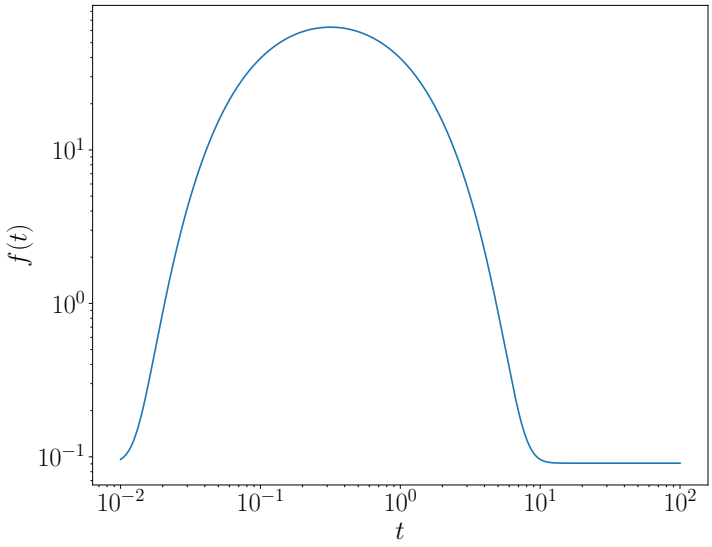

Figure 3.1: Accretion outburst profile, $f(t)$, as a function of time, t, where $F_{\rm t} = 10$, $f_{\rm max}/f_{\rm min} = 693.97$ and $T_{\rm recurrence} = 100$. The accretion rate and time have arbitrary units. [Recreated from D'Angelo (2017).]

3.3 Gravitational radiation from a rotating star

In order for a spinning neutron star to emit gravitational radiation, it must host a non-axisymmetric mass deformation. This is made obvious through the quadrupole-moment tensor, given by (2.65) in the Newtonian limit. The quadrupole moment is particularly relevant for calculating the gravitational-wave strain of a given source.

Indeed, it turns out that the dominant multipole moment for gravitational-wave emission is the $(\ell, m) = (2, 2)$ moment, Q_{22}, which is defined by (2.78). A rotating source with a quadrupole moment will radiate gravitational waves at a frequency that is double its rotation frequency. Gravitational waves carry energy and angular momentum away from the source. The gravitational-wave luminosity is given by (2.113), thus, the torque that spins down the star is

$$N_{\rm GW} = -\frac{L_{\rm GW}}{\Omega} = -\frac{G}{c^5}\frac{1}{5\Omega}\langle \partial_t^3 Q_{ij} \partial_t^3 Q^{ij} \rangle, \tag{3.19}$$

One can show that a uniformly spinning star has

$$\langle \partial_t^3 Q_{ij} \partial_t^3 Q^{ij} \rangle = \frac{256\pi}{15}\Omega^6 Q_{22}^2, \tag{3.20}$$

which gives

$$N_{\rm GW} = -\frac{256\pi}{75}\frac{G\Omega^5 Q_{22}^2}{c^5}. \tag{3.21}$$

Equation (3.21) describes the rate at which the deformed star loses angular momentum due to a quadrupole deformation.

In addition to the quadrupole moment, it is fashionable to consider the fiducial ellipticity, which is defined as (Owen, 2005)

$$\epsilon \equiv \sqrt{\frac{8\pi}{15}}\frac{Q_{22}}{I_{zz}}, \tag{3.22}$$

where the principal stellar moment of inertia is taken to have the fiducial value of $I_{zz} = 10^{45}\,\mathrm{g\,cm^2}$. It should be noted that this fiducial principal moment of inertia can be different to the star's actual principal moment of inertia by a factor of a few. This parameter is often reported in observational papers.

The braking torque due to gravitational waves (3.21) corresponds to a spin-down rate of

$$\dot{P}_{\rm GW} \approx 1.4 \times 10^{-19} \left(\frac{I_{zz}}{10^{45}\,\mathrm{g\,cm^2}}\right)^{-1} \left(\frac{Q_{22}}{10^{37}\,\mathrm{g\,cm^2}}\right)^{2} \left(\frac{P}{1\,\mathrm{s}}\right)^{-3} \mathrm{s\,yr^{-1}}. \tag{3.23}$$

In order to estimate how strong a quadrupole is needed in order to considerably influence the spin evolution of the neutron star, it is useful to balance (3.21) with the accretion-

magnetosphere torque from (3.11). This leads to

$$Q_{22} \approx 4.2 \times 10^{37}\, \xi^{1/4} \left(\frac{M}{1.4\, M_\odot}\right)^{3/14} \left(\frac{\mu}{10^{30}\,\mathrm{G\,cm^3}}\right)^{1/7} \left(\frac{\dot{M}}{10^{-9}\, M_\odot\,\mathrm{yr^{-1}}}\right)^{3/7} \times \left(\frac{f}{500\,\mathrm{Hz}}\right)^{-5/2} (1-\omega_\mathrm{s})\ \mathrm{g\,cm^2}. \tag{3.24}$$

For a typical accreting millisecond X-ray pulsar with $B \sim 10^8$ G and $\dot{M} \sim 10^{-11}\, M_\odot\,\mathrm{yr}^{-1}$, this gives a quadrupole moment of $Q_{22} \sim 10^{36}\,\mathrm{g\,cm^2}$ in order to achieve spin equilibrium at $f \sim 500$ Hz. One can express a mass quadrupole in terms of the fiducial ellipticity (3.22). Therefore, in order to balance the accretion torque with gravitational-wave spin-down, one requires $\epsilon \sim 10^{-9}$. This is far smaller than the maximum deformation a neutron-star crust can sustain for most reasonable equations of state (see Chaps. 4 and 5). A recent population-based analysis has suggested that $\epsilon \approx 10^{-9}$ is the minimum ellipticity of millisecond pulsars (Woan *et al.*, 2018).

An outstanding problem in understanding rapidly spinning accreting neutron stars is their peculiar spin distribution (see Fig. 3.2). It is this unusual shape and, in particular, the sharp cut-off at $\sim$ 600 Hz that has motivated the search for gravitational waves from these systems. This is an appealing explanation since the braking torque due to gravitational waves scales as the fifth power of the spin frequency for deformed, rotating neutron stars [see (3.21)]. Patruno *et al.* (2017) have shown that among accreting millisecond X-ray pulsars and nuclear-powered X-ray pulsars, there appear to be two sub-populations. One sub-population is at a relatively low spin-frequency, with a mean spin of $\approx$ 300 Hz. The second sub-population has a higher peak and a mean of $\approx$ 575 Hz. This faster sub-population has a very narrow range and is composed of a mixture of accreting millisecond X-ray pulsars and nuclear-powered X-ray pulsars. The two sub-populations are separated by a transition region around $\approx$ 540 Hz. Patruno *et al.* (2017) argued that, when considering various accretion torque models, no model naturally explains the presence of a fast sub-population and postulated that, whatever mechanism that causes this clustering, it must set in quickly – as soon as the pulsars reach a certain spin threshold. It was noted by Patruno *et al.* (2017) that this is a subtly different problem to the one of accreting neutron stars not spinning close to their break-up frequency. These two problems make gravitational waves a promising avenue to explore. Gravitational waves can help justify the transition region between the two sub-populations and provide a physical meaning to it (the region in which gravitational-wave emission starts to become significant), and naturally explain the cut-off at $\sim$ 600 Hz. [See Hessels (2008) and Papitto *et al.* (2014) for additional work on the spin-frequency distribution of millisecond pulsars.]

There are a number of different ways a mass asymmetry could arise in an accreting neutron star. Bildsten (1998) originally proposed that interior temperature asymmetries misaligned

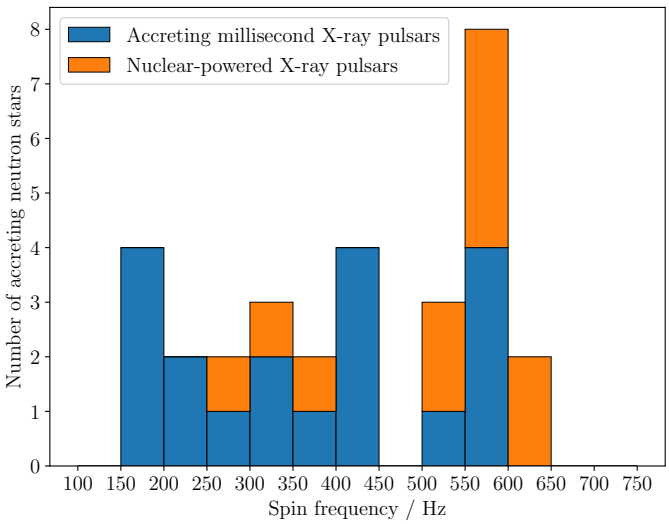

Figure 3.2: Distribution of spin frequencies for accreting neutron stars with millisecond periods. The accreting neutron-star population comprises accreting millisecond X-ray pulsars (blue) and nuclear-powered X-ray pulsars (orange).

with respect to the spin-axis of the neutron star could produce a significant quadrupole through temperature-sensitive electron captures. Hotter regions of the crust would have electron captures at lower pressures and so the density drop would occur at higher altitudes in the hotter parts of the crust. This is known as a *thermal mountain* (Bildsten, 1998; Ushomirsky *et al.*, 2000; Melatos and Payne, 2005; Haskell *et al.*, 2006; Payne and Melatos, 2006). Another mechanism through which mass quadrupoles can be built are through mountains sustained by magnetic stresses, called *magnetic mountains* (Cutler, 2002; Haskell *et al.*, 2008). These can occur when a neutron star has a sufficiently large toroidal or poloidal magnetic field that will act to distort the neutron star into an oblate or prolate shape and will naturally produce a quadrupole if the spin- and magnetic-axes are misaligned. A third way through which gravitational waves can arise is through internal r-mode instabilities (Andersson, 1998; Andersson *et al.*, 1999; Levin, 1999; Andersson *et al.*, 2000, 2002b; Heyl, 2002; Wagoner, 2002; Nayyar and Owen, 2006; Bondarescu *et al.*, 2007). In a perfect fluid, these modes are unstable for all rates of rotation due to gravitational-wave emission.

We explored whether gravitational waves could explain the observed distribution and, if so, whether there is a preference for any of the gravitational-wave-production mechanisms. For our analysis, we did not consider mountains solely created by the magnetic field, nor did we consider magnetic mountains built through accretion. For these cases, the magnetic fields are not strong enough to sustain sufficiently large mountains for the spin evolution of these systems to be noticeably affected (see Haskell *et al.*, 2008; Priymak *et al.*, 2011; Haskell and Patruno, 2017).

3.4 Spin-evolution model

We constructed a model for the spin evolution of an accreting neutron star. We incorporated the accretion-magnetosphere coupling by using the model of Ho *et al.* (2014) (3.12) and included a torque due to gravitational-wave spin-down (3.23). The spin rate is a first-order time derivative and so can be evolved numerically. Our assumed canonical values for a low-mass X-ray binary are shown in Table 3.1. For our canonical neutron star we did not include gravitational-wave effects. We assumed our neutron stars to be incompressible (that is, they have a constant density), which affected the moment of inertia. For simplicity, we did not model the magnetic-field evolution. The time a neutron star is evolved for is denoted as the evolution time.

Table 3.1: Canonical values for a low-mass X-ray binary.

M / $M_\odot$	R / km	B / G	Initial spin period / s	ξ	$\langle\dot{M}\rangle$ / $M_\odot\,\mathrm{yr}^{-1}$	Q_{22} / $\mathrm{g\,cm}^2$
1.4	10	10^8	0.1	0.5	5×10^{-11}	0

Our model can evolve both persistent and transient accretors. For transient accretors we used a fast-rise, exponential-decay function, described in Sec. 3.2.2 by Eqs. (3.16)–(3.18), and evolved the time-averaged spin-derivative, $\langle\dot{P}(P,\dot{M})\rangle$, which, for a given neutron star, is a function of the spin and accretion rate. This average was obtained by averaging the spin derivative over one outburst/quiescence cycle. The time-average was evolved rather than the instantaneous spin rate, $\dot{P}(P,\dot{M})$, to simplify the integration procedure. Otherwise the integration procedure would have needed to take into account the full fast-rise, exponential-decay features of the accretion profile. For persistent accretors this was not a problem and so we could simply evolve $\dot{P}(P,\dot{M})$. Unless specified otherwise we used the following values for the transient accretion profile: $F_\mathrm{t} = 10\,\mathrm{yr}$, $T_\mathrm{recurrence} = 100\,\mathrm{yr}$ and $f_\mathrm{max}/f_\mathrm{min} = 10^4$. This was chosen for simplicity and to limit the explorable parameter space. Most of our simulations turned out to be relatively insensitive to the exact values of these parameters. Of course, should one be interested in modelling individual systems with this profile, then particular care would need to be taken when tuning these parameters.

Figure 3.3 shows the spin evolution of the canonical accreting neutron star with persistent and transient accretion. As was found by D'Angelo (2017) and Bhattacharyya and Chakrabarty (2017), we see that the persistently accreting neutron star initially spins up faster and reaches a final spin of $\nu = 678\,\mathrm{Hz}$. The transient system spins up slower but obtains a faster final spin of $\nu = 1055\,\mathrm{Hz}$. However, neither of the systems were evolved long enough to reach spin equilibrium. The upper limit of $10^{10}\,\mathrm{yr}$ for the evolution time was chosen since no system can evolve for longer than the age of the Universe.

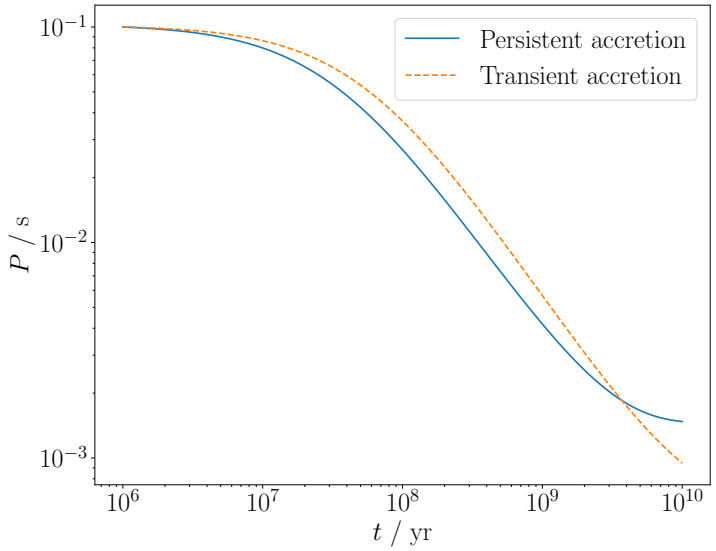

Figure 3.3: The spin evolution of the canonical accreting neutron star with persistent accretion (blue solid line) and transient accretion (orange dashed line) with initial values from Table 3.1. The persistent accretor initially spins up faster than the transient accretor. However, towards the end of its evolution the persistent accretor begins to slow down and the transient accretor overtakes and reaches a faster final spin.

3.5 Simulated populations

In order to obtain a distribution of spins with which to compare to the observed distribution, we used a Monte Carlo population-synthesis method to draw the initial parameters from a given set of distributions and evolve each neutron star [see Possenti *et al.* (1998) for another neutron-star population-synthesis study]. Each neutron star was assigned a mass M, radius R, magnetic-field strength B, initial spin period, average accretion rate $\dot{M}$, mass-quadrupole moment Q_{22} and evolution time. We evolved 1000 neutron stars in each simulation.

Table 3.2: Initial values and evolution parameters for population synthesis.

Parameter	Distribution	Values
M / $M_\odot$	Single-value	1.4
R / km	Single-value	10
$\log_{10}(B$ / G)	Gaussian	$\mu = 8.0$, $\sigma = 0.1$
Initial spin period / s	Flat	$0.01 - 0.1$
ξ	Single-value	0.5
$\log_{10}(\langle\dot{M}\rangle / M_\odot\,\mathrm{yr}^{-1})$	Gaussian	$\mu = -11.0 + \log_{10}(5)$, $\sigma = 0.1$
Q_{22} / g cm^2	Single-value	0
Evolution time / yr	Flat-in-the-log	$10^9 - 10^{10}$

The first simulations were evolved using the distributions shown in Table 3.2. We fixed

the masses and radii at $1.4\,M_\odot$ and 10 km, respectively, to match the canonical values for neutron stars. Typically, accreting millisecond X-ray pulsars are measured to have magnetic fields of $\sim 10^8$ G and so the field strength was taken from a log-Gaussian distribution with mean $\mu = 8.0$ and standard deviation $\sigma = 0.1$. The initial spin period was drawn from a flat distribution between $0.01 - 0.1$ s, which our simulations turned out to be relatively insensitive to. The correction factor ξ was chosen to be 0.5. The average accretion rate was motivated by observations of low-mass X-ray binaries and was given by a log-Gaussian with $\mu = -11.0 + \log_{10}(5)$ and $\sigma = 0.1$. For the initial simulations we assumed there was no gravitational-wave component. We found that for evolution times much less than 10^9 yr, the neutron stars would not have enough time to spin up to frequencies above 100 Hz and so the evolution time was taken from a flat-in-the-log distribution between $10^9 - 10^{10}$ yr. The distribution was chosen to be flat-in-the-log in order for it to be scale-invariant (as was used by Possenti *et al.*, 1998), thus, parametrising our uncertainty in the value of the evolution time.

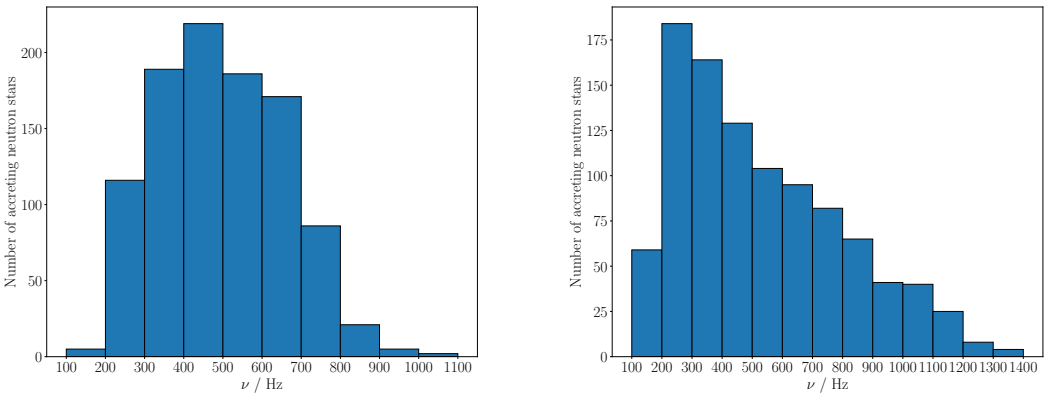

Figure 3.4: Distributions of spin frequencies for simulated persistently accreting neutron stars (left panel) and transiently accreting neutron stars (right panel) with initial distributions from Table 3.2.

The resultant spin-frequency distributions for persistent and transient accretors are shown in Fig. 3.4. One can see for this simple case that for both persistent and transient accretion, we do indeed obtain neutron stars that spin in excess of 1 kHz. More generally, we observe that we get many neutron stars that spin faster than the observed spin-frequency limit of ~ 600 Hz and, as one might expect, we find more high-frequency neutron stars for the transient case. This is because transient accretion enables these stars to spin to higher frequencies than with persistent accretion, provided they evolve for long enough. For both simulations, we have not obtained the characteristic behaviour of the observed distribution since there is no evidence for a pile-up of neutron stars at high frequencies.

In order to quantify how different our simulated populations are to the observed population, we applied a Kolmogorov-Smirnov test to the distributions. This test allows one to

compare two distributions by testing the null hypothesis that the two distributions are the same. We chose a significance level of 0.10 for this work, which meant that should we have found p-values less than this value we could reject the null hypothesis with 90% certainty for that case.[3] For the persistent accretors, we obtained a p-value of $p = 7.7 \times 10^{-2}$ and for the transient accretors, we obtained $p = 9.9 \times 10^{-4}$. This meant that we could reject the null hypothesis at the 10% significance level that the observed distribution is drawn from the persistent population or the transient population.

We explored the effect that magnetic-dipole radiation (3.15) has on transient accretors using the initial distributions in Table 3.2. The results are displayed in Fig. 3.5. The inclusion of this additional torque stops many of the systems from spinning up to sub-millisecond periods. We obtain $p = 0.20$ so we cannot rule out the null hypothesis with any statistical certainty. However, in regards to the shape of the distribution, we do not obtain a sharp peak at the observed spin-frequency limit. Instead, we find a broad peak in the range $200 - 600\,\mathrm{Hz}$.

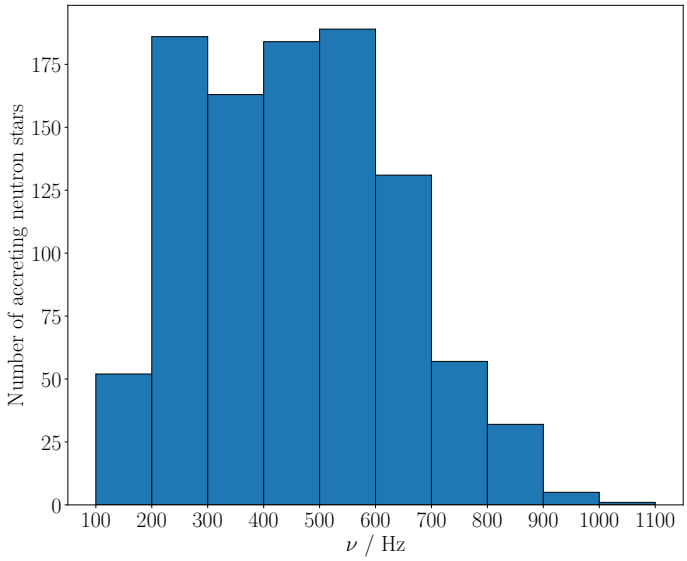

Figure 3.5: Distribution of spin frequencies for simulated transiently accreting neutron stars with initial distributions from Table 3.2 including the magnetic-dipole torque.

This demonstrates that a simple model for accretion is not sufficient to explain the observations of accreting neutron stars and also suggests that the inclusion of magnetic-dipole torques does not resolve this tension either. Therefore, an additional component needs to be included into the model.

[3]Note that p-values should not be confused with the isotropic fluid pressure p.

3.5.1 Including gravitational-wave torques

We explored whether including a gravitational-wave component to the spin evolution of accreting neutron stars could give us the observed spin distribution. Motivated by the necessary quadrupole in order to achieve torque balance (3.24), we repeated the same simulations but with a fixed $Q_{22} = 10^{36}\,\mathrm{g\,cm^2}$ for all neutron stars. (Physically, this can be interpreted as a permanent crustal mountain.) Figure 3.6 shows the final-spin distributions for these simulations. This quadrupole has notably stopped the neutron stars from spinning up to sub-millisecond periods and has resulted in a pile-up centred on the $500 - 550\,\mathrm{Hz}$ bin for the persistent accretors and at $550 - 600\,\mathrm{Hz}$ for the transient accretors. This has appeared since the gravitational-wave torque imposes a spin-frequency limit on the neutron stars. The peak for transient accretors is promising as this is where the peak lies for the spin distribution that we observe (*cf.* Fig. 3.2). Interestingly, there is also a broader peak at lower frequencies. We found that $\approx 19\%$ of persistently accreting neutron stars and $\approx 14\%$ of transiently accreting neutron stars reached spin equilibrium by the end of the simulation. The systems that had reached spin equilibrium were clustered around the high-frequency peaks. We obtained $p = 0.19$ and $p = 0.80$ for the persistent and transient cases, respectively, and, therefore, were unable to reject the null hypothesis for both populations.

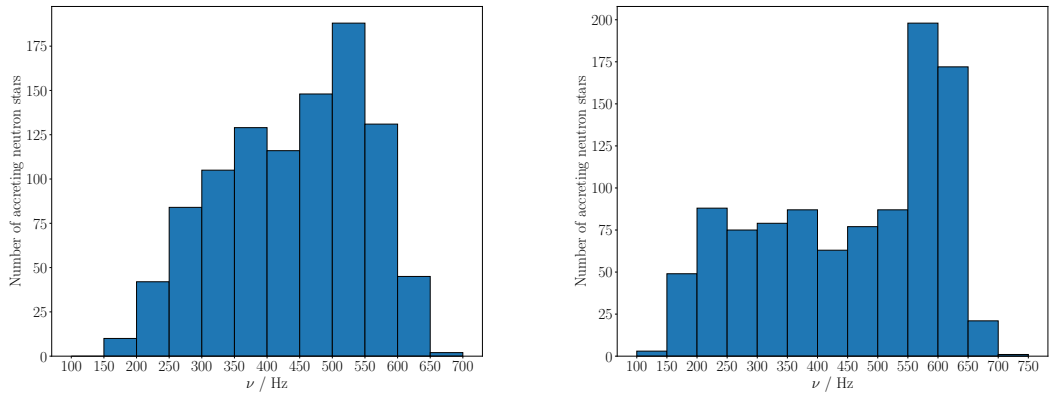

Figure 3.6: Distributions of spin frequencies for simulated persistently accreting neutron stars (left panel) and transiently accreting neutron stars (right panel) with initial distributions from Table 3.2 and a fixed quadrupole of $Q_{22} = 10^{36}\,\mathrm{g\,cm^2}$.

We considered how magnetic-dipole radiation affects this picture for systems undergoing transient accretion. We used the same quadrupole and obtained the results shown in Fig. 3.7. Interestingly, this distribution is qualitatively similar to the results without magnetic-dipole torques (right panel of Fig. 3.6). We recover a pronounced peak at higher frequencies $500 - 550\,\mathrm{Hz}$, which by comparison has shifted down by $50\,\mathrm{Hz}$. Since the features of the distribution remain the same we argue that one could obtain a distribution with a peak that matches the observed distribution through slight adjustment of the initial

values, *e.g.*, the quadrupole. Such an adjustment would be justifiable since there is significant uncertainty in many of these parameters. We could not reject the null hypothesis for these results with $p = 0.39$.

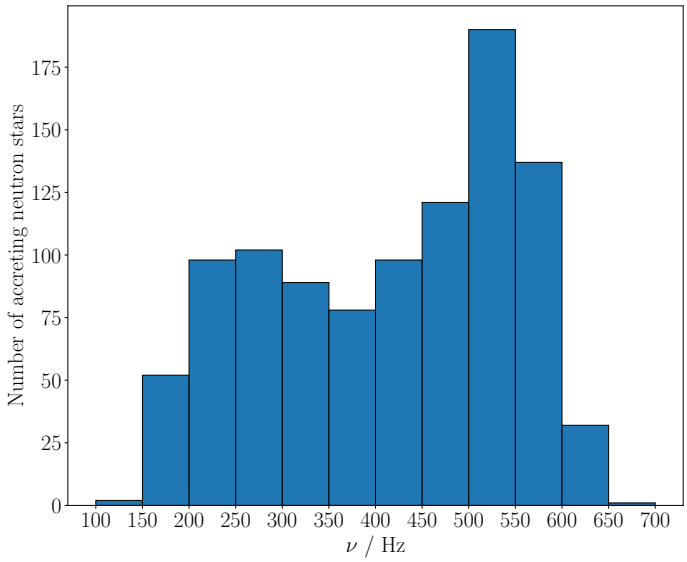

Figure 3.7: Distribution of spin frequencies for simulated transiently accreting neutron stars with initial distributions from Table 3.2 with a fixed quadrupole of $Q_{22} = 10^{36}\,\mathrm{g\,cm^2}$ and including the magnetic-dipole torque.

For accreting neutron-star systems the magnetic-dipole torque is expected to be negligible during outbursts, but it could play an important role during the quiescent phases. We explored a range of outburst durations, F_t distributed uniformly between $1 - 100\,\mathrm{yr}$, to assess the impact this made on the resultant spin distribution (Fig. 3.8). For this wide range of outburst lengths we find a broad peak between $450 - 600\,\mathrm{Hz}$. This contrasts the narrow peak in Fig. 3.2. In this case, we obtain a p-value of $p = 0.38$.

We investigated how sensitive the simulated populations were on the distribution of the evolution time. We ran a simulation with the same quadrupole and the evolution time distributed flat between $10^8 - 10^{10}\,\mathrm{yr}$ for transient accretors. This was motivated by assuming that neutron stars are born at a uniform rate, which is intuitively what one might expect, and that there are no selection effects to suggest that we are more likely to observe younger systems. The resultant spin-distribution is shown in Fig. 3.9. As was observed in the case when the time was distributed flat-in-the-log, there exists a pronounced peak towards the higher spin-frequencies. However, there are far fewer systems spinning at frequencies below this peak. For this simulation we obtained a p-value of $p = 1.2 \times 10^{-2}$ and, thus, could reject the null hypothesis. This distribution does not match what we observe.

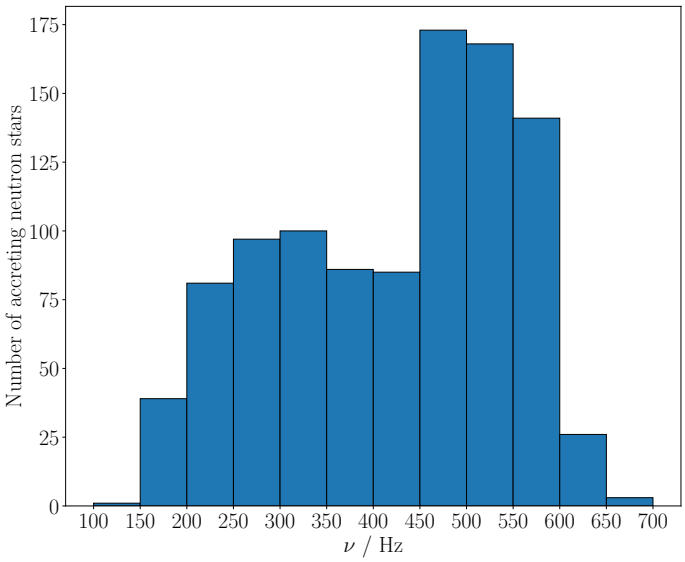

Figure 3.8: Distribution of spin frequencies for simulated transiently accreting neutron stars with initial distributions from Table 3.2 with a fixed quadrupole of $Q_{22} = 10^{36}\,\mathrm{g\,cm^2}$, including the magnetic-dipole torque and F_t distributed flat between $1 - 100\,\mathrm{yr}$.

3.5.2 Thermal mountains

One of the most promising avenues for producing a mass quadrupole on a fast-spinning, accreting neutron star is through thermal mountains built during accretion phases through asymmetries in pycnonuclear reaction rates (Haskell and Patruno, 2017). As a neutron star accretes matter composed of light elements, the matter becomes buried by accretion and is then compressed to higher densities. This causes the matter to undergo nuclear reactions such as electron captures, neutron emission and pycnonuclear reactions (Haensel and Zdunik, 1990). If the accretion flow is asymmetric, this can cause asymmetries in density and heating that can produce a quadrupole moment. The quadrupole moment due to asymmetric crustal heating from nuclear reactions is approximated by (Ushomirsky *et al.*, 2000)

$$Q_{22} \approx 1.3 \times 10^{37} \left(\frac{R}{10\,\mathrm{km}}\right)^4 \left(\frac{\delta T_\mathrm{q}}{10^7\,\mathrm{K}}\right) \left(\frac{E_\mathrm{th}}{30\,\mathrm{MeV}}\right)^3 \mathrm{g\,cm^2}, \tag{3.25}$$

where δT_q is the quadrupolar temperature increase due to the nuclear reactions and E_th is the threshold energy for the reactions to occur. The value δT_q will be a fraction of the total heating (Ushomirsky and Rutledge, 2001)

$$\delta T \approx 2 \times 10^5 \left(\frac{\mathcal{C}}{k_\mathrm{B}}\right)^{-1} \left(\frac{p_\mathrm{d}}{10^{30}\,\mathrm{dyn\,cm^{-2}}}\right)^{-1} \left(\frac{Q}{1\,\mathrm{MeV}}\right) \left(\frac{\Delta M}{10^{-9}\,M_\odot}\right) \mathrm{K}, \tag{3.26}$$

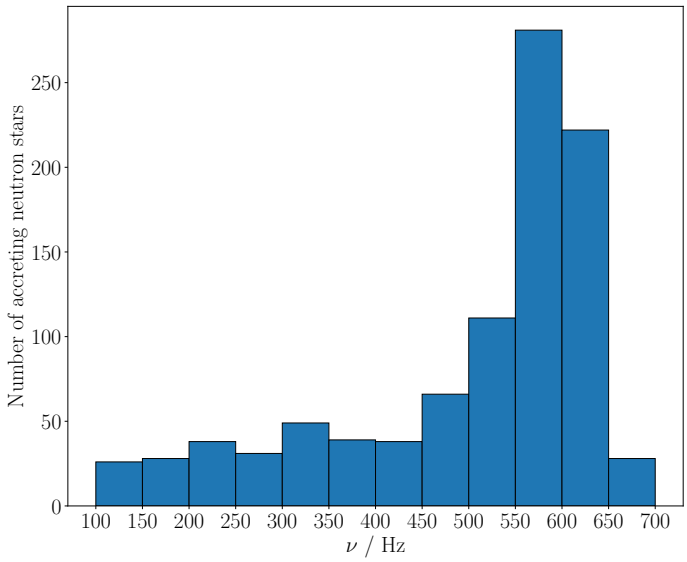

Figure 3.9: Distribution of spin frequencies for simulated transiently accreting neutron stars with initial distributions from Table 3.2 with a fixed quadrupole of $Q_{22} = 10^{36}\,\mathrm{g\,cm^2}$ and an evolution time distributed flat between $10^8 - 10^{10}\,\mathrm{yr}$.

where k_B is the Boltzmann constant, $\mathcal{C}$ is the heat capacity per baryon, p_d is the pressure at which the reaction occurs, Q is the heat released locally due the reactions and ΔM is the accreted mass. Some of this heating will be converted into the quadrupolar temperature increase, however, it is unclear quite how much will be converted. Ushomirsky *et al.* (2000) estimate that $\delta T_\mathrm{q}/\delta T \lesssim 0.1$, but in reality this ratio is poorly understood.

These thermal mountains are built during accretion outbursts. During quiescence phases, the deformations are washed away on a thermal timescale (Brown *et al.*, 1998)

$$\tau_\mathrm{th} \approx 0.2 \left(\frac{p_\mathrm{d}}{10^{30}\,\mathrm{dyn\,cm^{-2}}}\right)^{3/4} \mathrm{yr}. \tag{3.27}$$

If the system is in quiescence for longer than this timescale then the thermal mountain will be washed away and a new mountain will be built during the next outburst.

We implemented the expression for a quadrupole moment due to these reactions from (3.25) and assumed the following values for our neutron stars [as estimated by Haskell and Patruno (2017) for the pulsar J1023+0038]: $\mathcal{C} \approx 10^{-6} k_\mathrm{B}$, $E_\mathrm{th} = 30\,\mathrm{MeV}$, $p_\mathrm{d} = 10^{30}\,\mathrm{erg\,cm^{-3}}$ and $Q = 0.5\,\mathrm{MeV}$. This meant that the quadrupole due to these reactions was dependent only on the accreted mass ΔM and the fraction $\delta T_\mathrm{q}/\delta T$. For this mechanism, we only considered transient accretion since in persistent accretion these mountains will not wash away, but instead will get progressively larger until the crust can no longer

sustain them. This is effectively modelled through a fixed quadrupole that represents the largest mountain that can be built.

In our model, we calculated ΔM by numerically integrating the accretion profile from the beginning of the outburst up to $F_{\rm t}$. Our quiescence phases were long enough for the mountain to wash away during them. Unlike for our other prescriptions, we found that for thermal mountains, the specific values that parametrise the outburst features were very important in dictating the final-spin distribution. Based on observations of X-ray transients, we chose $F_{\rm t} = 0.1\,{\rm yr}$, $T_{\rm recurrence} = 2.0\,{\rm yr}$ and $f_{\rm max}/f_{\rm min} = 10^4$. We simulated neutron stars that built thermal mountains with $\delta T_{\rm q}/\delta T = 4 \times 10^{-4}$. The left panel of Fig. 3.10 shows the resultant distribution of final spins. We can see qualitatively that this distribution has similar features to the fixed quadrupole case (see the right panel of Fig. 3.6). Another promising aspect of the final-spin distribution is the prominence of the high-frequency peak. Like what is observed, this peak is narrow and much larger than the values in other frequency bins. We found a p-value of $p = 0.60$ for this distribution.

The only constraint on the ratio of quadrupolar to total heating comes from the non-detection of X-ray emission of quadrupolar flux perturbations during quiescence phases in low-mass X-ray binaries, which gives $\delta T_{\rm q}/\delta T \lesssim 0.1$ (Ushomirsky *et al.*, 2000). Currently, there is no reason to believe that this fraction should be constant for all neutron stars. To account for our uncertainty in this fraction, we distributed $\delta T_{\rm q}/\delta T$ flat-in-the-log between $10^{-4} - 10^{-2}$. The result of this simulation is shown in the right panel of Fig. 3.10. The distribution peaks at low frequencies and then falls off towards higher frequencies. We obtained $p = 7.0 \times 10^{-2}$ for this case which meant that we could reject the null hypothesis. This shows how this prescription favours $\delta T_{\rm q}/\delta T$ being a fixed value. Seeking a physical explanation for this preference of $\delta T_{\rm q}/\delta T$ being a fixed value as opposed to being distributed is beyond the scope of this study and has been left for future work.

3.5.3 Unstable *r*-modes

An r-mode is a fluid mode of oscillation for which the restoring force is the Coriolis force. Andersson (1998) demonstrated that gravitational radiation destabilises the r-modes of rotating stars. These modes are generically unstable to gravitational-wave emission (Friedman and Morsink, 1998) due to the Chandrasekhar-Friedman-Schutz instability, that facilitates the star finding lower energy and angular momentum configurations that allow the mode amplitude to grow (Chandrasekhar, 1970; Friedman and Schutz, 1978b).

The r-mode instability has long been considered a potential mechanism for imposing a spin limit on neutron stars in low-mass X-ray binaries (Andersson *et al.*, 1999). The typical picture involves a neutron star being spun up through accretion until it enters the r-mode instability window. This instability region depends primarily on the spin of the neutron star and its core temperature. Once a neutron star has entered this region, it

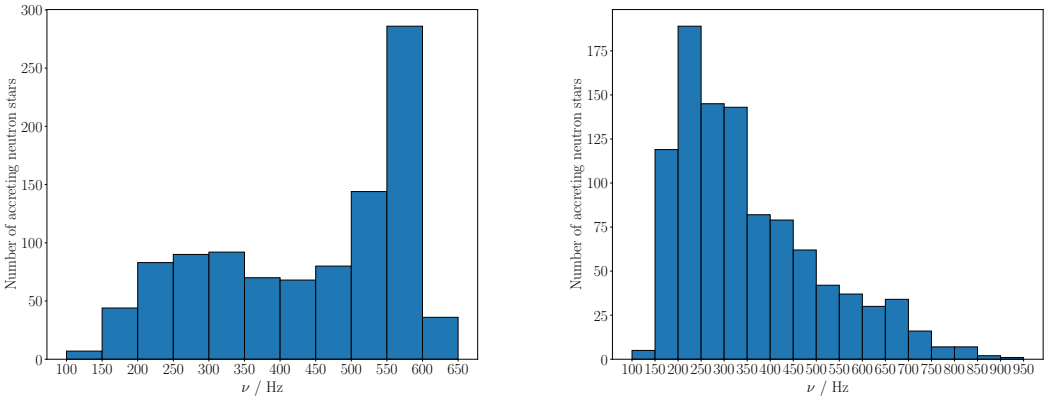

Figure 3.10: Distributions of spin frequencies for simulated transiently accreting neutron stars that built thermal mountains during outburst phases with initial distributions from Table 3.2. The left panel has a fixed $\delta T_{\rm q}/\delta T = 4 \times 10^{-4}$ and the right panel has $\delta T_{\rm q}/\delta T$ distributed flat-in-the-log between $10^{-4} - 10^{-2}$.

will emit gravitational radiation and begin to spin down until it reaches stability. This is expected to occur on a timescale much shorter than the age of the system and should result in most low-mass X-ray binaries being stable. However, theoretical models for the r-mode instability demonstrate that many of the observed accreting neutron stars, in fact, lie inside the instability window (Ho *et al.*, 2011). This result would be consistent if the saturation amplitude for these systems was small, $\alpha \approx 10^{-8} - 10^{-7}$, but this is at odds with predictions that suggest that the amplitude should be several orders of magnitude higher than this (Bondarescu *et al.*, 2007).

Owen *et al.* (1998) described a phenomenological model for the evolution of r-modes and the spin of the star. In this model the quadrupole moment for an incompressible neutron star that is unstable due to r-modes is given by

$$Q_{22} \approx 1.67 \times 10^{33} \left(\frac{\alpha}{10^{-7}}\right) \left(\frac{M}{1.4\,M_\odot}\right) \left(\frac{R}{10\,\mathrm{km}}\right)^3 \left(\frac{P}{1\,\mathrm{s}}\right)^{-1} \mathrm{g\,cm^2}. \tag{3.28}$$

An interesting feature of this expression is its dependence on the spin of the neutron star. As a neutron star spins faster the quadrupole moment grows. This is different to what is expected from mountains. In fact, r-modes and mountains could be differentiated from one another through the scaling of the associated quadrupoles as well as the frequency of the emitted gravitational waves; for mountains the gravitational-wave frequency is 2ν, whereas for r-modes the frequency is $4\nu/3$.[4]

In order to simulate accreting neutron stars with unstable r-modes, we implemented (3.28)

[4]This frequency comes from Newtonian calculations of r-modes with $\ell = 2$. In going to relativity, the expectation is that there will be some low-order correction to this value.

into our model. We assumed that the mode amplitude α remained constant for each neutron star. We repeated the previous simulations for persistent and transient accretors with unstable r-modes and $\alpha = 10^{-7}$. Figure 3.11 shows the final-spin distributions for those simulations. The unstable r-modes were sufficient in both cases to give a peak at high spin-frequencies. For the persistently accreting neutron stars, the peak was in the $500 - 550\,\mathrm{Hz}$ frequency bin and for the transient accretors, the peak was in the $550 - 600\,\mathrm{Hz}$ bin. These distributions are similar to the case of a permanent quadrupole $Q_{22} = 10^{36}\,\mathrm{g\,cm^2}$ (see Fig. 3.6). For transient accretion with unstable r-modes the peak is narrower and more pronounced indicating that the magnitude of the gravitational-wave torque sets in quickly. This is due to the scaling of the quadrupole in (3.28), since it depends linearly on the spin. For the persistent case we found a p-value of $p = 0.28$ and for the transient case $p = 0.57$.

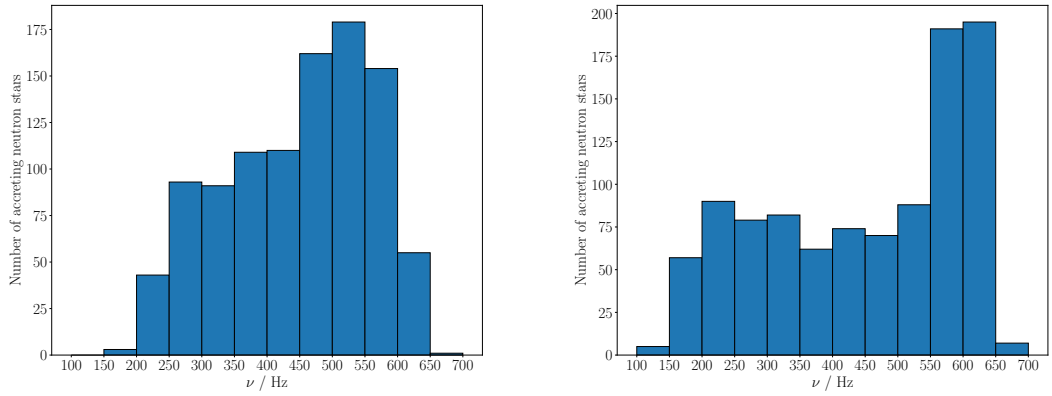

Figure 3.11: Distributions of spin frequencies for simulated persistently accreting neutron stars (left panel) and transiently accreting neutron stars (right panel) with unstable r-modes with initial distributions from Table 3.2 and $\alpha = 10^{-7}$.

We also conducted a simulation where α was distributed flat-in-the-log between $10^{-8} - 10^{-4}$. The result is shown in Fig. 3.12. We can see, similar to the thermal mountain distribution, that both distributions follow an exponentially decreasing behaviour. From these distributions we found $p = 1.2 \times 10^{-2}$ when the neutron stars were persistently accreting and $p = 1.5 \times 10^{-3}$ when they were transiently accreting. From these p-values we can reject the null hypothesis and note that the unstable-r-modes prescription produces more promising results when α is fixed, which is in agreement with current theoretical expectations (Arras *et al.*, 2003; Bondarescu *et al.*, 2007).

3.6 Summary

An unresolved problem in the study of low-mass X-ray binaries is the unusual spin distribution of rapidly accreting neutron stars and, in particular, why no neutron star has been observed to spin close to the centrifugal break-up frequency. A potential explanation

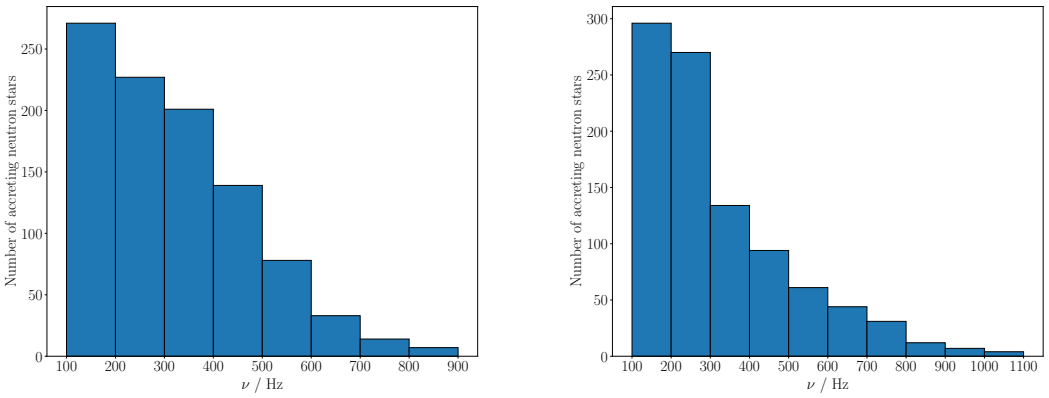

Figure 3.12: Distributions of spin frequencies for simulated persistently accreting neutron stars (left panel) and transiently accreting neutron stars (right panel) with unstable r-modes with initial distributions from Table 3.2 and α distributed flat-in-the-log between $10^{-8} - 10^{-4}$.

to this problem comes from gravitational waves. Theoretically, gravitational waves could be able to spin down these systems away from the break-up frequency. However, there are a number of different mechanisms that could give rise to gravitational radiation and it is unclear which are the most probable. It is also unclear whether gravitational waves are the only way to explain the observed distribution of accreting neutron stars. For example, it was recently suggested by Parfrey *et al.* (2016) that spin-down torques from an enhanced pulsar wind due to a disc-induced opening of the magnetic field could have a meaningful effect on the spin evolution of an accreting neutron star. Such a torque is not phenomenologically accounted for in our method and could be a direction for future work.

In this chapter, we have explored, within the context of our current understanding of accretion torques, whether an additional component is required in order to describe the spin evolution of accreting neutron stars. We investigated whether gravitational-wave emission could be one such explanation and have compared competing gravitational-wave mechanisms. We presented our model for the spin evolution of an accreting neutron star that accounts for accretion and magnetic-field effects, and also includes a gravitational-wave spin-down component. Our model is able to simulate persistent and transient accretors.

In our simulations with no gravitational-wave torques we obtained neutron stars with much higher spins than what is observed. We did not obtain any of the characteristic behaviour of the observed spin distribution. In particular, there was no evidence of a pile-up at high frequencies. However, by adding a permanent quadrupole moment, motivated by torque balance, of $Q_{22} = 10^{36}\,\mathrm{g\,cm^2}$ we obtained qualitatively similar behaviour to the observed distribution for the transiently accreting neutron-star population. This quadrupole is below the maximum neutron-star crusts can support, as we will see in Chaps. 4 and 5.

We considered the impact of magnetic-dipole radiation on the results. We found that in the case of no gravitational-wave emission one does not obtain the observed distribution. With the inclusion of gravitational-wave emission the resultant distribution is qualitatively similar to the case of no magnetic-dipole radiation. By varying the outburst duration with gravitational-wave and magnetic-dipole torques we obtained a distribution with a broad high-frequency peak.

We investigated two gravitational-wave-production prescriptions. For thermal mountains produced by asymmetric nuclear reactions in the crust, our model was sensitive to the precise features of the outburst profile, as well as the ratio of quadrupolar to total heating, $\delta T_{\rm q}/\delta T$. We found that a value of $\delta T_{\rm q}/\delta T = 4 \times 10^{-4}$ produced a similar distribution to what is observed. Promisingly, this gave the characteristic pile-up at high frequencies with a narrow, pronounced peak. We examined whether the distributions had a preference for $\delta T_{\rm q}/\delta T$ being a single value or being distributed and found strong evidence arguing that it should be a fixed value. Accreting neutron stars with unstable r-modes and $\alpha = 10^{-7}$ produced similar results to the case with a fixed quadrupole moment and the thermal mountain prescription. This prescription favoured α being fixed as opposed to being distributed.

The three cases that produced distributions that were qualitatively similar to the observed spin distribution – permanent quadrupole, thermal mountains and unstable r-modes – are almost indistinguishable from one another. Although, the r-mode-instability case could, in theory, be differentiated from the other prescriptions. This distinction could come from the fact that the quadrupole moment due to unstable r-modes scales linearly with the spin frequency of the star. Another key difference comes from the frequency of the gravitational waves that are emitted through this channel. Unstable r-modes emit gravitational waves with a frequency of $4\nu/3$, whereas, gravitational waves due to deformations on a neutron star have a frequency of 2ν. Therefore, a gravitational-wave detection would indicate which mechanism is active, motivating further searches.

For the r-mode scenario, the value for the saturation amplitude that we found to agree well with observation ($\alpha = 10^{-7}$) is many orders of magnitude below what is currently predicted. Theory would need to explain why this is so, or why the instability window is smaller than what is usually assumed.

We have not addressed the spin distribution of radio millisecond pulsars in this work. Future work could explore how the low-mass X-ray binary population evolves into the radio millisecond pulsar population and consider whether gravitational waves are relevant in this process and can explain the observed distribution.

In our modelling of transient accretion we considered a simple fast-rise, exponential-decay

function with a constant average accretion rate. However, in these systems it is expected that binary evolution will play a key role in the accretion rates and result in a long-term modulation of the accretion rate. This, of course, could have a significant effect on the resultant spin distribution. Such long-term variations could be explored in a future study.

CHAPTER 4

Neutron-star mountains

In Chap. 3, we explored whether gravitational waves could describe the spin evolution of rapidly rotating neutron stars found in accreting binaries. Promisingly, we found that by including a gravitational-wave component we could indeed recreate the spin distribution of these systems, thus, justifying further study into the mechanisms that could give rise to gravitational waves. In this chapter, we examine neutron-star mountains in a Newtonian framework, following Gittins *et al.* (2021).

We start, in Sec. 4.1, with an introduction to static perturbations of neutron stars and a review of prior efforts on estimating the maximum mountain. We summarise previous approaches and the important assumptions that provide the motivation for this work. In Sec. 4.2, we consider the necessary components of a neutron-star mountain calculation. We provide a detailed discussion on the usual method of calculating mountains and introduce our own scheme, demonstrating the validity and equivalence of both approaches. We detail the Newtonian perturbation formalism for our mountain scheme in Sec. 4.3 and pay particular attention to the boundary conditions of the problem. We consider three sources for the deformations in Sec. 4.4 and provide the maximum quadrupoles for each scenario. In Sec. 4.5, we end with a summary and discuss future directions.

4.1 Context

As, we have already noted, a rotating neutron star perturbed away from axial symmetry will emit gravitational waves. A fluid is continuously deformable. However, realistic neutron stars will have elastic crusts that are formed in the very early stages of their lives as they begin to cool. The crust can sustain shear stresses which, by definition, do not exist in a perfect fluid. It is the crust that sets the limit of how much a neutron star can be stretched and strained until it breaks. For this reason, it is a physically interesting question to ask how much can a neutron star be deformed by.

There have been a number of studies of the maximum quadrupole deformation of a neutron star. The earliest of these was conducted by Ushomirsky *et al.* (2000), who used the Cowling approximation in Newtonian gravity to derive an integral expression for the quadrupole moment (we describe their approach in detail in Sec. 4.1.1). They introduced the argument that the body will obtain its maximum mountain when the entire crust is strained to its elastic yield point. This argument enabled them to straightforwardly find the strain tensor that ensures that every point in the crust is maximally strained. Haskell *et al.* (2006) observed that the approach of Ushomirsky *et al.* (2000) did not respect the required boundary conditions at the base and top of the crust and that the Cowling approximation could have a large impact on the results. Therefore, they presented a perturbation formalism that relaxed the Cowling approximation and enabled them to treat the phase transitions appropriately. However, there are inconsistencies in their analysis that we explain later. More recent estimates of the maximum elastic deformation have been provided by Johnson-McDaniel and Owen (2013), who carried out their calculation in full relativity using a Green's function method. However, since they used the covariant analogue to the strain tensor from Ushomirsky *et al.* (2000), their calculation also ignored the boundary conditions on the crust. An important aspect of past studies is the fact that the maximum mountains they calculate are independent of the precise mechanisms that sourced them. They do not consider the deforming forces or evolutionary scenarios that lead to the formation of the mountains.

In Gittins *et al.* (2021), we return to this problem to address some of the assumptions of the previous work and detail a formalism that enables one to accurately compute the quadrupole deformation throughout the star. As we show, in order to satisfy the necessary boundary conditions of the problem, it is extremely helpful to characterise the source of the perturbations. This has not been done in past calculations. In addition, it is not clear whether strain configurations where the majority of the crust is maximally strained can actually be reached in a real neutron star. The largest realistic mountain may be significantly smaller. These points suggest that future progress on this subject will rely on evolutionary calculations that consider the complete formation of the mountains (Bildsten, 1998; Ushomirsky *et al.*, 2000; Osborne and Jones, 2020; Singh *et al.*, 2020).

We will decompose our perturbation variables using spherical harmonics as shown in (2.77). For this analysis, it will be sufficient to focus on the $(\ell, m) = (2, 2)$ mode relevant for gravitational radiation. For this reason, we will drop the mode subscript on our perturbation variables.[1] Because we restrict this analysis to Newtonian gravity, it is inappropriate to consider realistic equations of state and we assume a simple polytropic equation of state, along with a simple model for the crust elasticity (we refine this approach in our relativistic calculation in Chap. 5).

We consider perturbations of a non-rotating, equilibrium, fluid star with mass density ρ, isotropic pressure p and gravitational potential Φ, described by the Newtonian equations of structure (2.18). As we demonstrated in Sec. 2.3, we have the following fundamental expressions in perturbation theory: the Lagrangian variations of the velocity (2.45),

$$\Delta v^i = \partial_t \xi^i, \tag{4.1}$$

and the mass density (2.51),

$$\Delta \rho = -\rho \nabla_i \xi^i. \tag{4.2}$$

By considering perturbations of the Euler equation (2.13) and Poisson's equation (2.15) and making use of our static background, $\delta v^i = \Delta v^i = \partial_t \xi^i$, we obtain the following equations that govern the perturbations:

$$\delta\rho + \nabla_i(\rho \xi^i) = 0, \tag{4.3}$$

$$\rho \partial_t^2 \xi_i = -\nabla_i \delta p - \delta\rho \nabla_i \Phi - \rho \nabla_i \delta\Phi, \tag{4.4}$$

$$\delta p = c_{\mathrm{s}}^2 \delta\rho \tag{4.5}$$

and

$$\nabla^2 \delta\Phi = 4\pi G \delta\rho. \tag{4.6}$$

Since we focus on static perturbations, we amend the perturbed Euler equation (4.4) by

$$0 = -\nabla_i \delta p - \delta\rho \nabla_i \Phi - \rho \nabla_i \delta\Phi + f_i, \tag{4.7}$$

where f_i is the density of a force that sustains the perturbations. The inclusion of this force enables us to produce non-spherical models and will prove to be an important component of our analysis, since it enables one to satisfy all the boundary conditions of the problem. We note that f_i does not correspond to a physical force acting on the star. This force is a proxy for the (possibly quite complicated) formation history that results in its non-spherical shape. To study neutron stars with an elastic crust, we must modify (4.7) to

[1] One should note that, although we restrict ourselves to the $(\ell, m) = (2, 2)$ mode, other modes will contribute to the total strain, pushing the crustal lattice closer to the breaking strain, while not adding to the quadrupole.

include the shear stresses,

$$0 = -\nabla_i \delta p - \delta\rho \nabla_i \Phi - \rho \nabla_i \delta\Phi + \nabla^j t_{ij} + f_i, \tag{4.8}$$

where t_{ij} is the symmetric and trace-free, shear-stress tensor, assumed to enter at the perturbative level. Here, we have used the same sign for the shear-stress tensor as in Ushomirsky *et al.* (2000).

As we discuss in detail in Sec. 4.3.3, in order to connect the elastic crust of the star with the fluid regions, one needs to consider the traction vector. The traction vector is defined using the stress tensor. We can identify the perturbed traction from the perturbed Euler equation (4.8),

$$T^i = (\delta p g^{ij} - t^{ij}) \nabla_j r. \tag{4.9}$$

The traction must be continuous throughout the star.

We turn our attention to past work on estimating the maximum mountain, that we now summarise. We do this to critique some of the assumptions made and set the stage for our new calculation. A convenient simplification that this body of work makes is to not (explicitly) consider the perturbing force. This is the main conceptual difference in our approach. We show how the force enters the problem in Sec. 4.2 and demonstrate that the formulation is consistent.

4.1.1 Ushomirsky, Cutler and Bildsten

The first (and perhaps most well known) maximum-mountain calculation was performed by Ushomirsky *et al.* (2000), which we will review here. They tackled the problem in Newtonian gravity and adopted the Cowling approximation – neglecting perturbations of the star's gravitational potential, $\delta\Phi = 0$. The starting point for this computation is the perturbed Euler equation for the elastic crust [(4.8) with $f_i = 0$],

$$0 = -\nabla_i \delta p - \delta\rho \nabla_i \Phi - \rho \nabla_i \delta\Phi + \nabla^j t_{ij}. \tag{4.10}$$

As we shall elaborate upon in Sec. 4.2, one must carefully define what the perturbations are with respect to. The perturbation quantities in (4.10) connect the spherical, fluid star with the non-spherical, strained shape that hosts a mountain and the shear stresses come from the crust wishing to have a separate non-spherical, relaxed shape [*cf.* (4.34) and see Fig. 4.1]. There is no deforming force in (4.10) as the mountains are supported solely by the elastic stresses. With the Cowling approximation, one can ignore perturbations in the fluid regions of the star, since the absence of shear stresses means there is no support for the pressure perturbations by the fluid [see (4.10) with $\delta\Phi = 0$ and $t_{ij} = 0$]. Therefore, only perturbations in the crust contribute to the quadrupole moment.

It is convenient to decompose the shear-stress tensor using tensor spherical harmonics,[2]

$$t_{ij} = t_{rr}\left(\nabla_i r \nabla_j r - \frac{1}{2}e_{ij}\right) Y_{\ell m} + t_{r\perp} f_{ij} + t_\Lambda \left(\Lambda_{ij} + \frac{1}{2}e_{ij} Y_{\ell m}\right), \tag{4.11}$$

where t_{rr}, $t_{r\perp}$ and t_Λ are functions of r, $\beta = \sqrt{\ell(\ell+1)}$,

$$e_{ij} = g_{ij} - \nabla_i r \nabla_j r, \tag{4.12a}$$

$$f_{ij} = \frac{r}{\beta}(\nabla_i r \nabla_j Y_{\ell m} + \nabla_j r \nabla_i Y_{\ell m}), \tag{4.12b}$$

$$\Lambda_{ij} = \left(\frac{r}{\beta}\right)^2 \nabla_i \nabla_j Y_{\ell m} + \frac{1}{\beta} f_{ij}. \tag{4.12c}$$

We obtain an expression for the multipole moment by isolating the mode part of $\delta\rho$ from the perturbed Euler equation (4.10). We project the free index of (4.10) with $\nabla^i r$ to yield

$$\delta\rho + \frac{\rho}{d\Phi/dr}\frac{d\delta\Phi}{dr} = \frac{1}{d\Phi/dr}\left(-\frac{d\delta p}{dr} + \frac{dt_{rr}}{dr} + \frac{3}{r}t_{rr} - \frac{\beta}{r}t_{r\perp}\right). \tag{4.13}$$

We find an expression for δp in terms of the shear stresses by projecting (4.10) with $\nabla^i Y_{\ell m}$,

$$\delta p + \rho\delta\Phi = -\frac{1}{2}t_{rr} + \frac{r}{\beta}\frac{dt_{r\perp}}{dr} + \frac{3}{\beta}t_{r\perp} + \left(\frac{1}{\beta^2} - \frac{1}{2}\right)t_\Lambda. \tag{4.14}$$

We combine Eqs. (4.13) and (4.14) and insert them into (2.78) to obtain

$$\begin{aligned} Q_{\ell m} = \int_0^R \frac{r^4}{d\Phi/dr}\Bigg[&\frac{3}{2}\frac{dt_{rr}}{dr} + \frac{3}{r}t_{rr} - \frac{r}{\beta}\frac{d^2 t_{r\perp}}{dr^2} - \frac{4}{\beta}\frac{dt_{r\perp}}{dr} - \frac{\beta}{r}t_{r\perp} \\ &+ \left(\frac{1}{2} - \frac{1}{\beta^2}\right)\frac{dt_\Lambda}{dr} + \frac{d\rho}{dr}\delta\Phi\Bigg] dr. \end{aligned} \tag{4.15}$$

At this point, the Cowling approximation can be invoked, which means the multipole is given purely in terms of the shear stresses of the crust. Since the shear stresses vanish above and below the crust, by integrating by parts and discarding boundary terms, Ushomirsky *et al.* (2000) found

$$\begin{aligned} Q_{22} = -\int_{r_{\rm base}}^{r_{\rm top}} \frac{r^3}{d\Phi/dr}\Bigg[&\frac{3}{2}(4-U)t_{rr} + \sqrt{\frac{3}{2}}\left(8 - 3U + \frac{1}{3}U^2 - \frac{r}{3}\frac{dU}{dr}\right)t_{r\perp} \\ &+ \frac{1}{3}(6-U)t_\Lambda\Bigg] dr, \end{aligned} \tag{4.16}$$

where $r_{\rm base}$ and $r_{\rm top}$ are the positions of the base and top of the crust, respectively, and $U = d\ln(d\Phi/dr)/d\ln r + 2$. In discarding the boundary terms, it has been assumed that

[2] We have neglected pieces of axial parity in t_{ij} which are proportional to $(\nabla_i r\epsilon_{jkn} + \nabla_j r\epsilon_{ikn})\nabla^n r\nabla^k Y_{\ell m}$ and $(\nabla_i Y_{\ell m}\epsilon_{jkn} + \nabla_j Y_{\ell m}\epsilon_{ikn})\nabla^n r\nabla^k Y_{\ell m}$.

the shear modulus, $\check{\mu}$, is zero at the base and top of the crust.

To obtain the maximum quadrupole, Ushomirsky *et al.* (2000) imposed their neutron-star crust to be in a shape such that it was strained everywhere to the breaking point. To define the elastic yield limit, Ushomirsky *et al.* (2000) used the von Mises criterion. This criterion states that the crust will yield when the von Mises strain $\bar{\sigma}$, defined by

$$\bar{\sigma}^2 \equiv \frac{1}{2}\sigma_{ij}\sigma^{ij}, \tag{4.17}$$

where $\sigma_{ij} = t_{ij}/(2\check{\mu})$ is the strain tensor,[3] exceeds the breaking strain,

$$\bar{\sigma} \geq \bar{\sigma}_{\max}, \tag{4.18}$$

with $\bar{\sigma}_{\max}$ being the breaking strain of the crust. One can show that

$$\sigma_{ij}\sigma^{ij} = \frac{3}{2}\sigma_{rr}^2 \mathrm{Re}(Y_{\ell m})^2 + \sigma_{r\perp}^2 \mathrm{Re}(f_{ij})^2 + \sigma_{\Lambda}^2 \mathrm{Re}\left(\Lambda_{ij} + \frac{1}{2}e_{ij}Y_{\ell m}\right)^2, \tag{4.19}$$

where σ_{rr}, $\sigma_{r\perp}$ and σ_{Λ} are the components of the strain tensor decomposed as in (4.11). Notice that this expression is a consequence of the orthogonality of the basis (4.12). For the $(\ell, m) = (2, 2)$ mode, there exists the identity

$$\frac{3}{4}\mathrm{Re}(Y_{\ell m})^2 + \frac{3}{4}\mathrm{Re}(f_{ij})^2 + \frac{9}{2}\mathrm{Re}\left(\Lambda_{ij} + \frac{1}{2}e_{ij}Y_{\ell m}\right)^2 = \frac{15}{32\pi}. \tag{4.20}$$

Hence, the crust will be strained at every point to the maximum when[4]

$$\sigma_{rr} = \sqrt{\frac{32\pi}{15}}\bar{\sigma}_{\max}, \tag{4.21a}$$

$$\sigma_{r\perp} = \sqrt{\frac{16\pi}{5}}\bar{\sigma}_{\max}, \tag{4.21b}$$

$$\sigma_{\Lambda} = \sqrt{\frac{96\pi}{5}}\bar{\sigma}_{\max}. \tag{4.21c}$$

For a star with mass $M = 1.4\,M_{\odot}$ and radius $R = 10\,\mathrm{km}$ strained according to Eqs. (4.21), Ushomirsky *et al.* (2000) reported a maximum quadrupole moment of

$$Q_{22}^{\max} \approx 1.2 \times 10^{39} \left(\frac{\bar{\sigma}_{\max}}{10^{-1}}\right) \mathrm{g\,cm^2}, \tag{4.22}$$

where $\bar{\sigma}_{\max}$ is the breaking strain of the crust, that we take to have the canonical value

[3] This is a factor of two different to the expressions in Ushomirsky *et al.* (2000) and Haskell *et al.* (2006) but the same as used in Johnson-McDaniel and Owen (2013).

[4] It is interesting to note that, although Eqs. (4.21) certainly constitute a strain configuration that is maximally strained at every point in the crust, there are conceivably many other solutions that satisfy the von Mises criterion.

$\bar{\sigma}_{\rm max} = 10^{-1}$ (Horowitz and Kadau, 2009). In terms of the fiducial ellipticity, this result corresponds to $\epsilon^{\rm max} \approx 1.6 \times 10^{-6}$ $(\bar{\sigma}_{\rm max}/10^{-1})$.

This approach, while elegant, does not enforce the continuity of the traction vector at the boundaries of the crust. At the base of the crust, there is a transition between the fluid core and the elastic crust. At the top, there is a transition between the elastic region and the fluid ocean. At these interfaces, there is expected to be a first-order phase transition where the crust sharply obtains a non-zero shear modulus. Since the fluid has a vanishing shear modulus, the traction can only be continuous if the appropriate strain components go to zero at these boundaries. However, due to the fact that Ushomirsky *et al.* (2000) demanded that the crust be maximally strained at every point, the strain components have finite values at the interfaces and, therefore, one cannot ensure continuity of the traction.

In defence of the Ushomirsky *et al.* (2000) approach, one might argue that the shear modulus may be assumed to smoothly go to zero at the phase transitions. However, this is still problematic. As we show in Sec. 4.3.3, such an assumption means that one does not have enough equations to uniquely determine the displacement, in the case where one does not know the strain. A more realistic assumption might be to take almost the entire crust to be at breaking strain, with the exception of an infinitesimally small region at the boundaries where the displacement is adjusted to satisfy the continuity of the traction.

Ultimately, the estimate (4.22) may give us an idea of the likely maximum mountain, but the calculation is not completely consistent.

4.1.2 Haskell, Jones and Andersson

Haskell *et al.* (2006) set out to relax some of the assumptions made by Ushomirsky *et al.* (2000). This included dropping the Cowling approximation and ensuring the traction is continuous at the appropriate boundaries. They also noted that, by insisting the star is strained to the maximum throughout the crust, one loses the freedom to impose the boundary conditions of the problem.

Haskell *et al.* (2006) derived a system of coupled ordinary differential equations that describe the perturbations in the elastic crust and the fluid core relative to a spherically symmetric background star. They numerically integrated the perturbation equations and fixed the perturbation amplitude to the maximum necessary to begin to break the crust at a point, according the von Mises criterion. In their study, Haskell *et al.* (2006) obtained the largest mountain when they assumed the core to be unperturbed, thus, allowing them to use a fully relativistic core combined with Newtonian perturbations in the crust. They reported a maximum quadrupole for a star with $M = 1.4\,M_{\odot}$, $R = 10\,$km of

$$Q_{22}^{\rm max} \approx 3.1 \times 10^{40} \left(\frac{\bar{\sigma}_{\rm max}}{10^{-1}}\right) \,{\rm g\,cm^2}, \tag{4.23}$$

that corresponds to an ellipticity of $\epsilon^{\max} \approx 4.0 \times 10^{-5}$ $(\bar{\sigma}_{\max}/10^{-1})$. This result is approximately an order of magnitude above that of Ushomirsky *et al.* (2000).

The calculation of Haskell *et al.* (2006) correctly treated the boundary condition at the crust-core interface by demanding that the traction was continuous. However, their calculation assumed the relaxed shape – which the strain is taken with respect to – to be spherical. In general, the relaxed shape must be non-spherical, to give an equilibrium solution with a non-zero mountain. They did however stipulate that the surface shape of the star was deformed in an $(\ell, m) = (2, 2)$ way. This effectively meant using an outer boundary condition where a traction-like force (*i.e.*, a force per unit area) acts at the very surface of the star. Because of this, the maximum quadrupoles calculated in this framework turn out to be insensitive to the shear modulus of the crust, as they are sustained by this applied surface force. The lack of inclusion of a body force (*i.e.*, a force per unit volume) in building the mountain meant that their formalism did not have the necessary freedom to ensure that the perturbed potential in the interior matches to the exterior solution. We discuss this particular subtlety further in Sec. 4.3.1.

By comparing with our new analysis we also note a number of typographical errors in their elastic perturbation equations. These errors turn out to have a surprisingly dramatic effect. Once they are corrected the maximum quadrupole increases by three orders of magnitude, in sharp contrast with other estimates. This, in turn, highlights the conceptual problem with the formulation.

4.1.3 Johnson-McDaniel and Owen

The most recent estimates for the largest possible mountain on a neutron star were provided by Johnson-McDaniel and Owen (2013). They generalised the Ushomirsky *et al.* (2000) argument to relativistic gravity while relaxing the Cowling approximation. They evaluated the required integral by employing a Green's function. For a $1.4\,M_\odot$ star, described by the SLy equation of state (Douchin and Haensel, 2001), they obtained the result

$$Q_{22}^{\max} \approx 2 \times 10^{39} \left(\frac{\bar{\sigma}_{\max}}{10^{-1}}\right) \text{ g cm}^2, \tag{4.24}$$

corresponding to $\epsilon^{\max} \approx 3 \times 10^{-6}$ $(\bar{\sigma}_{\max}/10^{-1})$.

In following the Ushomirsky *et al.* (2000) approach, the crust was taken to be strained to the maximum at every point, which means that the traction vector cannot be continuous at the crust boundaries. Furthermore, they do not use the correct expression for the perturbed stress-energy tensor, since it does not include variations of the four-velocity. This may be a minor detail, but it should still be noted.

In summary, although some of the above points may have a negligible impact on the

maximum quadrupole estimates, there are issues with all previous studies of the maximum-mountain problem.

4.2 Building mountains

In this section, we examine what must go into a consistent mountain calculation and discuss two methods for modelling mountains on neutron stars. The first approach, introduced in Ushomirsky *et al.* (2000), involves specifying the strain field associated with the mountain. We present a second method that, instead of starting with the strain, starts with a description of the perturbing force. Both approaches are valid and we demonstrate how they are equivalent.

To help develop intuition, we will start by briefly discussing the case of strains built up in a spinning-down star. We will therefore be considering the case of $(\ell, m) = (2, 0)$ perturbations relevant for rotational deformations, not the $(\ell, m) = (2, 2)$ relevant to the mountain case. Suppose a young neutron star with a molten crust spins at an angular frequency Ω. At this rotation rate, the star cools and the crust solidifies. The star then begins to spin down to frequency $\tilde{\Omega} < \Omega$.[5] Because the star has spun down, it changes shape according to the difference in the centrifugal force, $\propto (\Omega^2 - \tilde{\Omega}^2)$. This builds up strain in the crust as the shear stresses resist the change in shape. Should the star spin down sufficiently, the crust may fracture as stresses get too large. In fact, it has been suggested that the elastic yield of the crust in this process may be associated with the glitch phenomenon observed in some rotating pulsars (Baym and Pines, 1971; Keer and Jones, 2015).

Motivated by this example, that does not represent a neutron-star mountain, we consider neutron-star models forced away from sphericity by a perturbing force f_i, which we will choose to give mountain-like $(\ell, m) = (2, 2)$ perturbations. The elastic Euler equation (4.8) then becomes

$$0 = -\nabla_i p - \rho \nabla_i \Phi + \nabla^j t_{ij} + f_i. \tag{4.25}$$

For this exercise, we regard Eq. (4.25) as exact and consider perturbations of it below. In the fluid regions of the star, which cannot support shear stresses, the shear modulus goes to zero so the shear-stress tensor vanishes. To condense the notation, we define

$$H_i \equiv \nabla_i p + \rho \nabla_i \Phi, \tag{4.26}$$

which captures the familiar equation of hydrostatic equilibrium (2.16) when $H_i = 0$. Therefore, the Euler equation (4.25) can be expressed as

$$H_i = f_i + \nabla^j t_{ij}. \tag{4.27}$$

[5] This spin-down could be due to the usual radio emission that pulsars are well known for.

By considering a variation of H_i, we may write

$$\delta H_i = \nabla_i \delta p + \delta\rho \nabla_i \Phi + \rho \nabla_i \delta\Phi, \tag{4.28}$$

where the perturbed quantities will need to be carefully defined in what follows.

We now consider a family of four closely-related, equilibrium stars, illustrated in Fig. 4.1:

Star S – A spherical, fluid star with $(\rho_{\rm S}, p_{\rm S}, \Phi_{\rm S})$:

$$H_i^{\rm S} = 0. \tag{4.29}$$

Star A – A force is applied to star S, which produces a non-spherical, fluid star with $(\rho_{\rm A}, p_{\rm A}, \Phi_{\rm A})$:

$$H_i^{\rm A} = f_i. \tag{4.30}$$

Star $\tilde{\rm A}$ – The crust of star A solidifies while the force is maintained. This gives rise to a non-spherical, relaxed star with the same structure as star A, although (formally) with a non-zero shear modulus. The star has $(\rho_{\tilde{\rm A}} = \rho_{\rm A}, p_{\tilde{\rm A}} = p_{\rm A}, \Phi_{\tilde{\rm A}} = \Phi_{\rm A})$:

$$H_i^{\tilde{\rm A}} = H_i^{\rm A} = f_i. \tag{4.31}$$

Note that, because star A and star $\tilde{\rm A}$ have the same shape, in general, we only need to refer to star A in the following discussion when specifying the values of perturbed quantities.

Star B – The force on star $\tilde{\rm A}$ is removed, which builds up strain in the crust. The associated deformation between these two stars is described by the Lagrangian displacement vector field η^i. The star is non-spherical and strained with $(\rho_{\rm B}, p_{\rm B}, \Phi_{\rm B})$:

$$H_i^{\rm B} = \nabla^j t_{ij}(\eta). \tag{4.32}$$

Note that it is this star, star B, that we are ultimately interested in: this is the star with a mountain supported in a self-consistent way by elastic strains, with no external force acting.

Note that the force f_i has a simple physical interpretation: it is the force that, when applied to our equilibrium star with the mountain (star B), takes us to the corresponding unstrained star (star A or, equivalently, $\tilde{\rm A}$). Note, however, that there is no requirement whatsoever that, in reality, this force ever acted upon our star. For a realistic situation, the elastic strains that support the deformation of star B will likely have evolved through some

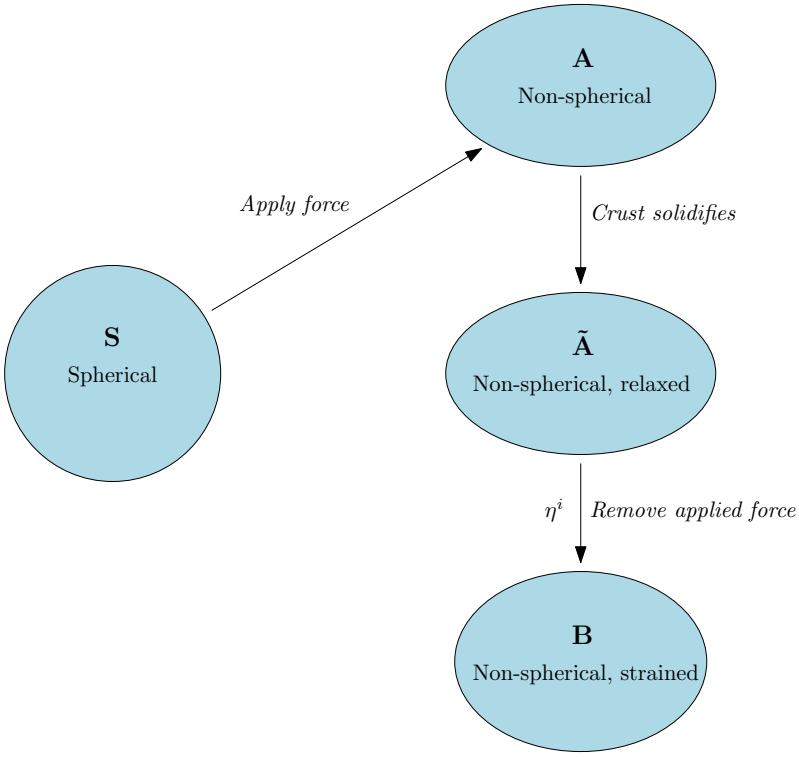

Figure 4.1: A schematic illustration showing the configurations involved in mountain calculations. Note that previous calculations have typically considered stars S and B, but not (explicitly) A or Ã.

complex process of plastic flow and cracking, possibly combined with whatever agent that caused the asymmetry to develop. The usefulness of f_i is two-fold. Firstly, it allows us to explicitly identify the unstrained configuration. Secondly, the explicit introduction of the force into the Euler equation provides the necessary freedom to determine the displacement vector and satisfy all the boundary conditions.

It is instructive to consider the differences between the stellar models described above. Thus, we introduce the notation

$$\delta H_i^{\rm AB} = H_i^{\rm B} - H_i^{\rm A}, \tag{4.33}$$

i.e., $\delta H_i^{\rm AB}$ is the quantity that must be added to $H_i^{\rm A}$ to obtain $H_i^{\rm B}$.

The difference between star B (4.32) and star S (4.29) is

$$\delta H_i^{\rm SB} = \nabla^j t_{ij}(\eta). \tag{4.34}$$

Expression (4.34) relates perturbations between the strained star – with a mountain – and the spherical, reference star to the shear stresses induced when the relaxed star is deformed according to the displacement η^i. This is the standard picture for understanding

neutron-star mountains and, indeed, it is this expression that is used to estimate the maximum quadrupole in Ushomirsky *et al.* (2000) and Johnson-McDaniel and Owen (2013). It is important to note that in these calculations one does not have to determine the relaxed shape and, indeed, stars A and $\tilde{\text{A}}$ did not appear explicitly in previous calculations. However, we demonstrate that the relaxed shape is, in principle, calculable in Sec. 4.2.1.

As we discuss in more detail below, for a fully consistent calculation that satisfies all the boundary conditions of the problem it is not convenient to use (4.34) alone. Rather, we present an alternative strategy that makes explicit use of the deforming force. To this end, we introduce two additional stars shown in Fig. 4.2:

Star $\tilde{\text{S}}$ – The crust of star S solidifies. This star has the same shape as star S with a non-zero shear modulus and ($\rho_{\tilde{\text{S}}} = \rho_{\text{S}}, p_{\tilde{\text{S}}} = p_{\text{S}}, \Phi_{\tilde{\text{S}}} = \Phi_{\text{S}}$):

$$H_i^{\tilde{\text{S}}} = H_i^{\text{S}} = 0. \tag{4.35}$$

Star C – A force is applied to star $\tilde{\text{S}}$. This induces stress in the crust, described by the Lagrangian displacement ξ^i and produces a non-spherical, strained star with ($\rho_{\text{C}}, p_{\text{C}}, \Phi_{\text{C}}$):

$$H_i^{\text{C}} = f_i + \nabla^j t_{ij}(\xi). \tag{4.36}$$

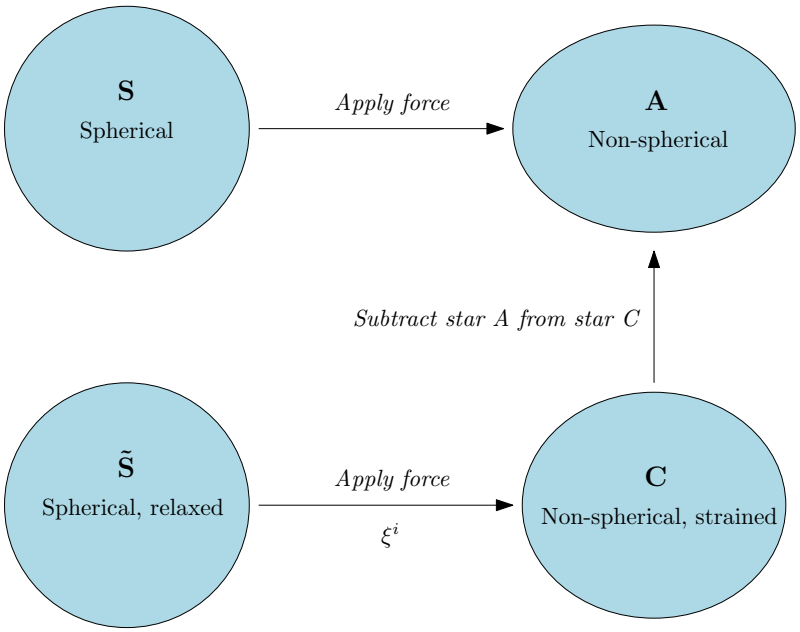

Figure 4.2: A schematic illustration showing the configurations in the force-based mountain scheme.

We can then consider the difference between stars A and C. By using (4.30) and (4.36),

we obtain

$$\delta H_i^{\mathrm{AC}} = \nabla^j t_{ij}(\xi). \tag{4.37}$$

We can note the similarity of (4.37) to (4.34). Indeed, comparing Figs. 4.1 and 4.2, we note the following. In Fig. 4.1, the addition of force f_i maps star B to star A, generating a displacement $-\eta^i$, while in Fig. 4.2, the addition of the force f_i maps star $\tilde{\mathrm{S}}$ to star C, generating a displacement field ξ^i. It follows that, to a good approximation, these vector fields are related by

$$\eta^i = -\xi^i. \tag{4.38}$$

Comparing (4.37) to (4.34) then gives the corresponding relation between the associated scalar perturbations,

$$\delta H_i^{\mathrm{SB}} = -\delta H_i^{\mathrm{AC}}. \tag{4.39}$$

These relations are not exact, as in Fig. 4.1 the force f_i acts upon star B, while in Fig. 4.2 it acts upon star $\tilde{\mathrm{S}}$, but these two stars themselves differ from one another only in a perturbative way, so the difference in the action of f_i on the two must be of second order.

This immediately suggests a strategy for computing the deformation of star B (*i.e.*, δH_i^{SB} and other perturbed quantities). We can easily compute the perturbations linking S and A (*i.e.*, δH_i^{SA} *etc.*), as this is just the perturbation of a spherical fluid star by the force f_i. We can, with only a little more effort, compute the perturbations linking star $\tilde{\mathrm{S}}$ and C (*i.e.*, δH_i^{SC} *etc.*), as this is just the perturbation of a spherical elastic star by f_i. Then, we can take the difference between these two configurations to give the difference between star A and C (*i.e.*, δH_i^{AC} *etc.*), which is, up to an overall sign, the deformation of star B relative to star S that we require, as per (4.39).

As we are interested in computing maximum mountains, we will choose the force f_i such that the breaking strain is reached at some point in the crust of star C. Note, however, that in this force-based approach, we will not be able to follow Ushomirsky *et al.* (2000) and find the solution where the strain is reached at *all* points (simultaneously) in the crust. This is a price one pays in adopting the force-based approach. (It is possible, at least in principle, that one could invent a force that takes the entire crust to breaking strain. However, this is beyond the scope of this work.) We have, however, reduced the calculation of the mountain to two simpler calculations, both taking place on a spherical background and with readily implementable boundary conditions.

4.2.1 Calculating the relaxed shape

We now briefly examine the relaxed configuration that is implied, but not calculated, in maximum-mountain calculations Ushomirsky *et al.* (2000) and Johnson-McDaniel and Owen (2013) to show that it is calculable.

Suppose one knows the strain of star B, $\sigma_{ij}(\eta)$ (see Fig. 4.1). [This is the case in Ushomirsky *et al.* (2000) and Johnson-McDaniel and Owen (2013).] From the strain tensor it is possible to obtain the displacement vector η^i that sources the strain.

We note the following relations: $\delta\rho$ and δp are related through the equation of state (4.5), the perturbed Poisson's equation (4.6) couples $\delta\rho$ and $\delta\Phi$ and (4.28) links $\delta\rho$, δp, $\delta\Phi$ and δH_i. Therefore, it follows that if any one of $(\delta\rho, \delta p, \delta\Phi, \delta H_i)$ are known, the other quantities can, in principle, be calculated.

We begin with (4.34). Since we know the strain tensor that takes one from star A to star B, we also know $\delta H_i^{\rm SB}$. This means we have $(\delta\rho_{\rm SB}, \delta p_{\rm SB}, \delta\Phi_{\rm SB})$. It is this logic, that enables Ushomirsky *et al.* (2000) and Johnson-McDaniel and Owen (2013) to compute the quadrupole moment from just the strain tensor.

By considering variations between star A (4.30) and star B (4.32), we find

$$\delta H_i^{\rm AB} = -f_i + \nabla^j t_{ij}(\eta). \tag{4.40}$$

We know $t_{ij}(\eta)$, but not f_i or $\delta H_i^{\rm AB}$. However, we can obtain $\delta H_i^{\rm AB}$. The quantity $\delta H_i^{\rm AB}$ is generated by the change in shape from star A to star B. This is described by the displacement η^i. In particular, the two density fields $\rho_{\rm A}$ and $\rho_{\rm B}$ are linked through the perturbed continuity equation (4.3). It, therefore, follows that

$$\delta H_i^{\rm AB} = \delta H_i^{\rm AB}(\eta). \tag{4.41}$$

We rearrange (4.40) to obtain an expression for the force,

$$f_i = -\delta H_i^{\rm AB}(\eta) + \nabla^j t_{ij}(\eta). \tag{4.42}$$

Provided η^i, we can calculate the force that takes the star from a spherical shape (star S) to the relaxed shape (star A).

Using (4.29) and (4.30), we have

$$\delta H_i^{\rm SA} = f_i. \tag{4.43}$$

This determines $\delta H_i^{\rm SA}$ and, therefore, also $(\delta\rho_{\rm SA}, \delta p_{\rm SA}, \delta\Phi_{\rm SA})$. This means one can obtain the shape of the relaxed star, supported by a force, f_i, with the property that when the force is removed the star obtains a strained configuration, according to the displacement vector η^i.

4.3 Newtonian perturbations

In order to develop the second strategy of calculating mountains in detail, we take the background star to be non-rotating and construct static perturbations on top of the background. The background is, thus, spherical and described by the Newtonian equations (2.18).

Star C is separated into three layers: a fluid core, an elastic crust and a fluid ocean, whereas star A is purely fluid. We choose to include a fluid layer outside the crust since at low densities the crustal lattice begins to melt and it also simplifies the matching to the exterior gravitational potential (Gittins *et al.*, 2020). The crust only comes into the structure equations at the perturbative level.

4.3.1 The fluid

In order to calculate the relaxed configuration (star A), we need to introduce the force f_i. For practical purposes, it is convenient to write the force as the gradient of a potential, χ,

$$f_i = -\rho \nabla_i \chi. \tag{4.44}$$

This is not the most general expression for the force but it allows us to combine χ with the gravitational potential, which simplifies the analysis. To make the notation more compact, we introduce the total perturbed potential $U = \delta\Phi + \chi$.

At this point, we note that this is where our calculation differs from previous work (Ushomirsky *et al.*, 2000; Haskell *et al.*, 2006; Johnson-McDaniel and Owen, 2013). Previous calculations set out to evaluate the perturbed Euler equation (4.34) where the strain is taken with respect to the relaxed shape the crust wants to have (see Fig. 4.1). In our method, we start with the deforming force and evaluate (4.37), using the subtraction scheme (taking the difference between stars C and A) set out in Sec. 4.2. The use of this force is a subtle, but important, detail since without it one does not have the necessary freedom to impose all the boundary conditions of the problem. We emphasise this point since this issue was somewhat confused in the analysis of Haskell *et al.* (2006) who calculate perturbations of a spherical star but do not explicitly consider the force that sources them. It is for this reason that they were unable to satisfy the boundary condition on the potential at the surface. This point is elucidated below.

Recall that, as we discussed earlier, we assume all perturbed quantities to be expanded in spherical harmonics, but it will be sufficient for our discussion to focus on the $(\ell, m) = (2, 2)$ mode. The system of equations that describes fluid perturbations then simplifies to a single second-order differential equation for the perturbed potential. From the perturbed

Poisson's equation (4.6), we get

$$\frac{d^2\delta\Phi}{dr^2} + \frac{2}{r}\frac{d\delta\Phi}{dr} - \frac{\beta^2}{r^2}\delta\Phi = 4\pi G\delta\rho. \tag{4.45a}$$

The perturbed Euler equation (4.7) returns

$$\delta\rho = -\frac{\rho}{c_{\rm s}^2}U. \tag{4.45b}$$

Therefore, provided a description of the perturbing force, Eqs. (4.45) give a second-order equation that describes the perturbations in the fluid.

The perturbed potential must satisfy two boundary conditions. At the centre of the star the solution must be regular and at the surface it must match to the external solution. Therefore, in addition to χ being regular at the centre of the star and continuous at all interfaces, we must have

$$\delta\Phi(0) = 0 \tag{4.46a}$$

and

$$R\frac{d\delta\Phi}{dr}(R) = -(\ell+1)\delta\Phi(R). \tag{4.46b}$$

Equation (4.46a) is simply the statement of regularity. Equation (4.46b) is mostly readily seen by examining the potential in the exterior, $r \geq R$, which must satisfy Laplace's equation, $\nabla^2\delta\Phi = 0$. As discussed in Appendix B, this admits two solutions, $c_1/r^{\ell+1}$ and $c_2 r^\ell$, with constants c_1 and c_2. Since the exterior solution must fall off as $r \to \infty$, we retain the decaying solution. It is simple to show that (4.46b) is satisfied if $\delta\Phi \propto 1/r^{\ell+1}$.

Using the regularity condition (4.46a), we consider a power-series expansion in small r and input this into (4.45) (as described in Appendix A.2) to obtain an initial condition,

$$\delta\Phi(r) = a_0 r^\ell[1 + \mathcal{O}(r^2)], \tag{4.47}$$

where a_0 is a constant that parametrises the amplitude of the perturbations. In the case when $\chi = 0$ and there is no driving force, this initial condition provides sufficient information to calculate the perturbations up to the surface. At the surface, however, there is no freedom left to impose the surface boundary condition (4.46b) – except in the special case of $a_0 = 0$ where there are no perturbations. [This is the issue that the formalism of Haskell *et al.* (2006) suffers from, and why in that analysis a surface force had to be effectively introduced via a boundary condition.] This serves as a simple demonstration of the fact that an unforced, fluid equilibrium is a spherical star. Equations (4.45) with the boundary conditions (4.46) provide the necessary information to calculate perturbations in the fluid regions of the star sourced by a perturbing force. A simple example of this is the tidal problem.

4.3.1.1 Aside: the tidal potential

An external tidal potential field is a solution of Laplace's equation, $\nabla^2\chi = 0$ (see, *e.g.*, Andersson and Pnigouras, 2020). Because of the constraint of regularity at the centre of the tidally deformed star, the tidal potential must have the form

$$\chi(r) = b_0 r^\ell, \tag{4.48}$$

where b_0 parametrises the strength of the tidal field. Therefore, the total perturbed potential, for small r, must be

$$U(r) = a_0 r^\ell [1 + \mathcal{O}(r^2)] + b_0 r^\ell. \tag{4.49}$$

At the surface of the star, the boundary condition (4.46b) must be satisfied. In some sense, this is achieved through a_0. The constant a_0 parametrises the amplitude of $\delta\Phi$, which is sourced by the external field. The response of a body due to an external tidal field is governed by the Love numbers k_ℓ. These are defined by the ratio of the perturbed potential to the tidal potential at the surface,

$$k_\ell \equiv \frac{1}{2}\frac{\delta\Phi(R)}{\chi(R)}, \tag{4.50}$$

where we recall that the perturbations $\delta\Phi$ are in a specific (ℓ, m) mode. Since the surface boundary condition must be physically satisfied, one can use this information to constrain k_ℓ and, therefore, a_0 for a given tidal field. Using (4.46b), we find

$$R\frac{dU}{dr}(R) + (\ell+1)U(R) = (2\ell+1)\chi(R). \tag{4.51}$$

Thus, defining $y \equiv R[dU(R)/dr]/U(R)$, (4.50) becomes

$$k_\ell = \frac{1}{2}\frac{\ell - y}{y + \ell + 1}, \tag{4.52}$$

which is the standard result. This serves as a simple demonstration of how the introduction of an external force can enable one to satisfy the boundary conditions of the problem.

4.3.2 The elastic crust

In order to calculate the strained star (star C) in our scheme outlined in Sec. 4.2 (Fig. 4.2), we must consider the role of the elastic crust. We reiterate that we consider perturbations with respect to a spherical, reference star.

The elastic material is characterised by the shear-stress tensor

$$t_{ij} = \breve{\mu}\left(\nabla_i\xi_j + \nabla_j\xi_i - \frac{2}{3}g_{ij}\nabla_k\xi^k\right), \tag{4.53}$$

where g_{ij} is the flat three-metric. This describes an elastic solid that obeys Hooke's law: the stress is linearly proportional to the strain. We use the static displacement vector appropriate for polar perturbations (Ushomirsky *et al.*, 2000)[6]

$$\xi^i = \xi_r(r)\nabla^i r Y_{\ell m} + \frac{r}{\beta}\xi_\perp(r)\nabla^i Y_{\ell m}, \tag{4.54}$$

where $\xi_r(r)$ and $\xi_\perp(r)$ account for the radial and tangential components of the displacement.

To make the application of the boundary conditions straightforward, we consider the perturbed traction vector (4.9),

$$T^i = [\delta p(r) - T_1(r)]\nabla^i r Y_{\ell m} - rT_2(r)\nabla^i Y_{\ell m}, \tag{4.55}$$

where we have defined the following two variables related to the radial and tangential components of the traction:

$$T_1(r)Y_{\ell m} \equiv t_{rr} = \frac{2\check{\mu}}{3r}\left(-2\xi_r + \beta\xi_\perp + 2r\frac{d\xi_r}{dr}\right)Y_{\ell m} \tag{4.56a}$$

and

$$T_2(r)\partial_\theta Y_{\ell m} \equiv \frac{t_{r\theta}}{r} = \frac{\check{\mu}}{\beta r}\left(\beta\xi_r - \xi_\perp + r\frac{d\xi_\perp}{dr}\right)\partial_\theta Y_{\ell m}. \tag{4.56b}$$

From the perturbed continuity equation (4.3), we then obtain

$$\begin{aligned}\delta\rho &= -\rho\frac{d\xi_r}{dr} - \left(\frac{2\rho}{r} + \frac{d\rho}{dr}\right)\xi_r + \frac{\beta\rho}{r}\xi_\perp \\ &= -\left(\frac{3\rho}{r} + \frac{d\rho}{dr}\right)\xi_r + \frac{3\beta\rho}{2r}\xi_\perp - \frac{3\rho}{4\check{\mu}}T_1.\end{aligned} \tag{4.57}$$

From the definitions of the traction variables (4.56), we have the following differential equations that describe the displacement vector:

$$\frac{d\xi_r}{dr} = \frac{1}{r}\xi_r - \frac{\beta}{2r}\xi_\perp + \frac{3}{4\check{\mu}}T_1 \tag{4.58a}$$

and

$$\frac{d\xi_\perp}{dr} = -\frac{\beta}{r}\xi_r + \frac{1}{r}\xi_\perp + \frac{\beta}{\check{\mu}}T_2. \tag{4.58b}$$

From the radial part of the perturbed Euler equation (4.8) combined with the perturbed

[6]Because we focus on polar deformations, we are able to ignore the axial part of the vector spherical harmonics, $\epsilon^{ijk}\nabla_j r\nabla_k Y_{\ell m}$, where ϵ^{ijk} is the antisymmetric Levi-Civita symbol. Just as the scalar spherical harmonics, $Y_{\ell m}$, form an orthogonal basis, so do the vector spherical harmonics, $\nabla^i r Y_{\ell m}$, $\nabla^i Y_{\ell m}$ and $\epsilon^{ijk}\nabla_j r\nabla_k Y_{\ell m}$.

continuity equation (4.57),

$$\begin{aligned}\left(1+\frac{3c_{\rm s}^2\rho}{4\check{\mu}}\right)\frac{dT_1}{dr} &= \rho\frac{dU}{dr}\\ &-\left\{\frac{d}{dr}(c_{\rm s}^2)\left(3\rho+r\frac{d\rho}{dr}\right)+c_{\rm s}^2\left[\frac{3\beta^2\rho}{2r}+\frac{d\rho}{dr}-\frac{r}{\rho}\left(\frac{d\rho}{dr}\right)^2+r\frac{d^2\rho}{dr^2}\right]\right\}\frac{1}{r}\xi_r\\ &+\left[\frac{d}{dr}(c_{\rm s}^2)3\rho+c_{\rm s}^2\left(\frac{3\rho}{r}+\frac{d\rho}{dr}\right)\right]\frac{\beta}{2r}\xi_\perp\\ &-\left[\frac{3}{r}+\frac{d}{dr}(c_{\rm s}^2)\frac{3\rho}{4\check{\mu}}+c_{\rm s}^2\left(\frac{3\rho}{r}-\frac{\rho}{\check{\mu}}\frac{d\check{\mu}}{dr}+\frac{d\rho}{dr}\right)\frac{3}{4\check{\mu}}\right]T_1\\ &+\left(1+\frac{3c_{\rm s}^2\rho}{2\check{\mu}}\right)\frac{\beta^2}{r}T_2.\end{aligned} \tag{4.58c}$$

Then, from the tangential piece of (4.8) we find

$$\begin{aligned}\frac{dT_2}{dr} = \frac{\rho}{r}U-c_{\rm s}^2\left(3\rho+r\frac{d\rho}{dr}\right)\frac{1}{r^2}\xi_r\\ +\left[\frac{3c_{\rm s}^2\rho}{2}+\left(1-\frac{2}{\beta^2}\right)\check{\mu}\right]\frac{\beta}{r^2}\xi_\perp\\ +\left(\frac{1}{2}-\frac{3c_{\rm s}^2\rho}{4\check{\mu}}\right)\frac{1}{r}T_1-\frac{3}{r}T_2.\end{aligned} \tag{4.58d}$$

We also have the perturbed Poisson's equation (4.45a), that combines with the perturbed continuity equation (4.57) to give

$$\begin{aligned}\frac{d^2\delta\Phi}{dr^2}+\frac{2}{r}\frac{d\delta\Phi}{dr}-\frac{\beta^2}{r^2}\delta\Phi = -4\pi G\left(\frac{3\rho}{r}+\frac{d\rho}{dr}\right)\xi_r\\ +6\pi G\frac{\beta\rho}{r}\xi_\perp-3\pi G\frac{\rho}{\check{\mu}}T_1.\end{aligned} \tag{4.58e}$$

Equations (4.58) form a coupled system of ordinary differential equations to describe the perturbations in the elastic material. We have compared our perturbation equations with that of Haskell *et al.* (2006) (in the limit of $\chi = 0$) and noted several discrepancies. We find that these mistakes increase the maximum quadrupole estimates of Haskell *et al.* (2006) by three orders of magnitude.

4.3.3 Interface conditions

At this point, we address the boundary conditions at the fluid-elastic interfaces since we wish to connect perturbations in the fluid core and ocean with the elastic crust for star C. Provided the density is smooth (which we assume), the perturbed potential $\delta\Phi$ and its derivative $d\delta\Phi/dr$ must be continuous at an interface. To see how the other perturbed quantities behave at an interface, we must consider the perturbed traction (4.55).

This admits two quantities that must be continuous: the radial and tangential components.

Since the shear modulus vanishes in the fluid, continuity of the radial traction $(\delta p - T_1)$ provides an algebraic relation that must hold true at an interface,

$$\begin{aligned}\rho U_{\rm F} = &\left(1 + \frac{3c_{\rm s}^2\rho}{4\check{\mu}}\right) T_{1\rm E} \\ &+ c_{\rm s}^2\left[\left(\frac{3\rho}{r} + \frac{d\rho}{dr}\right)\xi_{r\rm E} - \frac{3\beta\rho}{2r}\xi_{\perp\rm E}\right],\end{aligned} \tag{4.59}$$

where the subscripts F and E denote the fluid and elastic sides of the interface, respectively. We note that the radial displacement ξ_r must be continuous at a boundary, however, this does not necessarily have to be the case for the tangential piece $\xi_\perp$. From the tangential part of the traction, we have $T_2 = 0$ at a fluid-elastic interface.

In reference to the maximally strained approach of Ushomirsky *et al.* (2000) and Johnson-McDaniel and Owen (2013), we note that, if one assumes the shear modulus smoothly goes to zero at a fluid-elastic interface, then the tangential traction condition is trivially satisfied [see (4.56b)]. This would effectively result in the displacement vector in the crust being arbitrary since there are not enough boundary conditions to constrain it. It is not clear how to resolve this issue.

In the fluid regions of the star, the perturbations are governed by Eqs. (4.45) and so are described by the variables $(d\delta\Phi/dr, \delta\Phi)$. In the crust, we have a more complex structure with Eqs. (4.58) and quantities $(d\delta\Phi/dr, \delta\Phi, \xi_r, \xi_\perp, T_1, T_2)$. We assume the force is known. The perturbations in the elastic crust present a boundary-value problem. For the six variables, we have six boundary conditions: continuity of $d\delta\Phi/dr$ and $\delta\Phi$ at the core-crust transition and the two traction conditions – (4.59) and $T_2 = 0$ – at both interfaces. Therefore, the problem is well posed.

Additionally, it is straightforward to show that the boundary condition on the Lagrangian variation of the pressure $\Delta p(R, \theta, \phi) = 0$ is trivially satisfied by the background structure.[7]

4.4 The deforming force

The formalism we detail above requires a description of the deforming force that causes the star to have a non-spherical shape. Because of the abstract nature of this force, it is difficult to prescribe without a detailed evolutionary calculation of the history of the star. As a proof-of-principle calculation, we examine three example sources.

We use a polytropic equation of state (2.19). (See Appendix A.1 on how to generate

[7] This boundary condition is intuitive. In the background configuration, the surface is defined by $p(R) = 0$. During the perturbation, the individual elements of the star are moved according to the Lagrangian displacement ξ^i and, therefore, the surface will have moved to $R \to R + \xi^r(R, \theta, \phi)$. This corresponds to $\Delta p(R, \theta, \phi) = 0$. One can also convince themselves that this holds true by examining the definition of the Lagrangian variation (2.38) for p at the surface of the perturbed configuration.

polytropic models.) We work with $n = 1$ and generate background models with $M = 1.4\,M_\odot$, $R = 10\,\mathrm{km}$. For the shear-modulus profile in the crust, we consider a simple linear model (Haskell *et al.*, 2006),

$$\breve{\mu}(\rho) = \kappa\rho, \tag{4.60}$$

where $\kappa = 10^{16}\,\mathrm{cm}^2\,\mathrm{s}^{-2}$. We assume the core-crust transition to occur at $\rho_{\mathrm{base}} = 2 \times 10^{14}\,\mathrm{g\,cm}^{-3}$ (which is the same as Ushomirsky *et al.*, 2000), while the crust-ocean transition is at $\rho_{\mathrm{top}} = 10^6\,\mathrm{g\,cm}^{-3}$ (Gittins *et al.*, 2020).

We consider three sources for the perturbations: (i) a potential that satisfies Laplace's equation, (ii) a potential that satisfies Laplace's equation but does not act in the core and (iii) a thermal pressure perturbation. In reality, the fiducial force will depend on the evolutionary history of the star. Since this is a complex problem (beyond the scope of this work), the examples we consider are indicative in nature and should serve as illustrations of how one can calculate mountains using this scheme. The forces we use should not be interpreted as having an explicit link with the neutron-star physics. For each prescription, we generate two stars – a relaxed star, that experiences purely fluid perturbations (star A in Fig. 4.2), and a strained star, that experiences elastic perturbations in the crust (star C in Fig. 4.2). We normalise the perturbations by ensuring the strained star reaches breaking strain at a point in the crust, subject to the von Mises criterion, and that the relaxed star experiences the same force. This allows us to work out the quadrupole moment of each star. Our results for the three sources are summarised in Table 4.1.

Table 4.1: The maximum quadrupoles and ellipticities from the different models. For each case, we show the quadrupole Q_{22}^{A} and ellipticity ϵ^{A} for the relaxed star (star A) and the difference relative to the strained star (star C) with quadrupole Q_{22}^{C} and ellipticity ϵ^{C}.

Source	$\lvert Q_{22}^{\mathrm{A}}\rvert$ / g cm^2	$\lvert\epsilon^{\mathrm{A}}\rvert$	$\lvert Q_{22}^{\mathrm{C}} - Q_{22}^{\mathrm{A}}\rvert$ / g cm^2	$\lvert\epsilon^{\mathrm{C}} - \epsilon^{\mathrm{A}}\rvert$
Solution of Laplace's equation	2.4×10^{43}	3.1×10^{-2}	1.7×10^{37}	2.2×10^{-8}
Solution of Laplace's equation (outside core)	1.4×10^{41}	1.8×10^{-4}	4.4×10^{38}	5.7×10^{-7}
Thermal pressure perturbation	9.2×10^{38}	1.2×10^{-6}	4.0×10^{38}	5.2×10^{-7}

The structure in the fluid core of both stars may be straightforwardly calculated using Eqs. (4.45) with boundary condition (4.46a). The crust of star C presents a boundary-value problem with Eqs. (4.58) and the interface conditions described in Sec. 4.3.3. Both star A and C have fluid oceans, where one can integrate Eqs. (4.45) through to the surface. At this point, one can verify that the boundary condition at the surface (4.46b) is satisfied. The numerical scheme we follow for solving the perturbations is described in Appendix C.

4.4.1 A solution of Laplace's equation

The first example we consider is based on the form of the deforming potential for tidal deformations (Sec. 4.3.1.1). The source potential is taken to be a solution of Laplace's equation,

$$\nabla^2\chi = 0. \tag{4.61}$$

This example is particularly convenient since the perturbed Poisson's equation (4.6) is simply modified by $\delta\Phi \to U$. Therefore, we may write

$$\nabla^2 U = 4\pi G\delta\rho. \tag{4.62}$$

The total perturbed potential must be regular at the origin, $U(0) = 0$.

From (2.79), we can obtain the multipole moments from the exterior potential,

$$Q_{\ell m} = -\frac{(2\ell+1)R^{\ell+1}}{4\pi G}\delta\Phi(R). \tag{4.63}$$

By making use of the boundary conditions (4.46), one can also write the multipole in terms of the total perturbed potential,

$$Q_{\ell m} = \frac{R^{\ell+1}}{4\pi G}\left[R\frac{dU}{dr}(R) - \ell U(R)\right]. \tag{4.64}$$

The advantage of writing the multipole in this way is that one does not need to disentangle the two potentials (χ and $\delta\Phi$) from U.

The source potential must be of the form of (4.48). Its value will be chosen to ensure the star is maximally strained at some point in the crust. The source potential at the surface is given by

$$\chi(R) = \frac{1}{2\ell+1}\left[R\frac{dU}{dr}(R) + (\ell+1)U(R)\right]. \tag{4.65}$$

It is this quantity that we use to ensure that the relaxed and strained stars experience the same force.

To make sure the star is maximally strained we calculate the von Mises strain (4.17) and use the von Mises criterion (4.18). For $(\ell, m) = (2, 2)$ perturbations, we have[8]

$$\begin{aligned}\bar{\sigma}^2 = \frac{5}{256\pi}\Bigg\{6\sin^2\theta\Bigg[3\sin^2\theta\cos^2 2\phi\left(\frac{T_1}{\check{\mu}}\right)^2 \\ + 4(3+\cos 2\theta - 2\sin^2\theta\cos 4\phi)\left(\frac{T_2}{\check{\mu}}\right)^2\Bigg] \\ + (35 + 28\cos 2\theta + \cos 4\theta + 8\sin^4\theta\cos 4\phi)\left(\frac{\xi_\perp}{r}\right)^2\Bigg\}.\end{aligned} \tag{4.66}$$

Since the von Mises strain is a function of position, we can identify where the strain is highest (and, thus, the crust will break first) and take that point to be at breaking strain, that we assume to be $\bar{\sigma}_{\rm max} = 10^{-1}$ (Horowitz and Kadau, 2009). Other estimates for the magnitude of the breaking strain include Baiko and Chugunov (2018) who obtained the

[8] Since we focus on a specific harmonic, we take the real parts of σ_{ij} and then contract using (4.17).

smaller value of $\bar{\sigma}_{\rm max} = 0.04$. However, as was the case for previous maximum-mountain calculations, our results are linear in the breaking strain. Thus, a smaller breaking strain would result in less pronounced mountains.

Thus, for the strained star (star C) we integrate Eqs. (4.45) for the core and ocean and integrate Eqs. (4.58) in the elastic crust. The relaxed star (star A) is generated using Eqs. (4.45) for the entire star. The perturbations are normalised by ensuring that the point in the crust where the strain is highest reaches breaking strain, according to (4.66). The force associated with this deformation (4.65) is then taken to be the same for the relaxed star. Figures 4.3 and 4.4 show the results for the strained star. In Fig. 4.3 we show how the perturbed traction is continuous at the fluid-elastic interfaces. We note that Fig. 4.4 shows how the dominant contribution to the von Mises strain comes from the radial traction component. This is also true for the other forces we consider. It is at the top of the crust that the star is the weakest in the $(\ell, m) = (2, 2)$ mode. The quadrupoles are calculated using (4.64). The relaxed star attains a quadrupole of $|Q_{22}^{\rm A}| = 2.4 \times 10^{43}\,{\rm g\,cm^2}$, that corresponds to an ellipticity of $|\epsilon^{\rm A}| = 3.1 \times 10^{-2}$. The difference between the strained and relaxed star is $|Q_{22}^{\rm C} - Q_{22}^{\rm A}| = 1.7 \times 10^{37}\,{\rm g\,cm^2}$, $|\epsilon^{\rm C} - \epsilon^{\rm A}| = 2.2 \times 10^{-8}$.

The very different sizes of $|\epsilon^{\rm A}|$ and $|\epsilon^{\rm C} - \epsilon^{\rm A}|$ reported in Table 4.1 have a natural interpretation. The large ellipticity represented by $|\epsilon^{\rm A}|$ corresponds to a star whose deformation is supported by the external force f_i, with a size limited only by the crustal breaking strain. In this case, the (non-zero) shear modulus of the crust plays little role. [It is this sort of configuration that was effectively considered in Haskell *et al.* (2006), where in that case the force that was implicitly introduced was a force per unit area, applied at the surface.] In contrast, the ellipticity represented by $|\epsilon^{\rm C} - \epsilon^{\rm A}|$ is that supported by the shear strains of the crust when the external force is removed and, therefore, is sensitive to the crust's shear modulus. As is readily captured by simple back-of-the-envelope estimates, the relative sizes of these two ellipticities are related to the fact that the gravitational binding energy of the star is orders of magnitude larger than the Coulomb binding energy of the crustal lattice (see, *e.g.*, Jones, 2002).

We observe that the ellipticity $|\epsilon^{\rm C} - \epsilon^{\rm A}| = 2.2 \times 10^{-8}$ is notably smaller than what has been found in previous work [Eqs. (4.22)–(4.24)]. This is not surprising, as these previous studies considered strain fields that were maximal everywhere, as opposed to at a single point. With a view to producing larger ellipticities, we will, therefore, consider some different choices of external force field.

4.4.2 A solution of Laplace's equation outside the core

We consider a special case of the above source: a source potential that does not act in the core – instead, it only manifests itself in the crust and ocean. The motivation for considering this special case is regularity at the centre will not be a necessary condition

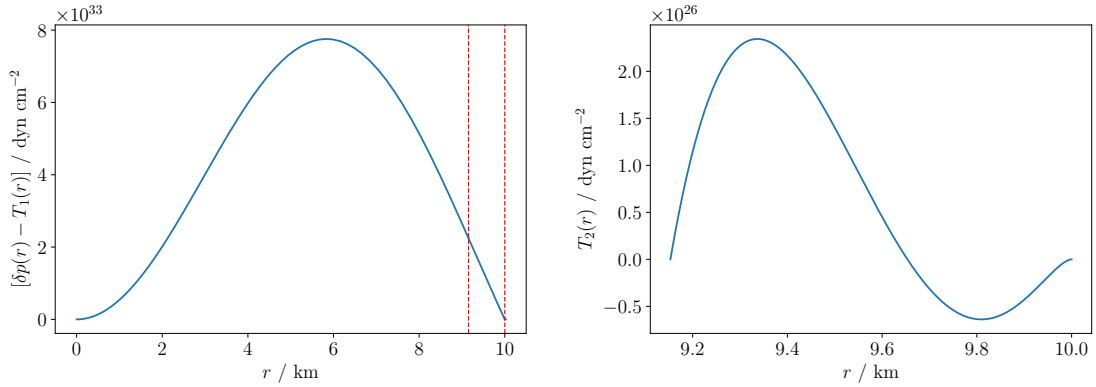

Figure 4.3: The radial (left panel) and tangential (right panel) components of the perturbed traction as functions of radius for the potential solution to Laplace's equation. The vertical red dashed lines in the left panel indicate the base and the top of the crust. Regarding the horizontal range in the right panel, recall that T_2 only has a finite value in the crust.

on the source potential since it does not exist at the origin. Also, we note that Haskell *et al.* (2006) found that a similar example produced their largest quadrupole moment. We then have the general solution to Laplace's equation (4.61),

$$\chi(r) = c_1/r^{\ell+1} + c_2 r^{\ell}. \tag{4.67}$$

This expression is taken to be true for the base of the crust and above.

As this model is somewhat artificial, we have to make a number of assumptions with regards to its prescription. We take the core to be unperturbed and have $\delta\Phi = \xi_r = 0$ in the core. With the introduction of the source potential in the crust, there will be a discontinuity in U at the core-crust interface. However, we insist that $\delta\Phi$ must be continuous. This discontinuity is relevant for the radial traction condition (4.59) where $U_{\mathrm{F}} = 0$, but has a finite value in the crust due to the source potential.

The quadrupole may be calculated from (4.63). The matching with the total perturbed potential needs to be adjusted to take into account the additional $1/r^{\ell+1}$ term from the external field. Therefore, we have

$$Q_{\ell m} = \frac{R^{\ell+1}}{4\pi G}\left[R\frac{dU}{dr}(R) - \ell U(R)\right] + \frac{2\ell+1}{4\pi G}B. \tag{4.68}$$

As in the previous case, we generate a relaxed star and a maximally strained star. One must vary either c_1 or c_2 to ensure the surface boundary condition (4.46b) is satisfied. We normalise the relaxed star so that it experiences the same source potential (4.67). The results for this case are shown in Figs. 4.5 and 4.6. As in the above example, the

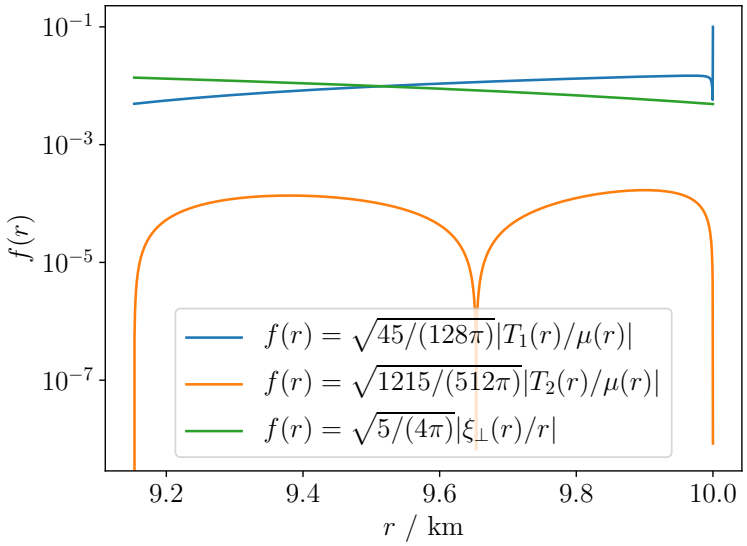

Figure 4.4: The strain components in (4.66) maximised over (θ, ϕ) against radius for the potential solution to Laplace's equation.

T_1 component dominates the von Mises strain and the crust breaks at the top. We find $|Q_{22}^{\mathrm{A}}| = 1.4 \times 10^{41}\,\mathrm{g\,cm^2}$, $|\epsilon^{\mathrm{A}}| = 1.8 \times 10^{-4}$ and $|Q_{22}^{\mathrm{C}} - Q_{22}^{\mathrm{A}}| = 4.4 \times 10^{38}\,\mathrm{g\,cm^2}$, $|\epsilon^{\mathrm{C}} - \epsilon^{\mathrm{A}}| = 5.7 \times 10^{-7}$.

Compared to the previous result, the quadrupole difference between the relaxed and strained stars has increased by an order of magnitude. This is within a factor of a few of previous maximum-mountain calculations, and illustrates the dependence on the force prescription.

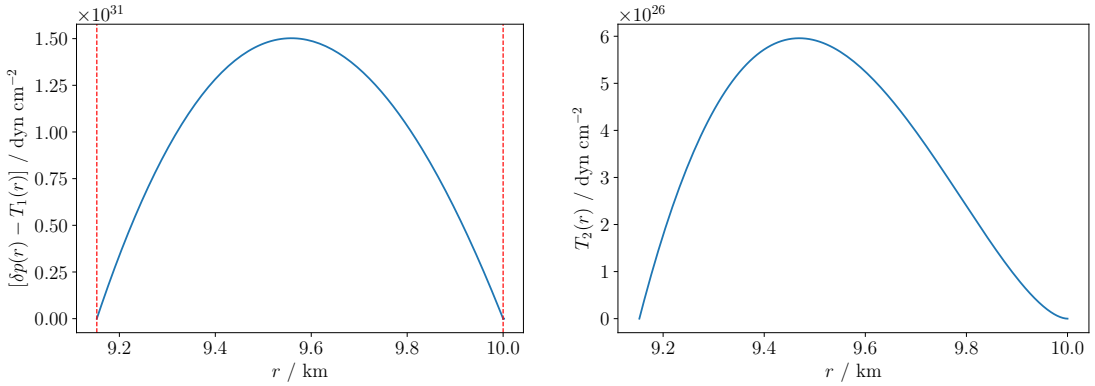

Figure 4.5: The radial (left panel) and tangential (right panel) components of the perturbed traction as functions of radius for the potential solution to Laplace's equation outside the core. The vertical red dashed lines in the left panel indicate the base and the top of the crust. Regarding the horizontal range in the right panel, recall that T_2 only has a finite value in the crust.

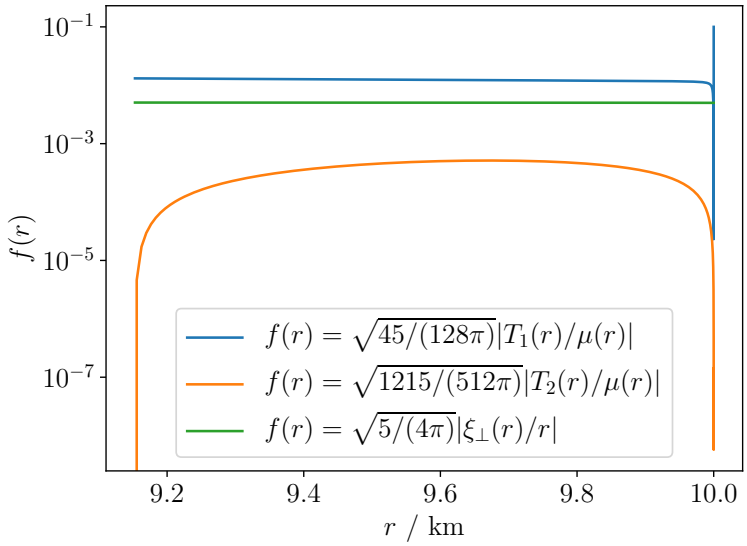

Figure 4.6: The strain components in (4.66) maximised over (θ, ϕ) against radius for the potential solution to Laplace's equation outside the core.

4.4.3 A thermal pressure perturbation

The third source for the perturbations we examine is motivated by a thermal pressure perturbation. Note that the approach we use for this example could be applied more generally to consider non-barotropic matter where the pressure is adjusted, relative to the barotropic case, at the perturbative level. We assume the thermal pressure to be of the ideal-gas form,

$$\delta p_{\rm th} = \frac{k_{\rm B}\rho}{m_{\rm b}}\delta T, \tag{4.69}$$

where δT is the temperature perturbation. To interpret this thermal pressure as a force, we identify

$$\rho\nabla_i\chi = \nabla_i\delta p_{\rm th} = \frac{k_{\rm B}}{m_{\rm b}}\nabla_i(\rho\delta T). \tag{4.70}$$

The temperature perturbation must be regular at the origin. For simplicity we assume it to be quadratic,

$$\delta T(r) = \left(\frac{r}{R}\right)^2 \delta T(R), \tag{4.71}$$

where $\delta T(R)$ corresponds to the perturbation of the temperature at the surface. Both the relaxed and strained configurations experience the same temperature perturbation. We show the results in Figs. 4.7 and 4.8.[9] We obtain the results $|Q_{22}^{\rm A}| = 9.2 \times 10^{38}\,{\rm g\,cm^2}$, $|\epsilon^{\rm A}| = 1.2 \times 10^{-6}$ and $|Q_{22}^{\rm C} - Q_{22}^{\rm A}| = 4.0 \times 10^{38}\,{\rm g\,cm^2}$, $|\epsilon^{\rm C} - \epsilon^{\rm A}| = 5.2 \times 10^{-7}$. This result is of the same order of magnitude as the potential outside the core.

[9] We found the crust breaks when $\delta T(R) = 3.5 \times 10^6\,{\rm K}$. The temperature reported here is not a physical temperature perturbation the star is subjected to, noting that the background is at zero temperature. It is simply a source term for the pressure perturbation (4.69).

It is interesting to note that while the values of the ellipticities $|\epsilon^{\mathrm{C}}|$ and $|\epsilon^{\mathrm{A}}|$ vary by about four orders of magnitude for the three deforming forces we consider, the variation in the actual ellipticity of the mountain, $|\epsilon^{\mathrm{C}} - \epsilon^{\mathrm{A}}|$, is relatively modest, about one order of magnitude (see Table 4.1). This is presumably a reflection of the fact that in all three cases we consider the same star with the same crustal breaking strain and shear modulus, so all stars have a similar ability to support deformations.

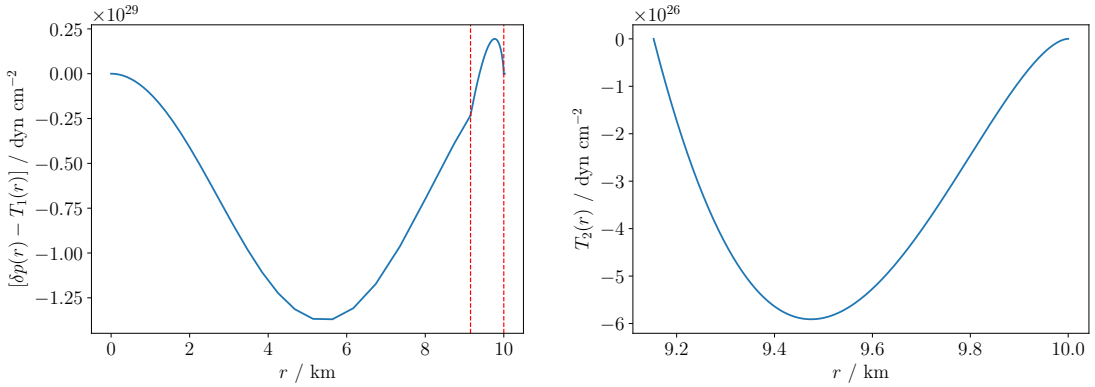

Figure 4.7: The radial (left panel) and tangential (right panel) components of the perturbed traction as functions of radius for the temperature perturbation. The vertical red dashed lines in the left panel indicate the base and the top of the crust. Regarding the horizontal range in the right panel, recall that T_2 only has a finite value in the crust.

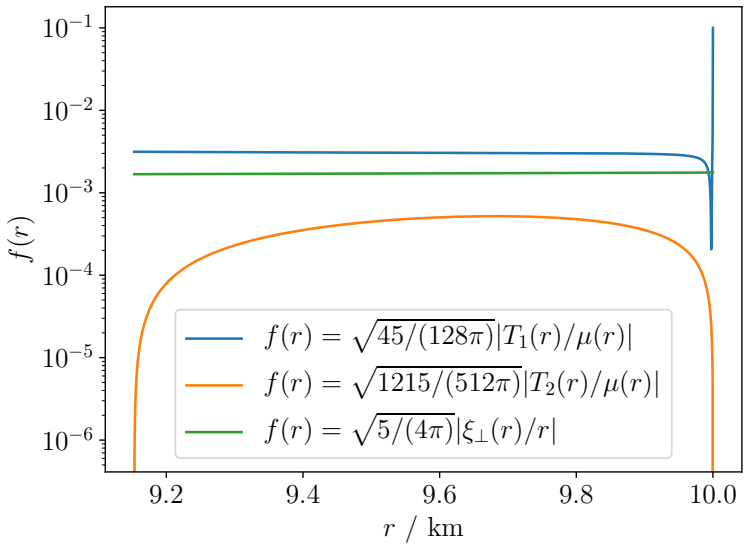

Figure 4.8: The strain components in (4.66) maximised over (θ, ϕ) against radius for the temperature perturbation.

4.5 Summary

The question of the maximum mountain a neutron-star crust can support is an interesting problem. Such an estimate provides upper limits on the strength of gravitational-wave

emission from rotating neutron stars, as well as having implications for the maximum spin-frequency limit that these systems can attain. In Chap. 3, we found that a fixed quadrupole of $Q_{22} = 10^{36}\,\mathrm{g\,cm^2}$ was sufficient to obtain the observed spin distribution of accreting neutron stars.

We returned to this problem to tackle some of the pertinent assumptions made in previous work. We have discussed how previous estimates have not dealt appropriately with boundary conditions that must be satisfied for realistic neutron-star models. The calculations of Ushomirsky *et al.* (2000) and Johnson-McDaniel and Owen (2013) both assumed a specific form for the strain that takes the star away from its relaxed shape and ensures the crust is maximally strained at every point. However, such a strain is somewhat unphysical since it does not respect the continuity of the traction vector. Additionally, the approach of Haskell *et al.* (2006), while satisfying the traction conditions at the crust-core boundary, did not obey the boundary condition on the potential at the surface. This was due to the calculation assuming the relaxed configuration is spherical and implicitly using a surface force to deform the star. There were also errors present in the perturbation equations of Haskell *et al.* (2006) that change their results by several orders of magnitude.

An important simplification of the previous studies was to not explicitly calculate the non-spherical, relaxed shape that the strain is taken with respect to. As we have shown, such a description requires the introduction of a perturbing force that takes the star away from sphericity. We found such a discussion was missing in prior studies and, hence, have provided a demonstration that shows, provided one has a description of the strain, how the relaxed shape can calculated.

We found that including this force is crucial in enabling one to satisfy all the boundary conditions. Therefore, we have introduced a novel scheme for calculating the maximum quadrupole deformation that a neutron star can sustain and have demonstrated how our scheme is entirely equivalent to the approach of preceding calculations. Crucially, the formalism satisfies all the boundary conditions of the problem. One of the key advantages of our approach is that one computes all relevant quantities, including the shape of the relaxed star. However, one must provide a prescription for the deforming force.

There is obviously significant freedom in what one may choose for the form of this force and, indeed, the formalism we have presented can be used for any deforming force that has the form (4.44). Furthermore, it would not be difficult to adjust this formalism for other forces. However, evolutionary calculations will be necessary to fully motivate the form of the force. Thus, we surveyed three simple examples for the source of the mountains. We obtained the largest quadrupole for the (somewhat artificial) case where the perturbing potential is a solution to Laplace's equation, but leaves the core unperturbed. All of our results are between a factor of a few to two orders of magnitude below that of prior

estimates for the maximum mountain a neutron star may support. That our results were smaller is not surprising, as our maximum mountains were constructed so that the breaking strain was reached at only a single point. An immediate question would be if there is a reasonable scenario that bridges the gap between relaxed configurations associated with a specific force and configurations following from specifying the strain. It seems inevitable that the answer will rely on evolutionary scenarios, leading to mountain formation, a problem that has not yet attracted the attention it deserves.

An example of a promising scenario through which a rotating neutron star may radiate gravitational waves is accretion from a binary companion. As the gas is accreted onto the surface of the star, chemical reactions take place that change the composition. Such changes in the composition can, in turn, result in the star attaining a non-trivial quadrupole moment (Bildsten, 1998; Ushomirsky *et al.*, 2000). Additionally, there has been some effort towards calculating mountains on accreting neutron stars that are sustained by the magnetic field (Melatos and Payne, 2005; Payne and Melatos, 2006; Priymak *et al.*, 2011). We note that, in our calculation, we only consider barotropic matter. This is appropriate to describe equilibrium stellar models. Indeed, if the star is in equilibrium, accreted and non-accreted matter may be described using barotropic equations of state (Haskell *et al.*, 2006). However, for evolutionary calculations, like those described above, one may need to consider non-barotropic features and, as we noted in Sec. 4.4.3, the formalism we have presented could be used with such aspects at the perturbative level.

As an (admittedly phenomenological) indication of a possible solution, it may be worth pointing out that our approach to elasticity is somewhat simplistic. We have followed the usual assumption that the crust can be well described as an elastic solid (represented by a linear stress-strain relation) until it reaches the breaking strain, at which point the crust fails and all the strain is released. This model accords well with the molecular-dynamics simulations of Horowitz and Kadau (2009), but it is worth noting that laboratory materials tends to behave slightly differently (Ottosen and Ristinmaa, 2005). In particular, one typically finds that material deforms plastically for some level of strain before the ultimate failure. This introduces the yield strain as the point above which the stress-strain relationship is no longer linear and raises (difficult) questions regarding the plastic behaviour (the matter may harden, allowing stresses to continue building, or soften, leading to reduced stress as the strain increases). State-of-the-art simulations suggest a narrow region of plastic behaviour before the crust fails (Horowitz and Kadau, 2009), but one should perhaps keep in mind that the levels of shear involved in the simulation may not lead to a true representation of matter that is deformed more gently. Let us, for the sake of the argument, suppose that this is the case and that the crust exhibits ideal plasticity above the chosen yield strain. If this were to happen, the strain would locally saturate at the yield limit even if the imposed force increased. One can then imagine applying a deforming force to source a neutron-star mountain and then increasing it until some point

in the crust reaches yield strain. This is essentially the calculation we have done, as we did not model the behaviour beyond this point. Allowing for (ideal) plastic flow as the force is further increased, one may envisage that the entire crust may saturate at the yield strain. This is, of course, pure speculation (although there have been several notable discussions about the relevance of plastic deformations of the neutron-star crust; see Smoluchowski and Welch, 1970; Jones, 2003; Chugunov and Horowitz, 2010), but it might explain how a real system could reach the maximum strain configuration imposed in the Ushomirsky *et al.* (2000) argument. As we already suggested, detailed evolutionary calculations that take into account the physical processes that produce the mountain will be required to make progress on the problem.

Another natural avenue for future research is to generalise our calculation to relativity. This would be an important step as it brings realistic equations of state into play. Indeed, this is what we shall explore in the next chapter.

CHAPTER 5

Mountains in relativity

In the previous chapter (Chap. 4), we discussed how one computes mountains on neutron stars. Due to issues with previous calculations, we introduced a novel scheme that enables one to satisfy all the relevant boundary conditions of the problem. In this chapter, we generalise this work to relativistic gravity, as was done in Gittins and Andersson (2021).

We dedicate Sec. 5.1 to deriving the fluid and elastic perturbation equations in relativity in order to construct fluid stars and stars with elastic crusts. As with the Newtonian calculation, the elastic crust presents a boundary-value problem, so we detail the relevant interface conditions. In Sec. 5.2, we consider three sources for the fiducial force that source the mountains. Because we conduct this work in relativity, we are able to consider the effect of the equation of state on the size of the deformations in Sec. 5.3. We summarise in Sec. 5.4.

5.1 Relativistic perturbations

Conceptually, the analysis of the mountain problem proceeds as in the Newtonian case (Sec. 4.3). We need to generate stellar models with and without elastic crusts (stars C and A, respectively; Fig. 4.2). As before, we build static perturbations on top of spherical backgrounds. In relativity, we use the relativistic structure equations (2.33) for the background.

5.1.1 The fluid

The standard approach to computing non-radial stellar perturbations in general relativity is to follow Thorne and Campolattaro (1967). We use the Regge-Wheeler gauge (Regge and Wheeler, 1957) and focus on static, polar $\ell \geq 2$ perturbations, which leads to the Eulerian perturbation of the metric

$$h_{ab}dx^a dx^b = e^{\nu} H_0 Y_{\ell m} dt^2 + 2H_1 Y_{\ell m} dt dr + e^{\lambda} H_2 Y_{\ell m} dr^2 + r^2 K Y_{\ell m}(d\theta^2 + \sin^2\theta\, d\phi^2), \quad (5.1)$$

where $H_0(r)$, $H_1(r)$, $H_2(r)$ and $K(r)$ describe the response of the spacetime to the perturbations. In the Newtonian limit, the terms in the perturbed metric – specifically H_0 – can be related to the perturbed potential $\delta\Phi$. The perturbed metric is sourced by the perturbations to the matter content of the spacetime, characterised by the linearised stress-energy tensor $\delta T_a{}^b$. This coupling is contained in the linearised Einstein equations [*cf.* a perturbation of (2.20)],

$$\delta G_a{}^b = 8\pi\, \delta T_a{}^b, \quad (5.2)$$

where $\delta G_a{}^b$ is the perturbed Einstein tensor. The derivation of the perturbed Einstein tensor is rather laborious and not particularly insightful, so we simply state the result (Kojima, 1992):

$$\begin{aligned}\delta G_a{}^b = h^{bc}\left(R_{ac} - \frac{1}{2}g_{ac}R\right) + \frac{1}{2}g^{bc}[&\nabla_d\nabla_a h_c{}^d + \nabla_d\nabla_c h_a{}^d - \nabla_d\nabla^d h_{ac} - \nabla_a\nabla_c h \\ &- h_{ac}R - g_{ac}(h^{de}R_{de} + \nabla_d\nabla^e h_e{}^d - \nabla_d\nabla^d h)],\end{aligned} \quad (5.3)$$

where $h \equiv h_a{}^a$ and the covariant derivatives are all associated with the background metric. Although we will not make use of them for this analysis, for the sake of completeness, we also have the linearised conservation equations from (2.21),

$$\delta(\nabla_b T_a{}^b) = 0. \quad (5.4)$$

One should note that the Eulerian perturbation and the covariant derivative do not, in general, commute. In order to evaluate (5.4), one needs to obtain the variation of the connection coefficients, $\delta\Gamma^a{}_{bc}$.

As noted in Sec. 2.3, in relativity, we have the Lagrangian perturbations to the four-velocity (2.52),

$$\Delta u^a = \frac{1}{2}u^a u^b u^c \Delta g_{bc}, \quad (5.5)$$

and the baryon number density (2.54),

$$\Delta n = -\frac{1}{2}n\perp^{ab}\Delta g_{ab}, \quad (5.6)$$

where we have the Lagrangian variation of the metric $\Delta g_{ab} = h_{ab} + \nabla_a\xi_b + \nabla_b\xi_a$ and the

projection operator orthogonal to the flow $\perp_a{}^b = u_a u^b + \delta_a{}^b$. At this point, we need to define the static displacement vector (Penner *et al.*, 2011),

$$\xi^a = \begin{bmatrix} 0 \\ r^{-1}W \\ r^{-2}V\partial_\theta \\ (r\sin\theta)^{-2}V\partial_\phi \end{bmatrix} Y_{\ell m}, \tag{5.7}$$

with functions $W(r)$ and $V(r)$ describing the radial and tangential displacements, respectively.[1] We can obtain the Eulerian perturbation to the four-velocity from (2.41) and (5.5),

$$\delta u^a = \frac{1}{2}u^a u^b u^c h_{bc} + \perp_b{}^a \mathcal{L}_u \xi^b, \tag{5.8}$$

which has components

$$\delta u^t = \frac{1}{2}e^{-\nu/2}H_0 Y_{\ell m}, \qquad \delta u^i = 0. \tag{5.9}$$

Similar to the Newtonian case, for static perturbations, the displacement vector does not appear in the linearised four-velocity.

Equation (5.6) guarantees that the total number of baryons in the star is conserved. Computing Eq. (5.6) explicitly gives

$$\Delta n = -\frac{n}{r^2}\left[r^2\left(K + \frac{1}{2}H_2\right) - \ell(\ell+1)V + r\frac{dW}{dr} + \left(1 + \frac{1}{2}r\frac{d\lambda}{dr}\right)W\right]Y_{\ell m}. \tag{5.10}$$

We continue to focus on barotropic matter, $\varepsilon = \varepsilon(n)$, (see discussion in Sec. 2.1) which means that

$$\Delta\varepsilon = \frac{d\varepsilon}{dn}\Delta n = \mu\Delta n, \tag{5.11}$$

where μ is the chemical potential. Therefore, we can also write $p = p(\varepsilon)$, that leads to the relations

$$\Delta p = \frac{dp}{d\varepsilon}\Delta\varepsilon = c_{\rm s}^2\Delta\varepsilon, \qquad \delta p = c_{\rm s}^2\delta\varepsilon, \tag{5.12}$$

where we have identified the relativistic speed of sound $c_{\rm s}$. We will use (5.12) to connect δp and $\delta\varepsilon$. By the first law of thermodynamics (2.10) for a single-species fluid composed of baryons, the baryon chemical potential is given by

$$\mu = \frac{\varepsilon + p}{n}. \tag{5.13}$$

Hence, (5.10) and (5.11) combine to give

$$\Delta\varepsilon = -\frac{1}{r^2}(\varepsilon+p)\left[r^2\left(K + \frac{1}{2}H_2\right) - \ell(\ell+1)V + r\frac{dW}{dr} + \left(1 + \frac{1}{2}r\frac{d\lambda}{dr}\right)W\right]Y_{\ell m}. \tag{5.14}$$

[1] Note that this form of the displacement vector is slightly different to the definition used in the Newtonian case (4.54).

Therefore, by (5.12),

$$\Delta p = -\frac{1}{r^2}c_{\rm s}^2(\varepsilon+p)\left[r^2\left(K+\frac{1}{2}H_2\right)-\ell(\ell+1)V+r\frac{dW}{dr}+\left(1+\frac{1}{2}r\frac{d\lambda}{dr}\right)W\right]Y_{\ell m}. \quad (5.15)$$

We also have, from the relation between Lagrangian and Eulerian variations (2.41),

$$\Delta p = \delta p + \xi^r\frac{dp}{dr} = \delta p - \frac{1}{2r}(\varepsilon+p)\frac{d\nu}{dr}WY_{\ell m}. \quad (5.16)$$

We will use Eqs. (5.15) and (5.16) to close our system of equations for the crustal perturbations. Indeed, Eqs. (5.15) and (5.16) hold throughout also in the fluid, but, because we are unable to determine the displacement in the fluid, we currently have no use for these expressions.

The matter content of the spacetime is encoded in the stress-energy tensor. To complete the specification of the linearised field equations, we use the stress-energy tensor for a perfect fluid (2.22) to obtain

$$\delta T_a{}^b = (\delta\varepsilon+\delta p)u_a u^b + \delta p\,\delta_a{}^b + (\varepsilon+p)(\delta u_a u^b + u_a\delta u^b). \quad (5.17)$$

Recall that, as we did in Chap. 4, we expand the perturbed quantities as shown in (2.77) and specialise to a particular (ℓ,m) mode. In this calculation, we have $(\ell,m)=(2,2)$.

One obtains the following second-order ordinary differential equation that governs the fluid perturbations by inserting Eqs. (5.17) and (5.3) into (5.2):

$$\begin{aligned}\frac{d^2H_0}{dr^2}+\left[\frac{2}{r}+\frac{1}{2}\left(\frac{d\nu}{dr}-\frac{d\lambda}{dr}\right)\right]\frac{dH_0}{dr}+\left\{\frac{2}{r^2}-[2+\ell(\ell+1)]\frac{e^\lambda}{r^2}\right.\\ \left.+\frac{2}{r}\left(2\frac{d\nu}{dr}+\frac{d\lambda}{dr}\right)-\left(\frac{d\nu}{dr}\right)^2\right\}H_0 = -8\pi e^\lambda(\delta\varepsilon+\delta p)\end{aligned} \quad (5.18a)$$

and

$$\delta p = \frac{e^{-\lambda}}{16\pi r}\left(\frac{d\nu}{dr}+\frac{d\lambda}{dr}\right)H_0. \quad (5.18b)$$

For completeness, the other metric quantities are given by

$$H_1 = 0, \quad (5.18c)$$

$$H_2 = H_0 \quad (5.18d)$$

and

$$[\ell(\ell+1)-2]e^\lambda K = r^2\frac{d\nu}{dr}\frac{dH_0}{dr}+\left[\ell(\ell+1)e^\lambda-2-r\left(\frac{d\nu}{dr}+\frac{d\lambda}{dr}\right)+r^2\left(\frac{d\nu}{dr}\right)^2\right]H_0. \quad (5.18e)$$

Equations (5.18) are the relativistic analogue to the Newtonian fluid perturbation equations (4.45). Indeed, by combining Eqs. (5.18a) and (5.18b), one has a second-order differential equation for H_0, that is analogous to Eqs. (4.45). We should note that the perturbation equations in this form do not necessarily include the force that sources the deformation – unless the force satisfies the relativistic analogue to the perturbed Laplace's equation, $\delta G_a{}^b = 0$. In this situation, which is effectively the tidal problem (see Chap. 6), the perturbed metric function H_0 contains both the gravitational and tidal potentials. However, in some sense, we can absorb the deforming force into a potential in H_0, like we did with U in the Newtonian case [see (4.44) and supporting text]. When we consider examples, we will demonstrate how one may explicitly include the force.

As remarked above, given the static nature of the problem, one is unable to calculate the displacement vector in the fluid, since the functions W and V do not appear in the perturbed stress-energy tensor.

As in the Newtonian problem, there are two boundary conditions that the perturbed metric potential must satisfy. At the origin, the solution must be regular,

$$H_0(0) = 0. \tag{5.19}$$

The surface boundary condition is a little more involved. As we show in Appendix D, the function H_0 must be continuous across all boundaries. In the vacuum exterior, $r \geq R$, one should note that $\nu = -\lambda$, therefore, Eqs. (5.18a) and (5.18b) reduce to

$$\frac{d^2H_0}{dr^2} + \left(\frac{2}{r} - \frac{d\lambda}{dr}\right)\frac{dH_0}{dr} - \left[\ell(\ell+1)\frac{e^\lambda}{r} + \left(\frac{d\lambda}{dr}\right)^2\right]H_0 = 0. \tag{5.20}$$

This is the relativistic analogue to Laplace's equation for polar perturbations. By a simple change of variables to $x = r/M - 1$, one can transform (5.20) to

$$\frac{d}{dx}\left[(1-x^2)\frac{dH_0}{dx}\right] + \left[\ell(\ell+1) - \frac{4}{1-x^2}\right]H_0. \tag{5.21}$$

Equation (5.21) is written in the form of the associated Legendre equation and has the general solution in terms of the associated Legendre polynomials $\mathcal{Q}_{\alpha\beta}(x)$ and $\mathcal{P}_{\alpha\beta}(x)$ with $\alpha = \ell$ and $\beta = 2$,[2]

$$H_0(r) = c_1\mathcal{Q}_{\ell 2}(r/M-1) + c_2\mathcal{P}_{\ell 2}(r/M-1), \tag{5.22}$$

where c_1 and c_2 are constants that determine the amplitude of the perturbations. When

[2]Usually Legendre polynomials are defined on the unit complex disc. We work with $x = r/M - 1 > 1$ and so we must change the sign in the argument of the logarithmic terms in $\mathcal{Q}_{\ell 2}(x)$, or, equivalently, take their real part.

we specialise to quadrupolar ($\ell = 2$) perturbations, the general solution becomes

$$H_0(r) = c_1 \left(\frac{r}{M}\right)^2 \left(1 - \frac{2M}{r}\right) \left[- \frac{M(M-r)(2M^2+6Mr-3r^2)}{r^2(2M-r)^2} + \frac{3}{2} \ln\left(\frac{r}{r-2M}\right) \right] + 3c_2 \left(\frac{r}{M}\right)^2 \left(1 - \frac{2M}{r}\right). \tag{5.23}$$

From (5.23), we observe two solutions to the relativistic Laplace's equation: a decreasing solution with c_1, that is associated with the gravitational potential of the star, and an increasing solution with c_2, that may be associated with an external tidal potential (should that be the physical source of the perturbations). For applications other than tidal deformations, one can assume $c_2 = 0$ and we have the boundary condition at the surface

$$-\frac{1}{2}(R-2M)\frac{dH_0}{dr}(R) = \left\{ -1 + \frac{M}{R} - 8M^5 \left[2MR(M-R)(2M^2+6MR-3R^2) + 3R^3(R-2M)^2 \ln\left(\frac{R-2M}{R}\right) \right]^{-1} \right\} H_0(R), \tag{5.24}$$

which is the relativistic analogue (for $\ell = 2$ perturbations) of the Newtonian boundary condition (4.46b). Thus, Eqs. (5.19) and (5.24) are the boundary conditions on the perturbed metric potential H_0.

Using regularity (5.19), we find, for small r,

$$H_0(r) = a_0 r^\ell [1 + \mathcal{O}(r^2)], \tag{5.25}$$

where a_0 is a constant. With the intuition we developed from the Newtonian problem in Sec. 4.3.1, we note that this initial condition enables one to solve the coupled ordinary differential equations (5.18) with no freedom to impose (5.24). Hence, one needs a perturbing force in order to construct non-spherical equilibria. Indeed, suppose one considers the case where the star is perturbed by a presence of a companion that exerts a tidal force on it. In this situation, H_0 includes the tidal potential and the gravitational potential part of H_0 automatically satisfies (5.24).

5.1.2 The elastic crust

For an elastic material with shear modulus $\check{\mu}$, the Lagrangian perturbation to the anisotropic stress tensor is (Andersson *et al.*, 2019)[3]

$$\Delta\pi_{ab} = -2\check{\mu}\Delta s_{ab}, \tag{5.26}$$

[3]Note that we use the opposite sign for our definition here to that used in Eq. (4.53).

where the perturbed strain tensor Δs_{ab} is given by

$$2\Delta s_{ab} = \left(\perp^{c}{}_{a}\perp^{d}{}_{b} - \frac{1}{3}\perp_{ab}\perp^{cd}\right)\Delta g_{cd}. \tag{5.27}$$

The anisotropic stress tensor is symmetric and trace-free. Because star C (Fig. 4.2) is relaxed in a spherical shape, we find

$$\delta\pi_{a}{}^{b} = -\check{\mu}\left(\perp^{c}{}_{a}\perp^{db} - \frac{1}{3}\perp_{a}{}^{b}\perp^{cd}\right)\Delta g_{cd}. \tag{5.28}$$

Summing the elastic stress tensor (5.28) and the fluid stress-energy tensor (5.17) and inserting these expressions into the linearised field equations (5.2) provides the information needed to solve the perturbations in the elastic crust.

For the application of the boundary conditions, it is convenient to define the following variables that are related to the traction components:[4]

$$T_1 Y_{\ell m} \equiv r^2\delta\pi_{r}{}^{r} = \frac{2\check{\mu}}{3}\left[r^2(K-H_2) - \ell(\ell+1)V - 2r\frac{dW}{dr} + \left(4 - r\frac{d\lambda}{dr}\right)W\right]Y_{\ell m} \tag{5.29a}$$

and

$$T_2\partial_\theta Y_{\ell m} \equiv r^3\delta\pi_{r}{}^{\theta} = -\check{\mu}\left(r\frac{dV}{dr} - 2V + e^{\lambda}W\right)\partial_\theta Y_{\ell m}. \tag{5.29b}$$

Due to the introduction of the elastic crust, the perturbation equations become more complicated when compared to the fluid case. However, some of the perturbed Einstein equations remain unchanged. Since $\delta\pi_{t}{}^{b} = 0$, the $[tt]$ component provides

$$\begin{aligned} e^{-\lambda}r^2\frac{d^2K}{dr^2} + e^{-\lambda}\left(3 - \frac{r}{2}\frac{d\lambda}{dr}\right)r\frac{dK}{dr} - \left[\frac{1}{2}\ell(\ell+1) - 1\right]K \\ -e^{-\lambda}r\frac{dH_2}{dr} - \left[\frac{1}{2}\ell(\ell+1) + e^{-\lambda}\left(1 - r\frac{d\lambda}{dr}\right)\right]H_2 = -8\pi r^2\delta\varepsilon. \end{aligned} \tag{5.30a}$$

Because $\delta\pi_{a}{}^{b}$ is traceless, we can take the trace of the perturbed Einstein equations to obtain another equation that has no explicit dependence on the elasticity. We combine the trace with (5.30a) to obtain

$$\begin{aligned} -r^2\frac{d^2H_0}{dr^2} + \left[r\left(\frac{1}{2}\frac{d\lambda}{dr} - \frac{d\nu}{dr}\right) - 2\right]r\frac{dH_0}{dr} + \ell(\ell+1)e^{\lambda}H_0 - \frac{1}{2}r^2\frac{d\nu}{dr}\frac{dH_2}{dr} \\ + \left[2(e^{\lambda}-1) - r\left(3\frac{d\nu}{dr} + \frac{d\lambda}{dr}\right)\right]H_2 + r^2\frac{d\nu}{dr}\frac{dK}{dr} = 8\pi e^{\lambda}r^2(\delta\varepsilon + 3\delta p). \end{aligned} \tag{5.30b}$$

[4] Note that here T_1 and T_2 are dimensionless, whereas, in the Newtonian calculation, their analogues have dimensions of stress (4.56).

Furthermore, we find from the $[tr]$ component that, as in the fluid case,

$$H_1 = 0. \tag{5.30c}$$

Now, we consider the non-zero components of $\delta\pi_a{}^b$ to include elasticity into the system. The difference between the $[\theta\theta]$ and $[\phi\phi]$ components leads to the algebraic relation

$$H_2 - H_0 = 32\pi\check{\mu}V, \tag{5.30d}$$

which will be useful to eliminate H_2 from our equations. This expression shows how the equality (5.18d) from the fluid perturbations is spoiled with the introduction of elasticity. We can use the $[r\theta]$ component and (5.30d) to provide

$$\frac{dK}{dr} = \frac{dH_0}{dr} + \frac{d\nu}{dr}H_0 + \frac{16\pi}{r}\left(2 + r\frac{d\nu}{dr}\right)\check{\mu}V - \frac{16\pi}{r}T_2. \tag{5.30e}$$

The sum of the $[\theta\theta]$ and $[\phi\phi]$ components gives

$$\begin{aligned}\delta p = \frac{e^{-\lambda}}{16\pi r}\left(\frac{d\nu}{dr} + \frac{d\lambda}{dr}\right)H_0 + \frac{e^{-\lambda}}{r^2}\Bigg\{&e^{\lambda}[2 - \ell(\ell+1)]\check{\mu}V \\ &+\frac{e^{\lambda}}{2}T_1 - r\frac{dT_2}{dr} - \left[\frac{1}{2}r\left(\frac{d\nu}{dr} - \frac{d\lambda}{dr}\right) + 1\right]T_2\Bigg\},\end{aligned} \tag{5.30f}$$

where we have simplified using (5.30d) and (5.30e). The final equation we will use from the perturbed Einstein equations is the $[rr]$ component combined with Eqs. (5.30d)–(5.30f),

$$\begin{aligned}[\ell(\ell+1) - 2]e^{\lambda}K = r^2\frac{d\nu}{dr}\frac{dH_0}{dr} + \Bigg[&\ell(\ell+1)e^{\lambda} - 2 - r\left(\frac{d\nu}{dr} + \frac{d\lambda}{dr}\right) \\ &+r^2\left(\frac{d\nu}{dr}\right)^2\Bigg]H_0 + 16\pi\left\{[\ell(\ell+1) - 2]e^{\lambda} + r^2\left(\frac{d\nu}{dr}\right)^2\right\}\check{\mu}V \\ &-24\pi e^{\lambda}T_1 + 16\pi r\frac{dT_2}{dr} - 8\pi\left[2 + r\left(\frac{d\nu}{dr} + \frac{d\lambda}{dr}\right)\right]T_2.\end{aligned} \tag{5.30g}$$

When $\check{\mu} = 0$, this reduces to (5.18e), as expected.

The next step is to formulate the system of equations in a way that is straightforward to integrate numerically. Clearly, there is a lot of freedom in how one can do this. We choose to work with the functions $(dH_0/dr, H_0, K, W, V, T_2)$ as our integration variables. It is useful to observe that through (5.30d) one can reduce the order of the system to eliminate H_2. In contrast to the fluid case, we are able to solve for the components of the displacement vector by using the definitions of the traction variables (5.29). To be precise,

we can integrate

$$\frac{dW}{dr} - \left(\frac{2}{r} - \frac{1}{2}\frac{d\lambda}{dr}\right) W = \frac{1}{2} r(K - H_0) - \left[16\pi r\check{\mu} + \frac{\ell(\ell+1)}{2r}\right] V - \frac{3}{4r\check{\mu}} T_1 \tag{5.31a}$$

and

$$\frac{dV}{dr} - \frac{2}{r} V = -\frac{e^\lambda}{r} W - \frac{1}{r\check{\mu}} T_2. \tag{5.31b}$$

We obtain an algebraic relation by combining (5.30f) and (5.30g) in such a way as to remove dT_2/dr. This gives us an equation that involves δp and T_1,

$$\begin{aligned} 16\pi r^2 e^\lambda \delta p = r^2 \frac{d\nu}{dr}\frac{dH_0}{dr} + \left[\ell(\ell+1)e^\lambda - 2 + r^2\left(\frac{d\nu}{dr}\right)^2\right] H_0 + [2 - \ell(\ell+1)]e^\lambda K \\ + 16\pi r^2 \left(\frac{d\nu}{dr}\right)^2 \check{\mu} V - 16\pi e^\lambda T_1 - 16\pi\left(2 + r\frac{d\nu}{dr}\right) T_2. \end{aligned} \tag{5.31c}$$

From (5.30f), we can obtain an equation to integrate for T_2,

$$\begin{aligned} \frac{dT_2}{dr} + \left[\frac{1}{2}\left(\frac{d\nu}{dr} - \frac{d\lambda}{dr}\right) + \frac{1}{r}\right] T_2 = -e^\lambda r\delta p + \frac{1}{16\pi}\left(\frac{d\nu}{dr} + \frac{d\lambda}{dr}\right) H_0 \\ + \frac{e^\lambda}{r}[2 - \ell(\ell+1)]\check{\mu} V + \frac{e^\lambda}{2r} T_1. \end{aligned} \tag{5.31d}$$

It is easy to see that (5.31d), when $\check{\mu} = 0$, reduces to give (5.18b). We combine Eqs. (5.30b)–(5.30e) to get

$$\begin{aligned} \frac{d^2 H_0}{dr^2} + \left[\frac{2}{r} + \frac{1}{2}\left(\frac{d\nu}{dr} - \frac{d\lambda}{dr}\right)\right]\frac{dH_0}{dr} + \left\{\frac{2}{r^2} - [2 + \ell(\ell+1)]\frac{e^\lambda}{r^2}\right. \\ \left. + \frac{1}{r}\left(3\frac{d\nu}{dr} + \frac{d\lambda}{dr}\right) - \left(\frac{d\nu}{dr}\right)^2\right\} H_0 = -8\pi\left\{e^\lambda(3\delta p + \delta\varepsilon) + 2\frac{d\nu}{dr}\frac{d(\check{\mu}V)}{dr}\right. \\ \left. + 8\left[\frac{1 - e^\lambda}{r^2} + \frac{1}{2r}\left(2\frac{d\nu}{dr} + \frac{d\lambda}{dr}\right) - \frac{1}{4}\left(\frac{d\nu}{dr}\right)^2\right]\check{\mu} V + \frac{2}{r}\frac{d\nu}{dr} T_2\right\}. \end{aligned} \tag{5.31e}$$

In the fluid, where the shear modulus vanishes, one can verify that (5.31e) reduce to give (5.18a). The final equation we need from the perturbed Einstein equations (5.30e), usefully, needs no further alteration,

$$\frac{dK}{dr} = \frac{dH_0}{dr} + \frac{d\nu}{dr} H_0 + \frac{16\pi}{r}\left(2 + r\frac{d\nu}{dr}\right)\check{\mu} V - \frac{16\pi}{r} T_2. \tag{5.31f}$$

To close this system of equations, we need to consider the thermodynamics. We can use the expressions we obtained from baryon-number conservation (5.15) and (5.16) to obtain a second algebraic relation involving δp and T_1 along with (5.31a),

$$\frac{3}{4\check{\mu}} T_1 = \frac{r^2}{(\rho + p)c_s^2}\delta p + \frac{3}{2} r^2 K - \frac{3}{2} l(l+1) V + \left(3 - \frac{r}{2c_s^2}\frac{d\nu}{dr}\right) W. \tag{5.31g}$$

We use (5.31c) and (5.31g) to determine δp and T_1. Equations (5.31) fully specify the elastic perturbation problem.

5.1.3 Interface conditions

In order to connect the fluid core and ocean to the elastic crust of star C, we must consider the interface conditions. By treating the crust as relaxed in a spherical configuration, we know that the background quantities will be continuous.[5] To determine how the perturbed quantities behave at an interface, we must calculate the first and second fundamental forms (also known as the intrinsic and extrinsic curvatures), which must be continuous throughout the spacetime. We describe this calculation in detail in Appendix D.

The first fundamental form implies that the functions H_0, K and W are continuous. From the second fundamental form, we find that the traction must be continuous: thus, $(T_1/r^2 + \delta p)$ and T_2 are continuous. We will continue to assume that the shear modulus is non-zero throughout the crust and, therefore, must be discontinuous at a fluid-elastic boundary. We can use continuity of the radial traction (D.17) along with (5.18e) to obtain an expression which is true in the elastic crust at an interface,

$$\begin{aligned} r^2 \frac{d\nu}{dr}\frac{dH_{0\mathrm{E}}}{dr} = &-\left[\ell(\ell+1)e^{\lambda} - 2 - r\left(\frac{d\nu}{dr}+\frac{d\lambda}{dr}\right) + r^2\left(\frac{d\nu}{dr}\right)^2\right] H_{0\mathrm{F}} \\ &+[\ell(\ell+1)-2]e^{\lambda}K_{\mathrm{F}} - 16\pi r^2\left(\frac{d\nu}{dr}\right)^2 \check{\mu} V_{\mathrm{E}}, \end{aligned} \tag{5.32}$$

where we re-introduce the subscripts F and E to denote fluid and elastic, respectively, to make explicit which side of the interface the perturbed quantities are on. From (D.17), we observe that, while the radial displacement must be continuous, this does not necessarily have to be the case for the tangential piece. From continuity of the tangential traction, we know that $T_2 = 0$ at the crustal boundaries.

In the core, we calculate $(dH_0/dr, H_0)$ using Eqs. (5.18) and, thus, obtain K via the algebraic equation (5.18e). In the crust, the order of the system increases, as we need to determine the additional functions W, V and T_2. The system that describes the crust is $(dH_0/dr, H_0, K, W, V, T_2)$ with Eqs. (5.31). With the six boundary conditions at the fluid-elastic interfaces – continuity of H_0 and K, $T_2 = 0$ and (5.32) – the system is well posed as a boundary-value problem.

[5] Of course, should one use an equation of state that involves discontinuities at such an interface, that would need to be taken into account. For a treatment that involves discontinuities in the equation of state see Pereira *et al.* (2020).

5.2 The deforming force

Now, we can turn our attention to considering some example forces in relativity. Because we can generate fully relativistic stellar models with this formalism, it is appropriate to consider a more realistic description of the nuclear matter. There are two quantities of the matter that we need to determine for our models: the fluid pressure-energy density relationship, $p(\varepsilon)$, and the shear modulus of the crust, $\check{\mu}$.

For the pressure-density relation, we first use the analytic BSk24 equation of state (Pearson *et al.*, 2018) for the high-density regions ($\varepsilon > 10^6\,\mathrm{g\,cm^{-3}}$) of the star and the Douchin and Haensel (2001) table for the low-density regions ($\varepsilon \leq 10^6\,\mathrm{g\,cm^{-3}}$). To prescribe the shear-modulus profile, we use the Ogata and Ichimaru (1990) result

$$\check{\mu} = 0.1994 \left(\frac{4\pi}{3}\right)^{1/3} \left(\frac{1 - X_\mathrm{n}}{A} n\right)^{4/3} (eZ)^2, \tag{5.33}$$

where X_n is the free-neutron fraction, A and Z are the atomic and proton numbers, respectively, n is the baryon-number density and e is the fundamental electric charge. We neglect any phase transitions in the crust, as they would significantly complicate the calculation. Should phase transitions exist at the boundaries of the crust, one would need to take into account the discontinuities in the background quantities. For the nuclear-matter parameters, we use the BSk24 results for the inner crust and the HFB-24 model (Goriely *et al.*, 2013) along with the experimental data from the 2016 Atomic Mass Evaluation (Wang *et al.*, 2017) for the outer crust (see Table 4 in Pearson *et al.*, 2018). The location of the core-crust transition is given by the BSk24 results and the crust-ocean transition is taken to be the lowest density in the outer-crust model. The complexity of this prescription is due to our attempt to use a consistent model for the neutron-star physics.

We consider three sources for the perturbations: (i) a deforming potential that is a solution to the relativistic Laplace's equation, (ii) a thermal pressure perturbation and (iii) a thermal pressure perturbation that only acts outside the core. Sources (i) and (ii) are the relativistic equivalents of two forces we considered in our Newtonian calculation (Chap. 4). As emphasised in the previous chapter, we note that the force in this problem will be related to the evolutionary history of the star. The examples we consider here have not been explicitly connected to any formation scenario. They should merely provide an illustration of how this calculation is carried out. To calculate the mountains for each example, we follow our scheme outlined in Section 4.2. The perturbations are normalised by ensuring star C reaches breaking strain at a point in its crust, according to the von Mises criterion (see the relativistic version below). In practice, this means we take the point in the crust where the strain is greatest and set that to breaking strain. The results for the different forces are summarised in Fig. 5.1.

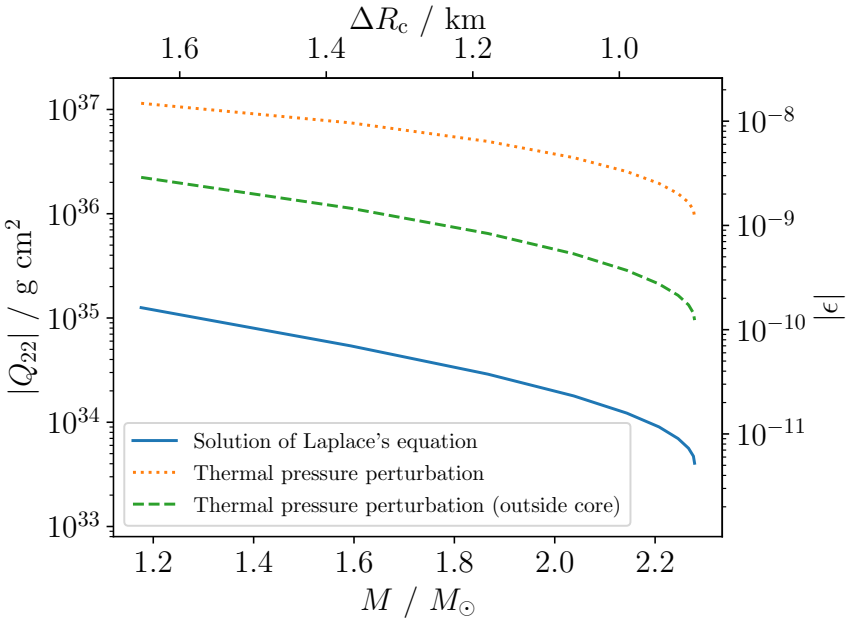

Figure 5.1: The maximum quadrupole and ellipticity due to the different forces as functions of stellar mass and crustal thickness, ΔR_c. We show results for the force corresponding to the solution of the relativistic Laplace's equation (solid blue line), the thermal pressure perturbation (dotted orange line) and the thermal pressure perturbation that acts outside the core (dashed green line).

We calculate the structure of the fluid core of stars A and C using Eqs. (5.18) with the boundary condition at the centre (5.19). For the crust of star C, we apply the interface conditions outlined in Sec. 5.1.3 to Eqs. (5.31). For the fluid ocean of both stars, we evaluate the fluid perturbation equations (5.18) up to the surface, where the gravitational potential part of H_0 must satisfy (5.24). The numerical scheme is explained in Appendix C.

5.2.1 A solution to the relativistic Laplace's equation

The relativistic Laplace's equation is given by the vacuum Einstein equations (5.20). By comparing (2.82) and (5.23), we identify

$$Q_{2m} = \frac{M^3 c_1}{\pi}, \tag{5.34}$$

in agreement with Eq. (41) in Johnson-McDaniel and Owen (2013). Thus, as in the Newtonian calculation, the quadrupole can be obtained by examining the exterior gravitational potential of the star. The challenge is to disentangle the other potentials acting on the star that will be contained in H_0.

From (5.23), we can calculate the constants c_1 and c_2 using H_0 and dH_0/dr at the surface:

$$c_1 = \frac{R(R-2M)}{8M^3}\left[R(2M-R)\frac{dH_0}{dr}(R) + 2(R-M)H_0(R)\right] \tag{5.35a}$$

and

$$\begin{aligned} c_2 = \frac{1}{48M^3R(2M-R)}\Bigg\{ &-2M\Big[R(4M^4+6M^3R-22M^2R^2+15MR^3-3R^4)\frac{dH_0}{dr}(R) \\ &+2(2M^4-2M^3R+13M^2R^2-12MR^3+3R^4)H_0(R)\Big] \\ &+3R^2(R-2M)^2\left[R(2M-R)\frac{dH_0}{dr}(R)+2(R-M)H_0(R)\right]\ln\left(\frac{R}{R-2M}\right)\Bigg\}. \end{aligned} \tag{5.35b}$$

At the surface, H_0 and its derivative are continuous, so we can use their values at this point to calculate the force amplitude (5.35b) and the quadrupole (5.34).

In the formalism of Andersson *et al.* (2019), the von Mises strain for a star with an unstrained background is

$$\Theta = \sqrt{\frac{3}{2}\Delta s_{ab}\Delta s^{ab}}. \tag{5.36}$$

The von Mises criterion states that a point in the crust fractures when the von Mises strain reaches the threshold, $\Theta \geq \Theta^{\text{break}}$, at some point. For $(\ell, m) = (2, 2)$ perturbations, we have the explicit expression

$$\begin{aligned} \Theta^2 = \frac{45}{512\pi}\Bigg\{ &\sin^2\theta\Bigg[3\sin^2\theta\cos^2 2\phi\left(\frac{T_1}{r^2\mu}\right)^2 \\ &+4e^{-\lambda}(3+\cos 2\theta-2\sin^2\theta\cos 4\phi)\left(\frac{T_2}{r^2\mu}\right)^2\Bigg] \\ &+(35+28\cos 2\theta+\cos 4\theta+8\sin^4\theta\cos 4\phi)\left(\frac{V}{r^2}\right)^2\Bigg\}. \end{aligned} \tag{5.37}$$

Following the results of molecular-dynamics simulations by Horowitz and Kadau (2009), we take the breaking strain to be $\Theta^{\text{break}} = 0.1$.

Therefore, we compute stars A and C using the fluid (5.18) and elastic perturbation equations (5.31) for $(\ell, m) = (2, 2)$ perturbations. At the surface, we obtain the amplitude of the force from (5.35b) and increase its amplitude until a point in the crust breaks according to (5.37). Then, once the two stars are normalised to the same force, we calculate the quadrupole moment with (5.34) and (5.35a).

Figure 5.1 shows the maximum deformations with such a force for varying stellar mass. In the equivalent Newtonian case, for a star with $M = 1.4\,M_\odot$, $R = 10\,\text{km}$, we found $Q_{22} =$

$1.7 \times 10^{37}\,\mathrm{g\,cm^2}$, $\epsilon = 2.2 \times 10^{-8}$. We see that the corresponding maximum deformation for a relativistic $M = 1.4\,M_\odot$ star is two orders of magnitude lower. This suppression has two contributions. In going from Newtonian to relativistic gravity, the maximum size of the quadrupole that a crust can support decreases. This suppression was observed by Johnson-McDaniel and Owen (2013) in their relativistic calculation and has also been seen in tidal- (Hinderer, 2008; Binnington and Poisson, 2009; Damour and Nagar, 2009; Hinderer *et al.*, 2010) and magnetic-deformation calculations (Ioka and Sasaki, 2004; Ciolfi *et al.*, 2010; Frieben and Rezzolla, 2012; Yoshida *et al.*, 2012). This behaviour has been attributed to the stiffness of the external, vacuum spacetime, that suppresses the quadrupole in the matching at the stellar surface (Johnson-McDaniel and Owen, 2013).

The second effect comes from the equation of state. Focusing on the role of the matter model in our calculations, we found that the point where the strain was the largest for all the forces we considered was the top of the crust. This is where the crust yields and this behaviour is consistent with previous calculations of neutron-star crusts (Gittins *et al.*, 2020, 2021). In Fig. 5.2, we compare the shear-modulus profile used in this work with the linear model used in the Newtonian calculation. Although the linear model appears to be a reasonable approximation to the more realistic model, there are key areas where the two differ. Of particular importance to the maximum-mountain calculation, the realistic shear-modulus profile is significantly weaker in the lower-density outer crust (approximately an order of magnitude smaller at the top of the crust). This plays a pivotal role in determining the size of the mountains that the crust can support as the breaking strain scales with the shear modulus.

Our results are notably at least two to three orders of magnitude smaller than the mountains obtained by Johnson-McDaniel and Owen (2013). As was noted in Chap. 4, the fact that our scheme produces smaller mountains than calculated in previous work is not particularly surprising. Indeed, the very nature of the Ushomirsky *et al.* (2000) approach [that Johnson-McDaniel and Owen (2013) follow] is to ensure that the *entire* crust is at breaking strain, whereas in our scheme (in order to correctly satisfy the boundary conditions of the problem) breaking strain is reached at a point. Clearly, the size of the mountains depend on the force, so it is natural to explore other choices to see if we can obtain larger deformations. We will go on to consider a couple of other examples.

5.2.2 A thermal pressure perturbation

The next source for the perturbations we consider is a thermal pressure. For this case, we assume that the pressure has a thermal component of the form reminiscent of (4.69),

$$\delta p_{\mathrm{th}} = \frac{k_{\mathrm{B}}\varepsilon}{m_{\mathrm{b}}}\delta T. \tag{5.38}$$

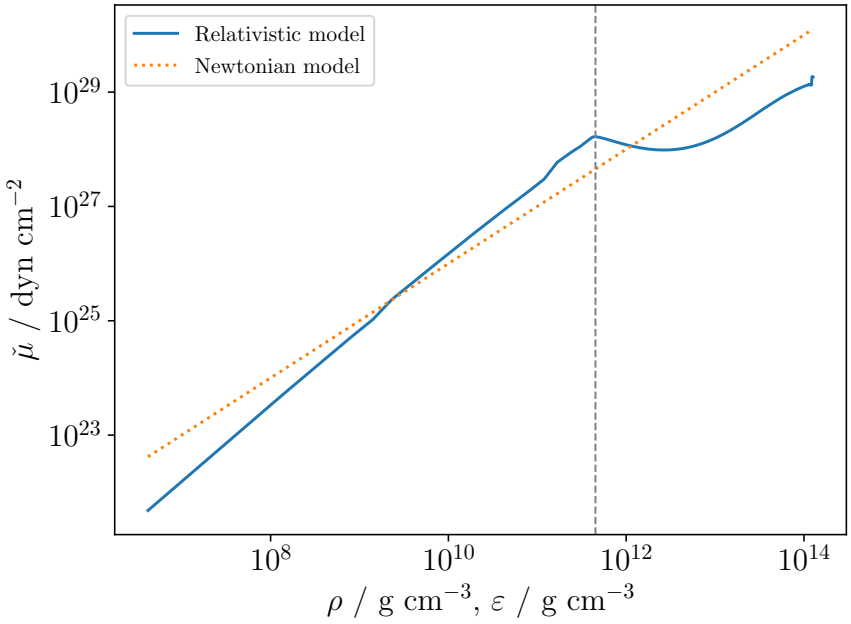

Figure 5.2: The shear modulus as a function of energy density, ε, for the model of the crust in this relativistic calculation (solid blue line) and as a function of mass density, ρ, for the linear model used in the Newtonian calculation (dotted orange line). We show the density of neutron drip, that corresponds to the inner-outer crust transition (dashed grey line).

We will assume the temperature is given by (4.71). To incorporate this force into the perturbation equations (5.18) and (5.31), they must be adjusted by $\delta p \to \delta p + \delta p_{\rm th}$. In this case, H_0 corresponds solely to the gravitational potential of the star.

For this example, the amplitude a_0 in (5.25) is connected to the magnitude of the temperature perturbation. It is constrained by ensuring the function H_0 matches the exterior solution (5.23) with $c_2 = 0$. At the surface, the solution must satisfy (5.24). The temperature perturbation, $\delta T(R)$, is then increased until a point in the crust breaks.[6]

The maximum mountains built using this force are shown in Fig. 5.1. Compared to the solution to the relativistic Laplace's equation, the thermal pressure perturbation produces mountains approximately two orders of magnitude larger. As we saw in the Newtonian calculation, this illustrates that the size of the mountains that can be built are highly dependent on their formation history.

For comparison, the corresponding force in our Newtonian calculation gave $Q_{22} = 4.0 \times 10^{38}\,\mathrm{g\,cm^2}$, $\epsilon = 5.2 \times 10^{-7}$. Hence, the suppression for the thermal pressure is weaker than

[6]For a canonical $M = 1.4\,M_\odot$ star, we found the crust breaks when $\delta T(R) = 9.4 \times 10^4\,\mathrm{K}$. As before, this temperature perturbation is simply a source term for the pressure perturbation (4.69) and not a specific physical mechanism.

in the previous example.

We also considered the situation where the top of the crust was moved to neutron drip in order to assess the impact of removing the weaker regions of the crust. In this case, for an $M = 1.4\,M_\odot$ star, we obtained $Q_{22} = 5.9 \times 10^{38}\,\mathrm{g\,cm^2}$, $\epsilon = 7.7 \times 10^{-7}$, which is even larger than what was obtained in the Newtonian calculation. This is not particularly surprising since we only focus on the inner crust, which is orders of magnitude stronger in the shear modulus than most of the outer crust (see Fig. 5.2). We also found that the crust no longer yielded at the top. This illustrates the role the shear modulus plays in supporting the mountains.

5.2.3 A thermal pressure perturbation outside the core

We also consider the case where the thermal pressure perturbation does not reach into the core. One could imagine a scenario where the surface of the neutron star is heated and this heating does not penetrate to the core. We will assume that the thermal pressure has a finite value at the base of the crust and exists in the crust and ocean. We use the same form for the temperature perturbation (4.71).

Due to the specific nature of this force, one must be careful in setting up the calculation. Since the core is unperturbed, we will assume $H_0(r_{\rm base}) = W(r_{\rm base}) = 0$. Because the force suddenly appears at the base, we assume that $dH_0(r_{\rm base})/dr$ is non-zero. For the fluid star (star A), this is sufficient to calculate the mountains. The precise value of dH_0/dr at the base is determined by ensuring the surface boundary condition (5.24) is satisfied.

For the star with a crust (star C), we need to pay attention to the traction conditions. Since dH_0/dr needed to have a finite value at the base of the crust in the fluid star, we effectively violated the radial traction condition (D.17). However, we can still use the tangential traction condition to demand $T_2(r_{\rm base}) = 0$. This leaves two free values, $K(r_{\rm base})$ and $V(r_{\rm base})$. At the top of the crust we still impose both traction conditions, which constrains $K(r_{\rm base})$ and $V(r_{\rm base})$ and, thus, the problem is well posed. As was the case for the fluid star, $dH_0(r_{\rm base})/dr$ is constrained via (5.24).

We plot the maximum mountains for this case in Fig. 5.1. As compared to the thermal pressure that acts throughout the star, the mountains produced in this example are approximately an order of magnitude smaller.

In summary, we have seen with all our examples in Fig. 5.1 that the maximum deformations the crust can sustain are small. Nevertheless, it is interesting to note that our results are, in principle, large enough not to contradict the minimum deformation argument of Woan *et al.* (2018) and the quadrupoles that can describe the accreting millisecond pulsar population (Chap. 3).

5.3 Dependence on the equation of state

As the calculation is done in full general relativity, we have the opportunity to assess the impact of the equation of state. We explore a subset of the chiral effective-field-theory models combined with a speed-of-sound parametrisation (see Tews *et al.*, 2018). [These models were recently used by Capano *et al.* (2020) to obtain constraints on neutron-star radii from observational data.] Chiral effective field theory is a systematic framework for low-energy hadronic interactions. For low densities, the theory describes matter using nucleons and pions, where the interactions are expanded in powers of momenta and all the relevant operators in strong interactions are included (Weinberg, 1990, 1991; van Kolck, 1994; Epelbaum *et al.*, 2009; Machleidt and Entem, 2011). One then uses quantum Monte Carlo methods to solve the many-body Schrödinger equation to obtain an equation of state (Hebeler and Schwenk, 2010; Krüger *et al.*, 2013; Carlson *et al.*, 2015; Tews *et al.*, 2018). Chiral effective field theory is expected to describe matter well up to between one to two times nuclear saturation density. Tews *et al.* (2018) extended the equations of state to higher densities, outside the low-energy regime of the chiral effective field theory, using a speed-of-sound parametrisation to ensure that causality was not violated.

We consider a selection of models for the pressure-density relation [supplemented by the Douchin and Haensel (2001) table for the low-density region ($\varepsilon \leq 10^6\,\mathrm{g\,cm^{-3}}$)] and subject the stars to thermal pressure perturbations (as described in Sec. 5.2.2). We choose this mechanism since it produced the largest mountains from the examples we considered. The results are shown in Fig. 5.3.

It should be noted that there are observational and theoretical constraints on the mass and radius of neutron stars. From observations, it is apparent that the true nuclear-matter equation of state must be able to support $2\,M_\odot$ neutron stars (Antoniadis *et al.*, 2013). Additionally, there are recent constraints on the radius from NICER: PSR J0030+0451, with mass $M = 1.34\,M_\odot$, was measured to have $11.52 \lesssim R\ /\ \mathrm{km} \lesssim 13.85$ (Riley *et al.*, 2019) and PSR J0740+6620, with mass $M = 2.08\,M_\odot$, was measured to have $11.41 \lesssim R\ /\ \mathrm{km} \lesssim 13.69$ (Riley *et al.*, 2021). There have been studies combining observations and theory to constrain the radius of a canonical $M = 1.4\,M_\odot$ neutron star. Raaijmakers *et al.* (2020) used the NICER observation of PSR J0030+0451 along with GW170817 to obtain a constraint of $11.75 \lesssim R\ /\ \mathrm{km} \lesssim 13.5$. However, there is some degree of statistical uncertainty associated with this range and such constraints will need to be updated with future detections. Indeed, the study of Capano *et al.* (2020), that combined nuclear theory with observations of GW170817, found the contrasting (and more stringent) range $10.4 \lesssim R\ /\ \mathrm{km} \lesssim 11.9$ for an $M = 1.4\,M_\odot$ neutron star. We indicate $M = 2\,M_\odot$ and the radius ranges from the NICER measurements to the right panel of Fig. 5.3. The majority of the equations of state that we consider support stars with $M = 2\,M_\odot$. To give some indication of the accepted range of equations of state in the mass-radius

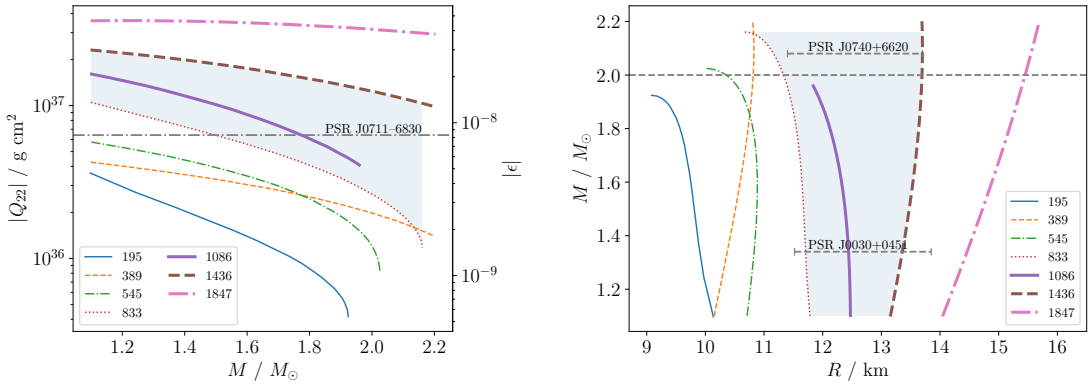

Figure 5.3: The maximum quadrupole and ellipticity due to thermal pressure perturbations as functions of stellar mass for different chiral effective-field-theory equation-of-state models (left panel) and the corresponding mass-radius diagram traced out by the background stellar models (right panel). To compare with observational constraints, we indicate $M = 2\,M_\odot$ (middle dashed grey line) and the range of radii $11.52 \leq R \;/\; \mathrm{km} \leq 13.85$ (bottom dashed grey line) and $11.41 \leq R \;/\; \mathrm{km} \leq 13.69$ (top dashed grey line) measured by NICER for PSR J0030+0451 and PSR J0740+6620, respectively, in the right panel. We shade the region between the two models 833 and 1436 that (roughly) satisfy the constraints to give an indication of the range of possible maximum deformations for this force. In the left panel, we indicate the upper limit on the ellipticity of PSR J0711–6830 from gravitational-wave searches, $\epsilon < 8.3 \times 10^{-9}$ (dash-dotted grey line). The equations of state are indexed according to their radii for an $M = 1.4\,M_\odot$ star. All stellar models considered are stable to radial perturbations.

diagram, we shade the region between models 833 and 1436, which (roughly) satisfy the observational constraints. In order to give context for some of the most constrained upper limits from gravitational-wave data, we show the deformation constraint for PSR J0711–6830 of $\epsilon < 8.3 \times 10^{-9}$ in the left panel (Abbott *et al.*, 2020b).

In the left panel of Fig. 5.3, we show the maximum deformations due to thermal pressure perturbations for the different equations of state. It is perhaps surprising to observe that there is a range of approximately two orders of magnitude across all the equations. Thus, these mountain calculations are quite sensitive to the equation of state. However, as indicated by the shaded region of Fig. 5.3, the range of maximum deformations is narrower when we consider recent observational constraints on the equation of state.

One can also see that there is a relationship between the radius, R, of a star with a given mass, M, and the maximum deformation it supports. This should not be surprising, since equations of state that produce stars with larger radii will also have thicker crusts that can support larger deformations.

5.4 Summary

There is hope on the horizon that we will soon detect gravitational waves from rotating neutron stars for the very first time. Indeed, there are continued efforts to improve the data-analysis techniques (see, *e.g.*, Dergachev and Papa, 2020; Beheshtipour and Papa, 2021; Dergachev and Papa, 2021; Steltner *et al.*, 2021; Zhang *et al.*, 2021), along with plans in development for third-generation gravitational-wave detectors to be constructed in the (hopefully) not-too-distant future (Maggiore *et al.*, 2020).

In Chap. 4, we surveyed previous maximum-mountain calculations and found that there were issues relating to boundary conditions that must be satisfied for realistic neutron stars. In particular, the usual approach to calculating maximum neutron-star mountains of Ushomirsky *et al.* (2000) assumes a strain field that violates continuity of the traction. We introduced a new scheme for calculating mountains that gives one full control of the boundary conditions at the cost of requiring a knowledge of the deforming force that sources the mountains. However, it is unclear what this force should be. In reality, the force is related to the formation history of the star, that may involve complex mechanisms like quakes and accretion from a companion. Therefore, in order to get a handle on the force, evolutionary calculations that consider the history of neutron stars will be necessary. It should be noted that such calculations would need to be ambitious in order to take into account the physics that may be important in the evolution of the crust, such as cooling, freezing, spin down, magnetic fields and cracking (to name but a few mechanisms).

In this study, we generalised our scheme from Chap. 4 to relativity. We considered three examples for the deforming force and found the most promising results for thermal pressure perturbations. In constructing relativistic stellar models with a realistic equation of state, we noted that the size of the mountains was suppressed (in some cases, quite significantly). This was generally due to two factors: (i) using relativistic gravity and (ii) the shear modulus of the crust was weaker at points than the simple model used in our Newtonian study. For most of the examples we examined, the crust yielded first at the top, where the shear modulus is the weakest. These results also point towards the necessity of evolutionary calculations in making progress on mountain calculations. This is evident from the role the deforming force plays in how large the mountains can be.

We have also demonstrated how the mountains are sensitive to the fluid pressure-density relationship for nuclear matter, suggesting a range of uncertainty larger than an order of magnitude for a range of equations of state that satisfy current observational constraints on the mass and radius. For this analysis we considered a subset of equations of state from chiral effective field theory, that all obey causality, and subjected the stars to thermal pressure perturbations.

We made an effort to build a consistent neutron-star model, based on the BSk24 equation of state (Pearson *et al.*, 2018). However, our treatment of the crust is still somewhat simplistic: we assume that the crust behaves like an elastic solid up to some breaking strain, at which it yields and all the strain is subsequently released. As discussed in Sec. 4.5, a possible solution to constructing larger mountains than the ones we have been able to obtain perhaps lies in plasticity. Plastic solids behave elastically up to some strain and, beyond that strain, deform in such a way that they retain some of the strain. It is perhaps likely that neutron-star crusts exhibits some of this behaviour. Suppose a neutron-star crust is modelled as an ideal plastic. It is then deformed up to its elastic yield limit at a point in the crust and the strain saturates. Even if the force is increased, the strain stays the same. One could then continue to apply forces to the crust in order to build as large a mountain as possible. This could connect real neutron stars to the maximally strained configuration imposed in Ushomirsky *et al.* (2000). At present, this is speculation, even though there have been some interesting discussions of plasticity in neutron-star crusts (Smoluchowski and Welch, 1970; Jones, 2003; Chugunov and Horowitz, 2010). This idea certainly seems worthy of future studies.

CHAPTER 6

Tidal deformations

We have discussed how one calculates mountains in a self-consistent manner in Chaps. 4 and 5. We have seen that, in order to obtain the mountains, one must specify the fiducial force that gives the star its non-spherical shape. At present, we do not have a good understanding of what such a force should be (at least not at a level that would be calculable) and, indeed, progress in this direction may have to rely on detailed evolutionary calculations of physical scenarios that lead to mountains. However, there are neutron-star gravitational-wave scenarios where we do know what the deforming mechanism will be: binary neutron stars experiencing tidal perturbations. In this chapter, we will study static tidal deformations of neutron stars with elastic crusts, following Gittins *et al.* (2020).

We set the scene in Sec. 6.1 by introducing the tidal Love numbers in general relativity and showing how they can be extracted from the metric. In Sec. 6.2, we apply the relativistic perturbation formalism outlined in Sec. 5.1 to compute the tidal deformations of a neutron star with an elastic crust using a realistic equation of state. In Sec. 6.3, we explore whether the crust will break during a binary inspiral. At the end of the chapter, we summarise in Sec. 6.4.

6.1 Definition of the tidal Love number

Neutron stars undergoing binary inspiral and merger are confirmed (and highly celebrated) gravitational-wave sources. In 2017, the LIGO and Virgo detectors observed a

gravitational-wave signal from a binary neutron star, GW170817 (Abbott *et al.*, 2017f). More recently, in 2019, another binary merger was detected, GW190425 (Abbott *et al.*, 2020a) and, in 2020, two neutron star-black hole binaries were observed (Abbott *et al.*, 2021c). Prior to these detections, it had long been considered the case that binary-neutron-star systems would be promising candidates for gravitational-wave emission (Cutler *et al.*, 1993; Cutler and Thorne, 2002).

One of the exciting prospects of gravitational-wave observations is that they can provide model-independent constraints on the equation of state and, indeed, have done in the case of GW170817 (Abbott *et al.*, 2017f; Bauswein *et al.*, 2017; Abbott *et al.*, 2018c; Annala *et al.*, 2018; De *et al.*, 2018; Most *et al.*, 2018; Raithel *et al.*, 2018; Abbott *et al.*, 2019d). The gravitational-wave signal emitted from inspiralling neutron stars differs slightly from that of inspiralling black holes. The very fact that neutron stars are extended bodies introduces finite-size corrections to the gravitational-wave signal.[1] The dominant finite-size effect comes from the tidal deformation that each star's gravitational field induces on the other. Since this effect depends on the density distribution of the star, it may be used as a diagnostic to probe the neutron-star interior. However, neutron stars are believed to have solid crusts close to their surfaces, which introduce further complexity into prospective descriptions of the interior (Chamel and Haensel, 2008). In recent years, there have been a few efforts in the direction of understanding the impact that the inclusion of an elastic crust makes on tidal deformations in neutron stars (Penner *et al.*, 2011; Biswas *et al.*, 2019), including our own work (Gittins *et al.*, 2020).

For tidal deformations, it is appropriate to work in the *adiabatic limit*, where the variations in the tidal field are assumed to be slow compared to the timescale associated with the star's internal response (Andersson and Pnigouras, 2019). Therefore, one uses static perturbations.

A star immersed in a time-independent, external, quadrupolar tidal field $\mathcal{E}_{ij}$ will develop a quadrupole moment Q_{ij} in response. In the Newtonian limit, Q_{ij} is given by [see (2.65)][2]

$$Q_{ij} = \int_V \delta\rho(x^i)\left(x_i x_j - \frac{1}{3}r^2 g_{ij}\right) dV. \tag{6.1}$$

To linear order, one can relate the quadrupole moment to the tidal field by (Hinderer, 2008)

$$Q_{ij} = -\frac{2}{3}\frac{R^5}{G}k_2\mathcal{E}_{ij}, \tag{6.2}$$

where we meet the $\ell = 2$ tidal Love number k_2 (see Sec. 4.3.1.1 for a brief introduction to

[1] It is important to accurately track the orbital dynamics of each neutron star during the inspiral in order to build up a large enough signal-to-noise ratio for a confident detection.

[2] It is assumed that the tidal field is weak and thus affects the mass-density distribution of the star in a perturbative way.

the tidal Love numbers in Newtonian gravity). Since much of this analysis will make use of the Newtonian limit, we will reinstate factors of G and c in relevant expressions. We briefly review the procedure of calculating the tidal Love number below. For other detailed discussions on the subject of tidal deformations in general relativity, see Hinderer (2008), Binnington and Poisson (2009), Damour and Nagar (2009) and Abdelsalhin (2019).

The Love number can be extracted from the exterior metric. We specialise the perturbing potential in (2.82) to the tidal field (see, *e.g.*, Binnington and Poisson, 2009),

$$-\frac{1+g_{tt}+h_{tt}}{2} = -\frac{M}{r} + \sum_{m=-\ell}^{\ell}\left[-\frac{4\pi}{2\ell+1}B_\ell(r)\frac{Q_{\ell m}}{r^{\ell+1}} + \frac{4\pi(\ell-2)!}{(2\ell+1)!!}A_\ell(r)r^\ell\mathcal{E}_{\ell m}\right]Y_{\ell m}(\theta,\phi), \tag{6.3}$$

where $A_\ell(r)$ is a function that goes to unity in the Newtonian limit (this is given as A_1 in Table I of Binnington and Poisson, 2009). Because we work with quadrupolar deformations, we have $\ell = 2$.

We are free to work with either the tensors Q_{ij} and $\mathcal{E}_{ij}$ or their spherical-harmonic counterparts Q_{2m} and $\mathcal{E}_{2m}$ (see Sec. 2.4.1). By comparing (2.70) and (2.75), we find[3]

$$Q^\ell_{ij\ldots q}\hat{x}^i\hat{x}^j\ldots\hat{x}^q = \frac{4\pi\ell!}{(2\ell+1)!!}\sum_{m=-\ell}^{\ell}Q_{\ell m}Y_{\ell m}, \tag{6.4}$$

where $\hat{x}^i = x^i/r$ is the unit position vector in the exterior of the star and $Q^\ell_{ij\ldots q}$ is the multipole moment tensor of order ℓ given by (2.68). For quadrupolar deformations,

$$Q_{ij}\hat{x}^i\hat{x}^j = \frac{8\pi}{15}\sum_{m=-2}^{2}Q_{2m}Y_{2m}. \tag{6.5a}$$

Thus, we also have

$$\mathcal{E}_{ij}\hat{x}^i\hat{x}^j = \frac{8\pi}{15}\sum_{m=-2}^{2}\mathcal{E}_{2m}Y_{2m}. \tag{6.5b}$$

Furthermore, one can verify that Q_{ij} vanishes for any perturbation with $\ell \neq 2$. Hence, by (6.2), we have

$$Q_{2m} = -\frac{2}{3}\frac{R^5}{G}k_2\mathcal{E}_{2m}. \tag{6.6}$$

We can, without any loss of generality, assume that only one $\mathcal{E}_{2m}$ is non-vanishing (Hinderer, 2008).

[3]One could also obtain this expression using the decomposition in Hinderer (2008) based on the formalism developed in Thorne (1980). However, one would need to take into account the different conventions for the multipole moments (see earlier footnote 13 in Chap. 2). Additionally, one could brute force this calculation by inserting pure mass-density perturbations of order ℓ into the quadrupole moment tensor (6.1) and contracting the free indices with $\hat{x}^i$.

One can identify the coefficients c_1 and c_2 with the quadrupole and the tidal field, respectively, by comparing the exterior solution to the vacuum field equations (5.23) to the form of the exterior metric (6.3):

$$c_1 = \pi \frac{c^4}{G^2 M^3} Q_{2m}, \tag{6.7a}$$

$$c_2 = -\frac{8\pi}{45} \frac{G^2 M^2}{c^6} \mathcal{E}_{2m}, \tag{6.7b}$$

and, thus, using (6.6), obtain

$$\frac{c_1}{c_2} = \frac{15}{4} \frac{k_2}{C^5}, \tag{6.8}$$

where $C \equiv GM/(c^2 R)$ is the star's compactness. Because H_0 and dH_0/dr are continuous between the interior and the vacuum at the surface, we can use (5.23) to determine the ratio c_1/c_2 in terms of the interior solutions at $r = R$. This gives the result (Hinderer, 2008)

$$\begin{aligned} k_2 = \frac{8C^5}{5}(1-2C)^2[2+2C(y-1)-y]\Big\{ & 2C[6-3y+3C(5y-8)] \\ & + 4C^3[13-11y+C(3y-2)+2C^2(1+y)] \\ & + 3(1-2C)^2[2-y+2C(y-1)]\ln(1-2C)\Big\}^{-1}, \end{aligned} \tag{6.9}$$

where we have introduced the parameter $y \equiv R[dH_0(R)/dr]/H_0(R)$. It is interesting to note that for the computation of the Love number the amplitude a_0 in the initial condition (5.25) may be chosen freely. The reason for this is intuitive. Since the tidal Love number is a measure of how deformable a star is in the presence of a quadrupolar field, it is independent of the exact details of the external field and, therefore, the calculation of this quantity is insensitive to the magnitude. We see this in (6.9) as the ratio y means that dependence on a_0 exactly cancels. For our analysis, we will focus on the dimensionless tidal deformability parameter,

$$\Lambda = \frac{2}{3} \frac{k_2}{C^5}, \tag{6.10}$$

to enable direct comparison with gravitational-wave constraints (see, *e.g.*, Abbott *et al.*, 2018c).

6.2 The impact of an elastic crust

We assume the background of the star to be relaxed. Thus, the elastic perturbation formalism we developed in Sec. 5.1.2 is valid. The star is partitioned into three regions: a fluid core, a solid crust and a fluid ocean.

To accurately prescribe the crust-ocean transition, we consider the melting point of the

crust. The Coulomb lattice melts when the thermal energy,

$$E_{\rm th} = k_{\rm B}T, \tag{6.11}$$

exceeds the interaction energy of the lattice,

$$E_{\rm Coul} = \frac{Z^2e^2}{a}, \tag{6.12}$$

where a is the mean spacing between nuclei, by a critical factor $1/\Gamma$,

$$E_{\rm th} \geq \frac{1}{\Gamma}E_{\rm Coul}, \tag{6.13}$$

where $\Gamma \approx 173$. We assume that the crust forms a body-centred cubic lattice, which effectively has two nuclei per unit cube, so given the number density of nuclei, $n_{\rm n}$, we have

$$n_{\rm n}a^3 = 2. \tag{6.14}$$

The mass density at which the crust begins to melt is, therefore, obtained from

$$\rho_{\rm top} = Am_{\rm b}n_{\rm n} = 2Am_{\rm b}\left(\frac{\Gamma k_{\rm B}T}{Z^2e^2}\right)^3 \approx 6.72\times10^5\ \left(\frac{A}{56}\right)\left(\frac{Z}{26}\right)^{-2/3}\left(\frac{T}{10^7\,{\rm K}}\right)^3\ {\rm g\,cm^{-3}}. \tag{6.15}$$

For our prescription, we assume that the outer parts of the crust are composed of iron, $Z = 26$ and $A = 56$, and a temperature of $T = 10^7\,{\rm K}$. We assume, towards the surface of the star, that $\varepsilon_{\rm top} \approx \rho_{\rm top}$.

We use the BSk19 analytic equation of state (Potekhin *et al.*, 2013) for the high-density parts ($\varepsilon > 5\times10^5\,{\rm g\,cm^{-3}}$) of the star and the equation-of-state table from Douchin and Haensel (2001) for the low-density regions ($\varepsilon \leq 5\times10^5\,{\rm g\,cm^{-3}}$). We parametrise each stellar model according to its central density and integrate Eqs. (2.33) for the background. The background is solved along with Eqs. (5.18) in the fluid regions of the star and Eqs. (5.31) in the crust. The results of the integrations are summarised in Table 6.1. The mass and radius of each stellar model is presented in Fig. 6.1 to show that they are all stable to radial perturbations.

For each stellar model, we compute the tidal deformability in the presence of an elastic crust, $\Lambda_{\rm crust}$, as well as when a crust is not present, $\Lambda_{\rm fluid}$, for comparison. We also calculate the thickness of the crust, $\Delta R_{\rm c}$. We show these quantities in Fig. 6.2 against the central density. In agreement with Penner *et al.* (2011), we find that the inclusion of an elastic crust has an almost negligible impact on the tidal deformability – the correction is the largest for the least compact stars at around two parts in 10^7. This is because, as the compactness decreases, the crust takes up a much larger fraction of the star. Moreover, as one would expect, the crust works to resist the star's deformation which is why the tidal

Table 6.1: Results of the numerical integrations of the perturbation equations using the BSk19 equation of state for the high-density regions (Potekhin *et al.*, 2013) and the equation of state from Douchin and Haensel (2001) for the low-density layers of the star. Each stellar model is determined by the central density ε_c. We provide the radius R, mass M, compactness C and crustal thickness ΔR_c for each star. The tidal deformability for the fluid stars, Λ_{fluid}, and those with elastic crusts, Λ_{crust}, are shown, along with the relative difference between them, where $\Delta\Lambda \equiv \Lambda_{\text{crust}} - \Lambda_{\text{fluid}}$. From the differences between the tidal deformabilities, we see that the correction due to the presence of a crust is very small.

ε_c / $10^{15}\,\mathrm{g\,cm^{-3}}$	R / km	M / $M_\odot$	C	Λ_{crust}	Λ_{fluid}	$\Delta\Lambda/\Lambda_{\text{fluid}}$	ΔR_c / km
2.500	10.309	2.162	0.310	3.954 523 688 61	3.954 523 756 13	-1.707×10^{-8}	0.278
2.203	10.548	2.146	0.301	5.473 047 436 30	5.473 047 538 79	-1.873×10^{-8}	0.307
1.941	10.787	2.112	0.289	8.015 526 753 84	8.015 526 923 67	-2.119×10^{-8}	0.343
1.710	11.019	2.056	0.276	12.498 815 797 78	12.498 816 109 13	-2.491×10^{-8}	0.391
1.507	11.234	1.974	0.260	20.878 484 560 88	20.878 485 200 87	-3.065×10^{-8}	0.451
1.327	11.423	1.864	0.241	37.579 285 484 91	37.579 286 978 64	-3.975×10^{-8}	0.529
1.170	11.576	1.725	0.220	73.256 419 235 36	73.256 423 237 91	-5.464×10^{-8}	0.629
1.031	11.686	1.560	0.197	155.283 837 413 39	155.283 849 832 42	-7.998×10^{-8}	0.758
0.908	11.748	1.375	0.173	358.777 734 157 82	358.777 779 026 99	-1.251×10^{-7}	0.926
0.800	11.768	1.178	0.148	903.803 599 914 09	903.803 789 190 34	-2.094×10^{-7}	1.144

deformabilities computed with a crust are smaller.

To facilitate direct comparison with Penner *et al.* (2011) we also integrated the perturbation equations with a polytropic equation of state and a shear modulus that scales linearly with the pressure. We used the same parameters as Penner *et al.* (2011) and moved the core-crust transition to $\varepsilon_{\text{base}} = 2 \times 10^{14}\,\mathrm{g\,cm^{-3}}$ and the crust-ocean transition to $\varepsilon_{\text{top}} = 10^{7}\,\mathrm{g\,cm^{-3}}$. The result is shown in Fig. 6.3. In our calculation, we find that the tidal deformability is approximately an order of magnitude less sensitive to the inclusion of an elastic crust than reported by Penner *et al.* (2011). This quantifies the effect of the error we corrected in (5.30g). (It is interesting to note that the crust has a more significant effect in this simple model as compared to the results from the realistic equation of state.)

Furthermore, we note that our results are in stark contrast with those of Biswas *et al.* (2019) who find that the crust can make corrections to the tidal deformability of the order of $\sim 1\%$. The reason for this disagreement is twofold. Firstly, Biswas *et al.* (2019) write down expressions for the components of the displacement vector in the fluid and, thus, supposedly compute them in the fluid. This enables them to treat the system of coupled ordinary differential equations as an initial-value problem for the entire star and they use the continuity of the traction in order to match the fluid and elastic regions. As we noted in Sec. 5.1.1, due to the static nature of the problem, extracting equations for the components of the displacement vector in the fluid is impossible. Additionally, by computing the perturbations as an initial-value problem means that one does not have the necessary freedom to enforce the traction conditions to be satisfied at the top of the crust, since the boundary conditions at the centre and the continuity conditions at the core-crust interface are sufficient to carry out the integrations. The second reason is due to the fact that Biswas *et al.* (2019) do not have an outer fluid ocean in their stellar model, but

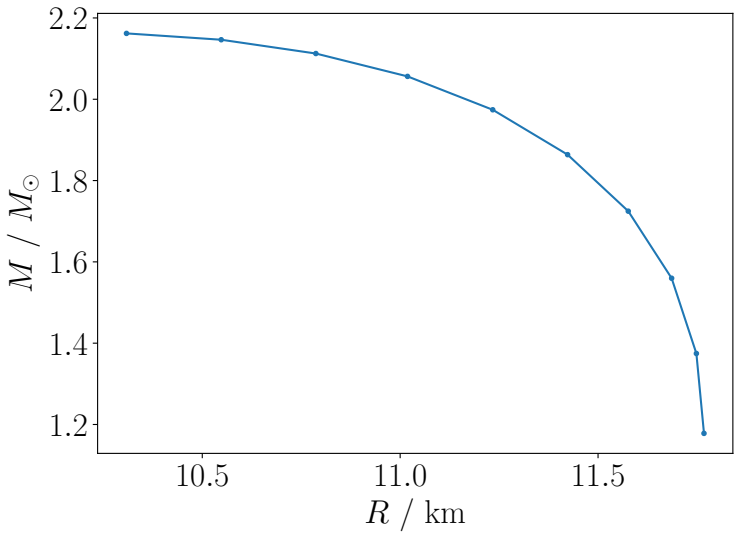

Figure 6.1: The mass-radius diagram for the central densities considered, showing that the stellar models considered are stable to radial perturbations.

instead have an exposed crust. In such a model, dH_0/dr is discontinuous [see (D.17)] and, therefore, one cannot use (6.9) as they do in order to compute the Love number. However, we note that the shear modulus at the top of the crust is expected to be small and so the discontinuity in dH_0/dr will be small. The difference in these results is important. If one assumes that third-generation gravitational-wave detectors will be able to constrain Λ to within a few percent (Maggiore *et al.*, 2020), then our results show that the effect of the crust will not be measurable, which is at odds with the results of Biswas *et al.* (2019).

6.3 Crustal failure during inspiral

The formalism described in Sec. 5.1 allows us to calculate the interior structure of a neutron star with an elastic crust that is experiencing static, polar perturbations. We can apply this formalism to determine when and where the crust will begin to fracture during a binary-neutron-star inspiral, as was done in Penner *et al.* (2012). In contrast to the computation of the tidal Love number, the amplitude of the perturbations is important for this calculation. Therefore, we must normalise our perturbations by matching the interior solution to the exterior at the surface and, thus, constrain the amplitude.

We consider a binary separated by distance d where the companion star is of mass $M_{\rm comp}$. We assume $d \gg r$, as is appropriate in the adiabatic regime, and work in the Newtonian limit for the normalisation. By Kepler's third law, the angular frequency of the binary $\Omega_{\rm orbit}$ is given by

$$\Omega_{\rm orbit}^2 = \frac{G(M + M_{\rm comp})}{d^3}. \tag{6.16}$$

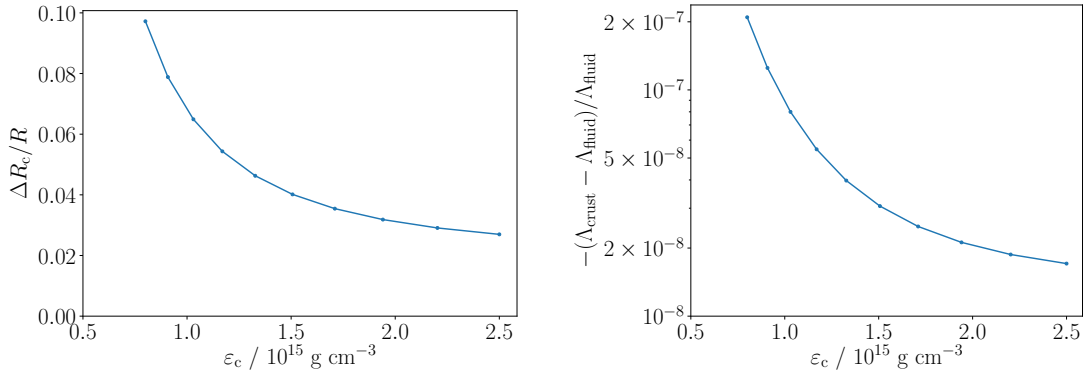

Figure 6.2: The ratio of crustal thickness to stellar radius (left panel) and the relative change in tidal deformability due to the presence of a crust (right panel) as functions of central density. As the central density approaches the core-crust transition (which occurs at $\varepsilon_{\rm base} = 1.3 \times 10^{14}\,{\rm g\,cm^{-3}}$) the crust occupies a much larger fraction of the star, so both quantities become more significant.

This is related to the orbital frequency of the binary, $f_{\rm orbit}$, by $\Omega_{\rm orbit} = 2\pi f_{\rm orbit}$. First, let us estimate the gravitational-wave frequency at merger for an equal-mass binary, $M = M_{\rm comp}$. We assume that the point of merger corresponds to when the two stars touch, $d = 2R$, and since gravitational waves radiate at twice the orbital frequency, $f_{\rm GW} = 2f_{\rm orbit}$, we find

$$f_{\rm GW}^{\rm merger} = \frac{1}{2\pi}\sqrt{\frac{GM}{R^3}} \approx 2170 \left(\frac{M}{1.4\,M_\odot}\right)^{1/2} \left(\frac{R}{10\,{\rm km}}\right)^{-3/2} {\rm Hz}. \tag{6.17}$$

Expanding around $r = 0$, one can show that the external field due to the presence of the companion is

$$\Phi_{\rm ext}(x^i) = -\frac{GM_{\rm comp}}{d} - \frac{GM_{\rm comp}}{d^2} r\hat{m}_i\hat{x}^i - \frac{3}{2}\frac{GM_{\rm comp}}{d^3} r^2 \left(\hat{m}_i\hat{m}_j - \frac{1}{3}g_{ij}\right)\hat{x}^i\hat{x}^j + \mathcal{O}(r^3), \tag{6.18}$$

where $\hat{m}^i$ is the unit vector that points from the centre of the star to the centre of the companion. The tidal piece can be expressed using the $(\ell, m) = (2, 0)$ spherical harmonic,

$$\Phi_{\rm tidal}(x^i) = -\sqrt{\frac{4\pi}{5}}\frac{GM_{\rm comp}}{d^3} r^2 Y_{20}. \tag{6.19}$$

This means that the binary is orientated such that $\theta = 0$ points in the direction of $\hat{m}^i$. The tidal multipole in the Newtonian limit is given by, using (6.18),

$$\mathcal{E}_{ij} = \frac{\partial^2\Phi_{\rm ext}}{\partial x^i \partial x^j} = -3\frac{GM_{\rm comp}}{d^3}\left(\hat{m}_i\hat{m}_j - \frac{1}{3}g_{ij}\right). \tag{6.20}$$

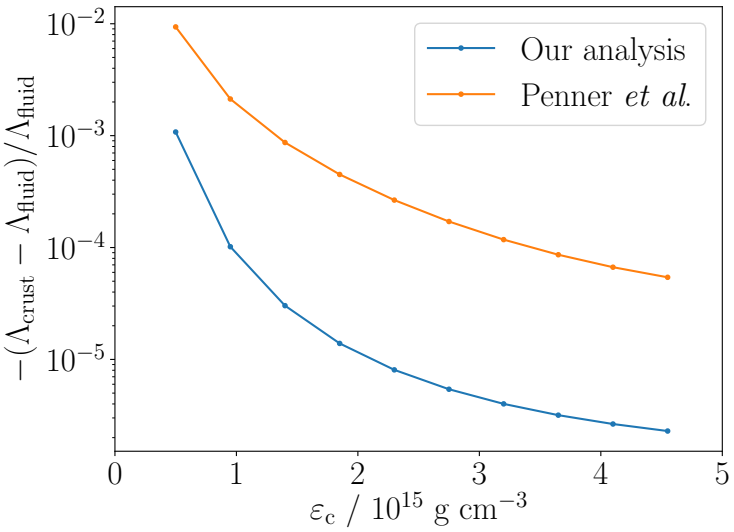

Figure 6.3: The relative change in the tidal deformability due to the presence of a crust against the central density for a polytropic equation of state with a linear shear modulus. We compare our results (blue) with those of Penner *et al.* (2011) (orange).

Using the decomposition of (6.5) one can show that the non-vanishing $\mathcal{E}_{2m}$ is

$$\mathcal{E}_{20} = -\frac{3}{2}\sqrt{\frac{5}{\pi}}\frac{GM_{\rm comp}}{d^3}, \tag{6.21}$$

and, therefore, by (6.7b) we find

$$c_2 = \frac{4}{3}\sqrt{\frac{\pi}{5}}\frac{G^3M^2M_{\rm comp}}{c^6d^3} = \frac{4\pi^2}{3}\sqrt{\frac{\pi}{5}}\frac{G^2M^2M_{\rm comp}}{c^6(M+M_{\rm comp})}f_{\rm GW}^2. \tag{6.22}$$

Here we have chosen to parametrise the point in the inspiral by the gravitational-wave frequency over the separation by using (6.16). Equations (6.8) and (6.22) provide the necessary information to normalise the perturbations to a binary that is emitting gravitational waves with frequency $f_{\rm GW}$.

We use the von Mises criterion to determine when the crust begins to break. We obtain the von Mises strain, where the unperturbed configuration is unstrained, through (5.36). The crust fractures when the von Mises strain reaches the threshold yield point. Using the definition of the traction variables (5.29) with (5.27) and specialising to $(\ell, m) = (2, 0)$ perturbations, one finds

$$\Theta^2 = \frac{45}{256\pi}\frac{1}{r^4}\left[(3\cos^2\theta - 1)^2\left(\frac{T_1}{\breve{\mu}}\right)^2 + 12e^{-\lambda}\sin^2(2\theta)\left(\frac{T_2}{\breve{\mu}}\right)^2 + 48\sin^4\theta V^2\right]. \tag{6.23}$$

The advantage of using the von Mises strain is that it is a function of position, and so

we can identify where the crust is the weakest as well as when it breaks. Taking the breaking strain to be $\Theta^{\rm break} = 0.1$ (Horowitz and Kadau, 2009), we can calculate when the crust will break, at each point, by imposing that the strain in (6.23) is equal to $\Theta^{\rm break}$ to normalise the perturbations and then determining the gravitational-wave frequency $f_{\rm GW}^{\rm break}$ which corresponds to that amplitude using (6.8) and (6.22).

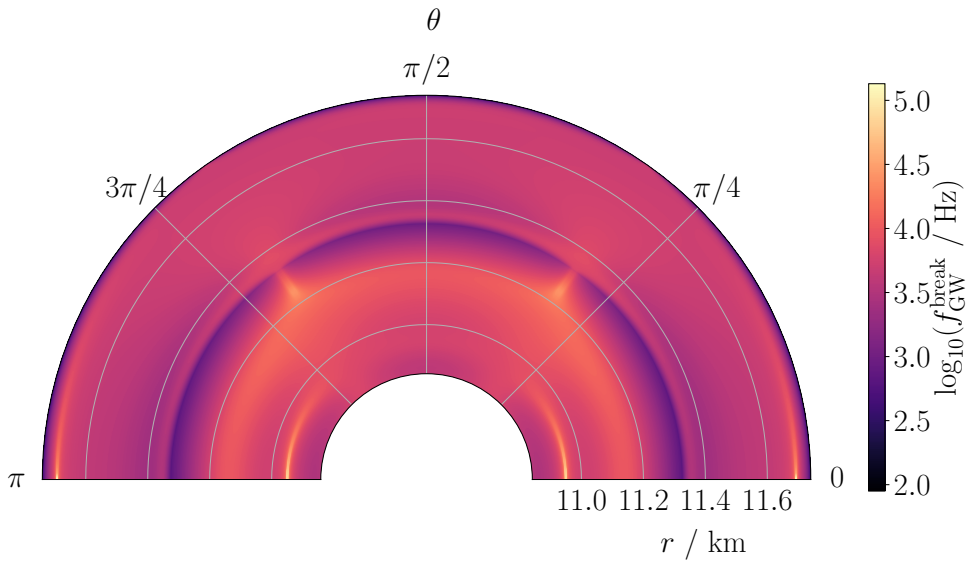

Figure 6.4: The gravitational-wave frequency at failure across the elastic crust. We can see that the majority of the crust will not fail before merger.

As an illustration, we use the same equation of state as in Sec. 6.2. We assume the binary is equal mass with $M = M_{\rm comp} = 1.4\,M_\odot$, for which we obtain a star with radius $R = 11.74\,$km. In Fig. 6.4 we show the gravitational-wave frequency when the crust breaks at each point. Figure 6.5 focuses on the regions of the star that break before merger. There is a clear phase transition at neutron drip (around $r = 11.3\,$km), where the inner crust is, on average, stronger than the outer crust. The crust is notably strong at neutron drip close to $\theta \approx \pi/4$ and $3\pi/4$. The reason for this is, as the star becomes more oblate, the parts closest to the poles and equator are stretched the most. The region that stretches the least is in between these two regions at $\theta \approx \pi/4$ and $3\pi/4$. This effect can be seen in Figs. 6.6 and 6.7 where the tangential functions $T_2/\breve{\mu}$ and V combine to give a local minimum in the von Mises strain at these angles and, thus, a local maximum in the breaking frequency. The maxima along the equator, $\theta = 0$ and π, are where the magnitude of the radial traction function $T_1/\breve{\mu}$ reaches a local minimum (as shown in Fig. 6.7).

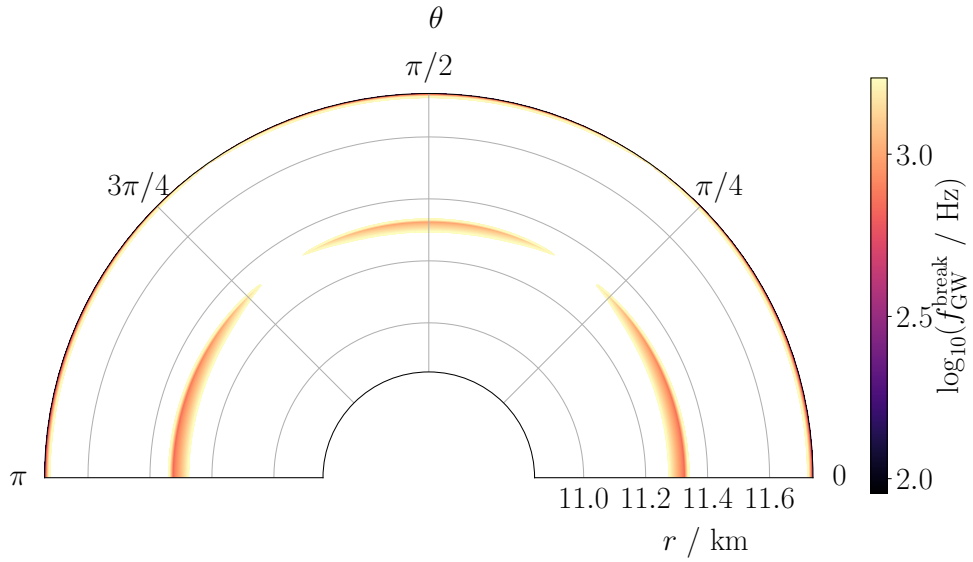

Figure 6.5: The gravitational-wave frequency at failure for the locations in the elastic crust that yield before merger. This shows that the stars will merge with the crust largely intact.

We note that, as compared to typical merger frequencies (6.17), our results suggest that the vast majority of the crust will not fracture before merger. In fact, the crust will only fail at neutron drip and in the very outermost part of the crust before coalescence. This is in contrast to the results of Penner *et al.* (2012), who obtain significantly lower breaking frequencies throughout the crust. This is likely related to the errors in the analysis of Penner *et al.* (2011) that we have pointed out above. Since the crust will be mostly intact by the point of merger, there is unlikely to be a significant amount of strain energy released available for an associated electromagnetic signal. However, it has been suggested that the resonant excitation of oscillation modes may lead to electromagnetic flares, although this is a different mechanism (Tsang *et al.*, 2012).

6.4 Summary

With the advent of gravitational-wave detections of binary-neutron-star mergers, we have a promising new method of constraining the equation of state of nuclear matter. The gravitational waveforms from these events are sensitive to tidal effects in the binaries which carry model-independent information on the equation of state.

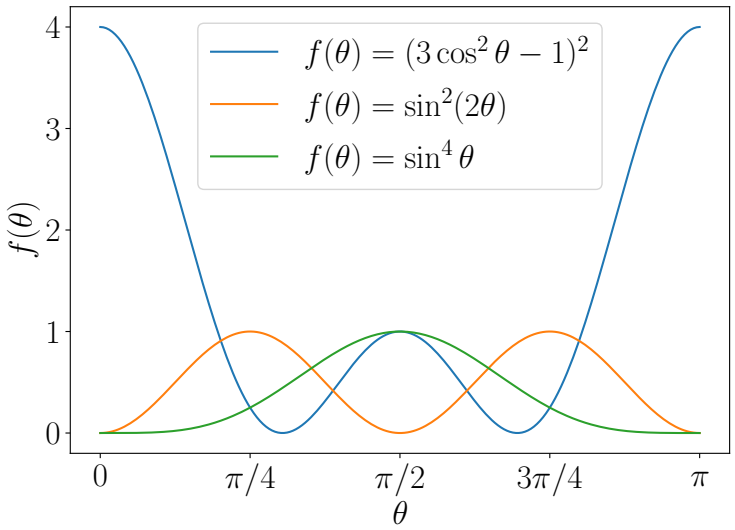

Figure 6.6: The angular basis of the von Mises strain for $(\ell, m) = (2, 0)$ perturbations.

In this chapter, we have explored the impact of an elastic crust on tidal deformations of neutron stars. We used the formalism detailed in Sec. 5.1 which enables one to compute static, polar perturbations of a neutron star with an elastic component. This was necessary to resolve discrepancies between previous studies (Penner *et al.*, 2011; Biswas *et al.*, 2019). There are mistakes in the crustal perturbation equations presented by Penner *et al.* (2011), in particular arising from the analogous equation to (5.30g). This meant they marginally overestimated the impact of a crust on tidal deformations and consequently this affected their analysis on when the crust will break in a binary inspiral (Penner *et al.*, 2012). Meanwhile, the work of Biswas *et al.* (2019) calculates the static displacement vector in the fluid regions of the star. However, such a calculation should not be possible due to the static nature of the problem. This means that they cannot correctly impose continuity of the traction at the top of the crust. Moreover, Biswas *et al.* (2019) do not correctly calculate the tidal Love number for the assumed stellar model with an exposed crust.

We have applied our formalism to the computation of static, quadrupolar perturbations of a neutron star sourced by an external tidal field. We calculated the quadrupolar perturbations for a realistic equation of state that includes an elastic crust. We have shown that the inclusion of an elastic crust has a very small effect on the tidal deformability of a star, in the range of $\sim 10^{-8} - 10^{-7}$ for realistic models – even smaller than what one would calculate using simplistic equations of state. We found that our results are an order of magnitude smaller than what was reported by Penner *et al.* (2011) and significantly smaller than the results of Biswas *et al.* (2019). This means the impact of a crust on binary-neutron-star mergers is not expected to be detectable for current and next-generation gravitational-wave detectors.

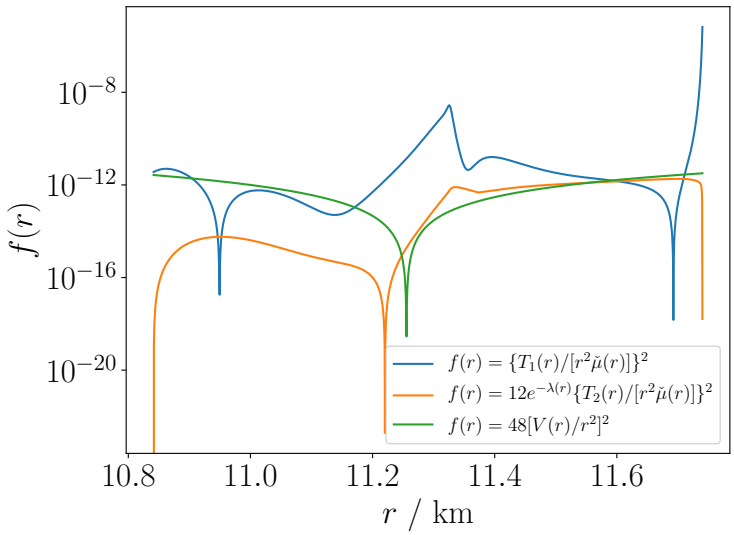

Figure 6.7: The radial dependence of the radial and tangential traction variables and the tangential displacement function normalised to a binary radiating gravitational waves with $f_{\rm GW} = 10\,{\rm Hz}$. At neutron drip, around $r = 11.3\,{\rm km}$, we find that the tangential functions combine to give local minima for most values of θ. Note that the vertical axis is in logarithmic scale – the cusps correspond to when the functions cross zero and change sign.

We used our integrations to calculate when and where the crust would fail during a binary inspiral with component masses $M = M_{\rm comp} = 1.4\,M_\odot$. We found that the crust is much stronger than estimated in previous work (Penner *et al.*, 2012). Only the small regions close to neutron drip and the outer layers of the crust will fracture before merger.

CHAPTER 7

Conclusions

Neutron stars are weird and wonderful objects. We have been aware of their existence for over half a century and yet there is still much more we can learn about them. Their status as the most compact state of matter (that we know of) means they provide a remarkable opportunity to study various aspects of cutting-edge physics. Perhaps the most exciting prospect is to uncover details about the ultra-dense equation of state.

With the aid of kilometre-long gravitational-wave interferometers, we have witnessed some of the Universe's most impressive sights: the coalescence of black holes and neutron stars. These events had never been seen before. The first observation of a binary-neutron-star inspiral and merger presented the opportunity to constrain the equation of state in a uniquely model-independent fashion. The hope is that we will continue to detect binary neutron stars and eventually start observing other neutron-star scenarios with gravitational-wave instruments.

In this thesis, we have studied how neutron stars can be deformed with the presence of a mountain and by the tidal field of a companion star. Both these situations can give rise to gravitational radiation.

Although we are yet to detect rotating neutron stars with gravitational waves, there are other signatures we can look for to get an indication of whether we should expect such radiation to play a significant role in their dynamics. An unresolved problem in the study

of accreting neutron stars is the fact that none of the observed systems spin close to the centrifugal break-up frequency. This suggests that there must be some (as yet unaccounted for) mechanism acting in these systems that takes angular momentum away from the star.

We considered whether gravitational-wave emission could explain the features of the observed spin distribution of accreting neutron stars in Chap. 3. To answer this question, we simulated populations of accreting neutron stars. We used a model for the torques acting on the neutron star that accounted for accretion and magnetic-field effects. We also worked with persistent and transient accretion. Promisingly, we found that one could recreate the observed spin distribution with the inclusion of gravitational-wave torques. In addition to a permanent deformation, we showed that one could also obtain this behaviour from thermal mountains and unstable r-modes. However, based on the distributions alone, it is difficult to distinguish between the competing mechanisms.

A natural extension of this study would be to try to connect the accreting-neutron-star population with the population of rapidly rotating radio pulsars. In particular, it would be interesting to see whether gravitational waves are relevant in this process and can obtain the spin distribution of radio pulsars. Towards building a realistic model for the spin evolution, one could consider a more sophisticated treatment for transient accretion that takes into account variable outburst/quiescent cycles.

In this work, we obtained the observed spin distribution for accreting neutron stars with a permanent quadrupole moment of $Q_{22} = 10^{36}\,\mathrm{g\,cm^2}$ (corresponding to an ellipticity of $\epsilon \approx 10^{-9}$). We found similar results for thermal mountains with the fractional quadrupolar heating of $\delta T_\mathrm{q}/\delta T = 4 \times 10^{-4}$ and unstable r-modes with amplitude $\alpha = 10^{-7}$. Understanding why there is a preference for these values will require further investigation.

In light of this result, we went on to consider how neutron-star mountains are calculated in Newtonian gravity in Chap. 4. Over the past two decades, there have been a number of studies on the maximum mountain that a neutron star can support before the elastic crust fractures. This is a relevant question since such a result would provide interesting context to the upper limits on these deformations that have been obtained thus far, as well as give an indication of the maximum spin-frequency pulsars should be able to obtain. However, previous maximum-mountain studies had issues with satisfying the boundary conditions of the problem.

In order to resolve these issues, we developed a new scheme for calculating mountains on neutron stars that explicitly includes the fiducial force which gives the star its non-spherical shape. By introducing the force, we have full control over the boundary conditions. One of the advantages of using our scheme is that one can compute all the relevant quantities. But, one must prescribe the deforming force. In reality, the force that gives rise to the

mountains is (presently) unknown. Indeed, to make progress on this, future evolutionary calculations will be necessary to motivate the form of the force. As a proof of principle, we calculated the mountains produced by a few example forces. We found that the maximum mountains the considered forces produced were in the range of a factor of a few to two orders of magnitude below previous estimates, $1.7 \times 10^{37} \leq Q_{22} \ / \ \mathrm{g\,cm^{-2}} \leq 4.4 \times 10^{38}$ ($2.2 \times 10^{-8} \leq \epsilon \leq 5.7 \times 10^{-7}$). This was not a surprising result since, in prescribing the force, the breaking strain was reached at a point – rather than throughout the entire crust, which previous studies assumed.

In Chap. 5, to construct more realistic models, we generalised the Newtonian scheme for neutron-star mountains to relativistic gravity. In addition to considering how the mountains depend on the deforming force in relativity, we also were able to explore how the equation of state impacted the size of the mountains. As has been noted for tidal- and magnetic-deformation calculations, we observed a suppression in the magnitude of the mountains in going from Newtonian to relativistic gravity. We also found that the shear modulus of the crust is important in supporting the mountains: in particular, for the sources we looked at, the shear modulus at the top of the crust was a limiting factor. Finally, we demonstrated how the mountains are sensitive to the fluid pressure-density relationship. For equations of state that satisfy current observational constraints, the deformations spanned a range of approximately an order of magnitude for a given deforming force.

In studying mountains in both Newtonian gravity and full general relativity, we have seen that there is a great deal of uncertainty in what the *maximum* mountain is that the neutron-star crust can sustain. It is clear that the formation history of the star plays a crucial role in how large the mountains can be. Additionally, the equation of state of the neutron-star matter is also important.

A potentially promising direction for future work is what role plasticity may play in maximally strained neutron-star mountains. Plastic materials hold on to some of the strain when the yield limit is reached. It is possible that plastic flow in the crust could enable the star to attain a higher strain configuration and perhaps a larger quadrupole moment.

In Chap. 6, we went on to study a scenario in which the deforming force is well known. We explored the impact of an elastic crust in tidal deformations of neutron stars in general relativity. With the recent detections of binary neutron stars, it proves timely to go beyond the usual approximation of neutron stars as perfect-fluid bodies and consider the role of the crust.

We found that the crust has a very small effect on the tidal deformability of a star, in the range of $\sim 10^{-8} - 10^{-7}$. Such an effect is beyond the expected sensitivity of third-

generation gravitational-wave detectors. We also computed when and where the crust would fail during a equal-mass binary inspiral with component masses of $1.4\,M_\odot$. In comparison to previous work, we found that the crust is (perhaps surprisingly) robust and the majority of it will remain intact up until merger.

With the promise of more detections of binary-neutron-star inspirals, similar studies – extending the description of neutron stars beyond the standard perfect-fluid approximation – would be worthwhile. It would be interesting to study whether superfluidity and magnetic fields could leave measurable imprints on the waveform.

With the continued improvements of current-generation detectors and the developments of new, more-sensitive interferometers, alongside our improving theoretical understanding, there are good reasons to be optimistic about observing novel neutron-star scenarios using gravitational waves. However, in the meantime, there is plenty of work for us to do. The future is bright in gravitational waves.

APPENDIX A

Solving the equations of stellar structure

This appendix provides additional information on solving the equations of structure for non-rotating, spherical stellar models.

A.1 Polytropes

The polytropic relation is a popular idealisation for barotropic equations of state:

$$p(\rho) = K\rho^{1+1/n}, \tag{A.1}$$

where K is the polytropic constant and n is the polytropic index.

One can take the divergence of the equation of hydrostatic equilibrium (2.16) to write

$$\frac{1}{r^2}\frac{d}{dr}\left(\frac{r^2}{\rho}\frac{dp}{dr}\right) = -4\pi G\rho. \tag{A.2}$$

This equation may be written in dimensionless form by introducing the following variables:

$$\rho = \rho_c\theta^n, \quad r = a\xi, \tag{A.3}$$

where θ is the polytropic temperature, ξ is the dimensionless length and a is a constant

with dimensions of length. From the equation of state (A.1),

$$p = p_{\rm c}\theta^{n+1}, \tag{A.4}$$

where $p_{\rm c} = K\rho_{\rm c}^{1+1/n}$. One chooses a in order to simplify the differential equation,

$$a = \sqrt{\frac{(n+1)K\rho_{\rm c}^{1/n-1}}{4\pi G}}. \tag{A.5}$$

Thus, (A.2) becomes

$$\frac{1}{\xi^2}\frac{d}{d\xi}\left(\xi^2\frac{d\theta}{d\xi}\right) = -\theta^n. \tag{A.6}$$

Equation (A.6) is called the *Lane-Emden equation*. The Lane-Emden equation has the boundary conditions at the centre, $\xi = 0$,

$$\theta(0) = 1 \tag{A.7a}$$

and

$$\frac{d\theta}{d\xi}(0) = 0. \tag{A.7b}$$

Equation (A.7a) follows from the fact $\rho = \rho_{\rm c}\theta^n$. Equation (A.7b) is obtained by examining (2.18c) near the centre, noting that $m(r) \approx 4\pi\rho_{\rm c}r^3/3$ in this region.

A solution of (A.6) depends on one parameter only: the polytropic index n. The other two constants K and $\rho_{\rm c}$ are scaling parameters that provide dimensions to the physical star. The Lane-Emden equation can be integrated outwards from $\xi = 0$ until θ goes to zero at some ξ_1. This defines the surface of the polytrope. The physical radius is, thus, $R = a\xi_1$ and the total mass is $M = \int_0^R 4\pi r^2\rho dr$. Therefore, one can readily show that

$$R = \left[\frac{(n+1)K}{4\pi G}\right]^{1/2}\rho_{\rm c}^{(1-n)/(2n)}\xi_1 \tag{A.8}$$

and

$$M = 4\pi\left[\frac{(n+1)K}{4\pi G}\right]^{3/2}\rho_{\rm c}^{(3-n)/(2n)}\xi_1^2\left|\frac{d\theta}{d\xi}(\xi_1)\right|. \tag{A.9}$$

For a solution to a given polytropic index, one can choose K and $\rho_{\rm c}$ to give a specific R and M.

The Lane-Emden equation admits three analytic solutions: $n = 0$, which corresponds to an incompressible fluid with $\rho =$ const; $n = 1$, where $p \propto \rho^2$; and $n = 5$, known as the Roche model, which has an infinite extent. For $n = 1$ polytropes, which are useful for approximating Newtonian neutron stars, the polytropic temperature is given by

$$\theta(\xi) = \frac{\sin\xi}{\xi} \tag{A.10}$$

and the polytrope has its first root at $\xi_1 = \pi$.

A.2 Numerical integration of relativistic stars

We have the equations of stellar structure (2.33),

$$\frac{dm}{dr} = 4\pi r^2 \varepsilon, \tag{A.11a}$$

$$\frac{dp}{dr} = -\frac{(\varepsilon + p)(m + 4\pi r^3 p)}{r(r - 2m)} \tag{A.11b}$$

and

$$\frac{d\nu}{dr} = \frac{2(m + 4\pi r^3 p)}{r(r - 2m)}, \tag{A.11c}$$

along with a barotropic equation of state, $p = p(\varepsilon)$.

In order to solve the coupled system of differential equations (A.11), we must provide boundary conditions. We choose some central value for the energy density ε_c which has the corresponding pressure $p_\mathrm{c} = p(\varepsilon_\mathrm{c})$ at $r = 0$. At the stellar centre, the mass is zero, $m(0) = 0$. The surface of the star is defined as when the pressure vanishes, $p(R) = 0$. At this point, the interior metric must match smoothly to the exterior, $e^{\nu(R)} = 1 - 2M/R$. Usefully, because the metric potential neatly decouples from the other two equations, one is free to assign a constant to $\nu(0)$ and then correct this constant at the surface by satisfying the boundary condition.

The equations of stellar structure (A.11) present an initial-value problem. The numerical integration of these equations should begin at the centre, $r = 0$, with initial values for m, p and ν specified, and integrate through the star until $p = 0$. This determines the surface, $r = R$.

However, one should note that Eqs. (A.11) are singular at the origin. To begin integrating, one must start at a small value r away from the origin. The initial values for m and p are obtained by considering power-series expansions around $r = 0$, *e.g.*,

$$m(r) = \sum_{\alpha=0}^{\infty} \frac{1}{\alpha!} m_\alpha r^\alpha, \tag{A.12}$$

inserting these expansions into Eqs. (A.11) and comparing powers of r. One finds that the even powers of r in $m(r)$ vanish, as do the odd powers in $\varepsilon(r)$ and $p(r)$. For the non-zero

components, one finds

$$p_0 = p_\mathrm{c}, \tag{A.13a}$$

$$\varepsilon_0 = \varepsilon_\mathrm{c}, \tag{A.13b}$$

$$p_2 = -\frac{4\pi}{3}(\varepsilon_\mathrm{c} + p_\mathrm{c})(\varepsilon_\mathrm{c} + 3p_\mathrm{c}), \tag{A.13c}$$

$$\varepsilon_2 = \frac{p_2}{c_\mathrm{s}^2(0)}, \tag{A.13d}$$

$$m_3 = 8\pi\varepsilon_\mathrm{c}, \tag{A.13e}$$

$$m_5 = 48\pi\varepsilon_2, \tag{A.13f}$$

where $c_\mathrm{s}^2 = dp/d\varepsilon$ is the squared sound speed and $c_\mathrm{s}^2(0)$ is its central value. Therefore,

$$m(r) = \frac{4\pi}{3}\varepsilon_\mathrm{c} r^3 - \frac{8\pi^2}{15c_\mathrm{s}^2(0)}(\varepsilon_\mathrm{c} + p_\mathrm{c})(\varepsilon_\mathrm{c} + 3p_\mathrm{c})r^5 + \mathcal{O}(r^7), \tag{A.14a}$$

$$p(r) = p_\mathrm{c} - \frac{2\pi}{3}(\varepsilon_\mathrm{c} + p_\mathrm{c})(\varepsilon_\mathrm{c} + 3p_\mathrm{c})r^2 + \mathcal{O}(r^4), \tag{A.14b}$$

$$\varepsilon(r) = \varepsilon_\mathrm{c} - \frac{2\pi}{3c_\mathrm{s}^2(0)}(\varepsilon_\mathrm{c} + p_\mathrm{c})(\varepsilon_\mathrm{c} + 3p_\mathrm{c})r^2 + \mathcal{O}(r^4). \tag{A.14c}$$

The value $\nu(r)$ near the origin is arbitrary because it will be corrected at the surface.

APPENDIX B

The spherical harmonics

This appendix provides a brief introduction to the well-known (and very useful) spherical harmonics. Traditionally, one meets the spherical harmonics by examining the solutions of Laplace's equation. In Newtonian flat space, the Laplacian ∇^2 of a scalar quantity f is given by

$$\nabla^2 f = \frac{1}{r^2}\frac{\partial}{\partial r}\left(r^2\frac{\partial f}{\partial r}\right) + \frac{1}{r^2\sin\theta}\frac{\partial}{\partial\theta}\left(\sin\theta\frac{\partial f}{\partial\theta}\right) + \frac{1}{r^2\sin^2\theta}\frac{\partial^2 f}{\partial\phi^2}. \tag{B.1}$$

We look for solutions of Laplace's equation,

$$\nabla^2 f = 0, \tag{B.2}$$

using separation of variables, $f(r,\theta,\phi) = R(r)\Theta(\theta)\Phi(\phi)$. Thus, we obtain

$$\frac{1}{R}\frac{d}{dr}\left(r^2\frac{dR}{dr}\right) + \frac{1}{\Theta}\frac{1}{\sin\theta}\frac{d}{d\theta}\left(\sin\theta\frac{d\Theta}{d\theta}\right) + \frac{1}{\Phi}\frac{1}{\sin^2\theta}\frac{d^2\Phi}{d\phi^2} = 0. \tag{B.3}$$

Suppose we rearrange (B.3) so that all terms with a ϕ dependence sit on the right-hand side. Then, we note that the left-hand side depends on r and θ. This implies that we have a constant α so that

$$\frac{\sin^2\theta}{R}\frac{d}{dr}\left(r^2\frac{dR}{dr}\right) + \frac{\sin\theta}{\Theta}\frac{d}{d\theta}\left(\sin\theta\frac{d\Theta}{d\theta}\right) = -\frac{1}{\Phi}\frac{d^2\Phi}{d\phi^2} = \alpha. \tag{B.4}$$

We can solve (B.4) for Φ to find

$$\Phi(\phi) \propto e^{\sqrt{-\alpha}\phi}. \tag{B.5}$$

Because ϕ is a periodic variable, $\Phi(\phi + 2\pi) = \Phi(\phi)$, this implies that $\alpha = m^2$, where m is an integer. If $m = 0$, then the general solution is $\Phi(\phi) = a\phi + b$, with a and b as integration constants. Periodicity means that $a = 0$, therefore, only one solution is allowed.

Using similar logic as above, we put terms that depend on r on one side and terms that depend on θ on the other,

$$\frac{1}{R}\frac{d}{dr}\left(r^2\frac{dR}{dr}\right) = -\frac{1}{\Theta}\frac{1}{\sin\theta}\frac{d}{d\theta}\left(\sin\theta\frac{d\Theta}{d\theta}\right) + \frac{m^2}{\sin^2\theta} = \beta, \tag{B.6}$$

where we introduce the constant β. Therefore, we have the differential equation for the polar-angle function

$$\frac{1}{\sin\theta}\frac{d}{d\theta}\left(\sin\theta\frac{d\Theta}{d\theta}\right) + \left(\beta - \frac{m^2}{\sin^2\theta}\right)\Theta = 0. \tag{B.7}$$

By changing variables to $x = \cos\theta$, the differential equation (B.7) becomes

$$\frac{d}{dx}\left[(1-x^2)\frac{d\Theta}{dx}\right] + \left(\beta - \frac{m^2}{1-x^2}\right)\Theta = 0. \tag{B.8}$$

Equation (B.8) is in the form of the associated Legendre equation. It has a regular solution when $\beta = \ell(\ell+1)$, where ℓ is a positive integer and $|m| \leq \ell$. The solution is

$$\Theta(\theta) \propto \mathcal{P}_{\ell m}(\cos\theta), \tag{B.9}$$

where $\mathcal{P}_{\ell m}(x)$ is an associated Legendre polynomial,

$$\mathcal{P}_{\ell m}(x) = (-1)^m(1-x^2)^{m/2}\frac{d^m}{dx^m}\mathcal{P}_\ell(x), \tag{B.10}$$

and $\mathcal{P}_\ell(x)$ is a Legendre polynomial,

$$\mathcal{P}_\ell(x) = \frac{1}{2^\ell \ell!}\frac{d^\ell}{dx^\ell}(x^2-1)^\ell. \tag{B.11}$$

From (B.6), we obtain an equation for $R(r)$,

$$\frac{d}{dr}\left(r^2\frac{dR}{dr}\right) = \ell(\ell+1)R, \tag{B.12}$$

that has solutions of the form

$$R(r) \propto r^\ell, \qquad R(r) \propto 1/r^{\ell+1}. \tag{B.13}$$

Combining the above results, the general solution to Laplace's equation is

$$f(r,\theta,\phi) = (Ar^{\ell} + B/r^{\ell+1})\mathcal{P}_{\ell m}(\cos\theta)e^{im\phi}, \tag{B.14}$$

where A and B are constants.

At this point, we focus on the angular part of f, $g_{\ell m}(\theta,\phi) \propto \Theta(\theta)\Phi(\phi)$, which depends on the numbers ℓ and m. We can normalise $g_{\ell m}(\theta,\phi)$ so that

$$\int_{\theta=0}^{\pi}\int_{\phi=0}^{2\pi} g^{*}_{\ell' m'}(\theta,\phi)g_{\ell m}(\theta,\phi)\sin\theta d\theta d\phi = \delta_{\ell\ell'}\delta_{mm'}, \tag{B.15}$$

where $\delta_{\ell m}$ is the Kronecker delta and the star denotes complex conjugation. Here, we integrate over the differential solid angle on a two-sphere, $d\Omega = \sin\theta d\theta d\phi$. Therefore, we find

$$g_{\ell m}(\theta,\phi) = (-1)^m\sqrt{\frac{2\ell+1}{4\pi}\frac{(\ell-m)!}{(\ell+m)!}}\mathcal{P}_{\ell m}(\cos\theta)e^{im\phi} \equiv Y_{\ell m}(\theta,\phi), \tag{B.16}$$

which are the famous spherical harmonics $Y_{\ell m}(\theta,\phi)$. The phase factor $(-1)^m$ is a convention from quantum mechanics.

Let us examine some of the properties of the spherical harmonics. We observe from (B.16) that

$$Y_{\ell m} = (-1)^m Y^{*}_{\ell -m}. \tag{B.17}$$

We note through (B.15) that the spherical harmonics are orthonormal. Indeed, we also have

$$\sum_{\ell=0}^{\infty}\sum_{m=-\ell}^{\ell} Y^{*}_{\ell m}(\vartheta,\varphi)Y_{\ell m}(\theta,\phi) = \frac{\delta(\theta-\vartheta)\delta(\phi-\varphi)}{\sin\theta}, \tag{B.18}$$

where δ is the Dirac delta function. Thus, the spherical harmonics form an orthonormal basis on the two-sphere. Additionally, the spherical harmonics are complete. This means that they are linearly independent and no function of (θ,ϕ) exists that is orthogonal to all $Y_{\ell m}(\theta,\phi)$. Because they are complete, any well-behaved function of (θ,ϕ) can be expressed as

$$F(\theta,\phi) = \sum_{\ell=0}^{\infty}\sum_{m=-\ell}^{\ell} F_{\ell m}Y_{\ell m}(\theta,\phi), \tag{B.19}$$

with coefficients $F_{\ell m}$ given by

$$F_{\ell m} = \int_{\theta=0}^{\pi}\int_{\phi=0}^{2\pi} Y^{*}_{\ell m}(\theta,\phi)F(\theta,\phi)\sin\theta d\theta d\phi. \tag{B.20}$$

One can obtain the useful relation, using some of the above equations,

$$\nabla^2 Y_{\ell m} = -\frac{\ell(\ell+1)}{r^2}Y_{\ell m}. \tag{B.21}$$

It is worthwhile noting that (B.21) holds for all spacetimes in relativity that include the two-sphere [*e.g.*, the Schwarzschild metric (2.26)]. We also have the addition formula, which we show without proof,

$$\mathcal{P}_\ell(\cos\alpha) = \frac{4\pi}{2\ell+1}\sum_{m=-\ell}^{\ell} Y^*_{\ell m}(\hat{X}^i)Y_{\ell m}(\hat{x}^i), \tag{B.22}$$

where $\hat{X}^i$ and $\hat{x}^i$ are two unit vectors, separated by angle α.

APPENDIX C

Numerically solving the perturbation equations

Our approach to solving the interior perturbation equations is similar to as described in Lin *et al.* (2008) and Krüger *et al.* (2015). We divide our star with a crust into three layers: (i) a fluid core from $R_0 = 0$ to R_1, (ii) an elastic crust from R_1 to R_2 and (iii) a fluid ocean from R_2 to $R_3 = R$. We express the system of ordinary differential equations for a given layer i in the form

$$\frac{d\mathbf{Y}^{(i)}}{dr} = \mathbf{Q}^{(i)} \cdot \mathbf{Y}^{(i)}, \text{ for } r \in [R_{i-1}, R_i], \tag{C.1}$$

where $\mathbf{Y}^{(i)}(r) = [y_1(r), ..., y_{k_i}(r)]$ is an abstract k_i-dimensional vector field, $\mathbf{Q}^{(i)}(r)$ is a $k_i \times k_i$ matrix and $r = R_i$ denotes the end of layer i. As long as our differential equations are linear we are free to write the system in the above form.

Due to the linearity of the differential equations, we generate a set of k_i linearly independent solutions $\mathbf{Y}_j^{(i)}(r)$ for layer i and obtain the general solution using a linear combination of these solutions,

$$\mathbf{Y}^{(i)}(r) = \sum_{j=1}^{k_i} c_j^{(i)} \mathbf{Y}_j^{(i)}(r), \tag{C.2}$$

where the coefficients $c_j^{(i)}$ are constants to be determined from boundary and interface conditions. We generate these linearly independent solutions by choosing linearly independent start vectors $\mathbf{Y}_j^{(i)}(R_{i-1})$ and integrating through the layer using (C.1) up to $r = R_i$. (Note

that, in theory, there is no reason one could not do the reverse, integrating from $r = R_i$ to R_{i-1}, should they wish.) *A priori*, we do not have any additional information about layer i and would naïvely integrate k_i linearly independent start vectors. However, we can reduce the computational effort by applying relevant boundary conditions. For example, should a variable vanish at an interface, one could simply set this variable to zero in the start vectors and reduce the number of necessary linearly independent solutions by one.

We will initially focus this discussion to the Newtonian variables, but the logic still applies to the relativistic formulation. The fluid regions of the star are governed by Eqs. (4.45) and so we have the abstract two-dimensional vector field

$$\mathbf{Y}^{(k)}(r) = [d\delta\Phi(r)/dr, \delta\Phi(r)], \tag{C.3}$$

where $k = 1, 3$ denotes the core and ocean, respectively. The elastic region of the star is more complex and requires more functions [see Eqs. (4.58)] to describe its structure. Thus, we use the six-dimensional vector field

$$\mathbf{Y}^{(2)}(r) = [d\delta\Phi(r)/dr, \delta\Phi(r), \xi_r(r), \xi_\perp(r), T_1(r), T_2(r)]. \tag{C.4}$$

At a fluid-elastic interface, we know the variables $d\delta\Phi/dr$, $\delta\Phi$, ξ_r and T_2 are continuous. We know the values of $d\delta\Phi/dr$ and $\delta\Phi$ from the calculation in the fluid core and so we use their final values in the core to start the integration in the crust. Since the traction variables vanish in the fluid, we can simplify the integrations in the elastic by demanding that $T_2 = 0$ at an interface. For each of the solutions, we calculate the value for T_1 at the base using (4.59). These conditions mean that we must generate two linearly independent solutions with the initial values for the unknown functions ξ_r and $\xi_\perp$. [Notice that because of the condition (4.59), we could equivalently choose to generate solutions with T_1 instead of either ξ_r or $\xi_\perp$.] At the top of the crust, we demand that $T_2 = 0$ and T_1 be equal to the result of (4.59). We use these two constraints to solve for the coefficients of the general solution (C.2). At the top of the crust, we can straightforwardly continue the integration through the fluid ocean, since $d\delta\Phi/dr$ and $\delta\Phi$ are continuous.

In the relativistic formulation, we have Eqs. (5.18) for the fluid perturbations with variables $(dH_0/dr, H_0)$ and Eqs. (5.31) for the elastic perturbations with variables $(dH_0/dr, H_0, K, W, V, T_2)$. The idea is very similar to what is described above. However, dH_0/dr is not continuous. The functions H_0 and K are continuous across an interface and are used to begin integration in the crust. Again, we have $T_2 = 0$ at the base and the value for dH_0/dr is obtained from (5.32). These two conditions also hold for the top of the crust and constrain the functions W and V. In the fluid ocean, the initial value for dH_0/dr is calculated from H_0 and K using (5.18e).

APPENDIX D

The interface conditions

Since we consider a star with multiple layers that have phase transitions, we must address how the perturbation functions behave across an interface. We calculate the interface conditions using the geometrical approach explained in Andersson *et al.* (2002a).

Let us begin by considering the level surfaces of a scalar quantity A. We assume the level surfaces to be time-like and, therefore, have the normal,

$$\mathcal{N}^a = \frac{\nabla^a A}{\sqrt{\nabla^b A \nabla_b A}}, \tag{D.1}$$

where $\mathcal{N}^a \mathcal{N}_a = 1$ is true by construction. The first fundamental form (also known as the intrinsic curvature or induced three-metric) of these level surfaces is

$$\gamma_{ab} = P_a{}^c P_b{}^d g_{cd}, \tag{D.2}$$

where the projection operator along the level surfaces is given by

$$P_a{}^b = \delta_a{}^b - \mathcal{N}_a \mathcal{N}^b. \tag{D.3}$$

The second fundamental form (also known as the extrinsic curvature) of the level surfaces is defined as

$$K_{ab} = -P_a{}^c P_b{}^d \nabla_{(c} \mathcal{N}_{d)}. \tag{D.4}$$

Let us specialise and consider the useful decomposition of our scalar quantity of the form,

$$A(t, r, \theta, \phi) = A_0(r) + \delta A(t, r, \theta, \phi). \tag{D.5}$$

Using this decomposition we obtain the following components for the normal:

$$\mathcal{N}^t = -e^{-\nu+\lambda/2}\frac{\partial_t \delta A}{dA_0/dr} + e^{-\nu-\lambda/2}h_{tr}, \tag{D.6a}$$

$$\mathcal{N}^r = e^{-\lambda/2}\left(1 - \frac{1}{2}e^{-\lambda}h_{rr}\right), \tag{D.6b}$$

$$\mathcal{N}^\theta = \frac{e^{\lambda/2}}{r^2}\frac{\partial_\theta \delta A}{dA_0/dr}, \tag{D.6c}$$

$$\mathcal{N}^\phi = \frac{e^{\lambda/2}}{r^2\sin^2\theta}\frac{\partial_\phi \delta A}{dA_0/dr}. \tag{D.6d}$$

The level surfaces of A, thus, have the following non-zero components of the first fundamental form:

$$\gamma_{tt} = -e^{\nu} + h_{tt}, \tag{D.7a}$$

$$\gamma_{tr} = h_{tr} - e^{\lambda}\frac{\partial_t \delta A}{dA_0/dr}, \tag{D.7b}$$

$$\gamma_{r\theta} = -e^{\lambda}\frac{\partial_\theta \delta A}{dA_0/dr}, \tag{D.7c}$$

$$\gamma_{r\phi} = -e^{\lambda}\frac{\partial_\phi \delta A}{dA_0/dr}, \tag{D.7d}$$

$$\gamma_{\theta\theta} = r^2 + h_{\theta\theta}, \tag{D.7e}$$

$$\gamma_{\phi\phi} = r^2\sin^2\theta + h_{\phi\phi}. \tag{D.7f}$$

The non-trivial components of the second fundamental form are

$$K_{tt} = \frac{1}{2}\frac{d\nu}{dr}e^{\nu-\lambda/2} - e^{\lambda/2}\frac{\partial_t^2\delta A}{dA_0/dr} + e^{-\lambda/2}\partial_t h_{tr} - \frac{1}{2}e^{-\lambda/2}\partial_r h_{tt} - \frac{1}{4}\frac{d\nu}{dr}e^{\nu-3\lambda/2}h_{rr}, \tag{D.8a}$$

$$K_{tr} = \frac{1}{2}\frac{d\nu}{dr}\left(e^{\lambda/2}\frac{\partial_t\delta A}{dA_0/dr} - e^{-\lambda/2}h_{tr}\right), \tag{D.8b}$$

$$K_{t\theta} = -e^{\lambda/2}\left(\frac{\partial_t\partial_\theta\delta A}{dA_0/dr} - \frac{1}{2}e^{-\lambda}\partial_\theta h_{tr}\right), \tag{D.8c}$$

$$K_{t\phi} = -e^{\lambda/2}\left(\frac{\partial_t\partial_\phi\delta A}{dA_0/dr} - \frac{1}{2}e^{-\lambda}\partial_\phi h_{tr}\right), \tag{D.8d}$$

$$K_{r\theta} = \frac{e^{\lambda/2}}{r}\frac{\partial_\theta\delta A}{dA_0/dr} \tag{D.8e}$$

$$K_{r\phi} = \frac{e^{\lambda/2}}{r}\frac{\partial_\phi\delta A}{dA_0/dr}, \tag{D.8f}$$

$$K_{\theta\theta} = -e^{-\lambda/2}r - e^{\lambda/2}\frac{\partial_\theta^2\delta A}{dA_0/dr} - \frac{1}{2}e^{-\lambda/2}(\partial_r h_{\theta\theta} - e^{-\lambda}r h_{rr}), \tag{D.8g}$$

$$K_{\theta\phi} = -\frac{e^{-\lambda/2}}{dA_0/dr}\left(\partial_\theta\partial_\phi\delta A - \cot\theta\partial_\phi\delta A\right), \tag{D.8h}$$

$$\begin{aligned} K_{\phi\phi} = {} & -e^{-\lambda/2}r\sin^2\theta - e^{\lambda/2}\frac{\partial_\phi^2\delta A}{dA_0/dr} - e^{\lambda/2}\sin\theta\cos\theta\frac{\partial_\theta\delta A}{dA_0/dr} \\ & - \frac{1}{2}e^{-\lambda/2}(\partial_r h_{\phi\phi} - e^{-\lambda}r\sin^2\theta h_{rr}) \end{aligned} \tag{D.8i}$$

Both the first and second fundamental forms must be continuous across an interface (in the absence of surface degrees of freedom).

As was done by Finn (1990), we will consider the level surfaces of the radial shell, so we assign $A_0 = r$ and $\delta A = \xi^r$. We use the perturbed metric for polar perturbations (5.1). Because of how we set up the problem by assuming the background star is in a relaxed state, we know that the background quantities will all be continuous across an interface. We further assume that there is no discontinuity in the density or pressure. The first fundamental form with components γ_{tt}, γ_{tr}, $\gamma_{\theta\theta}$ and $\gamma_{r\theta}$ show

$$[H_0]_r = 0, \quad [H_1]_r = 0, \quad [K]_r = 0, \quad \left[\frac{\delta A}{dA_0/dr}\right]_r = 0, \tag{D.9}$$

where we have introduced the notation $[f]_r = \lim_{\epsilon\to 0}[f(r+\epsilon) - f(r-\epsilon)]$ to describe the continuity of a function $f(r)$ at a point r. The angular part of δA is decomposed using spherical harmonics. For the problem we are analysing, H_1 simply vanishes. The generic condition above translates to $[\xi^r]_r = 0$, which is equivalent to

$$[W]_r = 0. \tag{D.10}$$

This condition is equivalent to saying there must not be a gap in the perturbed material.

We have exhausted the information we can learn from continuity of the first fundamental form. We also notice that there is no additional information to be learned from the components K_{tr}, $K_{t\theta}$, $K_{t\phi}$, $K_{r\theta}$ and $K_{r\phi}$ of the second fundamental form; only components K_{tt} and $K_{\theta\theta}$ provide more interface conditions. Continuity of K_{tt} implies

$$\left[\partial_r h_{tt} + \frac{1}{2}\frac{d\nu}{dr}e^{\nu-\lambda}h_{rr}\right]_r = 0. \tag{D.11}$$

This gives

$$\left[\frac{dH_0}{dr}\right]_r = -\frac{1}{2}\frac{d\nu}{dr}[H_2]_r. \tag{D.12}$$

Similarly, we can infer from $K_{\theta\theta}$,

$$[\partial_r h_{\theta\theta} - e^{-\lambda}rh_{rr}]_r = 0 \quad \Rightarrow \quad \left[\frac{dK}{dr}\right]_r = \frac{1}{r}[H_2]_r. \tag{D.13}$$

We can combine (D.12) and (D.13) to obtain

$$\left[\frac{dK}{dr} - \frac{dH_0}{dr}\right]_r = \frac{1}{2r}\left(2 + r\frac{d\nu}{dr}\right)[H_2]_r. \tag{D.14}$$

Now, we need some information from the perturbed Einstein equations. The above expression can be further used along with (5.30e) to provide

$$\frac{16\pi}{r}\left(2 + r\frac{d\nu}{dr}\right)[\breve{\mu}V]_r - \frac{16\pi}{r}[T_2]_r = \frac{1}{2r}\left(2 + r\frac{d\nu}{dr}\right)[H_2]_r. \tag{D.15}$$

Using continuity of H_0 and (5.30d) we find

$$[H_2]_r = 32\pi[\breve{\mu}V]_r. \tag{D.16}$$

This condition states that we should expect a discontinuity in H_2 for two reasons: (i) the shear modulus vanishes in the fluid and has a finite value in the crust and (ii) there is no reason that the tangential displacement function V need be continuous. This further implies through (D.12) that dH_0/dr will be discontinuous,

$$\left[\frac{dH_0}{dr}\right]_r = -16\pi\frac{d\nu}{dr}[\breve{\mu}V]_r. \tag{D.17}$$

Equations (D.15) and (D.16) imply continuity of the tangential traction variable,

$$[T_2]_r = 0. \tag{D.18}$$

Finally, we use (5.31c), along with the continuity condition (D.17), to obtain

$$\left[\frac{T_1}{r^2} + \delta p\right]_r = 0. \tag{D.19}$$

Equations (D.18) and (D.19) simply mean that the radial and tangential stresses are continuous across a fluid-elastic interface. These interface conditions are necessary when considering how the functions behave across a fluid-elastic boundary and enable one to carry out the integration in the crust.

Bibliography

Aasi, J. *et al.* (2013). 'Einstein@Home all-sky search for periodic gravitational waves in LIGO S5 data'. *Phys. Rev. D* **87**, 042001. DOI: 10.1103/PhysRevD.87.042001. arXiv: 1207.7176 [gr-qc] (cited on p. 7).

— (2014). 'Gravitational Waves from Known Pulsars: Results from the Initial Detector Era'. *Astrophys. J.* **785**, 119. DOI: 10.1088/0004-637X/785/2/119. arXiv: 1309.4027 [astro-ph.HE] (cited on p. 7).

— (2015a). 'Directed search for gravitational waves from Scorpius X-1 with initial LIGO data'. *Phys. Rev. D* **91**, 062008. DOI: 10.1103/PhysRevD.91.062008. arXiv: 1412.0605 [gr-qc] (cited on pp. 7, 8).

— (2015b). 'Narrow-band search of continuous gravitational-wave signals from Crab and Vela pulsars in Virgo VSR4 data'. *Phys. Rev. D* **91**, 022004. DOI: 10.1103/PhysRevD.91.022004. arXiv: 1410.8310 [astro-ph.IM] (cited on p. 7).

Abadie, J. *et al.* (2010). 'TOPICAL REVIEW: Predictions for the rates of compact binary coalescences observable by ground-based gravitational-wave detectors'. *Classical Quant. Grav.* **27**, 173001. DOI: 10.1088/0264-9381/27/17/173001. arXiv: 1003.2480 [astro-ph.HE] (cited on p. 7).

— (2011a). 'Beating the Spin-down Limit on Gravitational Wave Emission from the Vela Pulsar'. *Astrophys. J.* **737**, 93. DOI: 10.1088/0004-637X/737/2/93. arXiv: 1104.2712 [astro-ph.HE] (cited on p. 7).

— (2011b). 'Search for gravitational waves associated with the August 2006 timing glitch of the Vela pulsar'. *Phys. Rev. D* **83**, 042001. DOI: 10.1103/PhysRevD.83.042001. arXiv: 1011.1357 [gr-qc] (cited on p. 7).

Abadie, J. *et al.* (2012). 'All-sky search for periodic gravitational waves in the full S5 LIGO data'. *Phys. Rev. D* **85**, 022001. DOI: 10.1103/PhysRevD.85.022001. arXiv: 1110.0208 [gr-qc] (cited on p. 7).

Abbott, B. *et al.* (2004). 'Setting upper limits on the strength of periodic gravitational waves from PSR J1939+2134 using the first science data from the GEO 600 and LIGO detectors'. *Phys. Rev. D* **69**, 082004. DOI: 10.1103/PhysRevD.69.082004. arXiv: gr-qc/0308050 [gr-qc] (cited on p. 7).

— (2005a). 'First all-sky upper limits from LIGO on the strength of periodic gravitational waves using the Hough transform'. *Phys. Rev. D* **72**, 102004. DOI: 10.1103/PhysRevD.72.102004. arXiv: gr-qc/0508065 [gr-qc] (cited on p. 7).

— (2005b). 'Limits on Gravitational-Wave Emission from Selected Pulsars Using LIGO Data'. *Phys. Rev. Lett.* **94**, 181103. DOI: 10.1103/PhysRevLett.94.181103. arXiv: gr-qc/0410007 [gr-qc] (cited on p. 7).

— (2007a). 'Searches for periodic gravitational waves from unknown isolated sources and Scorpius X-1: Results from the second LIGO science run'. *Phys. Rev. D* **76**, 082001. DOI: 10.1103/PhysRevD.76.082001. arXiv: gr-qc/0605028 [gr-qc] (cited on pp. 7, 8).

— (2007b). 'Upper limits on gravitational wave emission from 78 radio pulsars'. *Phys. Rev. D* **76**, 042001. DOI: 10.1103/PhysRevD.76.042001. arXiv: gr-qc/0702039 [gr-qc] (cited on p. 7).

— (2008a). 'All-sky search for periodic gravitational waves in LIGO S4 data'. *Phys. Rev. D* **77**, 022001. DOI: 10.1103/PhysRevD.77.022001. arXiv: 0708.3818 [gr-qc] (cited on p. 7).

— (2008b). 'Beating the Spin-Down Limit on Gravitational Wave Emission from the Crab Pulsar'. *Astrophys. J.* **683**, L45. DOI: 10.1086/591526. arXiv: 0805.4758 (cited on p. 7).

— (2009). 'Einstein@Home search for periodic gravitational waves in LIGO S4 data'. *Phys. Rev. D* **79**, 022001. DOI: 10.1103/PhysRevD.79.022001. arXiv: 0804.1747 [gr-qc] (cited on p. 7).

Abbott, B. P. *et al.* (2010). 'Searches for Gravitational Waves from Known Pulsars with Science Run 5 LIGO Data'. *Astrophys. J.* **713**, 671. DOI: 10.1088/0004-637X/713/1/671. arXiv: 0909.3583 [astro-ph.HE] (cited on p. 7).

— (2016a). 'Comprehensive all-sky search for periodic gravitational waves in the sixth science run LIGO data'. *Phys. Rev. D* **94**, 042002. DOI: 10.1103/PhysRevD.94.042002. arXiv: 1605.03233 [gr-qc] (cited on p. 7).

— (2016b). 'Observation of Gravitational Waves from a Binary Black Hole Merger'. *Phys. Rev. Lett.* **116**, 061102. DOI: 10.1103/PhysRevLett.116.061102. arXiv: 1602.03837 [gr-qc] (cited on p. 2).

— (2017a). 'A gravitational-wave standard siren measurement of the Hubble constant'. *Nature* **551**, 85. DOI: 10.1038/nature24471. arXiv: 1710.05835 [astro-ph.CO] (cited on p. 2).

— (2017b). 'All-sky search for periodic gravitational waves in the O1 LIGO data'. *Phys. Rev. D* **96**, 062002. DOI: 10.1103/PhysRevD.96.062002. arXiv: 1707.02667 [gr-qc] (cited on p. 8).
— (2017c). 'First narrow-band search for continuous gravitational waves from known pulsars in advanced detector data'. *Phys. Rev. D* **96**, 122006. DOI: 10.1103/PhysRevD.96.122006. arXiv: 1710.02327 [gr-qc] (cited on p. 7).
— (2017d). 'First Search for Gravitational Waves from Known Pulsars with Advanced LIGO'. *Astrophys. J.* **839**, 12. DOI: 10.3847/1538-4357/aa677f. arXiv: 1701.07709 [astro-ph.HE] (cited on p. 7).
— (2017e). 'Gravitational Waves and Gamma-Rays from a Binary Neutron Star Merger: GW170817 and GRB 170817A'. *Astrophys. J.* **848**, L13. DOI: 10.3847/2041-8213/aa920c. arXiv: 1710.05834 [astro-ph.HE] (cited on pp. 2, 3).
— (2017f). 'GW170817: Observation of Gravitational Waves from a Binary Neutron Star Inspiral'. *Phys. Rev. Lett.* **119**, 161101. DOI: 10.1103/PhysRevLett.119.161101. arXiv: 1710.05832 [gr-qc] (cited on pp. 2, 8, 114).
— (2017g). 'Search for gravitational waves from Scorpius X-1 in the first Advanced LIGO observing run with a hidden Markov model'. *Phys. Rev. D* **95**, 122003. DOI: 10.1103/PhysRevD.95.122003. arXiv: 1704.03719 [gr-qc] (cited on pp. 7, 8).
— (2017h). 'Upper Limits on Gravitational Waves from Scorpius X-1 from a Model-based Cross-correlation Search in Advanced LIGO Data'. *Astrophys. J.* **847**, 47. DOI: 10.3847/1538-4357/aa86f0. arXiv: 1706.03119 [astro-ph.HE] (cited on pp. 7, 8).
— (2018a). 'First Search for Nontensorial Gravitational Waves from Known Pulsars'. *Phys. Rev. Lett.* **120**, 031104. DOI: 10.1103/PhysRevLett.120.031104. arXiv: 1709.09203 [gr-qc] (cited on p. 7).
— (2018b). 'Full band all-sky search for periodic gravitational waves in the O1 LIGO data'. *Phys. Rev. D* **97**, 102003. DOI: 10.1103/PhysRevD.97.102003. arXiv: 1802.05241 [gr-qc] (cited on p. 8).
— (2018c). 'GW170817: Measurements of Neutron Star Radii and Equation of State'. *Phys. Rev. Lett.* **121**, 161101. DOI: 10.1103/PhysRevLett.121.161101. arXiv: 1805.11581 [gr-qc] (cited on pp. 8, 114, 116).
— (2019a). 'All-sky search for continuous gravitational waves from isolated neutron stars using Advanced LIGO O2 data'. *Phys. Rev. D* **100**, 024004. DOI: 10.1103/PhysRevD.100.024004. arXiv: 1903.01901 [astro-ph.HE] (cited on p. 8).
— (2019b). 'GWTC-1: A Gravitational-Wave Transient Catalog of Compact Binary Mergers Observed by LIGO and Virgo during the First and Second Observing Runs'. *Phys. Rev. X* **9**, 031040. DOI: 10.1103/PhysRevX.9.031040. arXiv: 1811.12907 [astro-ph.HE] (cited on p. 2).
— (2019c). 'Narrow-band search for gravitational waves from known pulsars using the second LIGO observing run'. *Phys. Rev. D* **99**, 122002. DOI: 10.1103/PhysRevD.99.122002. arXiv: 1902.08442 [gr-qc] (cited on p. 7).

Abbott, B. P. *et al.* (2019d). 'Properties of the Binary Neutron Star Merger GW170817'. *Phys. Rev. X* **9**, 011001. DOI: 10.1103/PhysRevX.9.011001. arXiv: 1805.11579 [gr-qc] (cited on pp. 9, 114).

— (2019e). 'Search for gravitational waves from Scorpius X-1 in the second Advanced LIGO observing run with an improved hidden Markov model'. *Phys. Rev. D* **100**, 122002. DOI: 10.1103/PhysRevD.100.122002. arXiv: 1906.12040 [gr-qc] (cited on pp. 7, 8).

— (2019f). 'Searches for Gravitational Waves from Known Pulsars at Two Harmonics in 2015-2017 LIGO Data'. *Astrophys. J.* **879**, 10. DOI: 10.3847/1538-4357/ab20cb. arXiv: 1902.08507 [astro-ph.HE] (cited on p. 7).

— (2020a). 'GW190425: Observation of a Compact Binary Coalescence with Total Mass $\sim 3.4\,M_\odot$'. *Astrophys. J.* **892**, L3. DOI: 10.3847/2041-8213/ab75f5. arXiv: 2001.01761 [astro-ph.HE] (cited on pp. 3, 114).

Abbott, R. *et al.* (2020b). 'Gravitational-wave Constraints on the Equatorial Ellipticity of Millisecond Pulsars'. *Astrophys. J.* **902**, L21. DOI: 10.3847/2041-8213/abb655. arXiv: 2007.14251 [astro-ph.HE] (cited on pp. 7, 110).

— (2021a). 'Diving below the Spin-down Limit: Constraints on Gravitational Waves from the Energetic Young Pulsar PSR J0537-6910'. *Astrophys. J.* **913**, L27. DOI: 10.3847/2041-8213/abffcd. arXiv: 2012.12926 [astro-ph.HE] (cited on p. 7).

— (2021b). 'GWTC-2: Compact Binary Coalescences Observed by LIGO and Virgo during the First Half of the Third Observing Run'. *Phys. Rev. X* **11**, 021053. DOI: 10.1103/PhysRevX.11.021053. arXiv: 2010.14527 [gr-qc] (cited on p. 2).

— (2021c). 'Observation of Gravitational Waves from Two Neutron Star-Black Hole Coalescences'. *Astrophys. J.* **915**, L5. DOI: 10.3847/2041-8213/ac082e. arXiv: 2106.15163 [astro-ph.HE] (cited on pp. 3, 114).

Abdelsalhin, T. (2019). 'Tidal deformations of compact objects and gravitational wave emission'. arXiv: 1905.00408 [gr-qc] (cited on p. 115).

Alpar, M. A., Cheng, A. F., Ruderman, M. A. and Shaham, J. (1982). 'A new class of radio pulsars'. *Nature* **300**, 728. DOI: 10.1038/300728a0 (cited on pp. 5, 38).

Andersson, N. (1998). 'A New Class of Unstable Modes of Rotating Relativistic Stars'. *Astrophys. J.* **502**, 708. DOI: 10.1086/305919. arXiv: gr-qc/9706075 [gr-qc] (cited on pp. 7, 47, 56).

Andersson, N., Kokkotas, K. D. and Stergioulas, N. (1999). 'On the Relevance of the R-Mode Instability for Accreting Neutron Stars and White Dwarfs'. *Astrophys. J.* **516**, 307. DOI: 10.1086/307082. arXiv: astro-ph/9806089 [astro-ph] (cited on pp. 7, 39, 47, 56).

Andersson, N., Jones, D. I., Kokkotas, K. D. and Stergioulas, N. (2000). 'R-Mode Runaway and Rapidly Rotating Neutron Stars'. *Astrophys. J.* **534**, L75. DOI: 10.1086/312643. arXiv: astro-ph/0002114 [astro-ph] (cited on p. 47).

Andersson, N., Comer, G. L. and Langlois, D. (2002a). 'Oscillations of general relativistic superfluid neutron stars'. *Phys. Rev. D* **66**, 104002. DOI: 10.1103/PhysRevD.66.104002. arXiv: gr-qc/0203039 [gr-qc] (cited on p. 141).

Andersson, N., Jones, D. I. and Kokkotas, K. D. (2002b). 'Strange stars as persistent sources of gravitational waves'. *Mon. Not. R. Astron. Soc.* **337**, 1224. DOI: 10.1046/j.1365-8711.2002.05837.x. arXiv: astro-ph/0111582 [astro-ph] (cited on p. 47).

Andersson, N., Glampedakis, K., Haskell, B. and Watts, A. L. (2005). 'Modelling the spin equilibrium of neutron stars in low-mass X-ray binaries without gravitational radiation'. *Mon. Not. R. Astron. Soc.* **361**, 1153. DOI: 10.1111/j.1365-2966.2005.09167.x. arXiv: astro-ph/0411747 [astro-ph] (cited on p. 38).

Andersson, N. (2019). *Gravitational-Wave Astronomy: Exploring the Dark Side of the Universe*. Oxford: Oxford University Press. DOI: 10.1093/oso/9780198568032.001.0001/oso-9780198568032 (cited on p. 30).

Andersson, N., Haskell, B., Comer, G. L. and Samuelsson, L. (2019). 'The dynamics of neutron star crusts: Lagrangian perturbation theory for a relativistic superfluid-elastic system'. *Classical Quant. Grav.* **36**, 105004. DOI: 10.1088/1361-6382/ab12a1. arXiv: 1811.09419 [gr-qc] (cited on pp. 98, 105).

Andersson, N. and Pnigouras, P. (2019). 'The g-mode spectrum of reactive neutron star cores'. *Mon. Not. R. Astron. Soc.* **489**, 4043. DOI: 10.1093/mnras/stz2449. arXiv: 1905.00010 [gr-qc] (cited on p. 114).

— (2020). 'Exploring the effective tidal deformability of neutron stars'. *Phys. Rev. D* **101**, 083001. DOI: 10.1103/PhysRevD.101.083001. arXiv: 1906.08982 [astro-ph.HE] (cited on p. 79).

Andersson, N. and Comer, G. L. (2021). 'Relativistic fluid dynamics: physics for many different scales'. *Living Rev. Relativity* **24**, 3. DOI: 10.1007/s41114-021-00031-6. arXiv: 2008.12069 [gr-qc] (cited on pp. 12, 18, 22, 24).

Annala, E., Gorda, T., Kurkela, A. and Vuorinen, A. (2018). 'Gravitational-Wave Constraints on the Neutron-Star-Matter Equation of State'. *Phys. Rev. Lett.* **120**, 172703. DOI: 10.1103/PhysRevLett.120.172703. arXiv: 1711.02644 [astro-ph.HE] (cited on pp. 9, 114).

Antoniadis, J. *et al.* (2013). 'A Massive Pulsar in a Compact Relativistic Binary'. *Science* **340**, 448. DOI: 10.1126/science.1233232. arXiv: 1304.6875 [astro-ph.HE] (cited on p. 109).

Arras, P., Flanagan, E. E., Morsink, S. M., Schenk, A. K., Teukolsky, S. A. and Wasserman, I. (2003). 'Saturation of the r-Mode Instability'. *Astrophys. J.* **591**, 1129. DOI: 10.1086/374657. arXiv: astro-ph/0202345 [astro-ph] (cited on p. 58).

Baade, W. and Zwicky, F. (1934a). 'Cosmic Rays from Super-novae'. *Proc. Natl. Acad. Sci.* **20**, 259. DOI: 10.1073/pnas.20.5.259 (cited on p. 4).

— (1934b). 'On Super-novae'. *Proc. Natl. Acad. Sci.* **20**, 254. DOI: 10.1073/pnas.20.5.254 (cited on p. 4).

Backer, D. C., Kulkarni, S. R., Heiles, C., Davis, M. M. and Goss, W. M. (1982). 'A millisecond pulsar'. *Nature* **300**, 615. DOI: 10.1038/300615a0 (cited on p. 5).

Baiko, D. A. and Chugunov, A. I. (2018). 'Breaking properties of neutron star crust'. *Mon. Not. R. Astron. Soc.* **480**, 5511. DOI: 10.1093/mnras/sty2259. arXiv: 1808.06415 [astro-ph.HE] (cited on p. 84).

Baker, T., Bellini, E., Ferreira, P. G., Lagos, M., Noller, J. and Sawicki, I. (2017). 'Strong Constraints on Cosmological Gravity from GW170817 and GRB 170817A'. *Phys. Rev. Lett.* **119**, 251301. DOI: 10.1103/PhysRevLett.119.251301. arXiv: 1710.06394 [astro-ph.CO] (cited on p. 2).

Bauswein, A., Just, O., Janka, H.-T. and Stergioulas, N. (2017). 'Neutron-star Radius Constraints from GW170817 and Future Detections'. *Astrophys. J.* **850**, L34. DOI: 10.3847/2041-8213/aa9994. arXiv: 1710.06843 [astro-ph.HE] (cited on pp. 8, 114).

Baym, G. and Pines, D. (1971). 'Neutron starquakes and pulsar speedup.' *Ann. Phys.* **66**, 816. DOI: 10.1016/0003-4916(71)90084-4 (cited on p. 71).

Beheshtipour, B. and Papa, M. A. (2021). 'Deep learning for clustering of continuous gravitational wave candidates. II. Identification of low-SNR candidates'. *Phys. Rev. D* **103**, 064027. DOI: 10.1103/PhysRevD.103.064027. arXiv: 2012.04381 [gr-qc] (cited on p. 111).

Bergmann, P. G. (1957). 'Summary of the Chapel Hill Conference'. *Rev. Mod. Phys.* **29**, 352. DOI: 10.1103/RevModPhys.29.352 (cited on p. 1).

Bhattacharyya, S. and Chakrabarty, D. (2017). 'The Effect of Transient Accretion on the Spin-up of Millisecond Pulsars'. *Astrophys. J.* **835**, 4. DOI: 10.3847/1538-4357/835/1/4. arXiv: 1612.04962 [astro-ph.HE] (cited on pp. 39, 43, 48).

Bildsten, L. (1998). 'Gravitational Radiation and Rotation of Accreting Neutron Stars'. *Astrophys. J.* **501**, L89. DOI: 10.1086/311440. arXiv: astro-ph/9804325 [astro-ph] (cited on pp. 7, 39, 46, 47, 64, 91).

Binnington, T. and Poisson, E. (2009). 'Relativistic theory of tidal Love numbers'. *Phys. Rev. D* **80**, 084018. DOI: 10.1103/PhysRevD.80.084018. arXiv: 0906.1366 [gr-qc] (cited on pp. 30, 106, 115).

Birkhoff, G. D. and Langer, R. E. (1923). *Relativity and Modern Physics*. Cambridge, MA: Harvard University Press (cited on p. 36).

Biswas, B., Nandi, R., Char, P. and Bose, S. (2019). 'Role of crustal physics in the tidal deformation of a neutron star'. *Phys. Rev. D* **100**, 044056. DOI: 10.1103/PhysRevD.100.044056. arXiv: 1905.00678 [gr-qc] (cited on pp. 114, 118, 119, 124).

Blanchet, L. (2006). 'Gravitational Radiation from Post-Newtonian Sources and Inspiralling Compact Binaries'. *Living Rev. Relativity* **9**, 4. DOI: 10.12942/lrr-2006-4 (cited on p. 35).

Bondarescu, R., Teukolsky, S. A. and Wasserman, I. (2007). 'Spin evolution of accreting neutron stars: Nonlinear development of the r-mode instability'. *Phys. Rev. D* **76**,

064019. DOI: 10.1103/PhysRevD.76.064019. arXiv: 0704.0799 [astro-ph] (cited on pp. 47, 57, 58).

Bondi, H. (1957). 'Plane Gravitational Waves in General Relativity'. *Nature* **179**, 1072. DOI: 10.1038/1791072a0 (cited on p. 2).

Brown, E. F., Bildsten, L. and Rutledge, R. E. (1998). 'Crustal Heating and Quiescent Emission from Transiently Accreting Neutron Stars'. *Astrophys. J.* **504**, L95. DOI: 10.1086/311578. arXiv: astro-ph/9807179 [astro-ph] (cited on p. 55).

Capano, C. D., Tews, I., Brown, S. M., Margalit, B., De, S., Kumar, S., Brown, D. A., Krishnan, B. and Reddy, S. (2020). 'Stringent constraints on neutron-star radii from multimessenger observations and nuclear theory'. *Nat. Astron.* **4**, 625. DOI: 10.1038/s41550-020-1014-6. arXiv: 1908.10352 [astro-ph.HE] (cited on p. 109).

Carlson, J., Gandolfi, S., Pederiva, F., Pieper, S. C., Schiavilla, R., Schmidt, K. E. and Wiringa, R. B. (2015). 'Quantum Monte Carlo methods for nuclear physics'. *Rev. Mod. Phys.* **87**, 1067. DOI: 10.1103/RevModPhys.87.1067. arXiv: 1412.3081 [nucl-th] (cited on p. 109).

Chadwick, J. (1932). 'The existence of a neutron'. *Proc. R. Soc. Lond. A.* **136**, 692. DOI: 10.1098/rspa.1932.0112 (cited on p. 4).

Chakrabarty, D., Morgan, E. H., Muno, M. P., Galloway, D. K., Wijnands, R., van der Klis, M. and Markwardt, C. B. (2003). 'Nuclear-powered millisecond pulsars and the maximum spin frequency of neutron stars'. *Nature* **424**, 42. DOI: 10.1038/nature01732. arXiv: astro-ph/0307029 [astro-ph] (cited on p. 38).

Chamel, N. and Haensel, P. (2008). 'Physics of Neutron Star Crusts'. *Living Rev. Relativity* **11**, 10. DOI: 10.12942/lrr-2008-10. arXiv: 0812.3955 [astro-ph] (cited on p. 114).

Chandrasekhar, S. (1970). 'Solutions of Two Problems in the Theory of Gravitational Radiation'. *Phys. Rev. Lett.* **24**, 611. DOI: 10.1103/PhysRevLett.24.611 (cited on p. 56).

Chugunov, A. I. and Horowitz, C. J. (2010). 'Breaking stress of neutron star crust'. *Mon. Not. R. Astron. Soc.* **407**, L54. DOI: 10.1111/j.1745-3933.2010.00903.x. arXiv: 1006.2279 [astro-ph.SR] (cited on pp. 92, 112).

Ciolfi, R., Ferrari, V. and Gualtieri, L. (2010). 'Structure and deformations of strongly magnetized neutron stars with twisted-torus configurations'. *Mon. Not. R. Astron. Soc.* **406**, 2540. DOI: 10.1111/j.1365-2966.2010.16847.x. arXiv: 1003.2148 [astro-ph.SR] (cited on p. 106).

Cook, G. B., Shapiro, S. L. and Teukolsky, S. A. (1994). 'Rapidly Rotating Neutron Stars in General Relativity: Realistic Equations of State'. *Astrophys. J.* **424**, 823. DOI: 10.1086/173934 (cited on p. 38).

Creminelli, P. and Vernizzi, F. (2017). 'Dark Energy after GW170817 and GRB170817A'. *Phys. Rev. Lett.* **119**, 251302. DOI: 10.1103/PhysRevLett.119.251302. arXiv: 1710.05877 [astro-ph.CO] (cited on p. 2).

Cutler, C. *et al.* (1993). 'The last three minutes: Issues in gravitational-wave measurements of coalescing compact binaries'. *Phys. Rev. Lett.* **70**, 2984. DOI: 10.1103/PhysRevLett.70.2984. arXiv: astro-ph/9208005 [astro-ph] (cited on p. 114).

Cutler, C. and Thorne, K. S. (2002). 'An Overview of Gravitational-Wave Sources', gr. arXiv: gr-qc/0204090 [gr-qc] (cited on p. 114).

Cutler, C. (2002). 'Gravitational waves from neutron stars with large toroidal B fields'. *Phys. Rev. D* **66**, 084025. DOI: 10.1103/PhysRevD.66.084025. arXiv: gr-qc/0206051 [gr-qc] (cited on p. 47).

D'Angelo, C. R. (2017). 'Spin equilibrium in strongly magnetized accreting stars'. *Mon. Not. R. Astron. Soc.* **470**, 3316. DOI: 10.1093/mnras/stx1306. arXiv: 1609.08654 [astro-ph.SR] (cited on pp. 39, 42–44, 48).

Damour, T. and Nagar, A. (2009). 'Relativistic tidal properties of neutron stars'. *Phys. Rev. D* **80**, 084035. DOI: 10.1103/PhysRevD.80.084035. arXiv: 0906.0096 [gr-qc] (cited on pp. 106, 115).

De, S., Finstad, D., Lattimer, J. M., Brown, D. A., Berger, E. and Biwer, C. M. (2018). 'Tidal Deformabilities and Radii of Neutron Stars from the Observation of GW170817'. *Phys. Rev. Lett.* **121**, 091102. DOI: 10.1103/PhysRevLett.121.091102. arXiv: 1804.08583 [astro-ph.HE] (cited on pp. 9, 114).

Dergachev, V. and Papa, M. A. (2020). 'Results from the First All-Sky Search for Continuous Gravitational Waves from Small-Ellipticity Sources'. *Phys. Rev. Lett.* **125**, 171101. DOI: 10.1103/PhysRevLett.125.171101. arXiv: 2004.08334 [gr-qc] (cited on pp. 8, 111).

— (2021). 'Results from high-frequency all-sky search for continuous gravitational waves from small-ellipticity sources'. *Phys. Rev. D* **103**, 063019. DOI: 10.1103/PhysRevD.103.063019. arXiv: 2012.04232 [gr-qc] (cited on pp. 8, 111).

Done, C., Gierliński, M. and Kubota, A. (2007). 'Modelling the behaviour of accretion flows in X-ray binaries. Everything you always wanted to know about accretion but were afraid to ask'. *Astron. Astrophys.* **15**, 1. DOI: 10.1007/s00159-007-0006-1. arXiv: 0708.0148 [astro-ph] (cited on p. 43).

Douchin, F. and Haensel, P. (2001). 'A unified equation of state of dense matter and neutron star structure'. *Astron. Astrophys.* **380**, 151. DOI: 10.1051/0004-6361:20011402. arXiv: astro-ph/0111092 [astro-ph] (cited on pp. 70, 103, 109, 117, 118).

Eddington, A. S. (1922). 'The propagation of gravitational waves'. *Proc. R. Soc. Lond. A* **102**, 268. DOI: 10.1098/rspa.1922.0085 (cited on p. 34).

Einstein, A. (1916a). 'Die Grundlage der allgemeinen Relativitätstheorie'. *Ann. Phys.* **354**, 769. DOI: 10.1002/andp.19163540702 (cited on p. 1).

— (1916b). 'Näherungsweise Integration der Feldgleichungen der Gravitation'. *Sitzungsber. K. Preuß. Akad. Wiss.*, 688 (cited on p. 1).

— (1918). 'Über Gravitationswellen'. *Sitzungsber. K. Preuß. Akad. Wiss.*, 154 (cited on pp. 1, 36).

Einstein, A. and Rosen, N. (1937). 'On gravitational waves'. *J. Franklin Inst.* **223**, 43. ISSN: 0016-0032. DOI: https://doi.org/10.1016/S0016-0032(37)90583-0. URL: https://www.sciencedirect.com/science/article/pii/S0016003237905830 (cited on p. 34).

Epelbaum, E., Hammer, H.-W. and Meißner, U.-G. (2009). 'Modern theory of nuclear forces'. *Rev. Mod. Phys.* **81**, 1773. DOI: 10.1103/RevModPhys.81.1773. arXiv: 0811.1338 [nucl-th] (cited on p. 109).

Ezquiaga, J. M. and Zumalacárregui, M. (2017). 'Dark Energy After GW170817: Dead Ends and the Road Ahead'. *Phys. Rev. Lett.* **119**, 251304. DOI: 10.1103/PhysRevLett.119.251304. arXiv: 1710.05901 [astro-ph.CO] (cited on p. 2).

Finn, L. S. (1990). 'Non-radial pulsations of neutron stars with a crust'. *Mon. Not. R. Astron. Soc.* **245**, 82 (cited on p. 143).

Frieben, J. and Rezzolla, L. (2012). 'Equilibrium models of relativistic stars with a toroidal magnetic field'. *Mon. Not. R. Astron. Soc.* **427**, 3406. DOI: 10.1111/j.1365-2966.2012.22027.x. arXiv: 1207.4035 [gr-qc] (cited on p. 106).

Friedman, J. L. and Schutz, B. F. (1978a). 'Lagrangian perturbation theory of nonrelativistic fluids.' *Astrophys. J.* **221**, 937. DOI: 10.1086/156098 (cited on p. 23).

— (1978b). 'Secular instability of rotating Newtonian stars'. *Astrophys. J.* **222**, 281. DOI: 10.1086/156143 (cited on p. 56).

Friedman, J. L. and Morsink, S. M. (1998). 'Axial Instability of Rotating Relativistic Stars'. *Astrophys. J.* **502**, 714. DOI: 10.1086/305920. arXiv: gr-qc/9706073 [gr-qc] (cited on p. 56).

Ghosh, P. and Lamb, F. K. (1978). 'Disk accretion by magnetic neutron stars.' *Astrophys. J.* **223**, L83. DOI: 10.1086/182734 (cited on p. 38).

— (1979). 'Accretion by rotating magnetic neutron stars. III - Accretion torques and period changes in pulsating X-ray sources'. *Astrophys. J.* **234**, 296. DOI: 10.1086/157498 (cited on pp. 40, 41).

Gittins, F. and Andersson, N. (2019). 'Population synthesis of accreting neutron stars emitting gravitational waves'. *Mon. Not. R. Astron. Soc.* **488**, 99. DOI: 10.1093/mnras/stz1719. arXiv: 1811.00550 [astro-ph.HE] (cited on pp. xv, 37).

Gittins, F., Andersson, N. and Pereira, J. P. (2020). 'Tidal deformations of neutron stars with elastic crusts'. *Phys. Rev. D* **101**, 103025. DOI: 10.1103/PhysRevD.101.103025. arXiv: 2003.05449 [astro-ph.HE] (cited on pp. xv, 77, 83, 106, 113, 114).

Gittins, F., Andersson, N. and Jones, D. I. (2021). 'Modelling neutron star mountains'. *Mon. Not. R. Astron. Soc.* **500**, 5570. DOI: 10.1093/mnras/staa3635. arXiv: 2009.12794 [astro-ph.HE] (cited on pp. xv, 63, 64, 106).

Gittins, F. and Andersson, N. (2021). 'Modelling neutron star mountains in relativity'. *Mon. Not. R. Aston. Soc.* **507**, 116. DOI: 10.1093/mnras/stab2048. arXiv: 2105.06493 [astro-ph.HE] (cited on pp. xv, 93).

Goriely, S., Chamel, N. and Pearson, J. M. (2013). 'Further explorations of Skyrme-Hartree-Fock-Bogoliubov mass formulas. XIII. The 2012 atomic mass evaluation and

the symmetry coefficient'. *Phys. Rev. C* **88**, 024308. DOI: 10.1103/PhysRevC.88.024308 (cited on p. 103).

Gralla, S. E. (2018). 'On the ambiguity in relativistic tidal deformability'. *Classical Quant. Grav.* **35**, 085002. DOI: 10.1088/1361-6382/aab186. arXiv: 1710.11096 [gr-qc] (cited on p. 29).

Haensel, P. and Zdunik, J. L. (1990). 'Non-equilibrium processes in the crust of an accreting neutron star'. *Astron. Astrophys.* **227**, 431 (cited on p. 54).

Hartle, J. B. (2003). *Gravity: An Introduction to Einstein's General Relativity*. San Francisco, CA: Addison-Wesley (cited on p. 17).

Haskell, B., Jones, D. I. and Andersson, N. (2006). 'Mountains on neutron stars: accreted versus non-accreted crusts'. *Mon. Not. R. Astron. Soc.* **373**, 1423. DOI: 10.1111/j.1365-2966.2006.10998.x. arXiv: astro-ph/0609438 [astro-ph] (cited on pp. 47, 64, 68–70, 77, 78, 81, 83, 85, 86, 90, 91).

Haskell, B., Samuelsson, L., Glampedakis, K. and Andersson, N. (2008). 'Modelling magnetically deformed neutron stars'. *Mon. Not. R. Astron. Soc.* **385**, 531. DOI: 10.1111/j.1365-2966.2008.12861.x. arXiv: 0705.1780 [astro-ph] (cited on p. 47).

Haskell, B. and Patruno, A. (2017). 'Are Gravitational Waves Spinning Down PSR J 1023 +0038 ?' *Phys. Rev. Lett.* **119**, 161103. DOI: 10.1103/PhysRevLett.119.161103. arXiv: 1703.08374 [astro-ph.HE] (cited on pp. 47, 54, 55).

Haskell, B., Zdunik, J. L., Fortin, M., Bejger, M., Wijnands, R. and Patruno, A. (2018). 'Fundamental physics and the absence of sub-millisecond pulsars'. *Astron. Astrophys.* **620**, A69. DOI: 10.1051/0004-6361/201833521. arXiv: 1805.11277 [astro-ph.HE] (cited on p. 38).

Hebeler, K. and Schwenk, A. (2010). 'Chiral three-nucleon forces and neutron matter'. *Phys. Rev. C* **82**, 014314. DOI: 10.1103/PhysRevC.82.014314. arXiv: 0911.0483 [nucl-th] (cited on p. 109).

Hessels, J. W. T., Ransom, S. M., Stairs, I. H., Freire, P. C. C., Kaspi, V. M. and Camilo, F. (2006). 'A Radio Pulsar Spinning at 716 Hz'. *Science* **311**, 1901. DOI: 10.1126/science.1123430. arXiv: astro-ph/0601337 [astro-ph] (cited on p. 38).

Hessels, J. W. T. (2008). 'The Observed Spin Distributions of Millisecond Radio and X-ray Pulsars'. *AIP Conf. Proc.* **1068**, 130. DOI: 10.1063/1.3031183. arXiv: 0903.0493 [astro-ph.SR] (cited on p. 46).

Hewish, A., Bell, S. J., Pilkington, J. D. H., Scott, P. F. and Collins, R. A. (1968). 'Observation of a Rapidly Pulsating Radio Source'. *Nature* **217**, 709. DOI: 10.1038/217709a0 (cited on p. 4).

Heyl, J. S. (2002). 'Low-Mass X-Ray Binaries May Be Important Laser Interferometer Gravitational-Wave Observatory Sources After All'. *Astrophys. J.* **574**, L57. DOI: 10.1086/342263 (cited on p. 47).

Hinderer, T. (2008). 'Tidal Love Numbers of Neutron Stars'. *Astrophys. J.* **677**, 1216. DOI: 10.1086/533487. arXiv: 0711.2420 [astro-ph] (cited on pp. 28, 106, 114–116).

Hinderer, T., Lackey, B. D., Lang, R. N. and Read, J. S. (2010). 'Tidal deformability of neutron stars with realistic equations of state and their gravitational wave signatures in binary inspiral'. *Phys. Rev. D* **81**, 123016. DOI: 10.1103/PhysRevD.81.123016. arXiv: 0911.3535 [astro-ph.HE] (cited on p. 106).

Ho, W. C. G., Andersson, N. and Haskell, B. (2011). 'Revealing the Physics of r Modes in Low-Mass X-Ray Binaries'. *Phys. Rev. Lett.* **107**, 101101. DOI: 10.1103/PhysRevLett.107.101101. arXiv: 1107.5064 [astro-ph.HE] (cited on p. 57).

Ho, W. C. G., Klus, H., Coe, M. J. and Andersson, N. (2014). 'Equilibrium spin pulsars unite neutron star populations'. *Mon. Not. R. Astron. Soc.* **437**, 3664. DOI: 10.1093/mnras/stt2193. arXiv: 1311.1969 [astro-ph.SR] (cited on pp. 41, 48).

Horowitz, C. J. and Kadau, K. (2009). 'Breaking Strain of Neutron Star Crust and Gravitational Waves'. *Phys. Rev. Lett.* **102**, 191102. DOI: 10.1103/PhysRevLett.102.191102. arXiv: 0904.1986 [astro-ph.SR] (cited on pp. 69, 84, 91, 105, 122).

Hulse, R. A. and Taylor, J. H. (1975). 'Discovery of a pulsar in a binary system.' *Astrophys. J.* **195**, L51. DOI: 10.1086/181708 (cited on pp. 4, 36).

Ioka, K. and Sasaki, M. (2004). 'Relativistic Stars with Poloidal and Toroidal Magnetic Fields and Meridional Flow'. *Astrophys. J.* **600**, 296. DOI: 10.1086/379650. arXiv: astro-ph/0305352 [astro-ph] (cited on p. 106).

Isaacson, R. A. (1968). 'Gravitational Radiation in the Limit of High Frequency. II. Nonlinear Terms and the Effective Stress Tensor'. *Phys. Rev.* **166** (5), 1272. DOI: 10.1103/PhysRev.166.1272. URL: https://link.aps.org/doi/10.1103/PhysRev.166.1272 (cited on p. 35).

Jebsen, J. T. (1921). 'On the General Spherically Symmetric Solutions of Einstein's Gravitational Equations in Vacuo'. *Ark. Mat. Astron. Fys.* **15**, 18 (cited on p. 36).

Johnson-McDaniel, N. K. and Owen, B. J. (2013). 'Maximum elastic deformations of relativistic stars'. *Phys. Rev. D* **88**, 044004. DOI: 10.1103/PhysRevD.88.044004. arXiv: 1208.5227 [astro-ph.SR] (cited on pp. 64, 68, 70, 74–77, 82, 90, 104, 106).

Jones, D. I. (2002). 'Gravitational waves from rotating strained neutron stars'. *Classical Quant. Grav.* **19**, 1255. DOI: 10.1088/0264-9381/19/7/304. arXiv: gr-qc/0111007 [gr-qc] (cited on p. 85).

Jones, P. B. (2003). 'Nature of Fault Planes in Solid Neutron Star Matter'. *Astrophys. J.* **595**, 342. DOI: 10.1086/377351. arXiv: astro-ph/0210207 [astro-ph] (cited on pp. 92, 112).

Kasen, D., Metzger, B., Barnes, J., Quataert, E. and Ramirez-Ruiz, E. (2017). 'Origin of the heavy elements in binary neutron-star mergers from a gravitational-wave event'. *Nature* **551**, 80. DOI: 10.1038/nature24453. arXiv: 1710.05463 [astro-ph.HE] (cited on p. 2).

Keer, L. and Jones, D. I. (2015). 'Developing a model for neutron star oscillations following starquakes'. *Mon. Not. R. Astron. Soc.* **446**, 865. DOI: 10.1093/mnras/stu2123. arXiv: 1408.1249 [astro-ph.SR] (cited on p. 71).

Kennefick, D. (2007). *Traveling at the Speed of Thought: Einstein and the Quest for Gravitational Waves*. Princeton, NJ: Princeton University Press (cited on p. 34).

Kojima, Y. (1992). 'Equations governing the nonradial oscillations of a slowly rotating relativistic star'. *Phys. Rev. D* **46**, 4289. DOI: 10.1103/PhysRevD.46.4289 (cited on p. 94).

Krüger, C. J., Ho, W. C. G. and Andersson, N. (2015). 'Seismology of adolescent neutron stars: Accounting for thermal effects and crust elasticity'. *Phys. Rev. D* **92**, 063009. DOI: 10.1103/PhysRevD.92.063009. arXiv: 1402.5656 [gr-qc] (cited on p. 139).

Krüger, T., Tews, I., Hebeler, K. and Schwenk, A. (2013). 'Neutron matter from chiral effective field theory interactions'. *Phys. Rev. C* **88**, 025802. DOI: 10.1103/PhysRevC.88.025802. arXiv: 1304.2212 [nucl-th] (cited on p. 109).

Lasota, J. P. (1997). 'Disc Instabilities and "Soft" X-Ray Transients'. *IAU Colloq. 163: Accretion Phenomena and Related Outflows*. Ed. by D. T. Wickramasinghe, G. V. Bicknell and L. Ferrario. Vol. 121. Astronomical Society of the Pacific Conference Series, 351. arXiv: astro-ph/9610068 [astro-ph] (cited on p. 43).

Lattimer, J. M. and Prakash, M. (2007). 'Neutron star observations: Prognosis for equation of state constraints'. *Phys. Rep.* **442**, 109. DOI: 10.1016/j.physrep.2007.02.003. arXiv: astro-ph/0612440 [astro-ph] (cited on p. 38).

Levin, Y. (1999). 'Runaway Heating by R-Modes of Neutron Stars in Low-Mass X-Ray Binaries'. *Astrophys. J.* **517**, 328. DOI: 10.1086/307196. arXiv: astro-ph/9810471 [astro-ph] (cited on p. 47).

Lin, L.-M., Andersson, N. and Comer, G. L. (2008). 'Oscillations of general relativistic multifluid/multilayer compact stars'. *Phys. Rev. D* **78**, 083008. DOI: 10.1103/PhysRevD.78.083008. arXiv: 0709.0660 [gr-qc] (cited on p. 139).

Machleidt, R. and Entem, D. R. (2011). 'Chiral effective field theory and nuclear forces'. *Phys. Rep.* **503**, 1. DOI: 10.1016/j.physrep.2011.02.001. arXiv: 1105.2919 [nucl-th] (cited on p. 109).

Maggiore, M. (2008). *Gravitational Waves: Volume 1: Theory and Experiments*. Oxford: Oxford University Press. DOI: 10.1093/acprof:oso/9780198570745.001.0001 (cited on p. 30).

Maggiore, M. *et al.* (2020). 'Science case for the Einstein telescope'. *J. Cosmol. Astropart. Phys.* **2020**, 050. DOI: 10.1088/1475-7516/2020/03/050. arXiv: 1912.02622 [astro-ph.CO] (cited on pp. 111, 119).

Melatos, A. and Payne, D. J. B. (2005). 'Gravitational Radiation from an Accreting Millisecond Pulsar with a Magnetically Confined Mountain'. *Astrophys. J.* **623**, 1044. DOI: 10.1086/428600. arXiv: astro-ph/0503287 [astro-ph] (cited on pp. 47, 91).

Miller, M. C. (2013). 'Astrophysical Constraints on Dense Matter in Neutron Stars'. arXiv: 1312.0029 [astro-ph.HE] (cited on p. 8).

Miller, M. C. and Lamb, F. K. (2016). 'Observational constraints on neutron star masses and radii'. *Eur. Phys. J. A* **52**, 63. DOI: 10.1140/epja/i2016-16063-8. arXiv: 1604.03894 [astro-ph.HE] (cited on p. 8).

Misner, C. W., Thorne, K. S. and Wheeler, J. A. (1973). *Gravitation*. San Francisco, CA: Freeman (cited on p. 17).

Most, E. R., Weih, L. R., Rezzolla, L. and Schaffner-Bielich, J. (2018). 'New Constraints on Radii and Tidal Deformabilities of Neutron Stars from GW170817'. *Phys. Rev. Lett.* **120**, 261103. DOI: 10.1103/PhysRevLett.120.261103. arXiv: 1803.00549 [gr-qc] (cited on pp. 9, 114).

Nättilä, J., Miller, M. C., Steiner, A. W., Kajava, J. J. E., Suleimanov, V. F. and Poutanen, J. (2017). 'Neutron star mass and radius measurements from atmospheric model fits to X-ray burst cooling tail spectra'. *Astron. Astrophys.* **608**, A31. DOI: 10.1051/0004-6361/201731082. arXiv: 1709.09120 [astro-ph.HE] (cited on p. 8).

Nayyar, M. and Owen, B. J. (2006). 'R-modes of accreting hyperon stars as persistent sources of gravitational waves'. *Phys. Rev. D* **73**, 084001. DOI: 10.1103/PhysRevD.73.084001. arXiv: astro-ph/0512041 [astro-ph] (cited on p. 47).

Ogata, S. and Ichimaru, S. (1990). 'First-principles calculations of shear moduli for Monte Carlo-simulated Coulomb solids'. *Phys. Rev. A* **42**, 4867. DOI: 10.1103/PhysRevA.42.4867 (cited on p. 103).

Oppenheimer, J. R. and Volkoff, G. M. (1939). 'On Massive Neutron Cores'. *Phys. Rev.* **55**, 374. DOI: 10.1103/PhysRev.55.374 (cited on pp. 4, 20).

Osborne, E. L. and Jones, D. I. (2020). 'Gravitational waves from magnetically induced thermal neutron star mountains'. *Mon. Not. R. Astron. Soc.* **494**, 2839. DOI: 10.1093/mnras/staa858. arXiv: 1910.04453 [astro-ph.HE] (cited on p. 64).

Ottosen, N. S. and Ristinmaa, M. (2005). *The Mechanics of Constitutive Modeling*. New York, NY: Elsevier. DOI: 10.1016/B978-0-08-044606-6.X5000-0 (cited on p. 91).

Owen, B. J., Lindblom, L., Cutler, C., Schutz, B. F., Vecchio, A. and Andersson, N. (1998). 'Gravitational waves from hot young rapidly rotating neutron stars'. *Phys. Rev. D* **58**, 084020. DOI: 10.1103/PhysRevD.58.084020. arXiv: gr-qc/9804044 [gr-qc] (cited on p. 57).

Owen, B. J. (2005). 'Maximum Elastic Deformations of Compact Stars with Exotic Equations of State'. *Phys. Rev. Lett.* **95**, 211101. DOI: 10.1103/PhysRevLett.95.211101. arXiv: astro-ph/0503399 [astro-ph] (cited on p. 45).

Özel, F., Psaltis, D., Güver, T., Baym, G., Heinke, C. and Guillot, S. (2016). 'The Dense Matter Equation of State from Neutron Star Radius and Mass Measurements'. *Astrophys. J.* **820**, 28. DOI: 10.3847/0004-637X/820/1/28. arXiv: 1505.05155 [astro-ph.HE] (cited on p. 8).

Papaloizou, J. and Pringle, J. E. (1978). 'Gravitational radiation and the stability of rotating stars'. *Mon. Not. R. Astron. Soc.* **184**, 501. DOI: 10.1093/mnras/184.3.501 (cited on pp. 6, 38, 39).

Papitto, A., Torres, D. F., Rea, N. and Tauris, T. M. (2014). 'Spin frequency distributions of binary millisecond pulsars'. *Astron. Astrophys.* **566**, A64. DOI: 10.1051/0004-6361/201321724. arXiv: 1403.6775 [astro-ph.HE] (cited on p. 46).

Parfrey, K., Spitkovsky, A. and Beloborodov, A. M. (2016). 'Torque Enhancement, Spin Equilibrium, and Jet Power from Disk-Induced Opening of Pulsar Magnetic Fields'. *Astrophys. J.* **822**, 33. DOI: 10.3847/0004-637X/822/1/33. arXiv: 1507.08627 [astro-ph.HE] (cited on p. 59).

Patruno, A. (2010). 'The Accreting Millisecond X-ray Pulsar IGR J00291+5934: Evidence for a Long Timescale Spin Evolution'. *Astrophys. J.* **722**, 909. DOI: 10.1088/0004-637X/722/1/909. arXiv: 1006.0815 [astro-ph.HE] (cited on p. 38).

Patruno, A., Haskell, B. and D'Angelo, C. (2012). 'Gravitational Waves and the Maximum Spin Frequency of Neutron Stars'. *Astrophys. J.* **746**, 9. DOI: 10.1088/0004-637X/746/1/9. arXiv: 1109.0536 [astro-ph.HE] (cited on p. 38).

Patruno, A., Haskell, B. and Andersson, N. (2017). 'The Spin Distribution of Fast-spinning Neutron Stars in Low-mass X-Ray Binaries: Evidence for Two Subpopulations'. *Astrophys. J.* **850**, 106. DOI: 10.3847/1538-4357/aa927a. arXiv: 1705.07669 [astro-ph.HE] (cited on p. 46).

Patruno, A. and Watts, A. L. (2021). 'Accreting Millisecond X-ray Pulsars'. *Astrophys. Sp. Sci. Lib.* **461**, 143. DOI: 10.1007/978-3-662-62110-3_4. arXiv: 1206.2727 [astro-ph.HE] (cited on p. 38).

Payne, D. J. B. and Melatos, A. (2006). 'Frequency Spectrum of Gravitational Radiation from Global Hydromagnetic Oscillations of a Magnetically Confined Mountain on an Accreting Neutron Star'. *Astrophys. J.* **641**, 471. DOI: 10.1086/498855. arXiv: astro-ph/0510053 [astro-ph] (cited on pp. 47, 91).

Pearson, J. M., Chamel, N., Potekhin, A. Y., Fantina, A. F., Ducoin, C., Dutta, A. K. and Goriely, S. (2018). 'Unified equations of state for cold non-accreting neutron stars with Brussels-Montreal functionals - I. Role of symmetry energy'. *Mon. Not. R. Astron. Soc.* **481**, 2994. DOI: 10.1093/mnras/sty2413. arXiv: 1903.04981 [astro-ph.HE] (cited on pp. 103, 112).

Penner, A. J., Andersson, N., Samuelsson, L., Hawke, I. and Jones, D. I. (2011). 'Tidal deformations of neutron stars: The role of stratification and elasticity'. *Phys. Rev. D* **84**, 103006. DOI: 10.1103/PhysRevD.84.103006. arXiv: 1107.0669 [astro-ph.SR] (cited on pp. 95, 114, 117, 118, 121, 123, 124).

Penner, A. J., Andersson, N., Jones, D. I., Samuelsson, L. and Hawke, I. (2012). 'Crustal Failure during Binary Inspiral'. *Astrophys. J.* **749**, L36. DOI: 10.1088/2041-8205/749/2/L36. arXiv: 1109.5041 [astro-ph.SR] (cited on pp. 119, 123–125).

Pereira, J. P., Bejger, M., Andersson, N. and Gittins, F. (2020). 'Tidal Deformations of Hybrid Stars with Sharp Phase Transitions and Elastic Crusts'. *Astrophys. J.* **895**, 28. DOI: 10.3847/1538-4357/ab8aca. arXiv: 2003.10781 [gr-qc] (cited on p. 102).

Pian, E. *et al.* (2017). 'Spectroscopic identification of r-process nucleosynthesis in a double neutron-star merger'. *Nature* **551**, 67. DOI: 10.1038/nature24298. arXiv: 1710.05858 [astro-ph.HE] (cited on p. 2).

Pirani, F. A. E. (1956). 'On the Physical significance of the Riemann tensor'. *Acta Phys. Polon.* **15**, 389 (cited on p. 2).

— (1957). 'Invariant Formulation of Gravitational Radiation Theory'. *Phys. Rev.* **105** (3), 1089. DOI: 10.1103/PhysRev.105.1089 (cited on p. 2).

Poisson, E. and Will, C. M. (2014). *Gravity*. Cambridge: Cambridge University Press. DOI: 10.1017/CBO9781139507486 (cited on p. 35).

Possenti, A., Colpi, M., D'Amico, N. and Burderi, L. (1998). 'Population Synthesis of Millisecond and Submillisecond Pulsars'. *Astrophys. J.* **497**, L97. DOI: 10.1086/311286. arXiv: astro-ph/9802257 [astro-ph] (cited on pp. 49, 50).

Potekhin, A. Y., Fantina, A. F., Chamel, N., Pearson, J. M. and Goriely, S. (2013). 'Analytical representations of unified equations of state for neutron-star matter'. *Astron. Astrophys.* **560**, A48. DOI: 10.1051/0004-6361/201321697. arXiv: 1310.0049 [astro-ph.SR] (cited on pp. 21, 117, 118).

Pringle, J. E. and Rees, M. J. (1972). 'Accretion Disc Models for Compact X-Ray Sources'. *Astron. Astrophys.* **21**, 1 (cited on p. 40).

Priymak, M., Melatos, A. and Payne, D. J. B. (2011). 'Quadrupole moment of a magnetically confined mountain on an accreting neutron star: effect of the equation of state'. *Mon. Not. R. Astron. Soc.* **417**, 2696. DOI: 10.1111/j.1365-2966.2011.19431.x. arXiv: 1109.1040 [astro-ph.HE] (cited on pp. 47, 91).

Raaijmakers, G. *et al.* (2020). 'Constraining the Dense Matter Equation of State with Joint Analysis of NICER and LIGO/Virgo Measurements'. *Astrophys. J.* **893**, L21. DOI: 10.3847/2041-8213/ab822f. arXiv: 1912.11031 [astro-ph.HE] (cited on p. 109).

Radhakrishnan, V. and Srinivasan, G. (1982). 'On the origin of the recently discovered ultra-rapid pulsar'. *Curr. Sci.* **51**, 1096 (cited on pp. 5, 38).

Raithel, C. A., Özel, F. and Psaltis, D. (2018). 'Tidal Deformability from GW170817 as a Direct Probe of the Neutron Star Radius'. *Astrophys. J.* **857**, L23. DOI: 10.3847/2041-8213/aabcbf. arXiv: 1803.07687 [astro-ph.HE] (cited on pp. 9, 114).

Regge, T. and Wheeler, J. A. (1957). 'Stability of a Schwarzschild Singularity'. *Phys. Rev.* **108**, 1063. DOI: 10.1103/PhysRev.108.1063 (cited on p. 94).

Riley, T. E. *et al.* (2019). 'A NICER View of PSR J0030+0451: Millisecond Pulsar Parameter Estimation'. *Astrophys. J.* **887**, L21. DOI: 10.3847/2041-8213/ab481c. arXiv: 1912.05702 [astro-ph.HE] (cited on p. 109).

— (2021). 'A NICER View of the Massive Pulsar PSR J0740+6620 Informed by Radio Timing and XMM-Newton Spectroscopy'. arXiv: 2105.06980 [astro-ph.HE] (cited on p. 109).

Salmi, T., Nättilä, J. and Poutanen, J. (2018). 'Bayesian parameter constraints for neutron star masses and radii using X-ray timing observations of accretion-powered millisecond pulsars'. *Astron. Astrophys.* **618**, A161. DOI: 10.1051/0004-6361/201833348. arXiv: 1805.01149 [astro-ph.HE] (cited on p. 8).

Schreier, E., Levinson, R., Gursky, H., Kellogg, E., Tananbaum, H. and Giacconi, R. (1972). 'Evidence for the Binary Nature of Centaurus X-3 from UHURU X-Ray Observations.' *Astrophys. J.* **172**, L79. DOI: 10.1086/180896 (cited on p. 5).

Schutz, B. F. (1985). *A First Course in General Relativity*. Cambridge: Cambridge University Press. DOI: 10.1017/CBO9780511984181 (cited on p. 17).

— (1986). 'Determining the Hubble constant from gravitational wave observations'. *Nature* **323**, 310. DOI: 10.1038/323310a0 (cited on p. 2).

Schwarzschild, K. (1916). 'Über das Gravitationsfeld eines Massenpunktes nach der Einsteinschen Theorie'. *Sitzungsber. K. Preuß. Akad. Wiss.*, 189 (cited on p. 19).

Singh, N., Haskell, B., Mukherjee, D. and Bulik, T. (2020). 'Asymmetric accretion and thermal 'mountains' in magnetized neutron star crusts'. *Mon. Not. R. Astron. Soc.* **493**, 3866. DOI: 10.1093/mnras/staa442. arXiv: 1908.05038 [astro-ph.HE] (cited on p. 64).

Smoluchowski, R. and Welch, D. O. (1970). 'Progressive Deformation of the Crust of Pulsars'. *Phys. Rev. Lett.* **24**, 1191. DOI: 10.1103/PhysRevLett.24.1191 (cited on pp. 92, 112).

Spitkovsky, A. (2006). 'Time-dependent Force-free Pulsar Magnetospheres: Axisymmetric and Oblique Rotators'. *Astrophys. J.* **648**, L51. DOI: 10.1086/507518. arXiv: astro-ph/0603147 [astro-ph] (cited on p. 43).

Steiner, A. W., Lattimer, J. M. and Brown, E. F. (2010). 'The Equation of State from Observed Masses and Radii of Neutron Stars'. *Astrophys. J.* **722**, 33. DOI: 10.1088/0004-637X/722/1/33. arXiv: 1005.0811 [astro-ph.HE] (cited on p. 8).

Steiner, A. W., Heinke, C. O., Bogdanov, S., Li, C. K., Ho, W. C. G., Bahramian, A. and Han, S. (2018). 'Constraining the mass and radius of neutron stars in globular clusters'. *Mon. Not. R. Astron. Soc.* **476**, 421. DOI: 10.1093/mnras/sty215. arXiv: 1709.05013 [astro-ph.HE] (cited on p. 8).

Steltner, B. *et al.* (2021). 'Einstein@Home All-sky Search for Continuous Gravitational Waves in LIGO O2 Public Data'. *Astrophys. J.* **909**, 79. DOI: 10.3847/1538-4357/abc7c9. arXiv: 2009.12260 [astro-ph.HE] (cited on pp. 8, 111).

Tews, I., Carlson, J., Gandolfi, S. and Reddy, S. (2018). 'Constraining the Speed of Sound inside Neutron Stars with Chiral Effective Field Theory Interactions and Observations'. *Astrophys. J.* **860**, 149. DOI: 10.3847/1538-4357/aac267. arXiv: 1801.01923 [nucl-th] (cited on p. 109).

Thorne, K. S. and Campolattaro, A. (1967). 'Non-Radial Pulsation of General-Relativistic Stellar Models. I. Analytic Analysis for $l \geq 2$'. *Astrophys. J.* **149**, 591. DOI: 10.1086/149288 (cited on p. 94).

Thorne, K. S. (1980). 'Multipole expansions of gravitational radiation'. *Rev. Mod. Phys.* **52**, 299. DOI: 10.1103/RevModPhys.52.299 (cited on pp. 28, 115).

Thorne, K. S. and Blandford, R. D. (2017). *Modern Classical Physics: Optics, Fluids, Plasmas, Elasticity, Relativity, and Statistical Physics*. Princeton, NJ: Princeton University Press (cited on p. 14).

Tolman, R. C. (1939). 'Static Solutions of Einstein's Field Equations for Spheres of Fluid'. *Phys. Rev.* **55**, 364. DOI: 10.1103/PhysRev.55.364 (cited on pp. 4, 20).

Tsang, D., Read, J. S., Hinderer, T., Piro, A. L. and Bondarescu, R. (2012). 'Resonant Shattering of Neutron Star Crusts'. *Phys. Rev. Lett.* **108**, 011102. DOI: 10.1103/PhysRevLett.108.011102. arXiv: 1110.0467 [astro-ph.HE] (cited on p. 123).

Ushomirsky, G., Cutler, C. and Bildsten, L. (2000). 'Deformations of accreting neutron star crusts and gravitational wave emission'. *Mon. Not. R. Astron. Soc.* **319**, 902. DOI: 10.1046/j.1365-8711.2000.03938.x. arXiv: astro-ph/0001136 [astro-ph] (cited on pp. 47, 54–56, 64, 66–71, 74–77, 80, 82, 83, 90–92, 106, 111, 112).

Ushomirsky, G. and Rutledge, R. E. (2001). 'Time-variable emission from transiently accreting neutron stars in quiescence due to deep crustal heating'. *Mon. Not. R. Astron. Soc.* **325**, 1157. DOI: 10.1046/j.1365-8711.2001.04515.x. arXiv: astro-ph/0101141 [astro-ph] (cited on p. 54).

van Kolck, U. (1994). 'Few-nucleon forces from chiral Lagrangians'. *Phys. Rev. C* **49**, 2932. DOI: 10.1103/PhysRevC.49.2932 (cited on p. 109).

Wagoner, R. V. (1975). 'Test for the existence of gravitational radiation.' *Astrophys. J.* **196**, L63. DOI: 10.1086/181745 (cited on p. 4).

— (1984). 'Gravitational radiation from accreting neutron stars'. *Astrophys. J.* **278**, 345. DOI: 10.1086/161798 (cited on pp. 6, 38, 39).

— (2002). 'Conditions for Steady Gravitational Radiation from Accreting Neutron Stars'. *Astrophys. J.* **578**, L63. DOI: 10.1086/344502. arXiv: astro-ph/0207589 [astro-ph] (cited on p. 47).

Wang, M., Audi, G., Kondev, F. G., Huang, W. J., Naimi, S. and Xu, X. (2017). 'The AME2016 atomic mass evaluation (II). Tables, graphs and references'. *Chin. Phys. C* **41**, 030003. DOI: 10.1088/1674-1137/41/3/030003 (cited on p. 103).

Wang, Y.-M. (1995). 'On the Torque Exerted by a Magnetically Threaded Accretion Disk'. *Astrophys. J.* **449**, L153. DOI: 10.1086/309649 (cited on p. 41).

— (1996). 'Location of the Inner Radius of a Magnetically Threaded Accretion Disk'. *Astrophys. J.* **465**, L111. DOI: 10.1086/310150 (cited on p. 40).

Watts, A. L., Krishnan, B., Bildsten, L. and Schutz, B. F. (2008). 'Detecting gravitational wave emission from the known accreting neutron stars'. *Mon. Not. R. Astron. Soc.* **389**, 839. DOI: 10.1111/j.1365-2966.2008.13594.x. arXiv: 0803.4097 [astro-ph] (cited on p. 8).

Weinberg, S. (1990). 'Nuclear forces from chiral lagrangians'. *Phys. Lett. B* **251**, 288. DOI: 10.1016/0370-2693(90)90938-3 (cited on p. 109).

— (1991). 'Effective chiral lagrangians for nucleon-pion interactions and nuclear forces'. *Nucl. Phys. B* **363**, 3. DOI: 10.1016/0550-3213(91)90231-L (cited on p. 109).

Weisberg, J. M., Nice, D. J. and Taylor, J. H. (2010). 'Timing Measurements of the Relativistic Binary Pulsar PSR B1913+16'. *Astrophys. J.* **722**, 1030. DOI: 10.1088/0004-637X/722/2/1030. arXiv: 1011.0718 [astro-ph.GA] (cited on p. 5).

White, N. E. and Zhang, W. (1997). 'Millisecond X-Ray Pulsars in Low-mass X-Ray Binaries'. *Astrophys. J.* **490**, L87. DOI: 10.1086/311018 (cited on p. 38).

Wijnands, R. and van der Klis, M. (1998). 'A millisecond pulsar in an X-ray binary system'. *Nature* **394**, 344. DOI: 10.1038/28557 (cited on p. 6).

Will, C. M. (2014). 'The Confrontation between General Relativity and Experiment'. *Living Rev. Relativity* **17**, 4. DOI: 10.12942/lrr-2014-4. arXiv: 1403.7377 [gr-qc] (cited on p. 1).

Woan, G., Pitkin, M. D., Haskell, B., Jones, D. I. and Lasky, P. D. (2018). 'Evidence for a Minimum Ellipticity in Millisecond Pulsars'. *Astrophys. J.* **863**, L40. DOI: 10.3847/2041-8213/aad86a. arXiv: 1806.02822 [astro-ph.HE] (cited on pp. 46, 108).

Yoshida, S., Kiuchi, K. and Shibata, M. (2012). 'Stably stratified magnetized stars in general relativity'. *Phys. Rev. D* **86**, 044012. DOI: 10.1103/PhysRevD.86.044012. arXiv: 1207.1942 [gr-qc] (cited on p. 106).

Zhang, Y., Papa, M. A., Krishnan, B. and Watts, A. L. (2021). 'Search for Continuous Gravitational Waves from Scorpius X-1 in LIGO O2 Data'. *Astrophys. J.* **906**, L14. DOI: 10.3847/2041-8213/abd256. arXiv: 2011.04414 [astro-ph.HE] (cited on pp. 7, 111).